Microstructure, Mechanical Properties, and Biocompatibility Studies on Severely Surface-Deformed Mg Alloys

Ph.D. Thesis

by

NILESH KASHINATH KUMBHAR

DEPARTMENT OF METALLURGICAL ENGINEERING AND MATERIALS SCIENCE
INDIAN INSTITUTE OF TECHNOLOGY INDORE
July 2025

Microstructure, Mechanical Properties, and Biocompatibility Studies on Severely Surface-Deformed Mg Alloys

A THESIS

Submitted in partial fulfillment of the
requirements for the award of the degree
of
DOCTOR OF PHILOSOPHY
by
NILESH KASHINATH KUMBHAR

DEPARTMENT OF METALLURGICAL ENGINEERING
AND MATERIALS SCIENCE
INDIAN INSTITUTE OF TECHNOLOGY INDORE
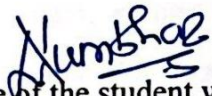**July 2025**

INDIAN INSTITUTE OF TECHNOLOGY INDORE

I hereby certify that the work which is being presented in the thesis entitled **MICROSTRUCTURE, MECHANICAL PROPERTIES, AND BIOCOMPATIBILITY STUDIES ON SEVERELY SURFACE-DEFORMED MG ALLOYS** in the partial fulfilment of the requirements for the award of the degree of **DOCTOR OF PHILOSOPHY** and submitted in the **DEPARTMENT OF METALLURGICAL ENGINEERING AND MATERIALS SCIENCE, Indian Institute of Technology Indore**, is an authentic record of my own work carried out during the time period from August 2021 to July 2025 under the supervision of **Prof. SANTOSH S. HOSMANI**, Department of Metallurgical Engineering and Materials Science, IIT Indore.

The matter presented in this thesis has not been submitted by me for the award of any other degree of this or any other institute.

Kumbhar 02.7.2025

Signature of the student with date

(Nilesh Kashinath Kumbhar)

This is to certify that the above statement made by the candidate is correct to the best of my/our knowledge.

02.07.2025

Signature of Thesis Supervisor with date

(Prof. Santosh S. Hosmani)

Nilesh Kashinath Kumbhar has successfully given his Ph.D. Oral Examination held on 1st July 2025

02.07.2025

Signature of Thesis Supervisor with date

(Prof. Santosh S. Hosmani)

ACKNOWLEDGEMENTS

NILESH KASHINATH KUMBHAR

**Dedicated to
My Gurus
and My
Family**

ABSTRACT

The Developing surface engineering strategies to enhance magnesium alloys' mechanical, tribological, and biological performance has received significant attention, particularly for biomedical and engineering applications. Surface Mechanical Attrition Treatment (SMAT), a severe surface plastic deformation technique, has emerged as a promising method for tailoring the surface properties of lightweight alloys through grain refinement, twin formation, and residual stress generation. In this work, two magnesium alloys were selected for investigation: (i) AZ91D alloy, which offers excellent mechanical and surface properties for general engineering applications but is limited in biomedical use due to its high aluminium content, and (ii) Mg5Zn0.2Ca alloy, a most biocompatible alloy free of aluminium, making it more suitable for biomedical applications. The present research systematically explores the role of SMAT process parameters, specifically ball velocity and surface coverage, on the microstructure evolution and mechanical, corrosion, and biocompatibility behaviour of the alloys.

In the initial phase of the research, the AZ91D alloy's surface was modified using SMAT at two different ball velocities: ~3 m/s and ~10 m/s (maintaining a constant percentage coverage). The SMATed specimens showed higher twin density near the surface, which was reduced gradually, and twin thickness was increased with increasing depth. Further, high-velocity balls caused more twin density and better grain refinement (~32 nm grain size at the surface). The higher ball velocity helped form a considerably thicker gradient layer (~3000 µm) with higher hardness (~1.98 GPa) and compressive residual stress (~281 MPa) within a shorter SMAT duration (~10 min). Ball velocity also influenced nanomechanical properties such as nanohardness, creep resistance, strain rate sensitivity (SRS), etc. The non-SMATed alloy's SRS was about 0.037-0.040. The gradient microstructure affected SRS. The SRS value near the SMATed surface (where the reduced grain size plays a dominating role) was about 0.018-0.027; however, it dropped suddenly to ~0.01 (with a slight increase in depth),

and subsequently, it raised with an increased distance in the SMATed layer (where twins played a dominating role).

The study was further extended to Mg5Zn0.2Ca alloy, a biodegradable alloy with excellent biocompatibility. A more comprehensive parameter space was explored, where the study presented the impact of colliding ball velocities (1, 5, and 10 m/s) and surface coverages (500, 1000, and 2000%) on the microstructure, hardness, and residual stress. SMAT formed a layer with a gradient in hardness, crystallite size, and twins. The surface hardness, ranging from 68 to 118 $HV_{0.05}$, increased with ball velocity and surface coverage. High ball velocity (~10 m/s) and surface coverage (2000%) induced high compressive residual stress of about -175.5 MPa at ~600 µm depth. The specimens SMATed with a ball velocity of ~5 m/s exhibited higher surface compressive residual stress for all surface coverages. The maximum compressive residual stress of about -153.5 MPa was observed at the surface for the specimens SMATed at ~5 m/s ball velocity and 500% coverage. The overall analysis revealed that the specimen treated at ~10 m/s ball velocity and 2000% surface coverage had the most refined grain structure, finely and densely distributed twins, maximum SMAT-induced thickness (~3000 µm), highest surface hardness (~2.1 times the non-SMATed specimen's hardness), and maximum compressive residual stress.

In the third phase, the study evaluated the biocorrosion and biocompatibility behaviour of SMATed Mg5Zn0.2Ca alloy. In this study, specimens were SMATed with ~5 and ~10 m/s ball velocities. A significant grain refinement occurred in surface-treated specimens, with higher ball velocity causing a fine grain size of ~21 nm and lower velocity instigating nano-twins near the surface. Moreover, SMAT improved the surface hardness by 1.7-2.0 times the non-treated specimen's hardness. Electrochemical and immersion tests performed in a cell culture medium indicated the highest corrosion resistance for the specimen SMATed using higher ball velocity, followed by the lower ball velocity, with the non-SMATed specimen exhibiting the least resistance. This response was ascribed to the thicker, more stable protective layer formation on the surface-treated specimens. Cytotoxicity tests performed by the extract method using murine fibroblast L929 showed lower cytotoxicity for the surface-treated specimens. This behaviour was linked to the lower corrosion rate with reduced Mg^{2+}

ion release and smaller pH increase. Enhanced bovine fibronectin adsorption on SMATed specimens further supported their improved biological performance. The grain refinement, increased surface energy, and grain boundary area positively influenced the biocompatibility behaviour of the SMATed alloy.

The final phase of this research evaluated the mechanical durability and surface integrity of SMATed Mg5Zn0.2Ca alloy. The influence of the gradient microstructure developed through SMAT on tensile, wear, and scratch properties was examined. Using the hardness attenuation model, surface strengthening characteristics were evaluated, and their correlation with tensile and wear performance was discussed. Between the two SMAT conditions, ~5 and ~10 m/s ball velocities, the latter produced finer grains, a deeper gradient layer, and higher surface hardness, translating into improved resistance to deformation. Tensile testing supported these results, with ~10 m/s ball velocity specimen achieving a yield strength of ~258 MPa and UTS of ~330 MPa, which were much higher than that of the non-treated specimens (YS: ~106 MPa and UTS: ~228 MPa). The UTS/YS ratio decreased from 2.15 (for non-treated specimens) to ~1.28 (for SMATed specimens), indicating reduced strain-hardening capacity. Wear experiments at 5, 10, and 20 N loads demonstrated a clear improvement in wear performance with increasing SMAT intensity, particularly for the ~10 m/s ball velocity condition, which showed reduced wear volume, wear rate, and coefficient of friction. Subsequent scratch tests under constant (50 N) and progressive (20-80 N) loading further confirmed this trend. Overall, specimen treated with ~10 m/s ball velocity showed the lowest wear rate (~0.6 × 10^{-3} mm^3/Nm), shallower scratch grooves, reduced material pile-up, and lower acoustic emission (AE), confirming enhanced resistance to surface damage and stable plastic flow under increasing contact stress.

In summary, the outcomes of this research demonstrate that SMAT is a highly effective technique for tailoring the surface and mechanical behaviour of magnesium alloys. While AZ91D benefits from enhanced surface strength and nanomechanical response for general engineering use, Mg5Zn0.2Ca exhibits exceptional improvements in mechanical, corrosion, and biocompatibility performance, making it an ideal candidate for biomedical applications. The systematic control of SMAT parameters

opens pathways for performance optimisation in engineering and bio-implant domains. Further, although previous studies have recognised the promise of SMAT for magnesium alloys, systematic investigations into how SMAT velocity (intensity) influences both mechanical and biomedical properties remain extremely limited. This thesis has successfully addressed that gap by establishing clear correlations between SMAT parameters, microstructural gradients, and multifunctional performance, representing an important and novel contribution to the field.

LIST OF PUBLICATIONS

1) **Nilesh K. Kumbhar**, A. Yamamoto, K. Wadhonkar, M.S. Baig, and S.S. Hosmani, "*The effect of severe surface deformation on microstructure refinement, corrosion, and biocompatibility of Mg5Zn0.2Ca alloy*", **Journal of Alloys and Compounds**, Vol. 1010, January 2025, Manuscript No. 178259 (2025). **DOI:** 10.1016/j.jallcom.2024.178259.

2) **Nilesh K. Kumbhar**, Vikesh Kumar, and S.S. Hosmani, "*Influence of Surface Mechanical Attrition Treatment Parameters on Microstructure and Residual Stress of Mg5Zn0.2Ca Alloy*", **Journal of Materials Engineering and Performance**, Vol. 33, No. 8 (April 2024), Pages 3746-3757 (2024). **DOI:** 10.1007/s11665-023-08714-7.

3) **Nilesh K. Kumbhar**, Vikesh Kumar, D. Singh, and S.S. Hosmani, "*Gradient Microstructure and Properties of Surface Mechanical Attrition Treated AZ91D Alloy: An Effect of Colliding Balls Velocity*", **Advanced Engineering Materials**, 27 July 2023, Manuscript No. 2300549, Pages 1-23 (2023). **DOI:** 10.1002/adem.202300549.

4) **Nilesh K. Kumbhar**, Manoj D. Joshi, Vikesh Kumar, and S.S. Hosmani, "*An Impact of the Recent Developments in Coating Materials and Techniques on the Corrosion Response of AZ91D Alloy: A Review*", **Advanced Engineering Materials**, 21 January 2023, Manuscript No. 202201680, Pages 1-27 (2023). **DOI:** 10.1002/adem.202201680.

x

TABLE OF CONTENTS

Chapter 5: Conclusions and Future Scope   148-157

LIST OF FIGURES

xxiii

LIST OF TABLES

NOMENCLATURE AND ACRONYMS

SPD	Severe Plastic Deformation
SSPD	Severe Surface Plastic Deformation
ASTM	American Society for Testing and Materials
EBSD	Electron Backscatter Diffraction
LAGBS	Low-Angle Grain Boundaries
HAGBS	High-Angle Grain Boundaries
SMAT	Surface Mechanical Attrition Treatment
SFE	Stacking Fault Energy
V	Impact Velocity
D	Ball Size
UFG	Ultrafine Grain
NG	Nanostructured Grain
GND	Geometrical Necessary Dislocations
TEM	Transmission Electron Microscopy
SAED	Selected-Area Electron Diffraction
BF	Bright-Field Image
COF	Coefficient of Friction
SEM	Scanning Electron Microscopy
E_{pit}	Pitting Potential
E_{corr}	Corrosion Potential
i_{corr}	Corrosion Current Density
R_S	Solution Resistance
R_a	Average Surface Roughness
XRD	X-ray Diffraction
SEM	Scanning Electron Microscopy
EDS	Energy Dispersive Spectroscopy
OM	Optical Microscopy
CT	Computed Tomography

h_{max}	Maximum Penetration Depth
h_f	Final Penetration Depth
A	Total Contact Area
h_c	Contact Depth
$\dot{\varepsilon}$	Creep Rate
H	Nanohardness
P_{max}	Maximum Load
m	Strain Rate Sensitivity
E-MEM	Eagle's Minimum Essential Medium
FBS	Fetal Bovine Serum
BSA	Bovine Serum Albumin
FN	Fibronectin
E	Surface Strengthening Energy
H_m	Matrix Microhardness
H_M	Maximum Microhardness
R	Decay Constant

Chapter 1: Introduction

Magnesium (Mg) is popularly known as the lightest structural metal. Its density (~1.74 g/cm^3) is lower than aluminium (~66%) and steel (~75%) [1]. This inherent lightweight nature, combined with a desirable strength-to-weight ratio, makes Mg alloys highly attractive for various industries where weight reduction is essential. Applications span across aerospace, automotive, biomedical, and consumer electronics sectors, where reduced mass can enhance performance, energy efficiency, and overall sustainability components [2, 3]. Due to their unique mechanical, thermal, and biological properties, Mg alloys have gained increasing attention for structural, functional, and biomedical purposes in recent years [4–6]. Their close mechanical compatibility with human bone, natural biodegradability, and biocompatibility have made specific Mg alloys promising candidates for next-generation medical implants and bioresorbable devices [7–11]. However, their surface characteristics strongly influence the performance of Mg alloys in real-world applications. Improving surface integrity without compromising bulk properties has become a critical research focus. Among the strategies explored, surface engineering techniques have shown great potential in tailoring the surface microstructure to meet application-specific demands [12–14].

One such promising technique is Surface Mechanical Attrition Treatment (SMAT), which belongs to the broader class of severe surface plastic deformation (SSPD) methods. SMAT modifies only the near-surface layers of materials through high-energy ball impacts, resulting in refined grain structures, enhanced hardness, and improved surface performance. Its unique ability to introduce a gradient microstructure makes it particularly suitable for Mg alloys, where surface-dominated properties such as wear, corrosion, and biocompatibility are of primary concern. In this context, the present research aims to investigate the effects of SMAT on Mg alloys, focusing on engineering and biomedical performance enhancements. The detailed scope, literature gaps, specific objectives of the study, and the current thesis structure are discussed in the following sections.

1.1 Scope of Study

AZ91D is one of the most widely used Mg alloys, particularly valued in engineering applications due to its well-balanced combination of mechanical and casting properties [15–17]. It offers several advantages over other magnesium grades, including excellent castability, good corrosion resistance, and enhanced creep resistance [18, 19]. These beneficial properties are primarily attributed to its relatively high aluminium content, which improves strength and thermal stability, especially under elevated temperatures. This behaviour makes AZ91D a promising material for critical load-bearing applications in the automotive and aerospace sectors. However, the aluminium content in this alloy limits its use in biomedical applications, as aluminium ion release during degradation can result in cytotoxic effects and inflammatory responses in vivo [20, 21].

To overcome these biocompatibility limitations, Mg-Zn-Ca alloy has emerged as a strong candidate for biomedical applications due to its favourable biocompatibility and controlled biodegradability [22, 23]. The alloy combines moderate mechanical properties with a safe chemical composition. Elemental optimisation studies in the literature have shown that the addition of small amounts of calcium (Ca) enhances ductility [24], whereas excessive Ca (>0.2 wt.%) leads to the formation of Mg_2Ca_2 phases at grain boundaries, reducing overall strength [24]. Zinc (Zn), on the other hand, strengthens grain boundaries and reduces the formation of harmful Ca-rich clusters [25]. However, when Zn content exceeds ~6 wt.%, the formation of the $Mg_{51}Zn_{20}$ phase accelerates corrosion [26]. The Mg5Zn0.2Ca composition strikes an optimal balance and is thus selected for this study. Despite its advantages, this alloy still has an opportunity to meet the better mechanical and corrosion resistance demands for long-term use in biomedical implants.

Recent advancements have also shown that even though AZ91D and Mg-Zn-Ca alloys possess a good balance of mechanical strength and corrosion resistance, further enhancement is necessary for their deployment in demanding engineering and biomedical environments. For instance, Sun et al. [23] demonstrated that extruded Mg-Zn-Ca alloys initially exhibited enhanced mechanical strength; however, prolonged immersion in simulated body fluid (SBF)

2

led to a substantial decline in yield strength (YS) and ultimate tensile strength (UTS), indicating a predicament of maintaining mechanical integrity during degradation. Similarly, grain refinement was found to control the corrosion rate of Mg alloys, where finer grains exhibited better resistance to localised corrosion due to the uniform distribution of precipitates and reduced susceptibility to micro-galvanic corrosion [27–29]. Therefore, improving surface properties such as hardness, wear resistance, corrosion behaviour, and biocompatibility is crucial [6, 12].

Various surface modification techniques have been investigated to address these concerns. Severe plastic deformation (SPD) processes like friction stir processing (FSP), high-pressure torsion (HPT), shot peening (SP), and equal channel angular pressing (ECAP) have been employed to refine surface grain structures [14, 17, 30, 31]. Moreover, laser surface melting, chemical treatments (like coatings and anodisation), and ion beam implantation with elements such as Fe, Ti, and Zr have improved wear resistance, corrosion behaviour, and cellular interactions [32, 33]. Among these methods, SMAT has shown exceptional promise in altering surface microstructure without affecting the bulk, offering controllable grain refinement, gradient structure formation, and enhanced mechanical and biological responses.

Although SMAT has been widely applied to materials like stainless steels [34, 35] and aluminium alloys [36], studies focusing on its impact on Mg alloys, particularly AZ91D and Mg5Zn0.2Ca, remain limited. Moreover, the available data on biodegradability, cytocompatibility, and protein adsorption behaviour after severe surface deformation often present inconsistent results. For example, Vignes et al. [17] found improved corrosion resistance in friction-stir processed AZ91D due to grain refinement, while Bagherifard et al. [13] reported increased corrosion rates and reduced cell viability in shot-peened AZ31, attributing the effects to surface roughness and defect density. These contradictory outcomes underscore the importance of controlling processing conditions and using physiologically relevant media for evaluation. Many prior studies employed simple saline solutions, failing to replicate human plasma's complexity, containing salts, proteins, and lipids [27, 37, 38].

In this context, the present study explores the application of SMAT on AZ91D and Mg5Zn0.2Ca alloys. Out of several SMAT parameters, this study aims to investigate how controlled variation of ball velocity and surface coverage influences gradient microstructure formation and, in turn, affects these alloys' mechanical, tribological, corrosion, and biological performance. Prior reports [39, 40] have indicated that SMAT-induced refinement of grains, formation of high-density twins, and development of compressive residual stresses can significantly improve surface-dominated properties [41]. However, a comprehensive understanding of how gradient structures influence nanomechanical properties, wear resistance, corrosion stability, and biocompatibility remains underdeveloped, especially in Mg alloys. Additionally, literature shows that variations in SMAT parameters, such as impact velocity and peening intensity, influence microstructure evolution. Gatey et al. [34] highlighted the influence of peening coverage on stainless steel, but such studies are lacking for HCP-structured Mg alloys. Moreover, the relationship between gradient microstructures and surface mechanical responses such as nanoindentation creep, strain rate sensitivity (SRS), or local deformation mechanisms is still poorly understood in the case of magnesium-based materials. In summary, the work aims to provide an integrated understanding of how SMAT can be tailored to improve the performance of Mg alloys.

1.2 Thesis Structure

Chapter 1 introduces the thesis, providing an overview of the scientific background, motivation, and objectives underlying the current PhD research.

Chapter 2 presents a comprehensive review of the literature related to SMAT and its effects on Mg alloys, with a particular focus on AZ91D and Mg5Zn0.2Ca. The chapter begins by outlining the importance of Mg alloys in structural and biomedical applications, followed by a detailed examination of their inherent limitations and the need for surface modification. It explores various SSPD techniques, highlighting the advantages of SMAT in inducing gradient nanostructures. The chapter further reviews studies on microstructure evolution, hardness gradients, nanomechanical behaviour, and residual stress development in SMATed Mg alloys. Special emphasis is placed on wear, corrosion, tensile, and

scratch behaviour studied through a surface engineering approach. Additionally, the chapter critically analyses recent findings on biocorrosion, cytocompatibility, and protein interactions in Mg-Zn-Ca alloys. Finally, the literature review identifies existing research gaps and establishes the scientific rationale for the current study.

Chapter 3 outlines the experimental methodology adopted in this study, detailing the preparation and processing of specimens. It provides an in-depth description of the SMAT procedure and the experimental protocols for microstructural characterisation, corrosion testing, cytocompatibility evaluation, protein adsorption analysis, tensile fracture testing, reciprocating dry wear assessment, and microscratch behaviour analysis. The chapter also includes the mechanical and electrochemical polishing steps applied during specimen preparation. A wide range of characterisation techniques used to analyse the microstructure, mechanical properties, and surface behaviour are presented, including optical microscopy (OM), scanning electron microscopy (SEM), energy-dispersive X-ray spectroscopy (EDS), electron backscatter diffraction (EBSD), transmission electron microscopy (TEM), X-ray diffraction (XRD), microhardness testing, nanoindentation, X-ray computed tomography (X-ray CT), pin-on-disc tribometer, and microscratch testing. This comprehensive overview provides a systematic understanding of all methodologies employed in the current research.

Chapter 4 presents a comprehensive analysis of the experimental findings and discussions structured to reflect the core objectives of the research. This chapter is divided into the following sections:

i. The chapter begins with a detailed investigation into the influence of SMAT ball velocity on the AZ91D Mg alloy, focusing on microstructure evolution, including twin density, grain refinement, and gradient layer development. The OM, SEM, TEM, and microhardness profiling outcomes are discussed alongside nanomechanical behaviour analysis using nanoindentation, emphasising the role of twin-mediated plasticity and strain rate sensitivity.

ii. Subsequently, the effect of SMAT parameters, specifically ball velocity and surface coverage, on the microstructure, surface hardness, and residual stress profile of the biodegradable Mg5Zn0.2Ca alloy is thoroughly examined. XRD-based $\sin^2\psi$ method is employed to evaluate the compressive residual

stress distribution, establishing a clear correlation between processing parameters and surface integrity.

iii. The following section evaluates the corrosion resistance and cytocompatibility of SMATed Mg5Zn0.2Ca alloy. This study includes immersion and electrochemical tests (OCP, EIS, and LSV) conducted in biological media to assess Mg^{2+} ion release, protective film stability, and degradation behaviour. Cytotoxicity is studied using murine fibroblast L929 cells, and protein adsorption behaviour is assessed to establish the biological efficacy of SMAT-modified surfaces under in vitro conditions mimicking human plasma.

iv. The final section addresses the impact of SMAT on mechanical performance, including tensile properties, wear resistance under circular loading (5, 10, and 20 N), and scratch behaviour under constant and progressive loading conditions. SEM, profilometry, and acoustic emission analysis assess surface deformation, material loss, and damage mechanisms. The synergistic effect of grain refinement, dislocation density, and gradient-structured layer on tensile behaviour and wear and scratch resistance is highlighted, confirming the effectiveness of SMAT in enhancing load-bearing capability and durability.

Collectively, Chapter 4 provides a holistic understanding of the microstructural, mechanical, electrochemical, and biological performance and related enhancements achieved through the controlled SMAT processing of AZ91D and Mg5Zn0.2Ca alloys.

Finally, **Chapter 5** comprises the overall conclusions of the current PhD thesis and the scope for future work.

Chapter 2: Literature Survey

2.1 Magnesium Alloys

2.1.1 Introduction

The increasing demand across various industries has accelerated the use of magnesium, primarily due to its low density and excellent strength-to-weight ratio. Consequently, in the twenty years, magnesium production has increased, and it is being alloyed with several other materials (Table 2.1) to make it suitable for different applications [4, 42, 43]. Prior research has thoroughly investigated the influence of alloying elements' proportions and combinations on Mg alloys' mechanical and chemical properties.

Table 2.1. The general influence of alloying elements on Mg alloys [44–48]

Alloying element	Properties enhanced
Aluminum (Al)	Hardness, strength, and ductility
Zinc (Zn)	Corrosion resistance, fluidity in casting, and room-temperature strength
Manganese (Mn)	Saltwater corrosion resistance
Rare Earth Metal	Corrosion and high-temperature creep resistance, strength, and decrease in weld cracking and porosity
Zirconium (Zr)	Grain refinement
Beryllium (Be)	Enhancement in oxidation resistance during welding and casting
Calcium (Ca)	Grain refinement

During the initial period of (2001-2011), different grades of Mg alloy, such as AZ91D [49], AM50 [50], AZ31B [51], AZ31 [52], ZK60 [53], AM60 [54], AM70 [55], ZE41 [45], ZK30 [56] and LAE442 [57] were explored. During this period, sufficient information about the properties of Mg alloys [44, 45, 58, 59] was obtained. Hence, most research focused on developing the technologies to alter their properties for different applications from 2012 onwards.

Mg alloys have gained significant attention as advanced lightweight materials. The mechanical characteristics of these alloys make them particularly

well-suited for applications where reducing weight contributes to enhanced efficiency and performance. As depicted in Figure 2.1, Mg alloys are utilised across various sectors, from mobility-focused areas like automotive and aerospace to compact electronics and precision biomedical devices [4, 5, 7, 42, 43]. Their compatibility with physiological environments has further advanced their role in medical implants and biodegradable scaffolds. Beyond these, their utility extends into industrial domains for components demanding strength, vibration control, and reduced weight. The broad spectrum of applications illustrates the growing importance of Mg alloys in both conventional and cutting-edge technologies.

01 Automotive Applications
Engine blocks, transmission housings, wheels, steering columns, seat frames and gearbox casings

02 Aerospace Applications
Aircraft fuselages, interior parts, gearbox housings, turbine housings and helicopter transmission casings

03 Electronics Applications
Laptop and mobile phone casings, camera bodies, power tools, and speaker frames

04 Biomedical Applications
Orthopedic implants, biodegradable stents, and temporary bone scaffolds, crucial for medical advancements

05 Industrial Applications
Chain saw housings, power tool enclosures, vibration damping parts, and robotics components

Figure 2.1: *Applications of Mg alloys*

The performance of Mg alloys in either application is highly dependent on their chemical composition and resulting microstructure, which directly influences properties such as tensile strength, ductility, corrosion resistance, and biocompatibility. Figure 2.2 presents an overview of several widely studied Mg alloys, summarising their typical composition, key mechanical or corrosion-related properties, and associated application areas [4, 47, 58]. This figure also reflects the strategic selection of alloy systems based on targeted functional requirements across various industrial and medical domains. Alloys such as AZ91D and AM60 are frequently cited for their use in automotive and consumer products due to their high strength, corrosion resistance, and castability.
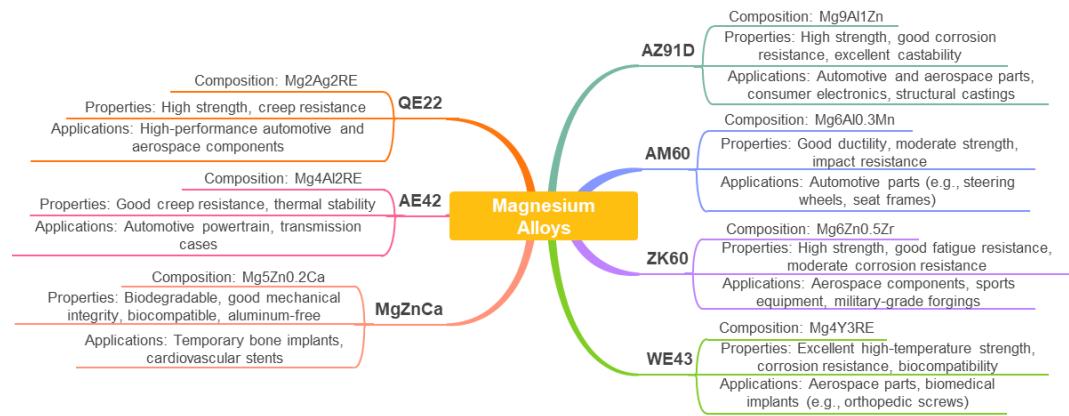
Figure 2.2: *Overview of common Mg alloys with their composition, properties, and applications*

Aerospace and high-performance applications often utilise AZ91D, ZK60, WE43, QE22, and AE42; each offers tailored benefits like fatigue resistance, thermal stability, or high-temperature strength. Thus, from the overall literature review, AZ91D remains one of the most commercially utilised Mg alloys, primarily appreciated for its excellent castability, moderate strength, and dimensional stability. Containing approximately 9 % aluminium and 1 % zinc, with minor manganese additions, AZ91D derives its strength from solid solution hardening and the precipitation of the β-$Mg_{17}Al_{12}$ phase. Its favourable strength-to-weight ratio makes it well-suited for automotive, aerospace, and electronic components such as engine casings, transmission housings, and portable electronic enclosures.

On the other hand, Mg-Zn-Ca alloys, particularly Mg5Zn0.2Ca, have emerged as promising candidates for bioresorbable implant applications [60]. These aluminium-free systems are designed to mitigate cytotoxicity while ensuring adequate mechanical integrity and controlled biodegradation.

2.1.2 Challenges

Despite their promising properties, Mg alloys face several challenges that limit their widespread adoption, particularly in harsh service environments and biomedical applications. Figure 2.3 presents a Venn diagram summarising the interconnected challenges that Mg alloys face in various applications. The diagram highlights the overlapping influence of corrosion, wear, tensile behaviour, and biocompatibility, with microstructural features (α/β phases, grain size, etc.) at the centre of these interactions. One of the most critical issues is their high

susceptibility to corrosion, especially in chloride-containing environments such as seawater or physiological fluids. This response is primarily due to the highly reactive nature of magnesium, which tends to form porous and unstable surface films that offer limited protection against aggressive ionic species [32, 61].
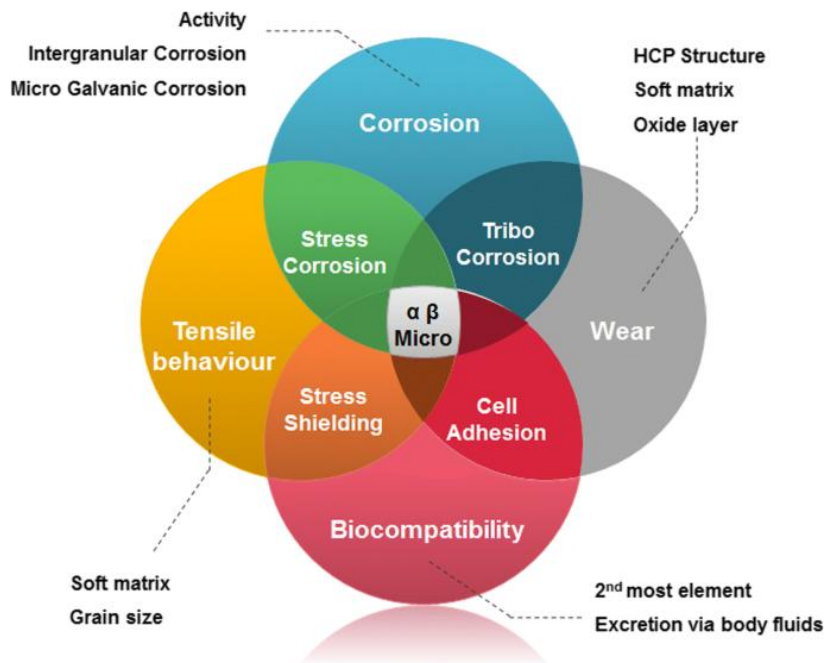
Figure 2.3: *Challenges associated with Mg alloys [62]*

Even though many Mg alloys, like AZ91D, have reasonably good mechanical properties, they exhibit limitations in high-temperature and corrosive environments. The β-phase, while beneficial for strength, can contribute to micro-galvanic corrosion due to its cathodic nature. Biocompatibility concerns in Mg alloys originate from their rapid in vivo degradation, risk of stress shielding, and uncontrolled ion release, particularly alloying elements like aluminium, which is associated with cytotoxic effects. The presence of aluminium, although structurally advantageous (for strength and castability), limits its use in biomedical applications due to its potential cytotoxicity. Further, rapid degradation compromises mechanical integrity over time and can lead to undesirable hydrogen gas evolution in biomedical implants. While magnesium is the second most abundant intracellular cation and is naturally excreted through body fluids, ensuring its safe degradation profile remains a critical challenge. Additionally, inconsistent cytocompatibility and unpredictable protein adsorption on corroding surfaces can negatively influence

cell adhesion, proliferation, and overall tissue integration, complicating their use in biomedical implant applications.

Wear-related limitations in Mg alloys primarily originate from their hexagonal close-packed (HCP) crystal structure, inherently low matrix hardness, and a brittle surface oxide film, all collectively compromising their resistance to material loss under tribological stress. Tribo-corrosion and stress corrosion represent overlapping zones where mechanical wear and electrochemical degradation coincide, posing severe durability limitations. Cell adhesion and stress shielding in the biomedical context impact the material's interaction with biological tissues. At the core, microstructure (e.g., α and β phase distribution) influences all these aspects, acting as the central link among these performance-limiting factors.

In addition, Mg alloys generally exhibit limited ductility and poor formability at room temperature. This behaviour is attributed to their HCP crystal structure, which restricts the number of active slip systems under low-temperature deformation. As a result, these alloys often suffer from early cracking or fracture under tensile loading or during forming operations. Furthermore, the low creep resistance and limited fatigue performance under cyclic loading raise concerns for applications requiring long-term structural reliability. Another significant limitation is their relatively low absolute strength compared to steel or titanium alloys, which restricts their use in high-load-bearing applications.

Overall, the combined mechanical and electrochemical limitations necessitate the development of novel alloy systems, microstructural control techniques, and advanced surface modification methods to enhance the overall performance of Mg alloys for both structural and biomedical use.

2.1.3 Addressing the Challenges to Enhance Properties

The osteostimulative nature of magnesium ions (Mg^{2+}) and mechanical properties closer to cortical bones make Mg alloy a promising biodegradable material for bone tissue restoration. Alloy design plays a vital role in governing the performance of alloys in various applications. For example, the Mg-Zn-Ca alloys are widely considered suitable for biodegradable medical devices. The elemental composition of the Mg-Zn-Ca system plays a crucial role in its performance. A

small amount of calcium addition to Mg alloys augments ductility [63]. It further promotes grain refinement and supports the formation of protective surface films, enhancing corrosion resistance. Conversely, Ca tends to form Ca-rich clusters (intermetallic Mg_2Ca phase) at grain boundaries, weakening their strength. The likelihood of Mg_2Ca formation increases with higher Ca content (greater than ~0.1 wt.%) [24]. Increased Ca content also leads to higher corrosion rates, increased local pH near the specimen surface, and more hydrogen gas evolution. Incorporating zinc primarily enhances grain boundary strength (in addition to the solid-solution strengthening) by improving cohesion and minimising the Ca-rich cluster formation in Mg alloys containing Ca. This improved boundary strength enables the material to withstand higher applied stresses, activating more complex deformation mechanisms without causing grain boundary cracking. Zn also increases the alloy's ductility and helps improve corrosion resistance. Zn addition up to 6 wt.% provides better mechanical properties and three times better corrosion protection; however, the $Mg_{51}Zn_{20}$ phase formation above 6 wt.% leads to a rapid corrosion rate.

Consequently, the Mg-Zn-Ca alloy containing ~5 wt.% Zn and ~0.2 wt.% Ca is a promising material. Further, intermetallic phases such as $Ca_2Mg_6Zn_3$ form a stable microstructure that regulates degradation rates in physiological environments. In vitro studies [64, 65] have demonstrated that Mg-Zn-Ca alloys degrade uniformly, minimising issues like localised corrosion or hydrogen gas evolution. With favourable protein response and natural ion excretion, their cytocompatibility positions them as a safer and more effective alternative for orthopaedic and cardiovascular implants.

Recent advancements have shown that even though Mg-Zn-Ca alloys possess a good balance of mechanical strength and corrosion resistance, challenges persist in their use in biomedical applications. For instance, Sun et al. [23] demonstrated that extruded Mg–Zn–Ca alloys initially exhibited enhanced mechanical strength; however, prolonged immersion in simulated body fluid (SBF) led to a substantial decline in yield and ultimate tensile strength, indicating a predicament of maintaining mechanical integrity during degradation. Similarly, grain refinement was found to control the corrosion rate of Mg alloys, where finer grains exhibited better resistance to localised corrosion due to the uniform

distribution of precipitates and reduced susceptibility to micro-galvanic corrosion [27, 66].

Despite these advancements, the current properties of Mg-Zn-Ca alloys remain insufficient for load-bearing implants, which demand a refined microstructure, superior corrosion resistance, and enhanced biocompatibility. Moreover, Mg alloys, like AD91D, which are popular for engineering applications, have certain limitations concerning the mechanical properties that impact their suitability for challenging functions.

Surface modification techniques have become increasingly important in addressing these challenges. Predominantly, material failures due to wear, fretting fatigue, and fatigue fractures originate at the surface; therefore, the surface engineering approach is hopeful. Unlike bulk alloying or thermomechanical processing, surface treatments allow for selective enhancement of surface properties without compromising the beneficial characteristics of the core material. This response is beneficial when a balance between surface durability and bulk mechanical compatibility is needed, as in the case of biodegradable implants or lightweight structural components. Improving corrosion resistance through surface engineering is a central focus, especially for biomedical applications where premature degradation can lead to loss of mechanical integrity and adverse biological responses. Surface modifications can also enhance microhardness, fatigue resistance, and wear behaviour, making Mg alloys more suitable for components exposed to friction, cyclic loading, or environmental stress.

In this regard, making the surface nanocrystalline via severe plastic deformation (SPD) processes is a topic of substantial interest [15, 16]. Among various approaches, mechanical surface treatments such as shot peening [67, 68], laser shock peening [18, 69], and surface mechanical attrition treatment (SMAT) [70, 71] have shown great promise. These methods refine the surface grain structure, induce compressive residual stresses, and create hardness gradients that improve overall performance. As research continues to evolve, surface engineering is expected to play a vital role in expanding the usability of Mg alloys across demanding applications.

2.2 Surface Severe Plastic Deformation (SSPD)

Severe plastic deformation techniques have been extensively studied over the past two decades for their ability to refine grain structures and improve metallic materials' mechanical and functional properties. Surface severe plastic deformation (SSPD) methods have gained particular attention due to their local nature, enabling surface modification without altering the material's bulk properties. These methods are especially beneficial for lightweight metals such as magnesium, which often suffer from poor surface hardness, low fatigue resistance, and high corrosion sensitivity. By inducing high strain rates and intense plastic deformation in the near-surface region, SSPD processes form gradient microstructures that significantly enhance surface performance.

As illustrated in the flowchart (Figure 2.4), SSPD encompasses a range of mechanical surface treatment techniques, including SMAT, SMRT (Surface Mechanical Rolling Treatment), USP (Ultrasonic Shot Peening), and conventional shot peening [18, 67, 70, 72]. These methods operate based on similar principles but differ in energy delivery, media type, and control parameters, such as intensity, temperature, etc. The key outcomes of SSPD can be broadly categorised into gradient modifications and property management. Gradient modifications include grain refinement, phase transformation, and the development of residual compressive stresses. These microstructural changes directly influence surface-related properties such as corrosion resistance, fatigue performance, hydrogen diffusion, and biocompatibility.
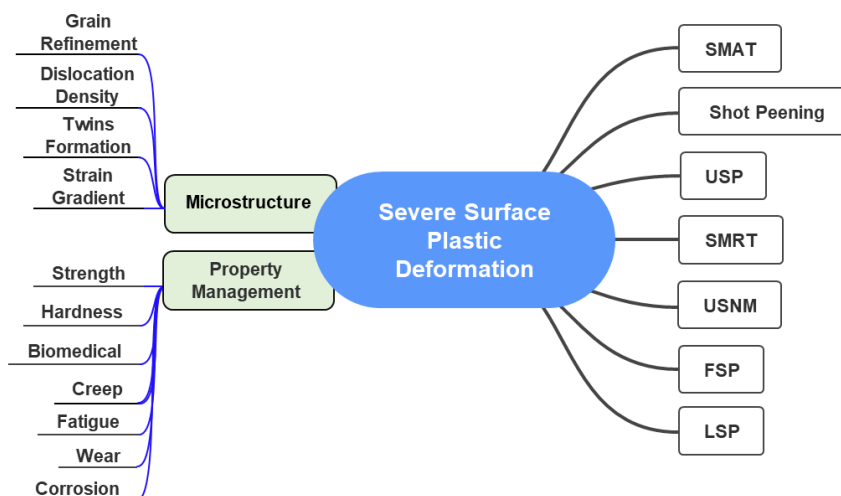
Figure 2.4: *Overview of SSPD techniques and their effects on microstructure and material properties*

The interdependence between structural gradient evolution and functional enhancement underscores the importance of process optimisation in SSPD. SMAT, in particular, has proven to be a versatile and scalable method for refining magnesium surfaces, making it a central focus in structural and biomedical material research. Compared to all SSPD techniques, SMAT has gained prominence for its efficiency, affordability, and ability to generate nanocrystalline layers on the material's surface, thereby significantly enhancing properties such as corrosion resistance, hardness, and wear performance. The concept of the SMAT process was proposed in 1999 [73]. SMAT was first applied to pure iron to create a nanostructured surface layer. Since its inception, the technique has been widely explored for modifying the surface characteristics of both ferrous and non-ferrous metals [70, 74]. SMAT has proven to be a highly effective method for enhancing the surface properties of Mg alloys by inducing controlled severe plastic deformation in the near-surface region [39, 68]. First, as shown in Figure 2.5, hardened steel balls (diameter: 1-10 mm) with a sufficient speed strike the specimen surface in random directions, generating intense localised impacts near the surface. The intensity of deformation gradually decreases toward the core, resulting in a strain gradient across the cross-section.
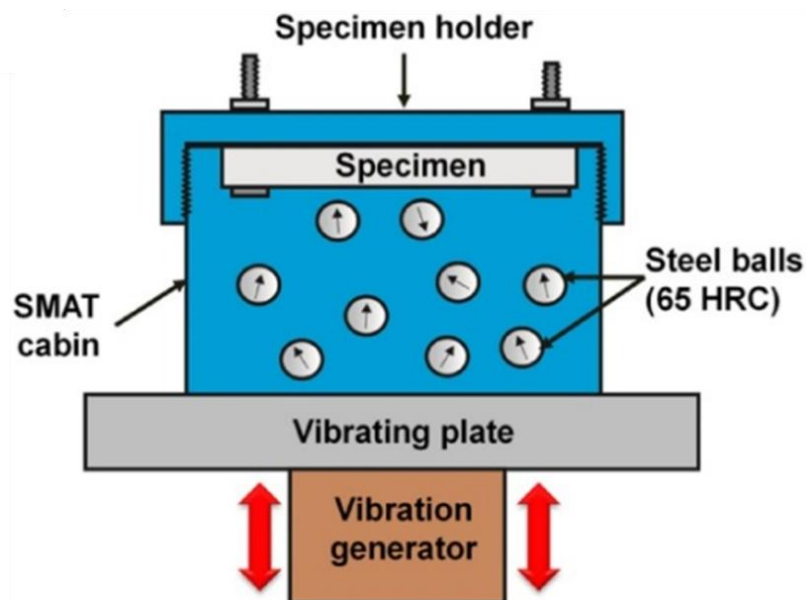
Figure 2.5: *Typical design of SMAT setup*

This strain accumulation activates various grain refinement mechanisms, the efficiency of which is influenced mainly by factors such as the alloy's crystal

structure and stacking fault energy (SFE). The treatment induces a high density of dislocations, grain refinement, and residual compressive stresses within a confined surface layer, resulting in a gradient microstructure that transitions from nanocrystalline grains at the topmost region to relatively coarse grains in the bulk. This gradient improves mechanical properties and imparts enhanced functional performance under service conditions.

The efficacy of SMAT depends heavily on processing parameters such as impact velocity, treatment duration, ball size, and surface coverage. These variables influence the depth and intensity of plastic deformation, thereby dictating the microstructural evolution and residual stress profile. In Mg alloys, which are inherently soft and have limited slip systems, the ability of SMAT to induce non-basal deformation mechanisms such as twinning and cross-slip is particularly beneficial, as it contributes to grain refinement and work hardening near the surface.

For AZ91D alloy, SMAT improved surface hardness, fatigue resistance, and wear behaviour without altering the alloy's bulk composition [68]. In the case of Mg-Zn-Ca alloys, SMAT could offer additional advantages by enhancing mechanical integrity and influencing corrosion behaviour and biocompatibility, which are critical for biodegradable implant applications. The refined grains and high defect density promote the rapid formation of protective passive films. At the same time, the compressive residual stresses act to suppress crack initiation and propagation during mechanical loading or corrosion-fatigue interactions.

Limited studies have recently demonstrated that systematic variation in SMAT parameters can be used to tailor the thickness of the gradient layer, optimise residual stress profiles, and fine-tune mechanical and electrochemical responses [40, 75]. This behaviour positions SMAT as a valuable surface engineering approach, particularly in applications demanding a combination of high strength, corrosion resistance, and functional surface durability without compromising bulk properties. Even though the SMAT parameters' role in steel's microstructure and properties has been broadly studied in the literature, such studies are lacking in the case of HCP-structured Mg alloys.

2.3 Microstructure Development and Mechanical Properties of the SMATed Mg Alloys

SMAT has been widely recognised as a potent surface modification technique capable of inducing profound microstructural refinement in Mg alloys. The high strain rate and repeated multidirectional impacts imparted by the process lead to severe plastic deformation confined to the near-surface region. This results in a gradient microstructure, characterised by nanocrystalline grains at the topmost layer, ultrafine grains in the intermediate zone, and progressively coarser grains towards the substrate [15, 68].

In Mg alloys, which have an HCP crystal structure with limited slip systems, deformation mechanisms such as twinning and grain boundary sliding dominate during SMAT. These mechanisms facilitate grain refinement under relatively moderate strain conditions [76, 77]. Mao et al. [78] investigated the effect of laser shock peening (LSP) on the twinning behaviour in AZ31B Mg alloy. Their results revealed a distinct gradient in twin density, with the highest concentration near the surface and gradually decreasing toward the core, as shown in Figure 2.6.
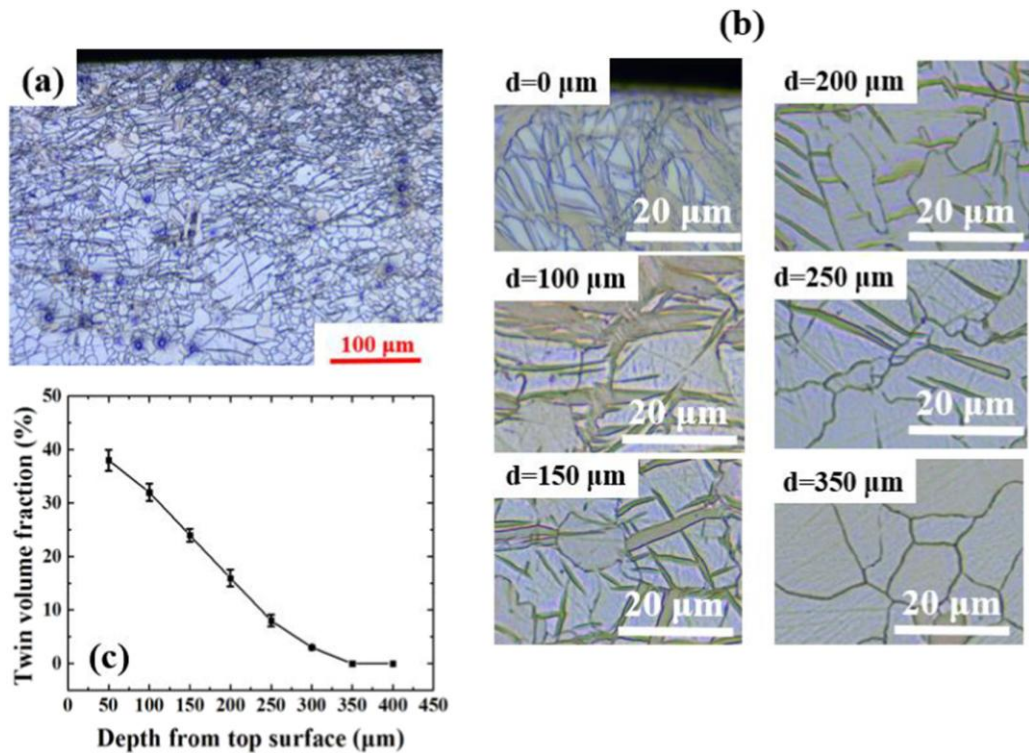
Figure 2.6: *Twinning microstructure in AZ31B Mg alloy after LSP: (a) optical micrograph showing gradient in twin structure, (b) variation in twin volume fraction (TVF) at different depths, and (c) plot of TVF versus depth from the surface [78]*

Further, Singh et al. [40] observed the formation of grains smaller than ~100 nm in AZ91D alloy after SMAT, primarily due to twinning-assisted dynamic recrystallisation. Shi et al. [79] also investigated the presence of nanograins near the SMATed surface of a Mg–Gd alloy, along with clear evidence of stacking faults, as shown in Figure 2.7. Transmission electron microscopy (TEM) and electron backscatter diffraction (EBSD) studies confirmed that SMAT leads to a high dislocation density and significant subgrain formation, especially within the top 50-200 μm of the surface [76, 80].
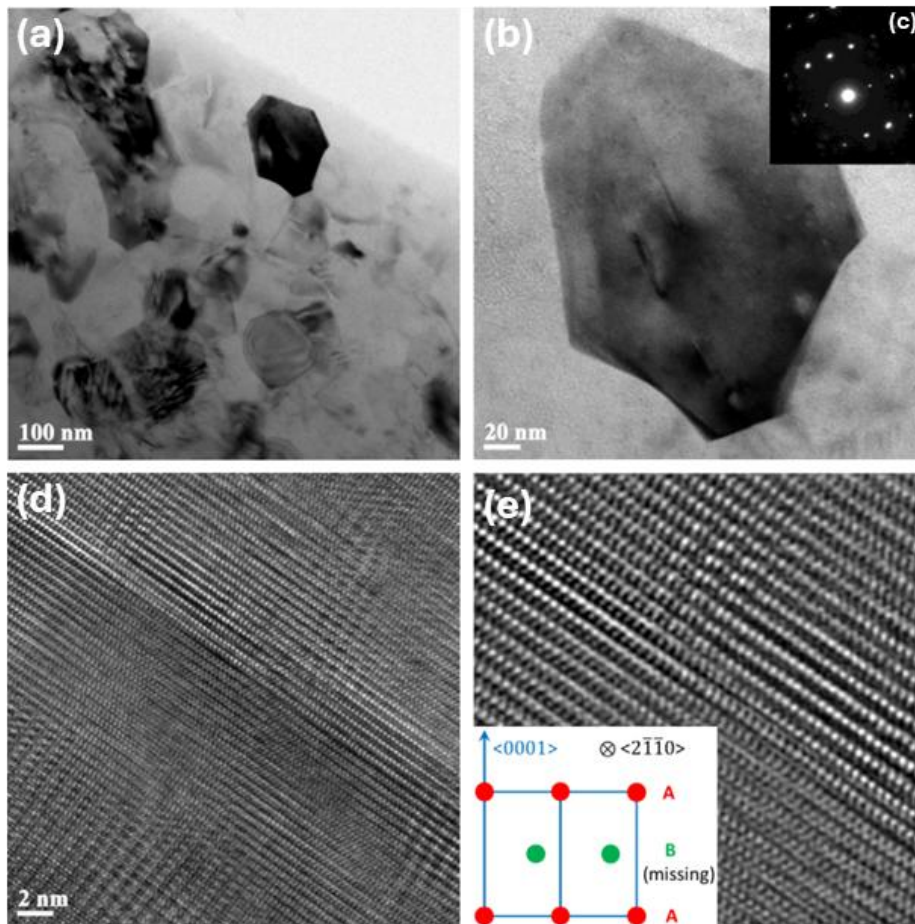
Figure 2.7: *(a) Bright-field TEM image showing nanograins, (b) magnified view of a selected grain, (c) SAED pattern with electron beam aligned along* $[2\bar{1}\bar{1}0]$ *(d) HRTEM image of the marked region, and (e) close-up showing stacking fault with schematic inset [79]*

These microstructural changes correlate strongly with improvements in surface mechanical properties. According to the Hall–Petch relationship, grain boundary strengthening becomes more pronounced as the average grain size

decreases, resulting in substantial increases in microhardness and yield strength in the SMAT-affected zone [81]. Several studies quantitatively demonstrated the mechanical benefits of SMAT in Mg alloys. For example, Wei et al. [82] reported increased surface hardness after SMAT at higher ball velocities. Similar trends have been observed in Mg-Zn-Ca alloys, where refined surface grains and the introduction of compressive residual stresses have led to improved wear resistance and fatigue life [83, 84]. In Mg5Zn0.2Ca alloy, refinement of surface grains down to the nanometer scale enhanced the mechanical integrity and improved surface passivation, which is particularly beneficial in biomedical contexts [85].

Furthermore, the gradient structure formed by SMAT offers the following unique advantage. The hard nanocrystalline surface provides excellent wear and fatigue resistance, while the relatively ductile core preserves overall toughness and deformation capacity [86]. This functional gradient design is especially desirable for components subjected to surface stress or cyclic loading, as it helps arrest crack initiation and propagation.

Overall, literature findings consistently confirm that SMAT is highly effective in enhancing the mechanical performance of Mg alloys through a synergistic combination of grain refinement, dislocation activity, and stress redistribution. These enhancements depend not only on the alloy system but are also strongly influenced by SMAT parameters such as impact velocity, treatment time, media characteristics, etc., all of which can be strategically optimised to tailor the mechanical response of the treated surface.

2.4 Biocompatibility of Mg Alloys and the Influence of Severe Deformation

Magnesium-based alloys have attracted considerable interest as temporary implant materials due to their favourable biomechanical properties, such as elastic modulus close to natural bone and biodegradability within physiological environments. Among these, Mg-Zn-Ca alloys have emerged as one of the most promising systems for biomedical applications, particularly because they avoid using cytotoxic elements such as aluminium or rare earth and offer a balanced combination of mechanical integrity, corrosion resistance, and biological safety. The chemical composition and microstructure strongly influence the

biocompatibility of Mg-Zn-Ca alloys. Zinc and calcium are essential for human metabolism – zinc supports enzymatic activity and cell proliferation, while calcium is critical for bone mineralisation. Therefore, substituting aluminium with zinc and calcium in the Mg matrix enhances corrosion resistance and promotes a more favourable biological response [87].

One of the key challenges in deploying Mg alloys in vivo is the rate and nature of biodegradation. Excessive degradation leads to rapid mechanical failure, accumulation of hydrogen gas, and local pH increase, all of which can trigger inflammatory responses. In Mg-Zn-Ca alloys, the degradation rate is significantly lower compared to commercial Mg alloys such as AZ91 or WE43. This controlled degradation is attributed to the formation of protective surface films, including magnesium hydroxide, zinc phosphate, and calcium phosphate compounds, which act as temporary barriers against aggressive body fluids [87, 88].

In vitro corrosion studies in simulated body fluids such as Hank's solution or Eagle's minimum essential medium (E-MEM) have demonstrated that Mg-Zn-Ca alloys release magnesium ions steadily without inducing cytotoxicity [12, 89]. Hayashi et al. [87] reported improved corrosion behaviour in physiological media, which is attributed to the formation of an insoluble salt layer. The schematic representation of this layer formation is shown in Figure 2.8.
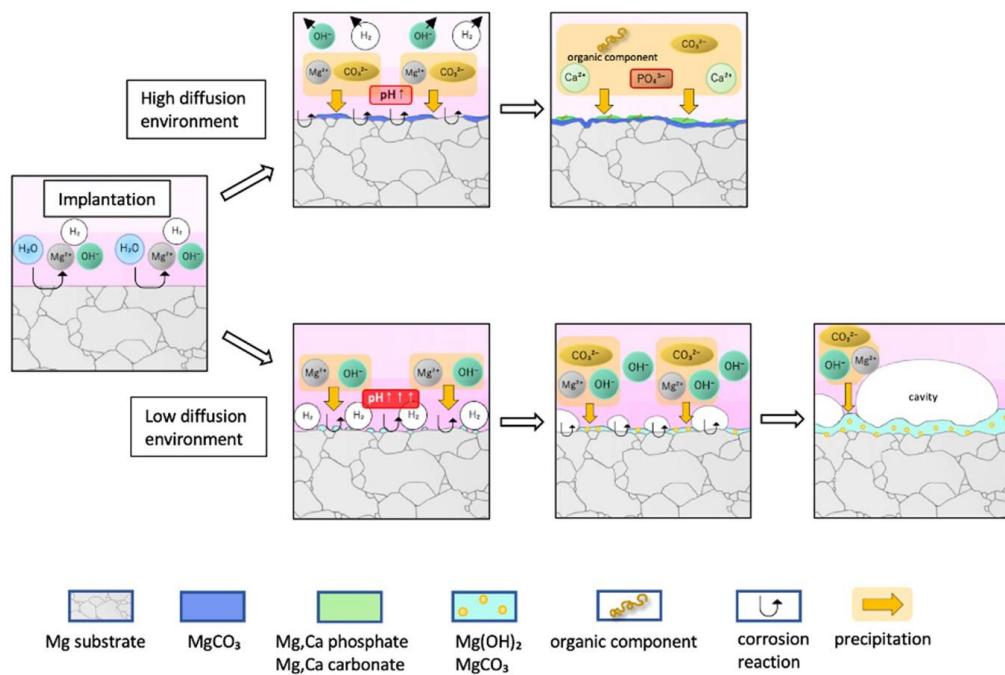
Figure 2.8: *Schematic representation of insoluble salt layer formation [87]*

The Mg-Zn-Ca alloys also support cell adhesion, proliferation, and differentiation, particularly for osteoblasts, indicating their compatibility with bone tissue regeneration. For instance, Meng et al. [66] showed that the degradation rate of the amorphous Mg-Zn-Ca alloy remained stable in vivo, with new bone tissue incorporated into the degraded area, which is considered a strong indicator of cytocompatibility. Regarding systemic response, animal model studies have reported minimal inflammation and acceptable degradation profiles when Mg-Zn-Ca alloys were implanted in femoral or subcutaneous locations. No severe fibrous encapsulation, necrosis, or toxicity was observed, indicating that these alloys are biocompatible at the cellular level and safe for in vivo use [65, 66].

Nevertheless, the available research articles on biodegradability, cytocompatibility, and protein adsorption behaviour of severely deformed Mg alloys often present ambiguous results. Some studies have shown that SSPDs positively affect corrosion resistance and biocompatibility, while others have reported negative impacts. For instance, Vignes et al. [17] reported that friction stir processing of AZ91D alloy led to a more uniform and stable protective layer formation, improving its corrosion resistance. This improvement was attributed to grain refinement and increased hardness [17]. Similarly, Lopes et al. [90] found that HPT-treated pure Mg, ZK60, AZ91, and AZ31 alloys exhibited enhanced corrosion protection (because of grain refinement and improved surface energy) and a similar level of cellular viability to that without HPT-treated Mg alloy specimens. According to Bagherifard et al. [13], severe shot peening of AZ31 alloy increased the corrosion rate (due to the increased surface roughness, craters, and high-density surface defects) and reduced osteoblast viability. Silva et al. [91] reported an impact of ECAP and HPT processing on the corrosion behaviour of pure Mg but no influence on its biocompatibility. The protective film formation and the physiological media's composition could play crucial roles in these contradictory results [37, 38, 92]. The most common physiological medium used in the literature was a sodium chloride solution. However, it has a simpler composition than human blood plasma, a representative body fluid containing various inorganic salts and organic compounds such as carbohydrates, proteins, and lipids. It is vital to employ an appropriate environment for Mg alloys to reasonably evaluate their corrosion and cytocompatibility for biodegradable implant applications.

Furthermore, surface modification of Mg-Zn-Ca alloys by micro-arc oxidation, plasma electrolytic oxidation, or mechanical treatments (like SMAT) significantly enhanced their corrosion resistance and bioactivity. The formation of dense and uniform passive layers reduced the burst release of magnesium ions and improved interaction with surrounding cells and tissues [37, 93]. The nanostructured surface layers introduced by mechanical attrition accelerated the deposition of calcium phosphate, thereby improving osteointegration [17, 91]. Anisimova et al. [94] observed the reduction in WE43 alloy's cytotoxicity after multiaxial deformation (MAD) treatment. Figure 2.9 illustrates the morphology and viability of MMSCs (murine mesenchymal stem cells) cultured in extracts of as-received and MAD WE43 specimens, showing live (green), dead (red), and nuclear-stained (blue) cells on the alloy surfaces at different magnifications.
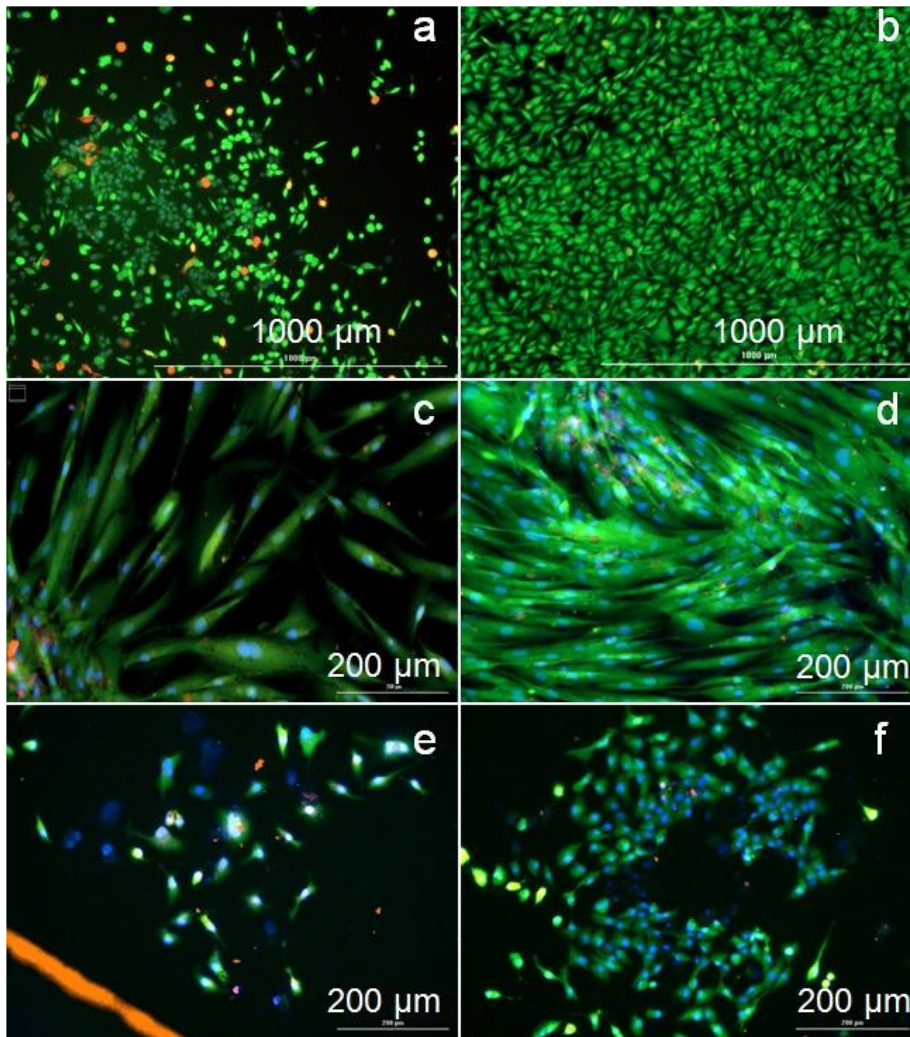
Figure 2.9: *MMSCs cultured in extracts of WE43 as-received (a, c) and WE43 MAD (b, d) at 100X and 200X magnifications and on alloy surfaces (e, f) [94]*

In conclusion, Mg alloys, especially Mg-Zn-Ca alloys, exhibit excellent biocompatibility due to their tailored degradation behaviour, absence of toxic alloying elements, and ability to support cell functions critical to tissue regeneration. Their combination of mechanical and biological performances makes them strong candidates for temporary orthopaedic and cardiovascular implants, warranting further optimisation through compositional tuning and surface engineering strategies.

2.5 Research Gaps

Despite extensive research on severe plastic deformation techniques for Mg alloys, the following gaps remain unaddressed and are explored in this work:

- While AZ91D Mg alloy is widely recognised for its potential in engineering applications, its relatively poor wear resistance and limited mechanical stability under extreme conditions restrict broader usage. Although SMAT has shown promise in enhancing surface properties, the influence of key SMAT parameters, such as ball velocity and surface coverage, on developing gradient microstructure and associated property enhancements in AZ91D has been inadequately explored.

- Most existing studies on SMAT focus on bulk mechanical improvements or surface refinement, but there is a limited investigation into the nanomechanical behaviour (such as nanohardness distribution, strain rate sensitivity, and creep response) across the gradient structure, particularly in SMATed AZ91D alloy. Understanding the depth-dependent evolution of these properties is critical for applications requiring surface durability under varying contact stresses.

- In the case of Mg5Zn0.2Ca alloy, a promising candidate for biodegradable implants, the effect of SMAT-induced microstructure on residual stress distribution is a key factor in enhancing properties like fracture toughness and fatigue resistance for bone fixation. Hence, this area needs deeper investigation. Furthermore, the correlation between SMAT parameters and the resulting surface integrity, including twin density, grain size, and dislocation structures, remains underexplored.

- Most studies evaluating the corrosion behaviour of Mg alloys have used simplified media such as NaCl solutions. However, the formation and stability of protective layers in physiologically relevant environments such as simulated body fluid (SBF), Dulbecco's modified eagle medium (D-MEM), Eagle's minimum essential medium (E-MEM) or other enriched cell culture mediums that closely mimic human blood plasma require further detailed investigations. This study includes the nature, thickness, and uniformity of corrosion product films formed on SMATed surfaces.

- The literature provides limited insights into how varying SMAT intensities influence the biological response, particularly regarding cytotoxicity, protein adsorption, and in vitro cell compatibility of Mg5Zn0.2Ca alloy. Clarifying these relationships is essential for assessing the clinical potential of this alloy.

- While some reports address the basic mechanical properties of SMATed Mg alloys, a comprehensive evaluation of tensile fracture behaviour, wear resistance, and scratch response under different SMAT conditions is still lacking. Understanding how SMAT-induced surface gradients influence failure modes and surface damage mechanisms under real-world conditions is necessary for engineering and biomedical applications.

2.6 Objectives

This research aims to investigate the effect of SMAT on the microstructure evolution and surface-dependent properties of AZ91D and Mg5Zn0.2Ca Mg alloys, focusing on enhancing their engineering and biomedical performance, respectively. To achieve this, the following specific objectives are framed:

1. To investigate the influence of vital SMAT parameters like ball velocity on the microstructure evolution and mechanical properties of AZ91D alloy, focusing on twin density, gradient thickness, grain refinement, and nanomechanical behaviour.

2. To study the effect of ball velocity and surface coverage on the SMAT processed microstructure, surface hardness, and residual stress profile of

Mg5Zn0.2Ca alloy and to establish a clear relationship between processing conditions and resulting surface integrity.

3. To evaluate the corrosion resistance and cytocompatibility of SMATed Mg5Zn0.2Ca alloy, emphasising Mg^{2+} ion release, passive film formation, and cellular response in E-MEM-based in vitro conditions.

4. To understand the effect of SMAT on the mechanical integrity of Mg5Zn0.2Ca alloy by studying tensile properties, wear performance, and scratch behaviour (under constant and progressive loads), accentuating material loss, friction, and acoustic responses.

Chapter 3: Experimental Strategy

This study investigated the influence of SMAT on the structural and functional performance of AZ91D and Mg5Zn0.2Ca magnesium alloys. The research methodology was systematically designed to align with the stated objectives. This section categorises the experimental approach into material preparation, SMAT processing, mechanical and microstructural characterisation, corrosion and cytocompatibility evaluation, and wear and scratch performance. The overall research plan of the current thesis is summarised in Figure 3.1.
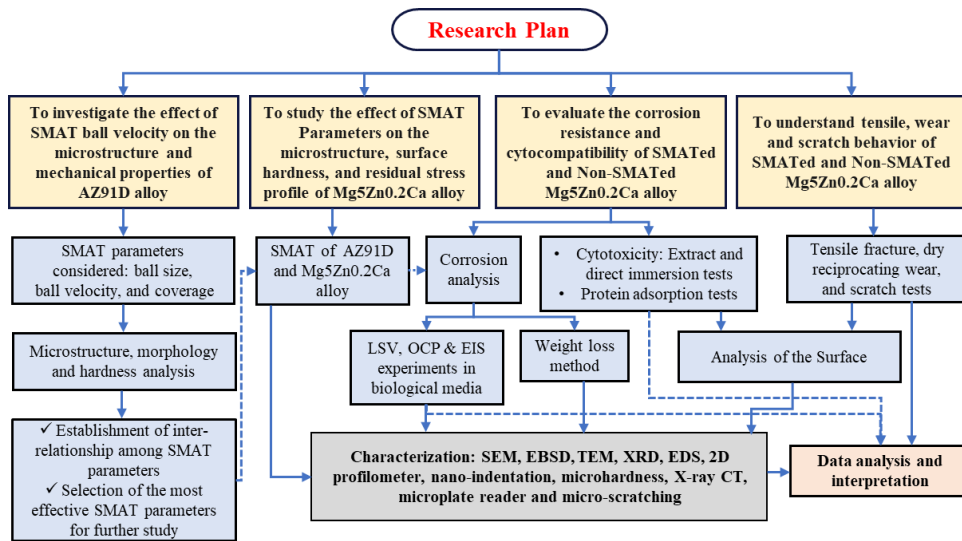
Figure 3.1: *Overall research plan of the current thesis*

3.1 Sample Preparation and SMAT Process

Commercial AZ91D and Mg5Zn0.2Ca alloys were selected for the investigations. Specimens of dimensions approximately 50 × 50 × 5 mm were polished using silicon carbide (SiC) papers, followed by sequential polishing with alumina and diamond suspensions. SMAT was performed using an in-house-developed mechanical vibration-assisted setup (Figure 2.5) comprising a SMAT chamber where hardened steel balls impacted the specimen surface at controlled velocities.

3.1.1 AZ91D Samples

The selected SMAT parameters and designations for AZ91D samples are presented in Table 3.1.

Table 3.1: Designations of AZ91D samples with SMAT parameters (here, 'coverage' is related to the percentage area of the SMAT cabin's floor occupied by the balls)

Sample designation	Sample condition	Ball velocity (m/s)	Coverage (i.e., ball packing ratio)	Ball diameter (mm)	SMAT duration (min)
NSM	Non-SMATed	-	-	-	-
SM-3v	SMATed	~3	25%	6	200
SM-10v	SMATed	~10	25%	6	10

The balls' kinetic energy (which depends on their size and velocity) and the attrition duration are critical parameters in the SMAT process. The two ball velocities (~5 m/s and ~10 m/s for Mg5Zn0.2Ca; ~3 m/s and ~10 m/s for AZ91D) were selected to study the influence of kinetic energy input during SMAT on the depth and extent of surface deformation. These values cover both moderate and high-energy regimes, allowing the investigation of strain gradients, twin evolution, grain refinement, and mechanical property variations systematically. The higher velocity (10 m/s) represents an aggressive deformation condition, while the lower one (3-5 m/s) provides a milder surface modification, allowing the gradient effect to be captured and correlated with performance outcomes (e.g., SRS, corrosion, cytotoxicity). To study the role of ball velocity in the SMAT processing of AZ91D alloy, the ball size, coverage factor of SMAT (i.e., the percentage area of the SMAT cabin's floor occupied by the balls), and percentage coverage of specimen surface (i.e., the percentage of the specimen surface impacted by the steel balls) were maintained constant for SM-3v and SM-10v specimens. In the SMAT process, 100% surface coverage took ~30 s at ~10 m/s and ~10 min at ~3 m/s. Therefore, to maintain the same percentage coverage of 2000% for both specimens, the attrition durations of 240 and 10 min were chosen for SM-3v and SM-10v specimens, respectively. Mathematically, the coverage can be expressed as:

$$\%Coverage = \frac{SMAT\ duration \times 100\%}{t_0}$$

where t_0 is the time for 100% coverage.

3.1.2 Mg5Zn0.2Ca Samples

Table 3.2 shows the selected SMAT process parameters and the samples' designations considered for the first part of the study on Mg5Zn0.2Ca alloy. The influence of ball velocity and surface coverage in the SMAT process on the Mg5Zn0.2Ca alloy was analysed while keeping other factors like ball size (6 mm diameter) and the number of balls (32) constant for all samples. Similar to AZ91D alloy, during the SMAT process, achieving 100% surface coverage took ~12 min at 1 m/s, ~70 s at 5 m/s and ~30 s at 10 m/s of ball velocity. For example, SMAT took ~30 s (i.e., ~0.5 min) at ~10 m/s for 100% surface coverage, corresponding to 1 peening intensity (PI). However, to achieve 500% surface coverage, a PI of 5 (i.e., 30 s × 5 = 150 s (2.5 min)) is considered. Similarly, a PI of 10 corresponds to a surface coverage of 1000%, and 20 PI corresponds to a 2000% surface coverage.

Therefore, different attrition durations were set (Table 3.2) to maintain an identical surface coverage percentage (500%, 1000%, and 2000%) for the three sets of samples.

Table 3.2: Sample designations and SMAT process parameters

Sample condition	Ball velocity (m/s)	Surface coverage (%)	SMAT duration (min)
SA1		500	60
SA2	1	1000	120
SA3		2000	240
SA4		500	6
SA5	5	1000	12
SA6		2000	23
SA7		500	2.5
SA8	10	1000	5
SA9		2000	10

The two most optimised samples, SA6 and SA9, were selected for the subsequent study phases. For clarity and consistency, SA6 will be referred to as 'SM-5v' and SA9 as 'SM-10v'.

3.2 Characterisation of Samples: Microstructure and Mechanical Properties

3.2.1 Microstructure and Microhardness

Post-SMAT, the cross-sections of all specimens were examined using optical microscopy (OM), scanning electron microscopy (SEM), and transmission electron microscopy (TEM) to study grain refinement, twin density, and deformation features. Phases, crystallite size, and residual stress vs depth profiles were investigated using X-ray diffraction (XRD) with Cu-K$_\alpha$ radiation. Residual stress was determined using the $\sin^2\psi$ method by progressively polishing the SMATed layer. Electron backscatter diffraction (EBSD) assessed grain orientation, twin structures, and dislocation density, while energy-dispersive X-ray spectroscopy (EDS) mapping provided elemental distribution.

For microstructural examinations, the specimens were first polished using SiC papers, navigated alumina, diamond suspensions (~3 μm, ~1 μm, and ~0.1 μm), and finally, with ~0.04 μm colloidal silica suspensions. Afterwards, these samples were chemically etched using the solution prepared with the following: 2.3 g picric acid, 5 ml acetic acid, 35 ml ethanol, and 5 ml distilled water. The etched specimens were examined under the OM and SEM. Electropolishing was performed after diamond polishing to reveal the microstructural features for EBSD analysis. Electropolishing was carried out using a 3:5 solution of orthophosphoric acid and ethanol (a total of 400 mL, with 250 mL ethanol). The sample (worked as anode) and cathode were securely held using tweezers and connected to a voltage-regulated circuit to facilitate electropolishing. Electropolishing was conducted in two steps: (i) 3 V for 30 s and (ii) 1.5 V for 2 min 15 s. The total electropolishing time was 2 min 45 s, ensuring a suitable surface quality for EBSD analysis of the specimens. The minute details of the SMATed specimens' microstructure were then investigated using the TEM.

The specimen surface was further studied with the help of the XRD technique (using Cu-K$_\alpha$ radiation). The crystallite size of the SMATed specimens was calculated employing the Scherrer formula (Eq. 3.1) [95]:

$$D = \frac{K\lambda}{\beta cos\theta} \tag{3.1}$$

where D = crystallite size (in nm), K = shape factor (= 0.9 for magnesium alloys), λ = wavelength of X-rays (for Cu-K$_\alpha$, λ = 0.15406 nm), β = Full Width at Half Maximum (FWHM) of the diffraction peak (in radians), and θ = Bragg angle (in radians). Following the crystallite size analysis, the Williamson–Hall (W-H) (Eq. 3.2) plot was used to calculate the lattice strain (ϵ) [95].

$$\beta cos\theta = \frac{K\lambda}{D} + 4\epsilon sin\theta \qquad (3.2)$$

For residual stress measurements across the SMATed layer, the material thickness was gradually reduced with the help of mechanical polishing. In this study, the $(104)_{\alpha\text{-hcp}}$ peak (2θ = 82.146°) was considered for the measurement, and the residual stresses generated within the deformed layers at different depths were quantified using the $\sin^2(\psi)$ method.

The Vickers microhardness tester (with ~10 s dwell time and 50 g load) was used for the hardness measurement. At every depth (d) from the SMATed surface, about ten indents were taken randomly to evaluate the microhardness distribution.

3.2.2 Nanomechanical Properties

The nanomechanical properties of the AZ91D alloy were investigated using a Hysitron TI-900 Nanoindenter equipped with a Berkovich tip. The measurements were carried out at 11-15 different depths from the SMATed surface. About five indentations were taken at each depth location (~100 μm apart). The nanoindentation technique was used to investigate the loading-unloading behaviour, nanohardness distribution, creep properties, pop-in effect, indentation size effect (ISE), and strain rate sensitivities (SRS) of NSM, SM-3v, and SM-10v samples.

The Oliver-Pharr approach was used to calculate the hardness [96]. As per this method, the hardness value can be calculated from the following equation (Eq. 3.3):

$$H = \frac{P_{max}}{A_c} \qquad (3.3)$$

where A_c is the contact area (nm^2), and P_{max} is the maximum indentation load (μN).

Along with H, creep is one of the dominant mechanisms affecting severely deformed materials' nanomechanical properties. It is the continuous deformation of

a material under a constant load as a function of time and temperature. In the constant load-holding indentation technique, creep can occur during dwell time. In this work, a load of 4 mN was applied at room temperature for around ~5 s holding time.

A creep rate for a crystalline material under steady-state conditions can be calculated using Eq. 3.4 [97]:

$$\dot{\varepsilon}_{creep} = \frac{AD_0 Gb}{kT} \left(\frac{b}{\delta}\right)^p \left(\frac{\sigma}{\mu}\right)^n exp\left(-\frac{\Delta Q}{kT}\right)^n \tag{3.4}$$

where δ is the grain size, T is the temperature, k is the Boltzmann constant, b is the Burgers vector, n is the stress exponent, p is the grain size exponent, ΔQ is the activation energy, G is the shear modulus, D_0 is the diffusion coefficient, A is a coefficient related to microstructure and temperature. Under the indenter, triaxial stresses are induced that can easily exceed the material's yield strength, even if the temperature is low. Thus, Eq. 3.4 is reduced to Eq. 3.5:

$$\dot{\varepsilon}_{ind.\ creep} = \left(\frac{1}{h}\right)\frac{dh}{dt} \tag{3.5}$$

where $\dot{\varepsilon}_{ind.creep}$ is the indentation creep rate (strain rate), and h is the instantaneous depth.

In general, indentation stress or hardness can be expressed in terms of an indentation load and instantaneous depth [98, 99]; however, to be more precise, the indenter's tip geometry was considered while calculating these values. Here, for a Berkovich indenter tip, the indentation stress ($\sigma_{ind.}$) or hardness (H) can be appropriately expressed as [97, 100]:

$$\sigma_{ind.} = \frac{P}{24.56\ (0.06R+h)^2} \tag{3.6}$$

where $\sigma_{ind.}$ is the indentation stress, R is the radius of the indenter tip (200 nm for this study), h is the instantaneous indentation depth, and P is the indentation load.

Further, strain rate sensitivity (SRS, m) mainly governs the rate-dependent behaviour of Mg alloys (related to formability, stress relaxation, creep, deformation rate change, etc.). The SRS was calculated by the slope of a linear part of a double logarithmic plot of indentation hardness vs creep rate (Eq. 3.7) [100].

$$m = \frac{\partial(\ln \sigma_{ind.})}{\partial(\ln \dot{\varepsilon}_{ind.creep})} \tag{3.7}$$

In the depth-sensing experiments, the value of m was a helpful parameter for identifying the dominant deformation and creep mechanisms.

3.2.3 Tensile Experiments

The tensile tests were conducted using an Instron 5967 testing machine with a 5 kN load capacity following the ASTM E8M standards. The tests were performed on NSM, SM-5v, and SM-10v Mg5Zn0.2Ca alloy specimens at a strain rate of 10^{-3} s^{-1}. The dimensions of the specimens used for the tensile experiments are presented in Figure 3.2. Both surfaces of such tensile samples were SMATed.
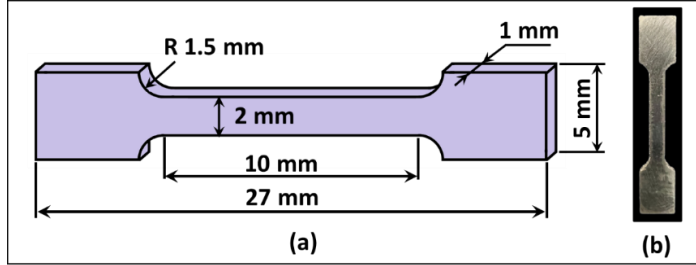
Figure 3.2: *(a) Dimensions of the micro-tensile specimen; (b) Original image of the specimen*

True stress-strain curves were generated from the engineering stress (σ_{eng}) - strain (ε_{eng}) data using the following standard Eqs. 3.8 and 3.9:

$$\text{True stress } (\sigma_t) = \sigma_{eng}(1 + \varepsilon_{eng}) \tag{3.8}$$

$$\text{True strain } (\varepsilon_t) = ln(1 + \varepsilon_{eng}) \tag{3.9}$$

Further, to analyse the material's work hardening behaviour, the strain hardening rate ($\theta = \frac{d\sigma_t}{d\varepsilon_t}$) was computed and plotted as a function of true strain. Additionally, the instantaneous strain hardening exponent (n) was calculated using the differential form of Hollomon's equation (Eq. 3.10):

$$n = \frac{d \ln \sigma_t}{d \ln \varepsilon_t} \tag{3.10}$$

A separate plot of instantaneous n vs true strain was included to highlight differences in strain hardening behaviour between SMATed and non-treated

specimens. This analysis provided insight into the effect of surface nanostructuring on the alloy's deformation mechanisms and plastic stability.

3.3 Biocompatibility Study

3.3.1 Biocorrosion

Eagle's minimum essential medium (E-MEM) added with 10 vol.% fetal bovine serum (FBS) was employed to assess the corrosion behaviour of the Mg5Zn0.2Ca alloy. Typical concentrations of major inorganic and organic components in E-MEM + 10% FBS (designated as 'EMEM-FBS' in the subsequent text) are shown in Table 3.3 [38, 87, 89], along with human and artificial plasma comparisons.

Table 3.3: Concentrations of major ions and organic components of human plasma, EMEM-FBS, and artificial plasma

Component	Human plasma	EMEM-FBS	Artificial plasma
Ca^{2+} (mol/L)	0.0025	0.0018	0.0018
Cl^- (mol/L)	0.103	0.1248	0.1253
Mg^{2+} (mol/L)	0.0015	0.0008	0.0008
K^+ (mol/L)	0.005	0.0054	0.0054
Na^+ (mol/L)	0.142	0.1412	0.1448
SO_4^{2-} (mol/L)	0.0005	0.0008	0.0008
HPO_4^{2-} (mol/L)	0.001	0.0011	0.0011
HCO_3^- (mol/L)	0.027	0.0262	0.0262
Glucose (g/L)	~1.1	1	—
Amino acids (g/L)	0.25-0.4	0.8596	—
Proteins (g/L)	3-5	63-80	—

Corrosion performance of the non-SMATed and SMATed specimens was assessed using electrochemical and immersion experiments. The former tests were performed using a conventional three-electrode system, which included the Mg5Zn0.2Ca alloy specimen with 0.264 cm^2 of exposure area (working electrode), a platinum wire (counter electrode) and a saturated Ag/AgCl electrode (3 M NaCl) (reference electrode). The electrodes were connected to a potentiostat integrated

with the frequency response analyser (VersaSTAT4, Princeton Applied Research, USA). The specimen was set into a sterile polycarbonate test chamber, which exposed only its top surface to the electrolyte. Before the test, EMEM-FBS was aerated overnight in a humidified air atmosphere with 5% CO_2 in an incubator maintained at 37 °C for pH adjustment by the dissolution of CO_2. Subsequently, 5 mL of pre-conditioned EMEM-FBS was added into the electrochemical test chamber and placed in the CO_2 incubator. Electrochemical impedance spectroscopy (EIS) was carried out at open circuit potential (OCP) following 2, 6, 12, and 24 h immersion periods. The measurements were conducted in the frequency range from $0.01 – 10^5$ Hz with an alternating current (AC) amplitude of 5 mV. The EIS data were analysed with an equivalent circuit model using Zview® software (ver. 4.0f, Scribner Associates, Inc. USA). Afterwards, potentiodynamic (PD) measurements were conducted at 0.5 mV/s scanning rate with a potential range starting from -0.25V vs. OCP until the current density exceeded 1 mA/cm^2. The corrosion potential (E_{corr}) and corrosion current density (i_{corr}) were obtained using the Tafel method. The pitting potential (E_{pit}), which is the potential giving the current density of 0.1 mA/cm^2, was also decided from the polarisation curves. The pH values of the electrolyte before and after the electrochemical test were also measured using a pH meter. Additionally, the corroded surface morphologies were examined using SEM and OM. All experiments were conducted in triplicate, at least.

For the immersion test, each specimen ($10 \times 10 \times {\sim}3.5$ mm) was immersed in 27.5 mL of the EMEM-FBS for 1, 4, and 7 days at 37 °C under the atmosphere of 5% CO_2 in humidified air, following the principles of ISO 10993-15 and in alignment with prior studies on corrosion testing of magnesium alloys [12, 61, 66] . After these periods, weight loss and pH measurements were performed, and the corrosion rate was calculated. After 1 day of immersion, the EMEM-FBS was collected for the Mg^{2+} release quantification using inductively coupled plasma optical emission spectrometry (ICP-OES). Three specimens were tested for each condition to ensure reproducibility. XRD analysis further confirmed the insoluble salt layer formation on the specimens immersed for 1, 4, and 7 days. The insoluble salt layer was then removed with a chromic acid solution (20 g CrO_3, 1 g $AgNO_3$, and 2 g $Ba(NO_3)_2$ in 100 mL ultrapure water). After acid cleaning, microfocus X-ray CT (SMX-90CT, Shimadzu Corp. Japan) images were captured optimally to

decide the pitting depth on the 7-day-immersed specimens. 2D slices with a resolution of 18 μm per pixel were used to calculate the pitting depth. After capturing a series of 2D slices through CT analysis, the pits were identified across these slices, with the pixel positions where each pit began and ended being noted. The pitting depth for each pit was then determined by multiplying the number of 2D slices (between the start and end of the pit) by the slice thickness of 18 μm per pixel. This process was repeated for the top 300 pits, and the average pitting depth was calculated. Moreover, the SEM micrographs and EDS results were obtained for the specimens after the immersion test.

3.3.2 Cytotoxicity assay by extract method

L929 murine fibroblasts (NCTC Clone 929, purchased from Dainippon Pharmaceutical Co. Ltd., Japan) were employed for *in vitro* cell culture experiments to assess the cytotoxicity of the material by the extract method described in ISO10993-5. The procedure of the cytotoxicity test is schematically presented in Figure 3.3. The Mg5Zn0.2Ca specimen was set into a sterile polycarbonate chamber with a silicone sponge lid for aeration. Only the specimen's top surface (0.95 cm^2) was exposed to 0.32 mL of the extract medium (EMEM-FBS), giving the surface area to extraction medium ratio of 3 cm^2/mL. The chamber was placed at 37 °C for 24 h in a 5% CO$_2$-containing humidified air atmosphere. After 24 h, the supernatant (extract) was collected and diluted to 3.1, 6.25, 12.5, 25, and 50% in EMEM-FBS.
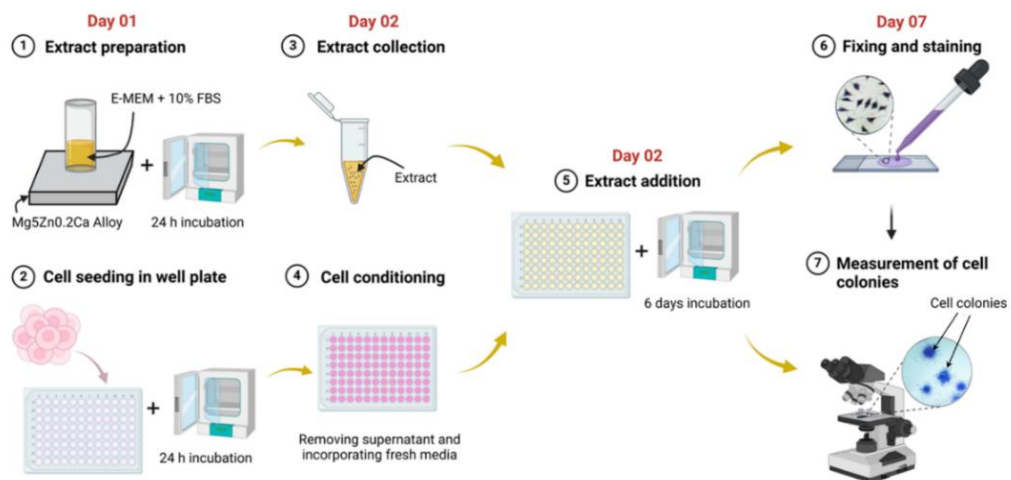
Figure 3.3: *Schematic explanation of cytotoxicity assay by extract method*

Parallelly, L929 cells were seeded at 50 cells per well into 24-well culture plates and allowed to attach for 24 h in a CO_2 incubator. After 24 h, the supernatant in the well was discarded, and 0.5 ml of extract (or its dilution) was transferred into it. The same EMEM-FBS portion was introduced into the control well. Three wells were used for each extract concentration to ensure repeatability. The microplate was incubated for 6 days in the CO_2 incubator. Following the second incubation, the cells were fixed with 25% glutaraldehyde and stained using a 10% Giemsa solution. The microplate was subsequently air-dried, and the colonies were counted. The relative plating efficiency (RPE) was then determined using Eq. 3.11:

$$RPE\ (\%) = (N_{sample}/N_{control}) \times 100 \tag{3.11}$$

where N_{sample} and $N_{control}$ represent the average number of colonies in the control wells with and without the extract, respectively. The inhibitive concentration giving RPE 50% (IC_{50}) was determined by converting RPE to a probit unit and applying the least-squares method against the logarithm of extract concentration.

3.3.3 Protein Adsorption Test

The solutions of bovine serum albumin (BSA, 20 µg/mL in artificial plasma) and bovine fibronectin (FN, 30 µg/mL in artificial plasma) were used for protein adsorption analysis. The composition of the artificial plasma is detailed in Table 3.3. First, each of the Mg5Zn0.2Ca specimens of $10 \times 10 \times \sim3.5$ mm (SM-5v and SM-10v) or $11 \times 11 \times \sim4$ mm (NSM) was placed in a 24-well microplate and immersed in $0.88 - 0.90$ mL (SM-5v and SM-10v) or 0.72 mL (NSM) of the protein solution. In the control well, 1.2 mL of the protein solution was poured. The amount of the protein solution was controlled to be the same depth in the well, which means the same wall area was exposed to the protein solution. The specimens were placed at 37 °C under a 5% CO_2 atmosphere in humidified air for 2 h. Then, the Coomassie Plus (Bradford) Assay Kit (Pierce Biotechnology, USA), following the protocol supplied, was employed to quantify protein concentration in the supernatant. Briefly, a 150 µL portion of the supernatant was poured into the well of the 96-well assay plate, and then a 150 µL portion of the Coomassie Plus reagent was added. Then, the plate was mixed in a microplate mixer for 30 s and left at room temperature for 10 min. The absorbance was measured at 595 nm using a microplate

reader (MultiskanTM SkyHigh, Thermo Scientific, USA), and the protein concentration in the solution was quantified using the calibration curves of BSA and FN. The adsorbed amount of the protein, A (µg/cm^2), was calculated using Eq. 3.12.

$$A = (C_{Control} - C_{Specimen}) \frac{V}{S_{Specimen}} \qquad (3.12)$$

where $C_{Control}$ and $C_{Specimen}$ represent the protein concentration of the supernatant in each control and sample well (µg/mL), respectively. V denotes the protein solution volume in the well (0.8 or 0.95 mL for NSM and SM-5v/SM-10v), and $S_{Specimen}$ indicates the whole surface area of the specimen (3.6 or 3.0 cm^2 for NSM and SM-5v/SM-10v).

3.4 Wear and Microscratching Experiments

The dry sliding wear performance of NSM, SM-5v, and SM-10v was evaluated using a ball-on-disc tribometer following ASTM G133. A schematic of the tribometer is shown in Figure 3.4.
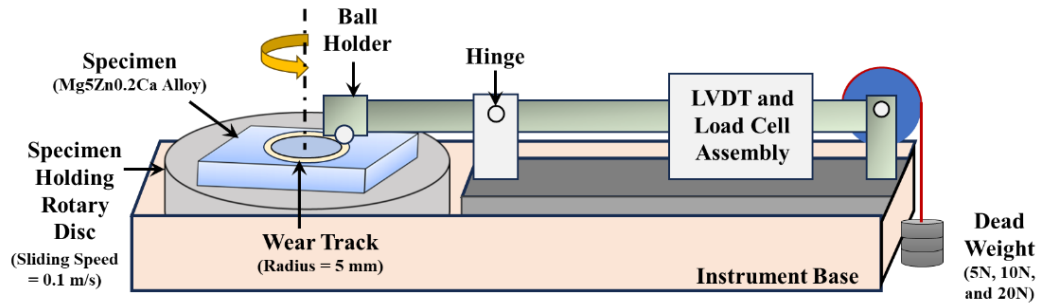
Figure 3.4: *Wear setup*

All experiments were conducted at ambient temperature (30-40°C) in laboratory conditions. An ~8 mm diameter alumina (Al$_2$O$_3$) ball, with hardness 1500-1650 HV and surface roughness of ~0.065 µm, served as the counter body. Tests were performed under normal loads (P) of 5, 10, and 20 N. The sliding velocity was fixed at ~0.1 m/s, and the wear track radius was maintained at ~5 mm. Each test was continued until a total sliding distance (D) of ~500 m was achieved. Before testing, the specimens and balls were ultrasonically cleaned with ethanol and dried. The coefficient of friction (COF) was monitored continuously throughout the test. COF profiles were recorded as a function of time, and average COF values

were calculated after eliminating the initial running-in period of ~400 s to reflect steady-state behaviour.

The wear volume loss of the specimens was calculated using wear track geometry. The wear track's 2-dimensional (2-D) profiles were captured at four positions using a contact 2-D profilometer to determine the average cross-sectional area (A). The wear volume (V) was then calculated by multiplying A with the corresponding track length. From the calculated wear volume, the wear rate ($= V/D$) and specific wear rate ($= V/(D \times P)$) were determined. To estimate wear on the alumina counter ball, the diameter of the wear scar was measured using a stereomicroscope. The depth (h) and volume loss (V_c) of the counter surface (mm^3) were calculated using Eqs. 3.13 and 3.14:

$$h = R - \sqrt{R^2 - r^2} \qquad\qquad (3.13)$$

$$V_c = \frac{\pi h}{6}(3r^2 + h^2) \qquad\qquad (3.14)$$

where R is the radius of the alumina ball (5 mm), r denotes the radius of the wear scar (mm), and h is the height (depth) of the wear scar (mm). All experiments were repeated three times to ensure reproducibility and average values were used in the analysis.

Following the ball-on-disc wear experiments, microscratch testing was conducted to gain deeper insight into the surface deformation behaviour of non-treated and SMATed Mg5Zn0.2Ca alloy specimens using a microscratch tester equipped with a conical diamond stylus. Two loading conditions were employed: a constant load of 50 N and a progressive load ranging from 20 to 80 N, applied over a 5 mm scratch length. Key parameters such as penetration depth, COF, and acoustic emission (AE) were recorded during the tests. Post-scratch surface features were analysed using a 2-D profilometer and SEM to assess groove morphology, material pile-up, and surface damage.

3.5 Statistical Analysis

Wherever required, statistical analysis was conducted to evaluate the significance of differences between experimental groups. All data are presented as mean ± standard deviation (SD) from a minimum of three independent measurements for each test condition. One asterisk (*) indicates a statistically

38

significant difference with $p < 0.05$, while two asterisks (**) represent a highly significant difference with $p < 0.01$. The statistical significance was determined using student t-test and one-way analysis of variance (ANOVA) followed by Tukey's post-hoc test to assess pairwise differences between groups. This analysis ensures the reliability and reproducibility of the reported results, and the asterisks in the graphs denote the level of statistical significance for the observed differences.

Chapter 4: Results and Discussion

This chapter presents a comprehensive interpretation and critical analysis of the experimental outcomes. The discussion focuses on correlating observed results with underlying theoretical frameworks, previously published literature, and established scientific principles. Each set of findings is meticulously examined to uncover underlying mechanisms, identify consistent trends or anomalies, and evaluate their implications within the broader context of the research objectives. Overall, this chapter aims to bridge the gap between raw data and scientific understanding, offering insightful explanations that contribute meaningfully to the current body of knowledge in the field.

4.1 Evolution of Gradient Structure in Surface Mechanical Attrition Treated AZ91D Alloy: An Effect of Colliding Balls Velocity

The surface properties of the AZ91D alloy can be altered using SMAT, a promising method of severe surface deformation, where the role of process parameters is crucial. This section initiates the results and discussion chapter by exploring the influence of ball impact velocity during SMAT on the microstructural evolution of AZ91D magnesium alloy. In this study, specimens are SMATed using ~3 m/s (SM-3v) and ~10 m/s (SM-10v) ball velocities (maintaining a constant percentage coverage) (Table 3.1). This study systematically examines the development of a gradient structure through variations in twin formation, grain refinement, and deformation depth. Comprehensive microstructural characterisation is performed using OM, SEM, and TEM, supported by microhardness profiling across the cross-section. Furthermore, nanomechanical behaviour is assessed via nanoindentation to evaluate nanohardness, creep behaviour and strain rate sensitivity, revealing the role of twin-mediated plasticity and gradient strengthening mechanisms. The findings provide crucial insights into the relationship between processing parameters and surface modification efficacy in the Mg alloy.

4.1.1 Microstructure of NSM, SM-3v, and SM-10v Specimens

The SEM micrographs and EDS results of the non-SMATed (NSM) specimen are shown in Figure 4.1.1. The grain boundaries of the specimen are enveloped by a thick compound/phase, which is accompanied by microconstituents with a lamellar morphology (Figure 4.1.1(a)). The EDS results show the Mg and Al (and a small proportion of Zn) enrichment along the grain boundaries (Figure 4.1.1(b)-(g)), which indicates that the compound phase formed in the specimen is β-$Mg_{17}Al_{12}$. The central region of the grains shows the dominance of Mg with some Al content (Figure 4.1.1(d)), which is an Mg-Al solid solution, called the α-phase. The lamellar microconstituents (close to the β-phase: see Figure 4.1.1(a)) are $\alpha+\beta$. Such a microstructure evolution occurs during the solidification of AZ91D alloy [18].
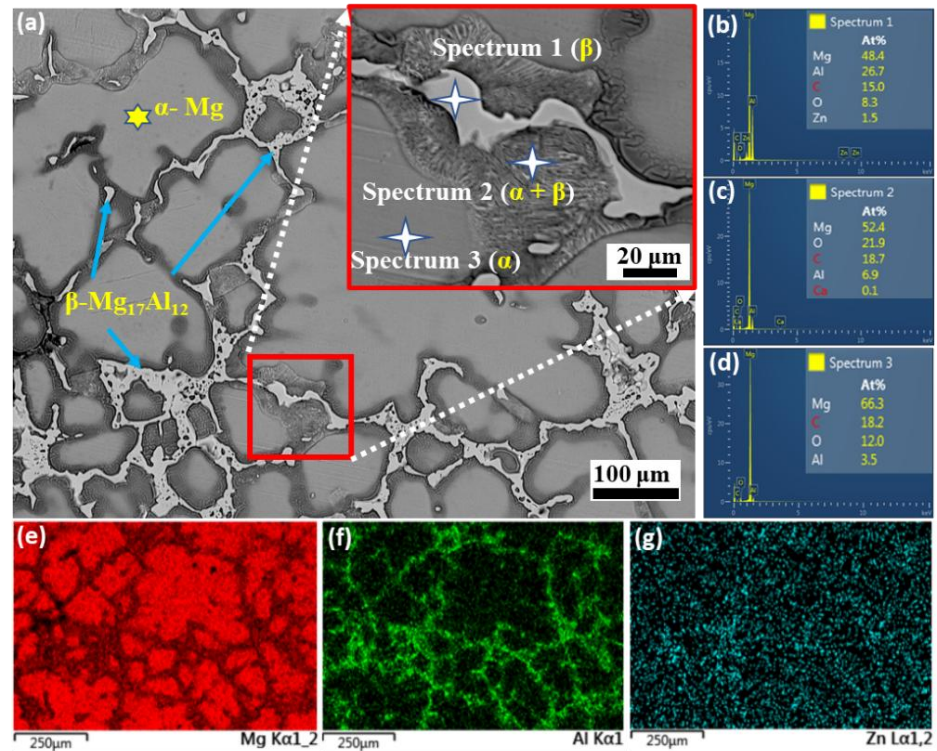
Figure 4.1.1: *(a) SEM micrographs, (b-d) EDS spectra of the locations indicated in (a), and (e-g) EDS maps of the NSM specimen*

During the initial die-casting stage, the Mg-Al (solid solution) grains form. The grain boundaries are enriched/supersaturated with Al during subsequent cooling, leading to the precipitation of the β-phase. The excess Al in the grain

boundary region causes the decomposition of the solid solution (with eutectic composition) into lamellar α+β during slow cooling.

The effect of SMAT on the AZ91D alloy's microstructure is observed in optical and SEM micrographs (Figures 4.1.2-4.1.4). Since AZ91D Mg alloy possesses low stacking fault energy, its plastic deformation is primarily caused by dislocation slip and twinning [3]. Therefore, the SM-3v and SM-10v specimens display a considerable presence of twins. These specimens show higher twin density near the SMATed surface (Figures 4.1.2-4.1.3), which is reduced gradually with increasing depth (*d*) from the SMATed surface (Figure 4.1.4). Wang et al. [68] also evidenced the presence of higher twin density near the surface of AZ91D alloy after shot peening. Twin density is more prominent and denser in the SM-10v specimen (even in the deeper regions: see Figure 4.1.3(b) and (e)) than in the SM-3v specimen.
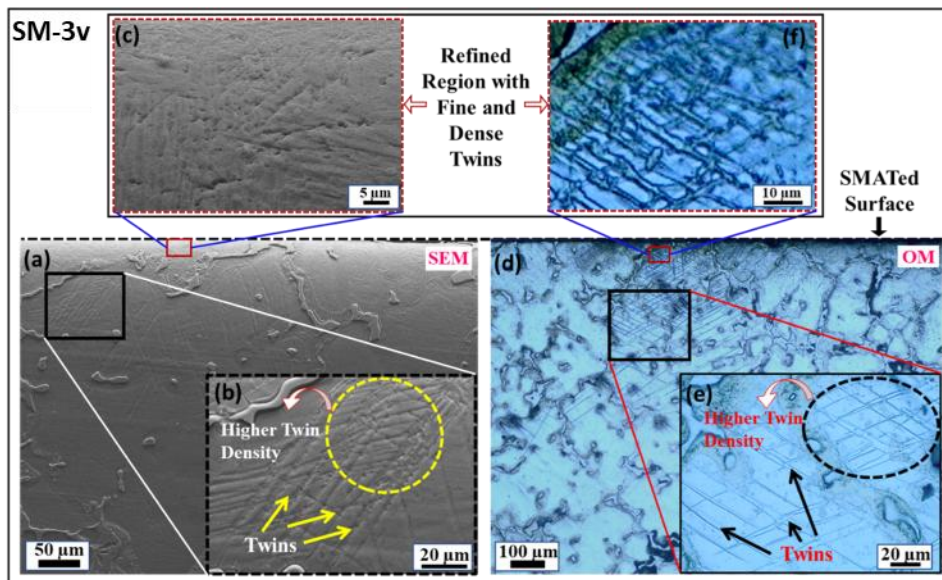
Figure 4.1.2: *SEM and optical micrographs of the near-surface region of the cross-section of the SM-3v specimen*
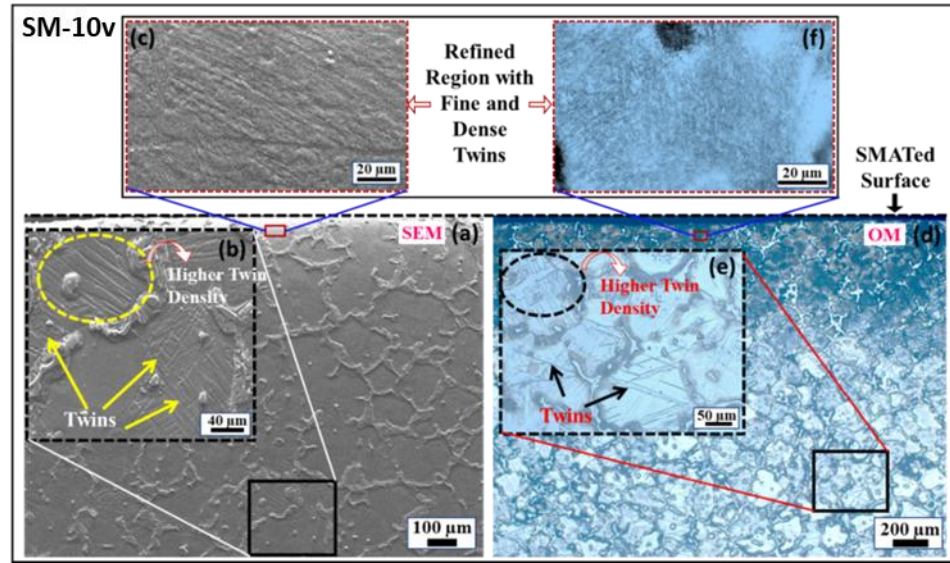
Figure 4.1.3: *SEM and optical micrographs of the near-surface region of the cross-section of the SM-10v specimen*

The SM-3v specimen shows the twins up to ~800 ± 200 μm depth (Figure 4.1.4(a)). The higher velocity of balls during SMAT causes the formation of the twins throughout the cross-section of SM-10v; however, they are more prominent up to ~3000 ± 500 μm depth (Figure 4.1.4(b)). Compared to SMAT, other methods of severe surface deformation generally give thinner deformed layers; for example, Mao et al. [78] observed twin-gradient microstructure up to ~350 μm depth due to the laser shock peening of AZ31B alloy surface.

The twin gradient microstructure results from the plastic strain gradient produced during SMAT [40, 78]. The twin density and the deformed layer's thickness depend on the strain and strain rate. The colliding balls transfer higher kinetic energy to the SM-10v specimen's surface due to their higher velocity, enhancing the deformation (concerning an increase in the dislocation density and the number of twins) and causing deeper SMAT-affected region (Figure 4.1.4(a) vs 4.1.4(b)). Further analysis of microstructural changes within the SMAT-affected regions is useful in understanding the mechanical properties (which are discussed in the subsequent sections) of SM-10v and SM-3v specimens.
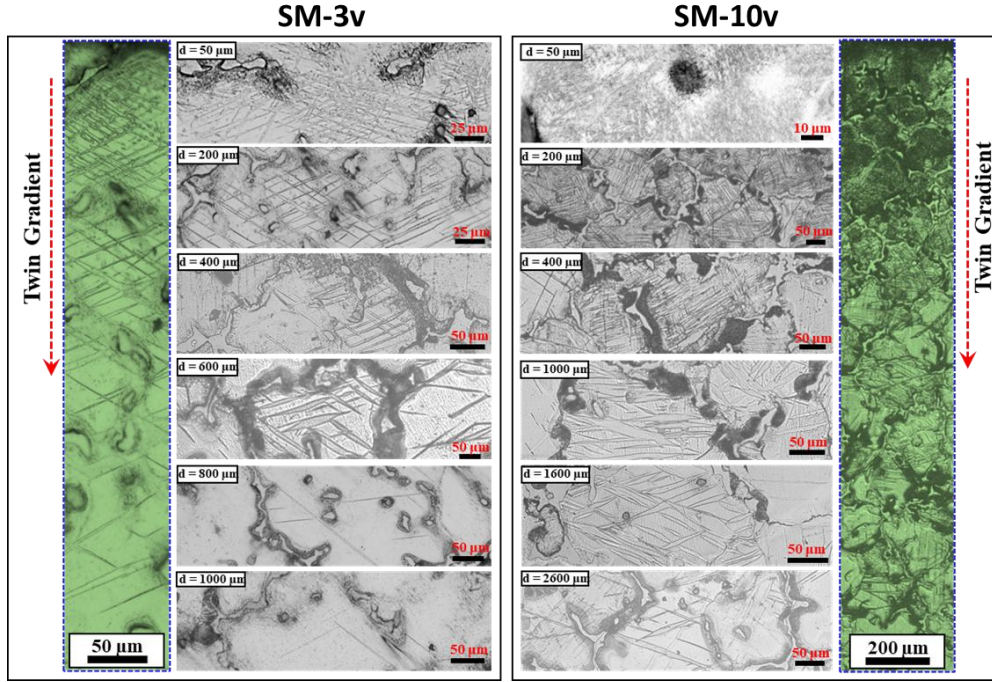
Figure 4.1.4: *Optical micrographs showing twin gradient microstructure across the cross-section of (a) SM-3v and (b) SM-10v specimens*

The NSM, SM-3v, and SM-10v specimens' XRD patterns, as shown in Figure 4.1.5(a), corroborate the presence of α- and β-phases. Noticeable broadening of α and β peaks is observed for the SMATed specimens. Figure 4.1.5(b) shows the full width at half maximum (FWHM) of α and β peaks. Compared to the non-SMATed sample, SM-3v and SM-10v specimens show ~49.6% and ~37.3% increase in the $(FWHM)_\alpha$, respectively. The $(FWHM)_\beta$ is lower than the $(FWHM)_\alpha$. The main reasons for XRD peak-broadening are lattice strain accumulation and grain refinement [101]. In SMAT, the specimen surface is bombarded with randomly moving balls with a considerable velocity, which gradually increases lattice strain with SMAT duration. Moreover, the intensity of β peaks almost disappears after SMAT (Figure 4.1.5(a): see at $2\theta = 35.98°$, $40.08°$, and $64.66°$), suggesting the dissolution of β-phase in α matrix during severe plastic deformation of SMATed surfaces. The material's abnormal (non-equilibrium) behaviour is possible due to severe deformation. The SMAT operation could enhance the solubility of Al in the α matrix due to an increased density of defects and strain accumulation, promoting the β-phase dissolution [68]. The surface region's volume percentage of the β-phase is reduced by ~28% and ~39% for SM-3v and SM-10v specimens, respectively, compared to the NSM specimen (Figure 4.1.5(c)).
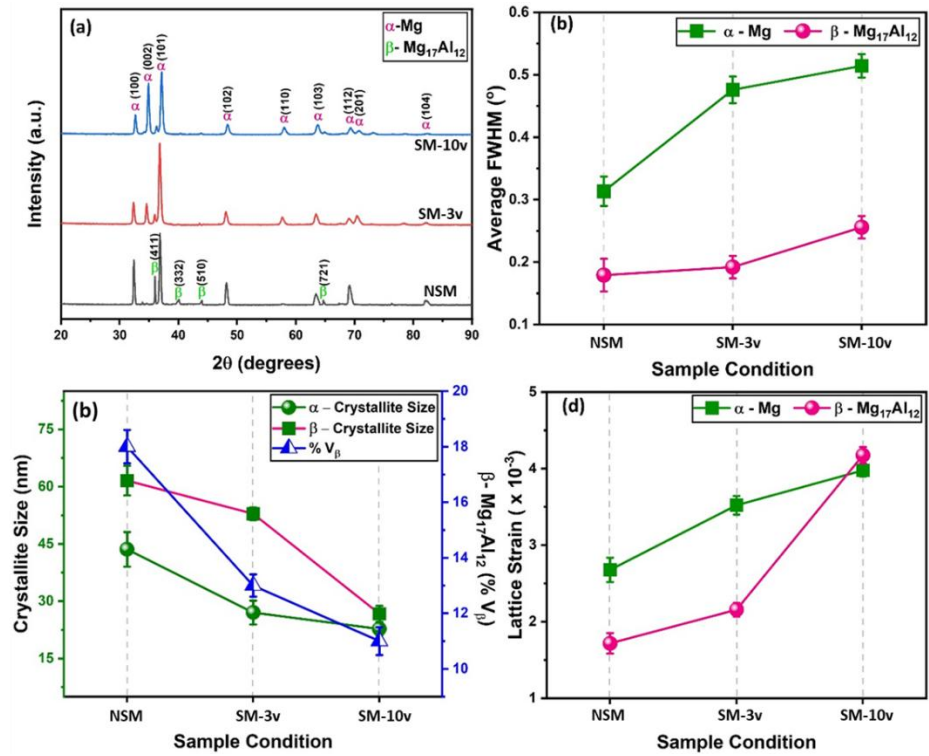
Figure 4.1.5: *(a) XRD diffraction patterns of NSM, SM-3v, and SM-10v specimens and corresponding (b) average FWHM, (c) volume percentage and crystallite size, and (c) lattice strain variation for α and β phases*

The XRD patterns are further analysed using Williamson-Hall (W-H) method (refer Eq. 3.2) to determine the average crystallite size and lattice strain. Eq. 3.2 represents a straight line, and by plotting $\beta\cos\theta$ vs $4\sin\theta$, the values of intercept ($K\lambda/D$) and slope (lattice strain) are obtained. The lattice strain in the β-$Mg_{17}Al_{12}$ is lower than α-phase (Figure 4.1.5(d)), which is possible due to its harder nature (relevant results are discussed in the subsequent section). SMAT causes an increase in α- and β-lattice strains, the extent of which is dependent on the velocity of balls during SMAT. The lattice strain in the α-phase of the non-SMATed specimen is about 2.7×10^{-3}; however, SM-3v and SM-10v surfaces show increased lattice strains of about 3.5×10^{-3} and 4.0×10^{-3}, respectively. Compared to the lower velocity SMAT, a rise in the β-lattice strain is more predominant at higher velocity (Figure 4.1.5(d)). These results suggest that a strain in β-lattice dominates with an increase in ball velocity, which could drive the dissolution of β in the α matrix (Figure 4.1.5(c)). Along with the lattice strain, the average crystallite size of specimens is also affected by SMAT. The average crystallite size (of α and β) of the SM-3v and SM-10v is ~40 nm and ~25 nm, respectively (Figure 4.1.5(c)), which

suggests an enhancement in grain refinement with an increased ball velocity in the SMAT process.

As mentioned above, SMAT produces a gradient microstructure in the deformed layer of AZ91D alloy. Such a microstructure evolution is caused by the strain gradient generated during SMAT. In other words, the specimen surface experiences severe deformation, and its severity gradually reduces with increased distance from the surface. The microstructure of the severely deformed surface evolves through various steps during the SMAT. The surface of the specimen initially experiences lower strain (which can be correlated with the microstructural development of deeper regions of SM-3v), followed by intermediate strain (which can be connected to the microstructure of the SM-3v specimen's near-surface regions) and higher strain (which is concurrent to the SM-10v specimen's microstructure in the near-surface regions). To reconnoitre the grain refinement of AZ91D alloy during SMAT, TEM analysis is performed at ~50 µm (subsurface region) and ~300 µm (deeper region) depths from the SM-3v surface and at ~50 µm (subsurface region) depth from the SM-10v surface.

Figure 4.1.6 shows the SM-3v specimen's bright field TEM images and SAED patterns captured at 300 µm depth from the SMATed surface. The presence of β-phase (BCC structure) is observed in the microstructure at such a deeper region (Figure 4.1.6(a)). The SMAT-induced dislocations are also evidenced in this region (Figure 4.1.6(b)). Dislocation slips are more prevalent (than twining) in the deeper region of the SMATed layer (because of the lower strain and strain rate). Numerous dislocations have been entangled, resulting in a non-uniform distribution of dislocations. Such a response of the material is further attributed to the formation of dislocation cells and tangles (Figure 4.1.6(b)).
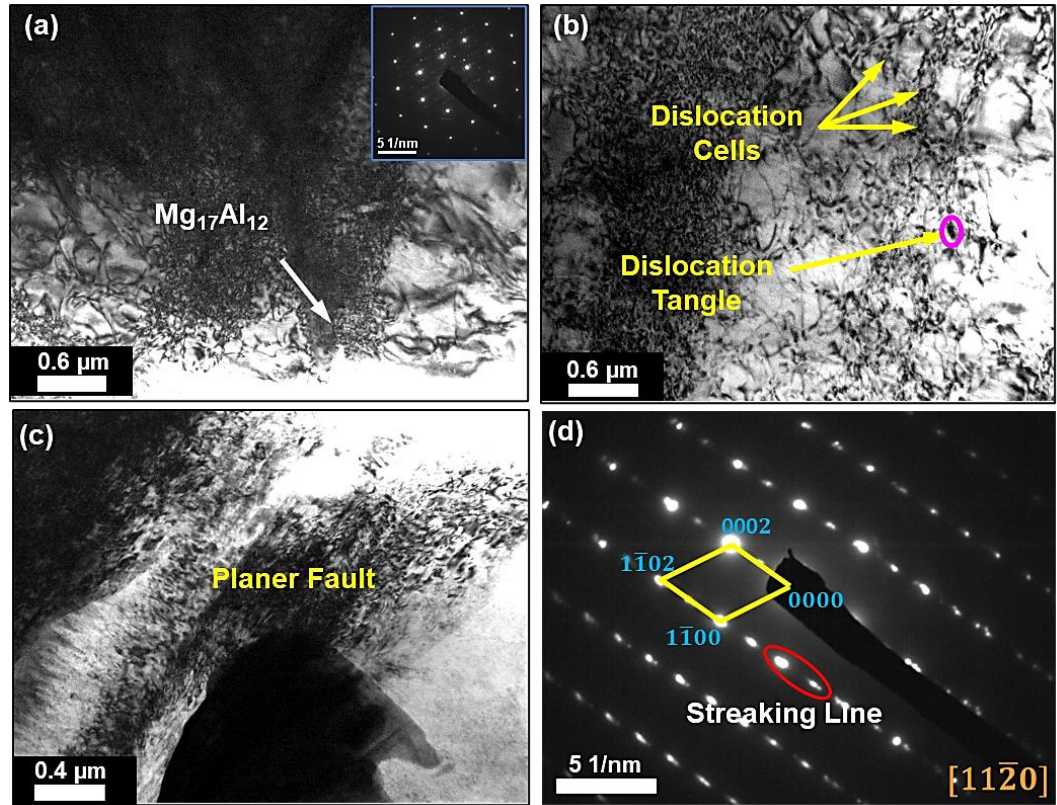
Figure 4.1.6: *BF TEM images showing (a) β-phase (Mg$_{17}$Al$_{12}$) with the corresponding SAED pattern (as an insert), (b) dislocation cells and tangles, and (c) planer fault with (d) corresponding SAED pattern of SM-3v specimen's deeper region*

Further, Figure 4.1.6(c) shows planer faults induced during the deformation. The corresponding SAED pattern in the [11$\bar{2}$0] zone axis is shown in Figure 4.1.6(d). Streaking lines along [0002] are visible on the diffraction spots of α-phase, suggesting the strong influence of crystal defects [67, 102]. Disruption in a crystal structure causes the formation of planer faults, which are typically associated with partial dislocations in the crystal lattice. During plastic deformation, dislocations move through the crystal lattice, creating localised regions with strain. Such dislocations can distort the crystal structure locally, forming stacking faults. The specific mechanisms that lead to stacking faults forming during plastic deformation depend on several factors, including strain, strain rate, creep resistance, stacking fault energy, etc. [103]. Figure 4.1.7 shows the bright field TEM image of coarser deformation-twins and related SAED pattern in [2$\bar{1}$$\bar{1}$0] zone axis. The lower strain in the SM-3v specimen's deeper region causes the formation of coarser twins. Dislocation cells, tangles, planer faults, and deformation twins are vital in grain refinement [104]
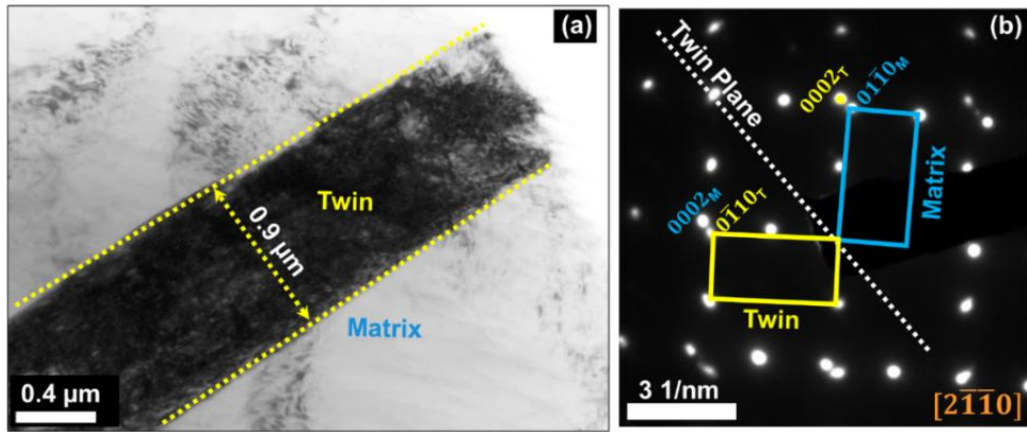
Figure 4.1.7: *(a) BF TEM image showing coarser deformation twin and (b) corresponding SAED pattern of SM-3v specimen's deeper region*

According to the von Mises yield criterion, five independent slip systems usually accomplish homogenous plastic deformation of polycrystalline materials. BCC and FCC structured materials with high SFE have more slip systems; hence, dislocation slip becomes more dominating during grain refinement. However, Mg alloys (being HCP structured materials) only have three independent slip systems. Prismatic and basal slips are easy to activate in the initial deformation stage, as they require less critical resolved shear stress (CRSS). However, at a later stage of deformation in the refined grains, a pyramidal <c+a> slip system activates, as it requires high CRSS [105, 106]

At room temperature, an insufficient amount of activated slip systems in the HCP structure leads to forming of deformation twins. $\{10\bar{1}2\} - \{10\bar{1}2\}$ and $\{10\bar{1}1\} - \{10\bar{1}2\}$ double twins, $\{10\bar{1}1\} < 10\bar{1}2 >$ compression twins and $\{10\bar{1}2\} < 10\bar{1}1 >$ tension twins are the four main types of twins that appear in Mg alloys [105]. Tension twins are usually observed at the early deformation stage, requiring a CRSS of about 2-5 MPa [105]. Therefore, the deformed region (at a larger depth) of the SM-3v specimen evidences the presence of $\{10\bar{1}2\} < 10\bar{1}1 >$ twin system (Figure 4.1.7(b)). During SMAT, strain hardening is induced by $\{10\bar{1}2\}$ twins to accommodate plastic deformation. Dislocation gliding is promoted due to the change in grain orientation (caused by twins), resulting in further straining of the α-matrix.

Figure 4.1.8(a) shows the presence of dense and fine deformation twins near the SMATed surface of the SM-3v specimen. The thinner twins are visible close to

the surface (Figure 4.1.8(a)), while coarser twins are present in deeper regions of the specimen (Figure 4.1.7(a)). The average thickness of the twins in the near-surface region is ~180 nm (Figure 4.1.8(a)). The presence of fine and dense twins is attributed to the severe deformation of the near-surface region by the multiple impacts of hard balls (i.e., accumulation of higher strain at the surface than the deeper regions). The twin density gradient across the SMATed layer (at a microscopic level) is observed in the optical micrographs (Figure 4.1.4). Additionally, the TEM study confirms the microstructural gradient nature of the SMATed layer at the minute level.
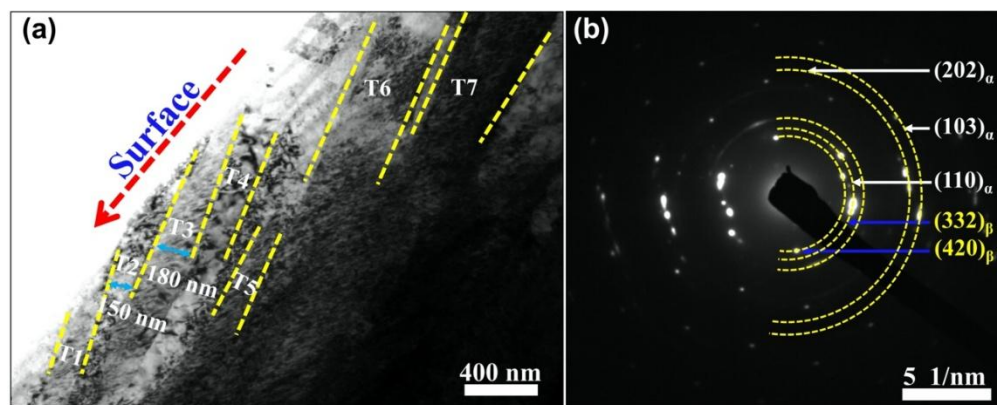
Figure 4.1.8: *(a) BF TEM image showing fine and dense twins and (b) corresponding SAED pattern of SM-3v specimen's near-surface region*

Figure 4.1.8(b) indicates the presence of α- and β-phases. Streaks on α-phase diffraction spots (see SAED pattern in Figure 4.1.8(b)) are caused by the high density of dislocations, deformation twins, and localised alteration in crystal orientation (grain refinement). However, the absence of continuous rings in the near-surface region's SAED pattern indicates the weaker grain refinement in the SM-3v specimen. This behaviour can be attributed to the relatively lower strain and strain rate associated with ~3 m/s ball velocity in the SMAT process. A TEM study is performed at the subsurface of the SM-10v specimen to understand the effect of higher ball velocity on grain refinement.

Figure 4.1.9 shows bright field TEM images, SAED patterns, and nanograins distribution in the sub-surface region of the SM-10v specimen. Figure 4.1.9(a) and (b) endorses the presence of α- and β-phases in the subsurface. In agreement with the XRD analysis (Figure 4.1.5), the β-phase only partially dissolves in the α-Mg matrix; therefore, it appears in Figure 4.1.9(a) and (b).

49

Continuity in the rings observed in the SAED pattern of SM-10v is better than that of the SM-3v specimen (Figures 4.1.8(b) vs 4.1.9(b)), which corroborates the better grain refinement of the SMATed surface by higher velocity balls. The average grain size observed at the SM-10v specimen's subsurface is 32 ± 12 nm (Figure 4.1.9(c) and (d)).
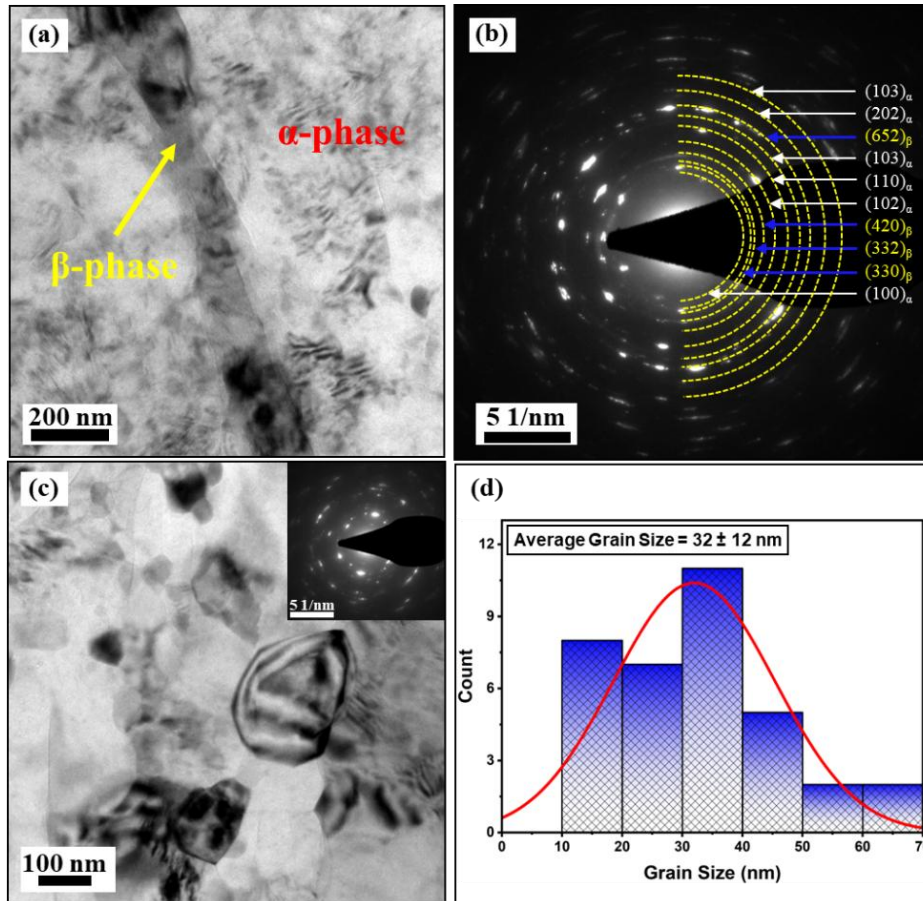
Figure 4.1.9: *TEM results of SM-10v specimen's sub-surface region: (a) BF TEM image and (b) corresponding SAED pattern confirming the presence α- and β-phases. (c) BF TEM image showing nanograins with the corresponding SAED pattern (as an insert) and (d) nanograins distribution*

4.1.2   Residual Stress Distribution

The XRD peak of $(104)_{\alpha\text{-hcp}}$ is selected for the residual stress measurements in the SMATed layer of SM-3v and SM-10v specimens (Figure 4.1.10). The 2θ vs $\sin^2(\psi)$ method is used for this purpose. An example of XRD peaks (at various ψ angles) and corresponding $\sin^2(\psi)$ plots at ~50 μm depth of SM-3v and SM-10v specimens are shown in Figure 4.1.10. Scattered data points are observed in $\sin^2(\psi)$ plots (Figure 4.1.10(e)), which are associated with the X-ray penetration depth [72]. The few factors affecting the peak position are the grain size, micro-texture, and

gradient structure produced due to SMAT [107]. However, such scattering in the data points is quite common and has been observed in several studies [40, 72, 107, 108].
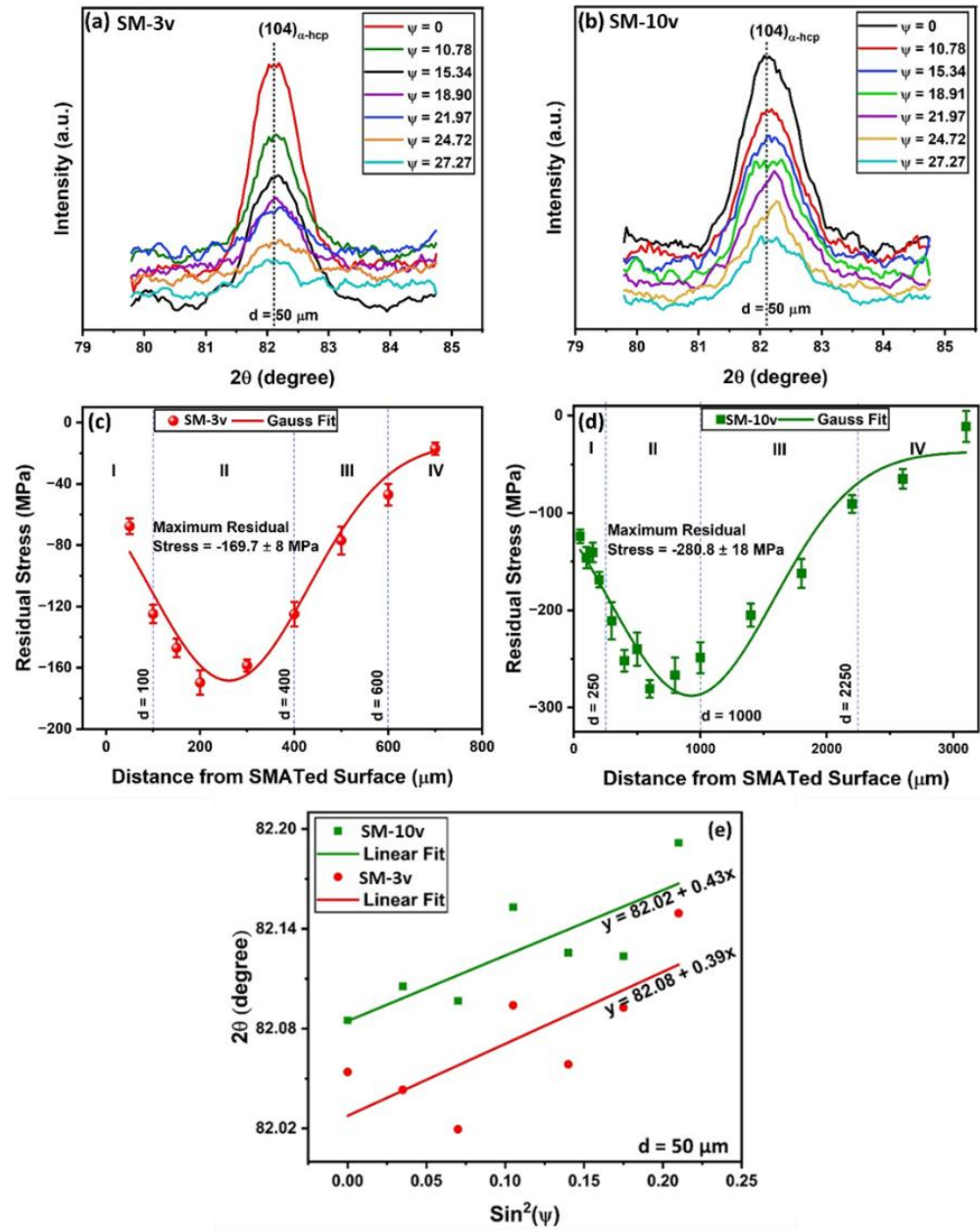
Figure 4.1.10: *(104)$_{α-hcp}$ XRD peaks for (a) SM-3v and (b) SM-10v specimens recorded at 50 μm depth. Residual stress distribution across the cross-section of (c) SM-3v and (d) SM-10v. (e) An example of 2θ vs sin²(ψ) plot for 50 μm depth of the SMATed specimens*

The residual stress vs depth (i.e., distance from the SMATed surface (*d*)) profiles of SM-3v and SM-10v specimens are shown in Figure 4.1.10(c) and (d), respectively. Compressive residual stresses are observed in the SMATed layer of these specimens. Initially, this stress becomes more negative with increased

distance from the SMATed surface (zone I), followed by the region with maximum compressive stress (zone II) and then decreases (zone III). In zone IV, stress is close to zero. This behaviour indicates that zone III is sandwiched between the maximum and minimum compressed zones.

The maximum residual stress of -281 ± 18 MPa is observed for SM-10v at ~600 μm depth, which is ~2.3 times the residual stress at the surface. However, SM-3v reports -170 ± 8 MPa as the maximum residual stress at ~200 μm depth, which is ~2.5 times the residual stress at the surface. The higher resistance to the material's flow during SMAT is the prime reason for the stress accumulation at the subsurface region.

The SMAT duration affects the thickness of the deformed layer at a constant ball velocity due to the change in percentage coverage or peening intensity (PI) [34]. In SM-3v and SM-10v specimens, even if the SMAT duration is different, they are SMATed using the same percentage coverage (i.e., 2000%) or peening intensity (i.e., PI = 20). The higher ball velocity with a shorter SMAT duration enables a considerably thicker layer (Figure 4.1.4) with higher compressive stress (at a given peening intensity) (Figure 4.1.10). Singh et al. [40] observed the maximum residual stress of about -128 MPa at ~100 μm depth of the SMATed (diameter of balls: 6 mm, ball velocity: ~3 m/s, and SMAT duration: 1 h) AZ91D alloy. A comparison of this result with the current study suggests that higher compressive stress at deeper depth could be achieved at a longer SMAT duration (when ball velocity is low, for example, ~3 m/s) due to increased peening intensity.

In other literature, Liu et al. [107] reported residual stress of about -206 MPa at ~50 μm depth after severe shot peening (SSP) (diameter of ZrO_2 balls: 0.35 mm, air pressure: 0.36-0.61 MPa, and duration: 60 s) of Mg-8Gd-3Y alloy. Comparing this result with the SMATed specimens suggests that reasonable compressive stress in the thinner layer could be achieved quickly by impacting small-size (< 1 mm) hard particles using a high-pressure air jet in the SSP process. However, in the SMAT process, the larger diameter (> 1 mm) balls with moderate velocities (e.g., 3-10 m/s) help obtain a thicker layer (Figure 4.1.4) with higher compressive stress (Figure 4.1.10).

4.1.3   Microhardness Distribution

Microhardness values measured on α- and β-phases at various depths are shown in Figure 4.1.11(a) and (c) for SM-3v and in Figure 4.1.12(a) and (c) for SM-10v specimens. Further, averages of these microhardness value at different depths are plotted in Figure 4.1.11(e) and 12(e) for SM-3v and SM-10v specimens, respectively. The slope of the microhardness-depth profiles is shown in Figure 4.1.11(b), (d), and (f), and Figure 4.1.12(b), (d), and (f) for SM-3v and SM-10v, respectively.
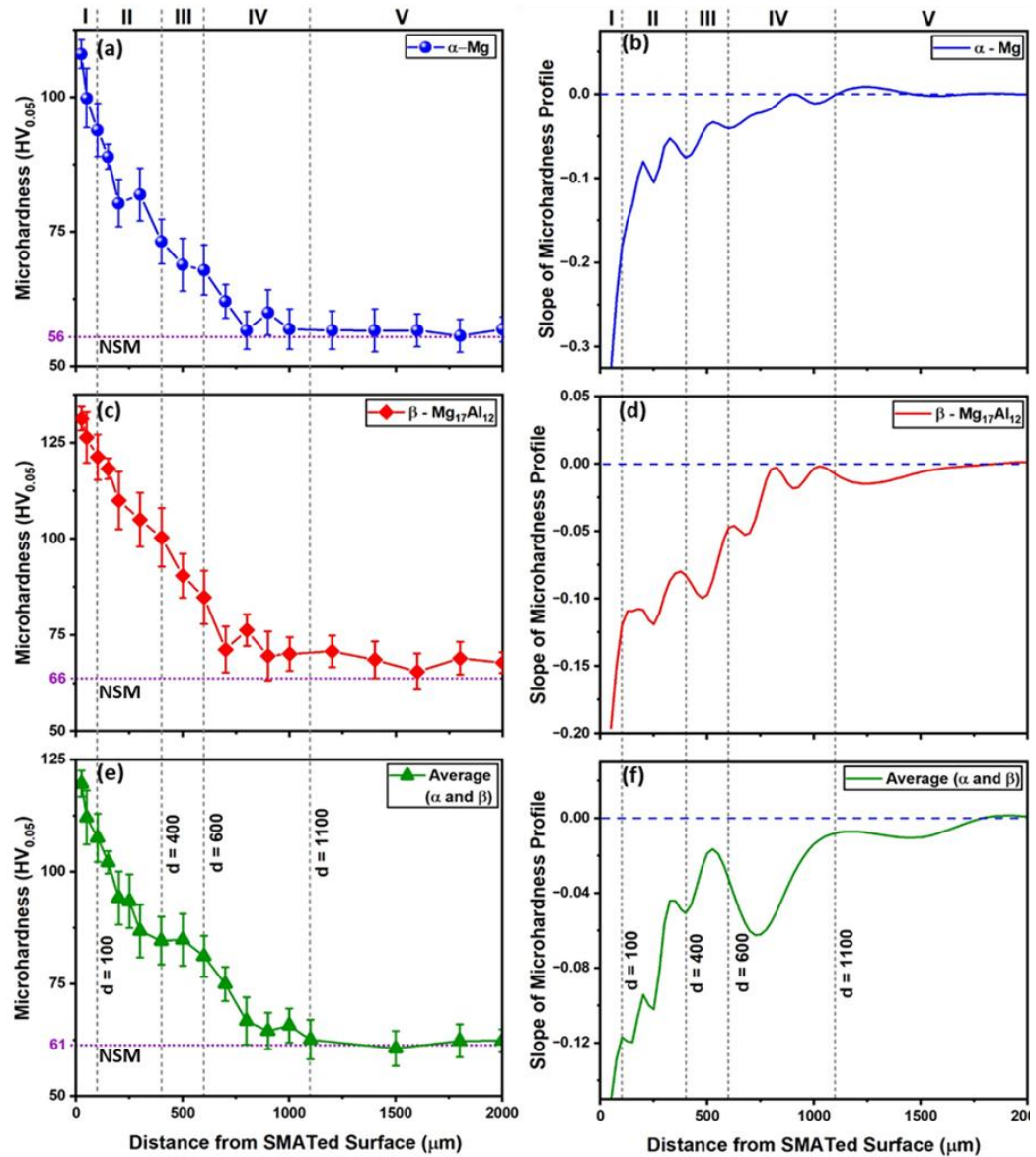
Figure 4.1.11: Microhardness profiles and variation in their slope with the distance from the SMATed surface of SM-3v specimen for (a, b) α-Mg, (c, d) β-$Mg_{17}Al_{12}$, and (e, f) an average of the results for α- and β-phases
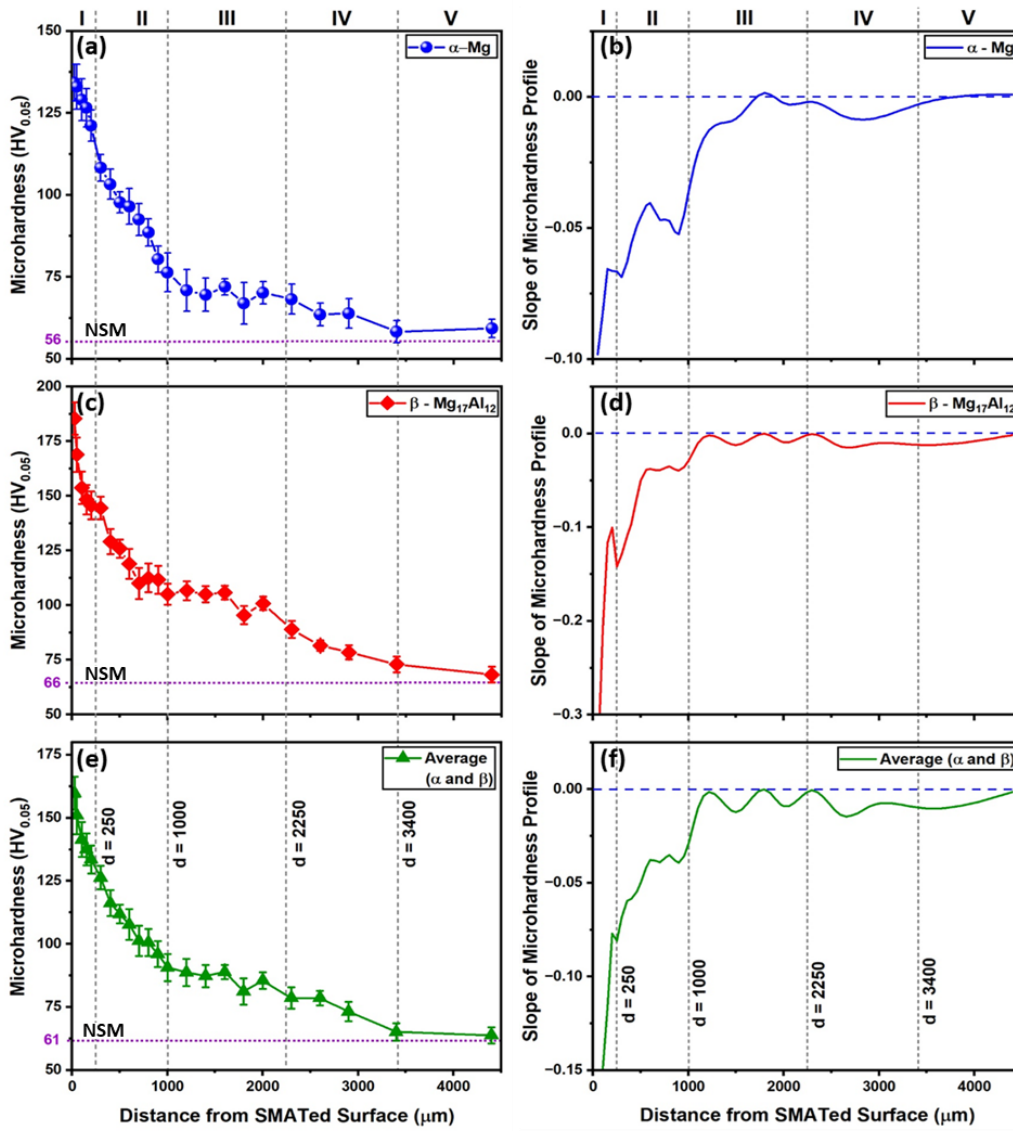
Figure 4.1.12: *Microhardness profiles and variation in their slope with the distance from the SMATed surface of SM-10v specimen for (a, b) α-Mg, (c, d) β-Mg₁₇Al₁₂, and (e, f) an average of the results for α- and β-phases*

Microhardness values measured on β-phase are higher than the microhardness of α-phase at different depths. In the NSM specimen, the microhardness values of α- and β-phases and an average of both are ~56 HV$_{0.05}$, ~66 HV$_{0.05}$ and ~61 HV$_{0.05}$, respectively. In the SM-3v and SM-10v specimens, five distinct zones are visible in the microhardness profiles. In zone I, the sharpest microhardness gradient is observed for SM-10v and SM-3v specimens, which is decreased in zone II. The slope of the microhardness-depth profile fluctuates closer to zero (i.e., plateaued trend) in zone III. The slope becomes more negative (i.e.,

hardness gradually reduces) in zone IV, and subsequently, it approaches zero in zone V (i.e., hardness profile reaches the core hardness).

Such a gradient microhardness in the SMATed layer of AZ91D alloy is a consequence of gradient microstructure [40, 102]. The noticeable microhardness gradient exists up to 1200 ± 200 μm depth for SM-3v and 3500 ± 500 μm depth for SM-10v. During SMAT processing of softer material like AZ91D alloy, the squeezing action on a surface by colliding balls could generate different zones of varying extent of deformation/compression (Figure 4.1.10). Such action leads to the non-uniform density of dislocations and twins (Figures 4.1.2-4.1.4), the thickness of twins (Figures 4.1.7 and 4.1.8), and grain size distribution in the SMATed layer [102].

Microhardness values of α-Mg, β-$Mg_{17}Al_{12}$, and the average of these two for NSM, SM-3v, and SM-10v specimens' surface regions are presented in Table 4.1.1. The SM-10v surface reports the highest average hardness value of ~160 $HV_{0.05}$, which is ~2.6 times the NSM specimen's hardness (~61 $HV_{0.05}$). However, the average hardness value observed for the SM-3v is ~120 $HV_{0.05}$, which is ~2 times the hardness of NSM. Like lattice strain (Figure 4.1.5(d)), the SMAT has considerably affected the hardness of α-Mg and β-$Mg_{17}Al_{12}$ phases. A considerable rise in the microhardness of these phases with an increased ball velocity is observed in Table 4.1.1. Despite the higher hardness of the β-phase than the α-phase, the percentage rise in the β-phase's hardness is more than that of the α-phase, suggesting the domination of the β-phase's straining during the SMAT.

Duan et al. [102] achieved ~72% enhancement in the SMATed surface's microhardness (from ~68 HV to ~117 HV) and ~500 μm deformed layer thickness of AZ31 Mg alloy after 6 min SMAT using 3 mm diameter balls and 20 kHz vibration frequency. Comparison of this behaviour with the SM-10v specimen suggests that significant layer thickness (~3500 μm) and hardness improvement (~164%) of an Mg alloy are achievable using larger diameter balls (e.g., ~6 mm) and high ball velocity (e.g., ~10 m/s) in the SMAT process.

Table 4.1.1: Surface microhardness and its percentage increase for SM-10v and SM-3v specimens with respect to the NSM specimen

Phases	Microhardness ($HV_{0.05}$)				
	NSM	SM-3v		SM-10v	
		Surface hardness	% Increase (with respect to NSM)	Surface hardness	% Increase (with respect to NSM)
α-Mg	56	108	94	134	141
β-$Mg_{17}Al_{15}$	66	131	100	186	183
The average hardness of α- and β-phases	61	120	98	160	164

The refined grains and considerable density of lattice defects in the SMATed layer are the main causes of microhardness improvements. The most dominant deformation mechanism of Mg alloys is twinning [76–78]. Therefore, strain-hardening induced through this mechanism is one of the factors for the hardness enhancement of the SMATed layer [40]. The twin boundaries impede the movement of dislocations produced during SMAT, limiting further slip. In other words, the interaction of dislocations and twins results in strain-hardening and improvement in the SM-3v and SM-10v specimens' hardness.

Hall–Petch relation can also be applied to the hardness, similar to the yield strength [109]. In this relation, the value of *k* (a material/strengthening constant) is strongly affected by the Taylor factor (which is linked to the grain/crystal orientations). If the Taylor factor increases, the value of *k* also increases. Magnesium has a larger Taylor factor than FCC and BCC structured materials, and it has a limited number of slip systems (being a material with an HCP structure). Consequently, the hardness of Mg alloy can easily be affected by a slight change in the grain size (which is altered due to SMAT). In other words, Mg-alloys' hardness is very sensitive to grain size. Further, a decrease in the crystallite size and volume fraction of β-phase (Figure 4.1.5(c)) causes an increased hardness of the SMATed surface.

Formation of nanograins (Figure 4.1.9) and fine and dense twins (Figures 4.1.2, 4.1.3, and 4.1.8) are dominating parameters in causing a high microhardness in zone-I (Figure 4.1.11 and 4.1.12). Duan et al. [102] established the grain size gradient in the SMATed layer of an Mg alloy. Moreover, a decrease in twin density (Figure 4.1.4) and an increase in twin thickness (Figures 4.1.7 and 4.1.8) with an increased distance from the surface causes a sharper drop in zones I and II of microhardness profiles (Figures 4.1.11 and 4.1.12). Zone III (which is squeezed between the maximum and minimum compressive stress: see Figure 4.1.10(c) and (d)) shows a plateaued hardness trend. Such a trend is observed because the density of twins (and, possibly, dislocation density and crystallite size also) does not change much in zone III (Figure 4.1.4) during microstructure refinement. In zone IV, the twin density is reduced drastically (Figure 4.1.4), and twins become coarser (i.e., the thickness of twins increases: Figures 4.1.7 versus 4.1.8), attributing a slightly inclined trend (with negative slope) in the microhardness profiles (Figures 4.1.11 and 4.1.12). Finally, the slope of hardness profiles approaches zero in the core (zone V). All these zones represent the overall response of AZ91D alloy to the SMAT process.

4.1.4   Nanoindentation Analysis

4.1.4.1 Load-Displacement Curves and Nanohardness

Compared to the indentation in microhardness measurements, the volume of material exposed to nanoindentation is tiny. Therefore, nanoindentation gives precise information about the role of the microstructure's minute features on the material's mechanical behaviour. At room temperature, the average load-displacement (p-h) profiles corresponding to a few depths are shown in Figure 4.1.13(a) and (b) for SM-3v and SM-10v specimens, respectively.

As shown in Figure 4.1.13(c) and (d), during the deformation of SMATed material beneath the nanoindenter, the loading regime of a few P-h curves exhibits a sudden depth burst that can be called a "pop-in" effect [110, 111]. The dislocation loops are typically nucleated and expanded homogeneously during a deformation, causing a suddenness of a pop-in event. Due to their rapid expansion and multiplication, the twinned regions are also known to appear under falling stress.

The interaction of twins and dislocations with grain boundaries results in pop-in effects [112]. Dislocations' annihilation or splitting, twins' migration or growth, and de-twining of the pre-existing twins could also cause the pop-ins [112].
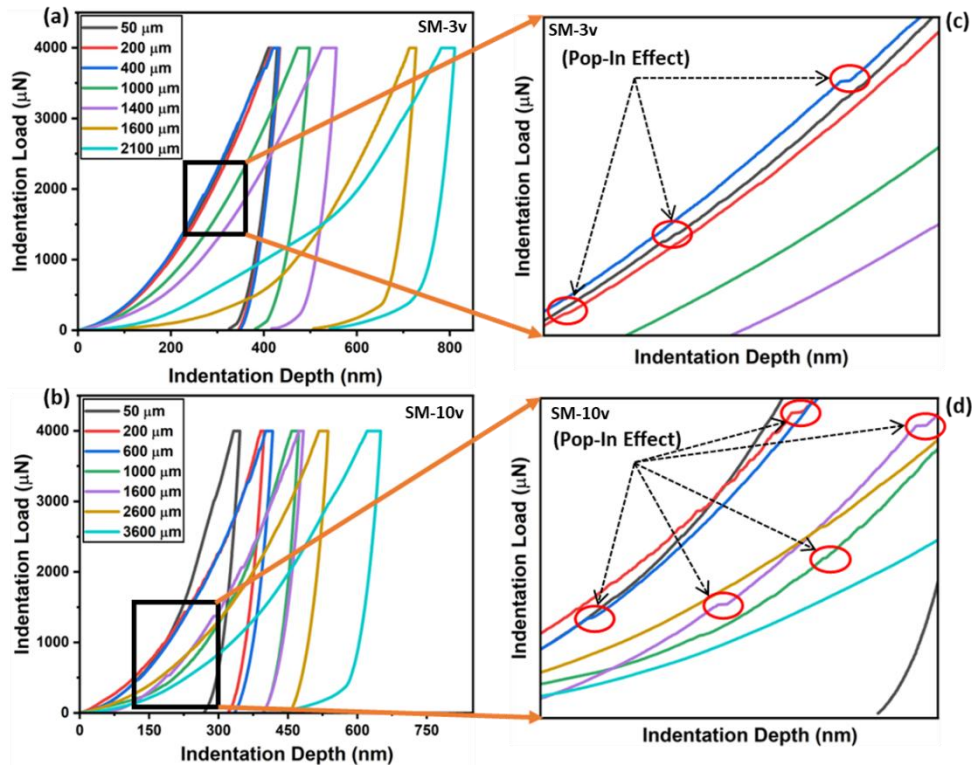
Figure 4.1.13: *Nanoindentation load-depth profiles for (a) SM-3v and (b) SM-10v specimens. The corresponding amplified region shows pop-ins for (c) SM-3v and (d) SM-10v specimens*

Severe surface deformation techniques influence the pop-in effect to a greater extent [110, 111]. The surface of SM-3v and SM-10v specimens are severely deformed; hence, the dislocations and twins are already present in the SMATed layer. These preconditions of the specimens could enhance the pop-in effect during nanoindentation. This effect is more prominent at shallower depths (i.e., close to SMATed surfaces: see Figure 4.1.13(c) and (d)). The degree/extent of plastic deformation is greater in the SM-10v specimen (due to the higher ball velocity), which ultimately increases the density of dislocations and twins compared to the SM-3v specimen (Figures 4.1.2 and 4.1.3). Such behaviour is linked to higher pop-ins in SM-10v than in SM-3v (Figures 4.1.13(d) vs (c)). Hu et al. [110] investigated that intergranular strain compatibility requirements cannot be fulfilled during severe plastic deformation (due to limited slip systems in the HCP structure). This fact favours the formation of dislocation tangles (Figure 4.1.6) and

non-uniform twinned regions (Figures 4.1.2-4.1.4, 4.1.7, 4.1.8) that greatly enhances the pop-in phenomenon.

Furthermore, a harder phase in the microstructure could restrict the dislocation activities, suppressing the pop-in effect [111]. In the SMATed layer of AZ91D alloy, the dissolution of the harder β-phase in a α-matrix is plausible due to the severe deformation (Figure 4.1.5(a) and (c)), which suggests the likelihood of a lesser hindrance to the dislocation activities near the SMATed surface (as compared to the deeper region). This behaviour could further support the occurrence of more pop-ins at shallower depths of the SM-3v and SM-10v specimens (Figure 4.1.13(c) and (d)).

The maximum value of contact depth for NSM is ~548 nm, and the average contact depth of indentations in the SMATed layer of SM-3v and SM-10v is about ~423 nm and ~376 nm, respectively. These results indicate that the SM-10v specimen is noticeably harder than SM-3v and NSM specimens. The nanohardness is derived from the loading and unloading curves. Figure 4.1.14(a) and (c) show the profiles of nanohardness vs distance from the SMATed surface, and the corresponding variation in slope is displayed in Figure 4.1.14(b) and (d) for SM-3v and SM-10v specimens, respectively. The nanohardness values of SM-10v and SM-3v specimens' surfaces are increased by ~3.1 and ~2.6 times the NSM specimen's hardness (~0.63 GPa), respectively. Moreover, the average nanohardness of the SMATed layer of SM-10v (1.39 GPa) is more than SM-3v (1.22 GPa).

Similar to the microhardness analysis, five zones are identified in the nanohardness profiles. A sharper drop is observed in zone-I (near the treated surface) of the nanohardness profiles of SM-3v and SM-10v specimens, which agrees well with the microhardness distribution (Figures 4.1.11 and 4.1.12). A gradient in an initial portion of the nanohardness profiles is linked to a sharp change in nano-twins' thickness (Figure 4.1.8). The nanohardness trend differs in zones II and III, especially the microhardness profiles' horizontal trend in zone III (Figures 4.1.11 and 4.1.12) is absent in nanohardness profiles (Figure 4.1.14). Moreover, the nanohardness gradient (with some fluctuations in their slope) is continued up to zone-V. Such behaviour is possible due to the gradual change (with an increased depth) in tiny features of microstructure like twin thickness (Figure 4.1.8), the

intersection of twins (Figure 4.1.4), dislocation cells (Figure 4.1.6(b)), and planar faults (Figure 4.1.6(c)).
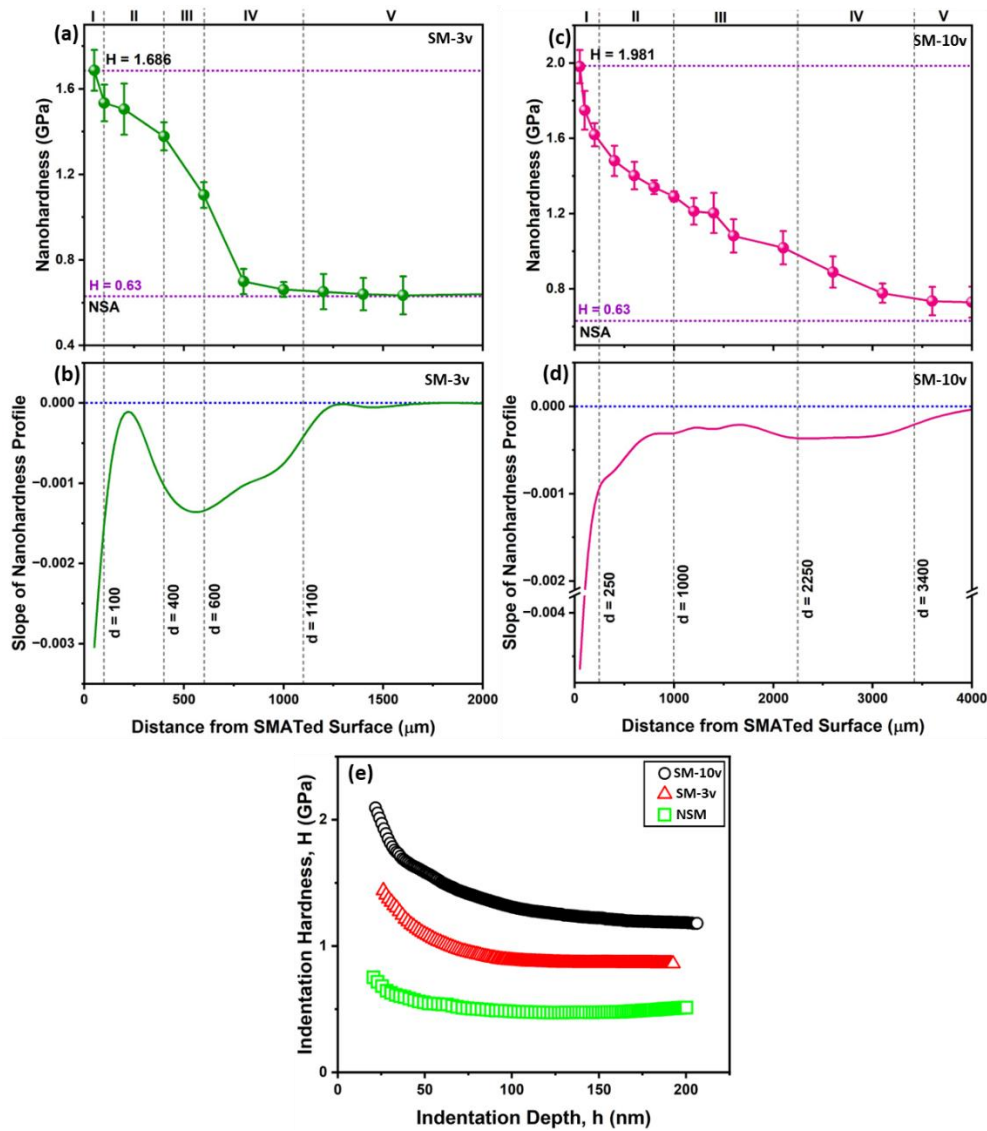
Figure 4.1.14: *Nanohardness distribution and corresponding slope variation with distance from the SMATed surface of (a, b) SM-3v and (c, d) SM-10v specimens. (e) Indentation size effect for NSM, SM-3v and SM-10v specimens*

4.1.4.2 Indentation Size Effect

Nanoindentation hardness (H) versus indentation depth (h) profile of NSM and that of the SM-3v and SM-10v specimens' SMATed layer are displayed in Figure 4.1.14(e). Classical plasticity does not account for the indentation size effect (ISE) phenomenon. According to classical plasticity, hardness is independent of the indentation depth (no matter indent is shallow or deep). However, hardness is

observed on the higher side at shallow indents in depth-sensing tests. This phenomenon is shown in Figure 4.1.14(e), where the higher hardness values are observed at shallow indent depths for NSM, SM-3v, and SM-10v specimens. The ISE effect can be better explained through strain gradient and dislocation-starved plasticity. According to dislocation-starved plasticity, a tiny volume is observed beneath the indenter when it encounters the surface. This volume is treated as a dislocation-free structure in an early stage of nanoindentation. Thus, the material's strength at this stage is higher (which could be close to its theoretical strength) [98, 99].

The further movement of the indenter into the specimen increases the affected volume, allowing more space for dislocations to form. A gradient plasticity theory usually attributes the ISE to geometrically necessary dislocations (GNDs) produced in the plastic zone under the indenter tip [97]. As a result of indentation penetration, lattice rotation occurs in the material, and to accommodate that, GNDs are generated. Compared to uniformly strained material, extra dislocations are created in a tiny region under the indenter tip. Thus, work-hardening or strain gradient results under the indenter (the collective effect of increased GNDs and loading rate) [97]. At further indenter penetration (at a larger depth), a plateaued trend is observed (Figure 4.1.14(e)).

4.1.4.3 Ratio of Final Displacement (h_f) and Maximum Displacement (h_{max})

Indentations' maximum displacement (h_{max}) and final displacement (h_f) values are obtained from P-h curves (Figure 4.1.13). Finally, the ratio of h_f and h_{max} (i.e., h_f/h_{max}) is plotted against a distance from the SMATed surface (Figure 4.1.15). When the h_f/h_{max} approaches 1, the material possesses negligible elastic recovery. As shown in Figure 4.1.15, the h_f/h_{max} values are lower near the SMATed surfaces (SM-3v and SM-10v) and gradually increase with an increase in the distance from the surface. This trend indicates that elastic recovery of the material close to the SMATed surface is more. The trend in the slope of the h_f/h_{max} (Figure 4.1.15(b) and (d)) vs distance from the SMATed surface is fairly similar to the trend in the microhardness-depth profiles' slope (Figures 4.1.11(f) and 4.1.12(f)), indicating the role of gradient microstructure of the SMATed layer. Considerable grain refinement (Figures 4.1.5(c) and 4.1.9), finer and denser deformation twins (Figures 4.1.2-4.1.4

and 4.1.8), and higher work hardening effect (Figures 4.1.11 and 4.1.12) are the most probable reasons for lower h_f/h_{max} ratios in the SMATed layer. These features are observed up to ~1100 μm depth for SM-3v and up to ~3400 μm for SM-10v. The residual stress (Figures 4.1.10(c) and (d)) could also affect the h_f/h_{max} ratios [113]. Hence, an increasing trend in the h_f/h_{max} ratios is observed in zones-I to IV, and subsequently, a negligible variation is found in zone V (Figure 4.1.15). Zhang et al. [113] calculated the plastic and elastic energy (from loading-unloading curves) of the AZ31 Mg alloy processed through spinning and found that a deformed surface region exhibits maximum elastic energy compared to the core region. In the current work, the h_f/h_{max} ratio varies from ~0.72 (near the surface) to ~0.82 (at ~1100 μm depth) for the SM-3v specimen; it is ranged between ~0.71 (near the surface) and ~0.85 (at ~3400 μm depth) for the SM-10v specimen.
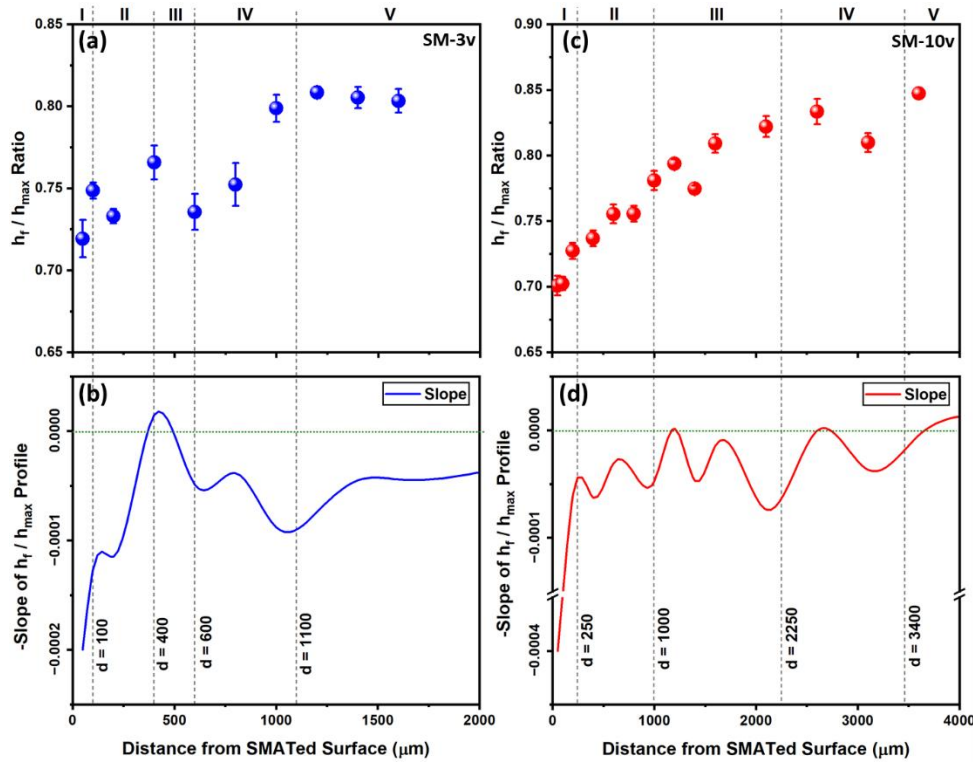
Figure 4.1.15: *The h_f/h_{max} ratio distribution through the cross-section and the corresponding slope variation for (a, b) SM-3v and (c, d) SM-10v specimens*

4.1.4.4 Creep Measurements

Figure 4.1.16 illustrates the relationship between creep displacement and holding time (5 s) at the constant load (4 mN) for the SMATed specimens. Within the SMATed regions, the creep displacements at different depths from the treated

surface are plotted against the holding time for SM-3v (Figure 4.1.16(a)) and SM-10v (Figure 4.1.16(c)). An enlarged view of such plots at 600 μm depth is shown (as an example) in Figure 4.1.16(b) and (d) for SM-3v and SM-10v, respectively.
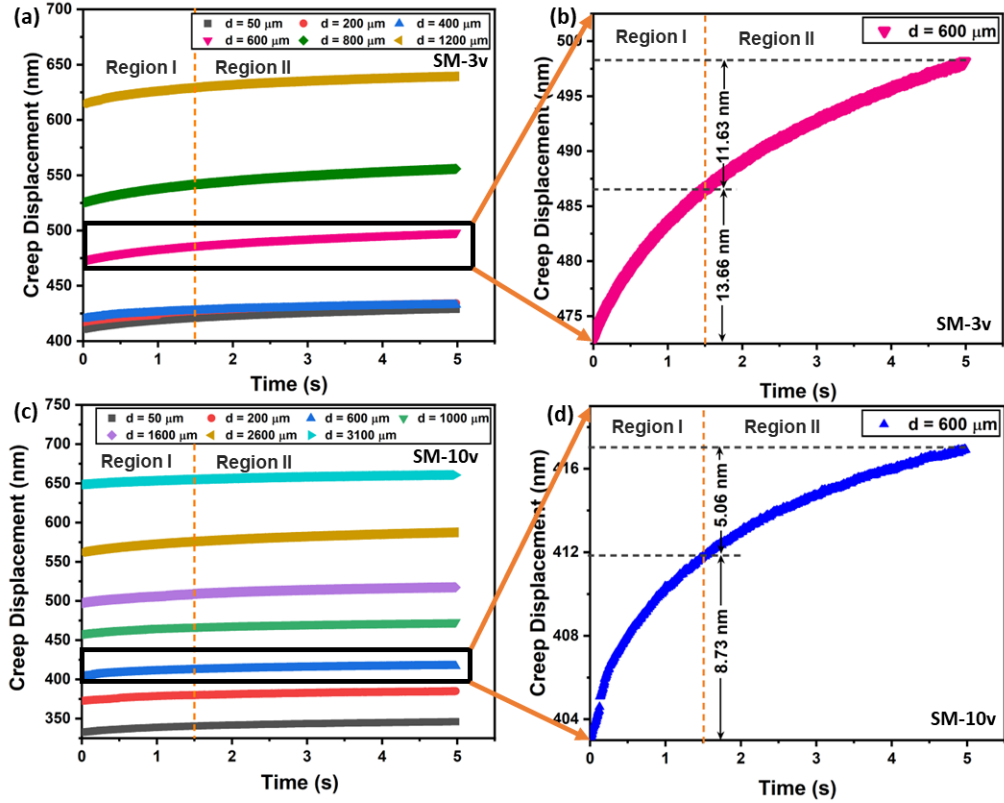
Figure 4.1.16: *Variation in creep displacement with holding time at different depth locations within the SMATed regions of (a) SM-3v specimen (with (b) an enlarged view at 600 μm depth) and (c) SM-10v specimen (with (d) an enlarged view at 600 μm depth)*

Creep-induced displacement is lower near the surface of SM-3v and SM-10v, which is ~429 nm (at ~50 μm depth) and ~346 nm (at ~50 μm depth), respectively. However, in the core of the specimens (i.e., the least affected region of the specimen's cross-section during SMAT), it is ~639 nm (at ~1200 μm depth) for SM-3v and ~660 nm (at ~3100 μm depth) for SM-10v. A positive shift in creep displacement curves with an increased distance from the SMATed layer is observed (Figure 4.1.16) due to the hardness gradient (Figures 4.1.11, 4.1.12, and 4.1.14), which is a consequence of the microstructure gradient. Region I (up to ~1.5 s) shows a sharp rise in the creep displacement for all curves, while region II shows a steady state creep. The maximum rise in creep displacement is observed in region-I; however, the extent of the rise in the creep displacement with time along the depth of the SMATed layer of SM-3v is different than that of the SM-10v specimen

(Figure 4.1.16). The change in creep displacement is slower for SM-10v than for SM-3v (Figure 4.1.16(b) and (d)). Moreover, this change is more sluggish in region-II than region-I for both specimens.
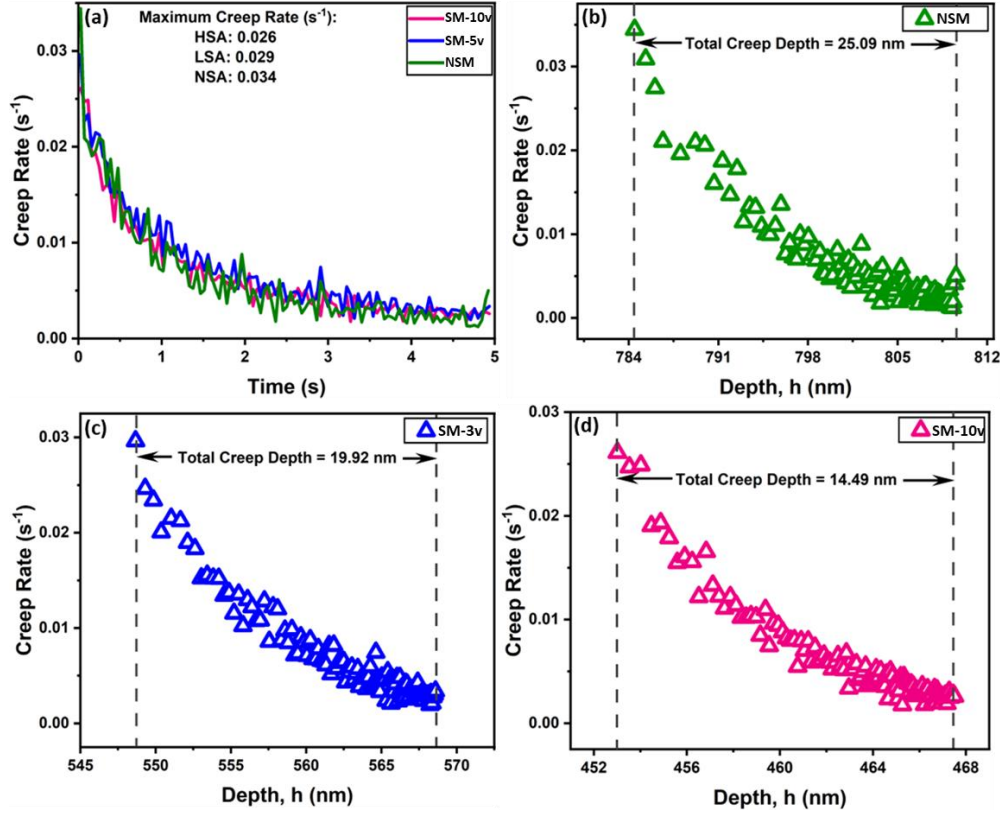
Figure 4.1.17: *Variation in creep rate with (a) holding time and (b)-(d) indentation depth for NSM, SM-3v, and SM-10v specimens*

The relationship between the creep rate and holding time derived using Eq. 3.5 for NSM, SM-3v, and SM-10v specimens is shown in Figure 4.1.17(a). The data presented is based on the average of indents taken at various depths within the SMATed zone of SM-3v and SM-10v specimens. For all specimen conditions (NSM, SM-3v, and SM-10v), the creep rate initially decreases sharply (transient creep). It then gradually approaches a steady state (steady state creep) as the dwell time increases. The highest creep rate is observed for NSM, followed by SM-3v and then SM-10v (Figures 4.1.16(b) and (d), and 4.1.17). Ball velocities play a vital role in governing the degree of deformation, grain refinement (Figures 4.1.5(c) and 4.1.9(d)), twins (their thickness and density: see Figures 4.1.2-4.1.4, 4.1.7, and 4.1.8), dislocation density, and hardness enhancement (Figures 4.1.11, 4.1.12, and 4.1.14); hence, the SM-10v specimen exhibits the lowest creep rate. It has also been noticed that the creep rate decreases with increasing indentation depth in the

holding stage (Figure 4.1.17(b)-(d)). This trend shows that the observed creep rates are high at shallower depths for all specimen conditions. The microstructural features are the probable reasons for such a creep rate behaviour of the SMATed and non-SMATed specimens [114].

Even if a small volume beneath the indenter is treated as a dislocation-free structure in an early stage of nanoindentation (according to dislocation-starved plasticity), the pre-existing/stored dislocations and twins are propagated and forwarded in the initial holding period during the loading regime. The opposite grain boundaries absorb these highly unstable dislocations, causing high creep displacements (transient creep). The generation of dislocations and their further movements are severely limited by the dislocation walls (Figure 4.1.6(b)) or twin boundaries (Figure 4.1.2-4.1.4) in the SMATed layer, which rapidly reduces the creep rate with an increased holding time. For the next holding period (1.5-5 s), the interaction between twin boundaries and dislocations could result in the dislocations' dynamic recovery, forming a relatively stable dislocation network [110]. As a result, rapidly reducing creep behaviour approaches a steady state; hence, an almost plateaued trend is observed after that (Figure 4.1.17(a)). The SM-10v specimen shows the lowest creep depth (Figure 4.1.17(b)-(d)), which suggests that a higher density of twins and dislocations in SM-10v offers higher resistance to creep.

4.1.4.5 Strain Rate Sensitivities

A material's rate-dependent strength (or hardness) behaviour is governed to a greater extent by strain rate sensitivity (SRS). However, due to the complex deformation mechanism, complex rate-sensitive behaviour is observed in Mg alloys [114–116]. Figure 4.1.18(a) and (c) show double logarithmic plots of creep rate vs nanohardness for SM-3v and SM-10v, respectively, at different depths from the SMATed surface. An enlarged view of one of these plots (corresponding to ~50 μm depth) and its linear portion fitting are presented in Figure 4.1.18(b) for SM-3v and in Figure 4.1.18(d) for SM-10v. The reciprocal of the fitted line's slope represents the SRS of the corresponding depth. The SRS values obtained by adopting this approach for different depths in the SMATed layer are presented in Figure 4.1.18(e).

The SRS of the non-SMATed core of the AZ91D alloy is in the range of 0.037-0.040. The SRS value in region-I (Figure 4.1.18(e)) at ~50 μm depth is ~0.018 for SM-3v and ~0.027 for SM-10v; however, it drops suddenly when the distance from the SMATed surface increases to some extent, and subsequently, it increases in region II. Due to magnesium's HCP crystallographic structure, several deformation mechanisms exist (with very different SRS values from each other), which have distinct roles under varying loading paths. Even though different deformation mechanisms have different SRS values, the rate-dependent behaviour of Mg alloys is commonly described through a single SRS scheme in many studies. Nevertheless, SRS values must be individually correlated with the different deformation mechanisms.

Grain size could affect the SRS of material [80, 116]. Choi et al. reported that grain refinement during the high-pressure torsion (HPT) enhances the SRS of as-extruded ZK60 Mg alloy (from ~0.035 to ~0.043) [116]. However, the deformation twinning demonstrates low SRS [114]. Due to the gradient microstructure of the SMATed layer, SRS behaviour depends on the microstructure's dominant feature. In the current study, the maximum grain refinement is observed near the SMATed surface, where nanocrystallites/nanograins are formed (Figures 4.1.5(c) and 4.1.9). Therefore, the reduced grain size dominates in causing higher SRS near the surface region (i.e., region-I) than region-II. As the SM-10v surface has better grain refinement than SM-3v (Figures 4.1.5(c), 4.1.8, and 4.1.9), region I of the SM-10v specimen shows higher SRS (Figure 4.1.18(e)). However, the lower value of SRS in region-I than in the non-SMATed specimen suggests the role of twinning in attenuating the dominance of grain refinement to control SRS.
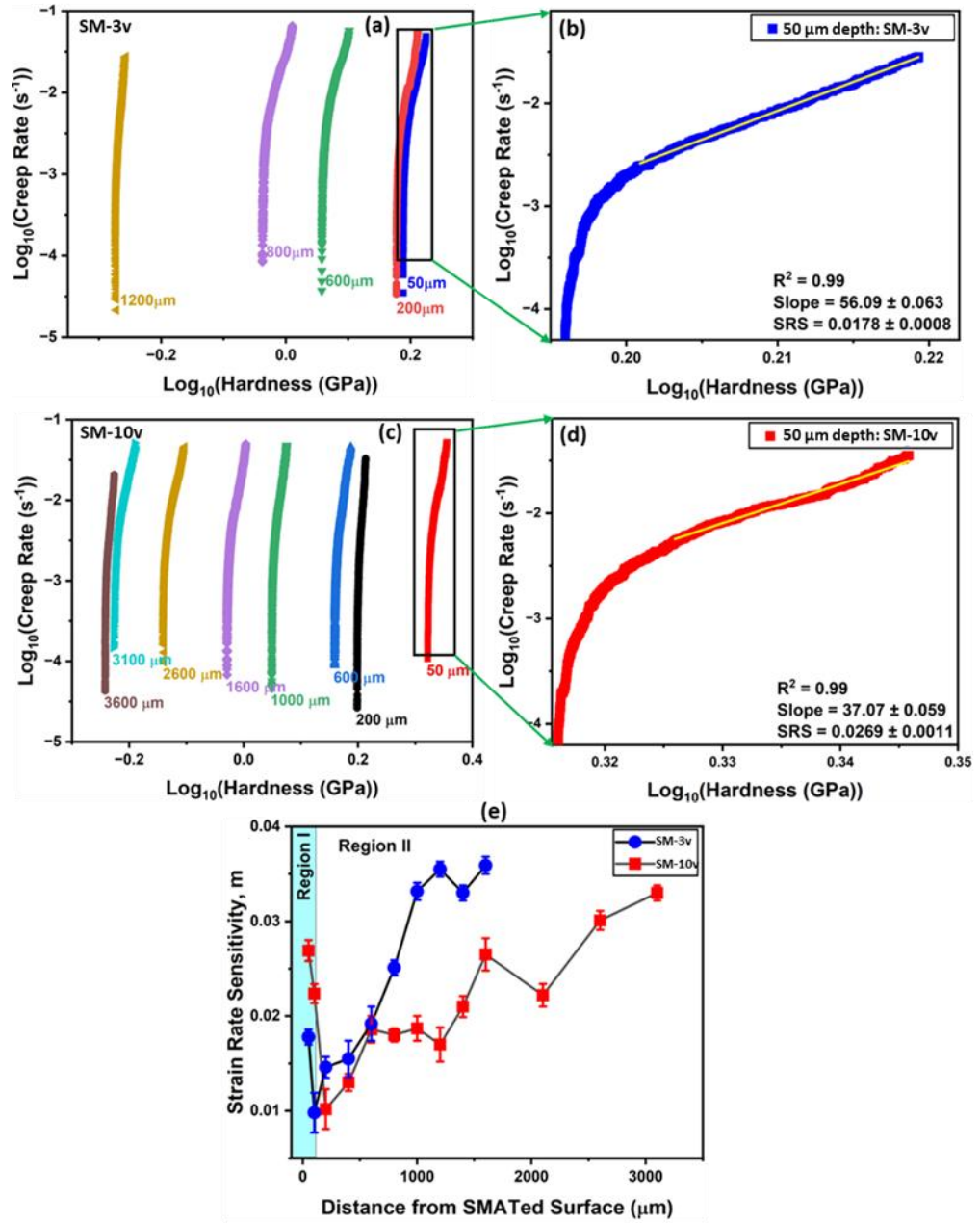
Figure 4.1.18: *Double-logarithmic plots of creep rate variation with hardness at different depths from the SMATed surface of (a) SM-3v specimen (an example of linear portion fitting at 50 μm (b)) and (c) SM-10v specimen (an example of linear portion fitting at 50 μm (d)). (e) Strain rate sensitivity variation in the SMATed region of SM-3v and SM-10v specimens*

As the distance increases from the SMATed surface (towards the region I/II interface), the increase in grain size and domination of twins reduce SRS. At the beginning of region II (at a depth of ~200 μm) of the SMATed specimens, the SRS is ~0.01 (Figure 4.1.18(e)). In region-II, SRS tends to increase as the distance from the SMATed surface increases and, finally, approaches the value of the non-treated specimen's SRS. The intermediate SRS values can be associated with the combined

effect of twin gradient and dislocation slip. In Mg alloys, extension twinning, pyramidal slip, prismatic slip, and basal slip are some of the most common deformation mechanisms [86, 114]. When twinning is the dominant deformation mechanism, an Mg alloy becomes rate-insensitive, where SRS values could be reduced to ~0.01 (or even lower) [114]. In the current study, the densely distributed twins are formed near the surface of SM-3v and SM-10v (Figures 4.1.2 and 4.1.3). As mentioned above, the lowest value of SRS (at the beginning of region-II) is associated with the deformation twins' dominance. An increasing trend in SRS is observed in region-II as the density of twins reduces with an increased distance from the SMATed surface (Figure 4.1.4). The SM-10v specimen shows lower SRS values throughout region-II, possibly due to the higher twin density in the SMATed layer of SM-10v (Figure 4.1.4).

4.1.5 Mechanism of Grain Refinement and Evolution of Gradient Microstructure and Properties of AZ91D During SMAT

In SMAT, strain and its rate are crucial in converting the strain-free microstructures into micro-, sub-micro-, and nanoscale-grained structures [80, 117, 118]. Applied strain and strain rate are comparatively higher at a SMATed surface and decrease along with depth. In other words, the specimen surface experiences severe deformation, and its severity gradually reduces with an increased distance from the surface. Various steps are involved in microstructure evolution during the SMAT (Figure 4.1.19). During SMAT, the specimen surface initially experiences lower strain, followed by intermediate strain and, finally, higher strain. Consequently, the microstructure in the deformed layer of AZ91D alloy gradually changes with time and the distance from the SMATed surface (Figure 4.1.19(a)).

The coarse-grained structure of the near-surface region transforms into the nanocrystalline layer after SMAT processing of the HCP-structured materials like Mg alloys (Figure 4.1.19(b)). Due to low-strain deformations at the beginning of SMAT, many dislocations appear within the coarse grains (Figure 4.1.6(b)). The nucleation of deformation twins is generally preceded by dislocation activity; hence, the deformation twins are observed at a later stage (Figure 4.1.7 and 4.1.8). The increased strain rate and strain accumulation further increase twin density (Figure 4.1.2-4.1.4) and alter the thickness of twins (Figure 4.1.7 vs Figure 4.1.8).

However, as the SMAT operation is performed at a lower (room) temperature, easily formed twins (due to increased strain rate) become difficult to grow compared to other SPD processes [68, 119]

The twin gradient microstructure (concerning the density and thickness of the twins) is a result of the plastic strain gradient produced during SMAT [40, 78]. The velocity of balls has an important role in governing the density of one- and two-dimensional lattice defects in the SMATed layer. The higher velocity of balls in SMAT causes the transfer of higher kinetic energy to the specimen surface, which increases the density of dislocations and twins and forms a deeper SMAT-affected region (Figure 4.1.4). The thickness of the SMATed layer and the accumulated strain increase with an increased SMAT duration (keeping other process parameters constant). An increased peening intensity or percentage coverage causes such a response.

Furthermore, with the progress of the SMAT duration, some twins start interacting with each other due to an increased twin density within the grains (Figures 4.1.2-4.1.4). The twins impede the dislocations during the deformation. Hence, twin-twin interactions and twin-dislocation arrangements lead to grain refinement (Figure 4.1.19(b)). Further deformation forms sub-grains/nanograins (with low-angle boundaries) and many defects due to lattice rotation [79]. Different rotation directions are plausible, depending on the type of dislocation slip system. An increased misorientation between sub-grains and the gradual rotation of substructures accommodate the higher strain [119]. This situation eventually leads to the formation of high-angle boundaries and, finally, nanosized grains of around 30-100 nm (Figure 4.1.9(d)). As the strain decreases with increasing depth, the grain size gradient occurs in the SMATed layer of an Mg alloy [102]. Moreover, a decrease in twin density (Figure 4.1.4) and twin thickness (Figures 4.1.7 and 4.1.8) occurs with an increased distance from the surface.
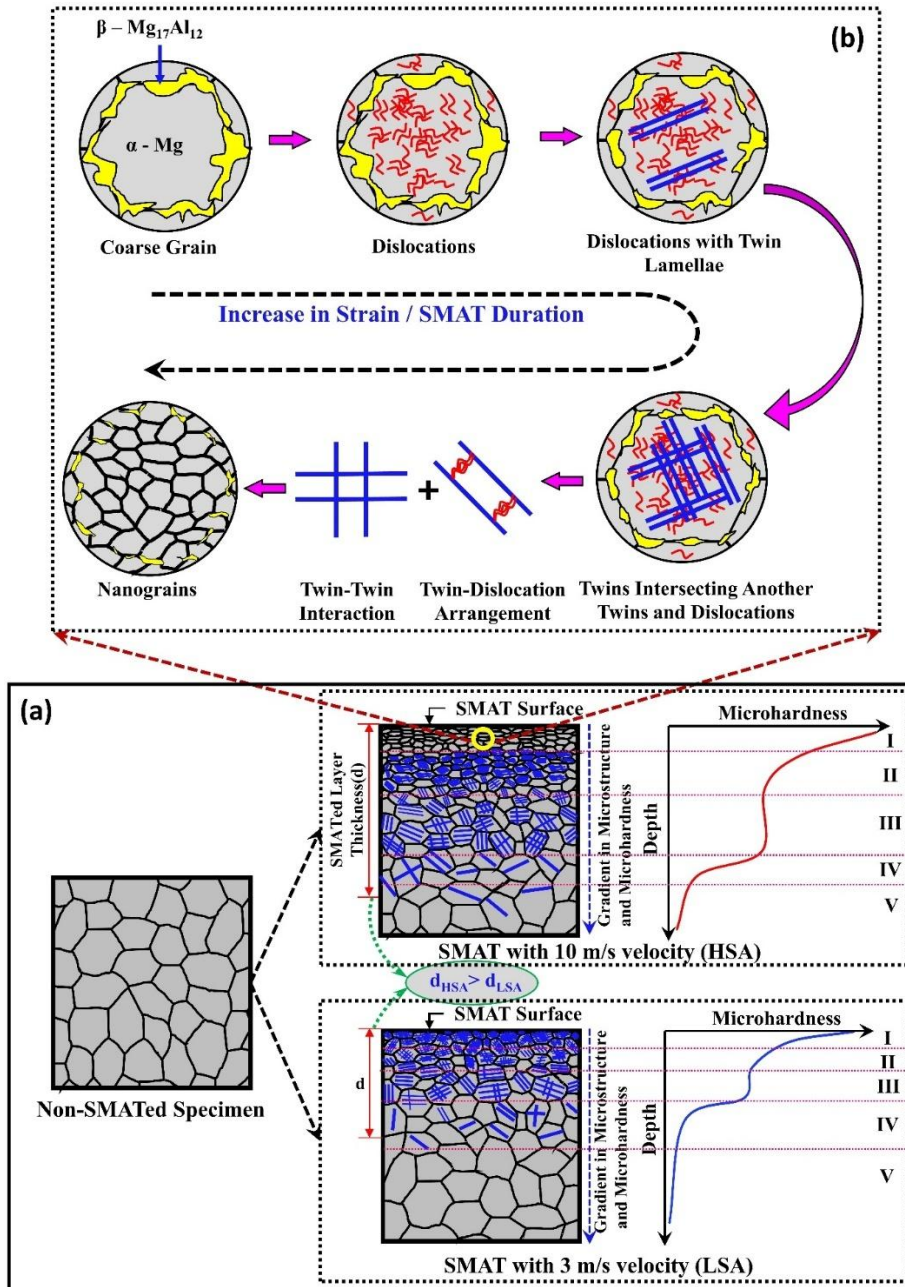
Figure 4.1.19: *Schematics showing (a) gradient in microstructure and microhardness (for low and high ball velocity situations) with (b) grain refinement mechanism in the near-surface region of the SMATed AZ91D alloy*

The material's abnormal (non-equilibrium) behaviour is possible due to a severe deformation during SMAT. In the case of AZ91D alloy, the α-grain boundaries are enveloped by a thick β-phase and microconstituents (α+β) (Figure 4.1.1). The SMAT operation promotes the β-phase dissolution (Figure 4.1.5(a) and (c)) [68] which is possible due to the enhanced solubility of Al in the α matrix (caused by an increased density of defects and strain accumulation). Moreover, a

70

strain in β-lattice dominates with an increase in ball velocity (Figure 4.1.5(d)), which could drive the dissolution of β in the α-matrix (Figure 4.1.5(c)).

The SMAT process alters the mechanical properties, which are changed with an increased depth in the SMATed layer (Figures 4.1.10-4.1.18). In the SMAT process, an elongation of the deformed layer (during the impacts of the balls) is inhibited by the non-deformed or less deformed underneath material (substrate/core), leading to the accumulation of compressive residual stress in the SMATed layer (Figure 4.1.10). Different zones with varying trends in residual stress across the SMATed layer are formed during the SMAT (Figure 4.1.10(c) and (d)). In other words, the squeezing action on a surface of softer material (like AZ91D alloy) by colliding balls during SMAT processing generates different zones of varying compression/deformation. This response leads to the non-uniform density of dislocations and twins (Figures 4.1.2-4.1.4), varying twin thicknesses (Figures 4.1.7 and 4.1.8), and grain size across the SMATed layer [102, 106]. Such a non-uniform distribution of the microstructural features generates a hardness gradient in the SMATed layer (Figures 4.1.11, 4.1.12, 4.1.14, and 4.1.19(a)). Nanomechanical behaviour also shows a gradient nature due to the gradient microstructure (Figures 4.1.13-4.1.18). Attrition of AZ91D specimen surface with higher velocity balls (e.g., ~10 m/s) is useful in forming a considerably thicker layer (~3500 μm) with higher hardness (~2 GPa at the surface) and compressive stress (about −281 MPa (max.) at ~600 μm depth) (for a peening intensity of 20) within a shorter SMAT duration (e.g., ~10 min).

4.2 Influence of Surface Mechanical Attrition Treatment Parameters on Microstructure and Residual Stress of Mg5Zn0.2Ca Alloy

This section extends the discussion by evaluating the impact of key SMAT parameters (Table 3.2), explicitly colliding balls velocity (1, 5, and 10 m/s) and surface coverages (500, 1000, and 2000%), on the microstructural refinement, surface hardness, and residual stress distribution of the biodegradable Mg5Zn0.2Ca alloy. The evolution of microstructural features and hardness gradients is assessed alongside the quantification of residual stresses using the X-ray diffraction-based $\sin^2\psi$ method. The findings underscore the critical role of SMAT-induced deformation in enhancing mechanical performance, contributing to the alloy's suitability for biomedical applications.

4.2.1 Results

4.2.1.1 Microstructure Analysis

SEM micrograph and EDS spectra shown in Figure 4.2.1(a-e) represent microstructural features of Mg5Zn0.2Ca alloy. Its microstructure consists of an α-Mg matrix, and secondary phase particles ($Ca_2Mg_6Zn_3$) are dispersed throughout the grain interior and boundary.
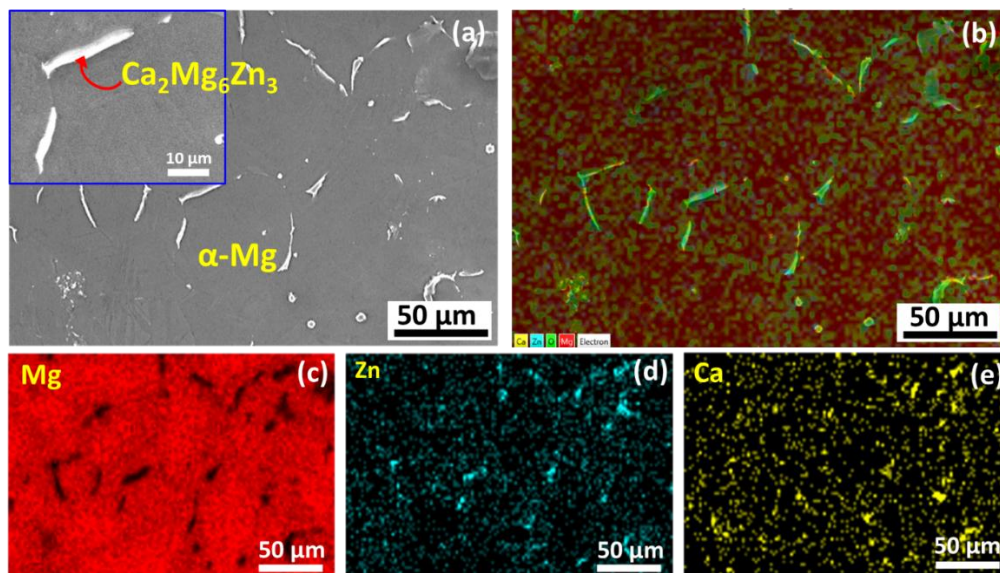
Figure 4.2.1: *(a) SEM micrograph and (b)-(e) corresponding EDS maps for non-SMATed Mg5Zn0.2Ca alloy*

A similar microstructure was reported in the literature [120]. The grain size of the as-cast Mg5Zn0.2Ca alloy is about 108 ± 5 μm. The literature has also reported an almost similar grain size of 114 ± 5 μm for as-cast Mg4Zn0.7Ca alloy [120]. Figure 4.2.2(a-i) shows optical micrographs of Mg5Zn0.2Ca alloy, which is SMATed with different ball velocities and surface coverages. For specimens SMATed at 10 m/s ball velocity (SA7, SA8 and SA9), fine and densely distributed twins are observed compared to the other specimens. Figure 4.2.3(a-c) shows the twins' distribution from the treated surface to the core for SA3, SA6 and SA9. Other specimens also exhibit similar behaviour in terms of the distribution of twins.
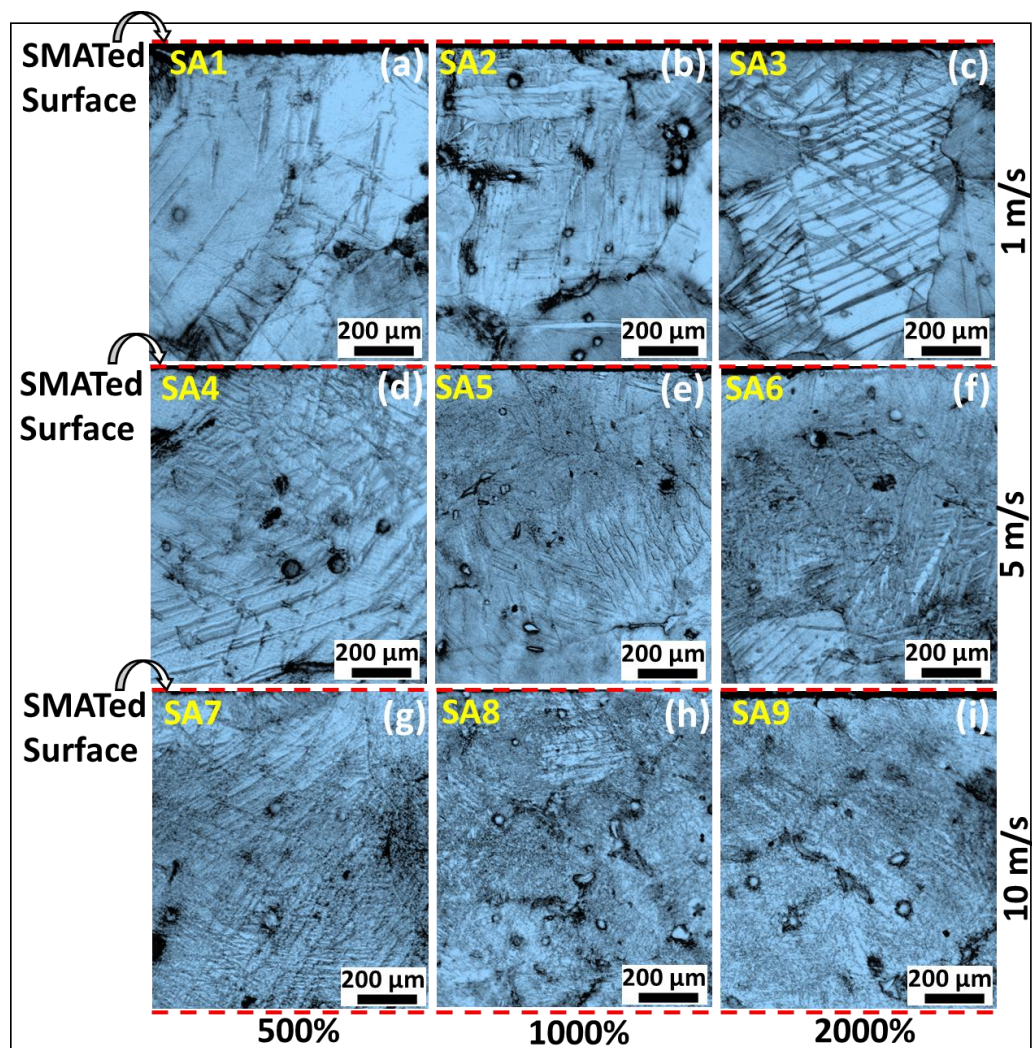
Figure 4.2.2: *(a)-(i) Microstructure of SMATed Mg5Zn0.2Ca alloy obtained using an optical microscope for different SMAT velocities and surface coverage*
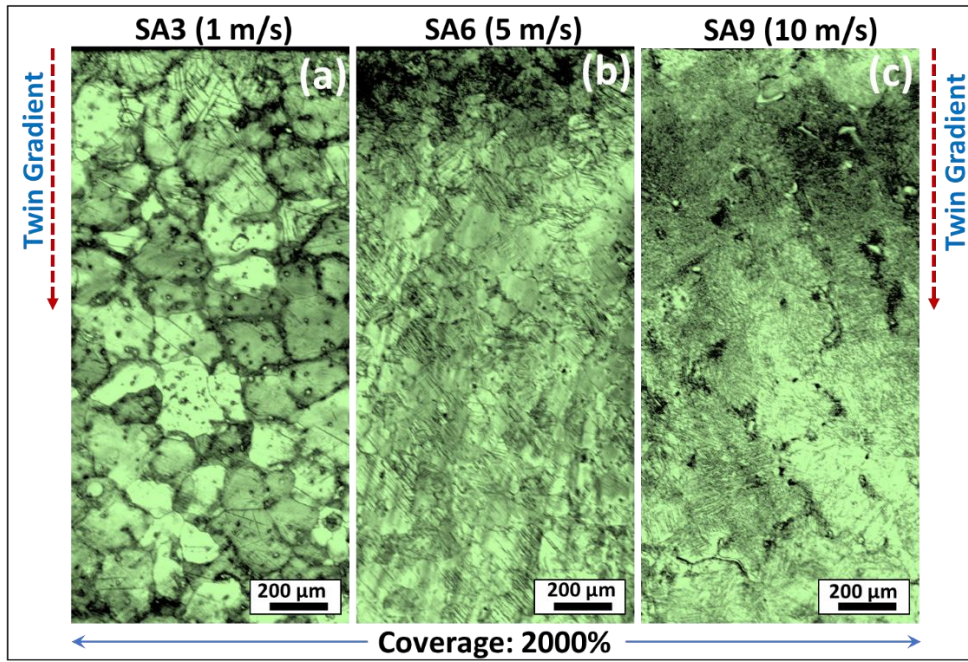
Figure 4.2.3: *Optical micrographs showing twin gradients across the cross-section of (a) SA3, (b) SA6, and (c) SA9 at a constant surface coverage of 2000%*

SA9 (Figure 4.2.3(c)) exhibits a dense distribution of fine twins near the treated surface. A transition from a fine twin morphology to coarser twins is observed when comparing SA9 to SA3. The thickness of the SMAT-affected layer influenced by the ball velocity and surface coverage is shown in Figure 4.2.4. In SA9, the presence of twins is evident up to a maximum depth of around 3000 ± 500 μm (Figure 4.2.4). Conversely, the lowest depth up to which twins are observed is around 400 ± 100 μm for SA1.
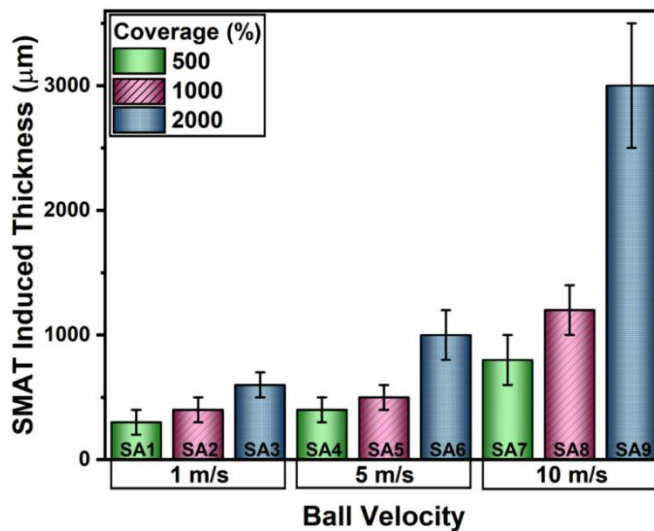
Figure 4.2.4: *Thickness of SMAT-affected regions for all specimens SMATed at different velocities of colliding balls and surface coverages*

Figure 4.2.5(a) shows XRD patterns of SMATed and non-SMATed specimens. They evidence the domination of α-Mg. A minute peak of $Ca_2Mg_6Zn_3$ phase (which has a minor quantity compared to α-Mg: see Figure 4.2.1) is evident in the non-SMATed specimen (amplified view of the relevant region of XRD is shown in the insert of Figure 4.2.4). Peak broadening is observed in all SMATed specimens.
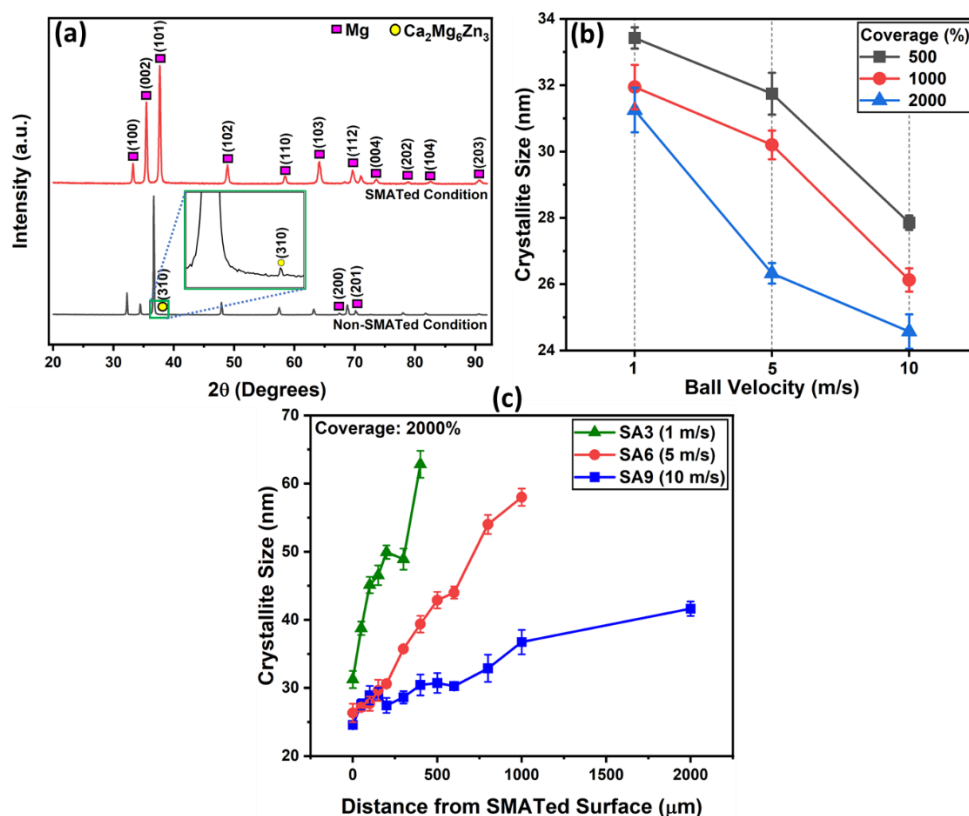
Figure 4.2.5: *(a) XRD patterns for non-SMATed and SMATed specimens, (b) Variation in crystallite size at SMATed surface for all specimens. (c) Crystallite size distribution within the SMATed layer (for SA3, SA6 and SA9) at a constant surface coverage of 2000%*

As shown in Figure 4.2.5(b-c), crystallite size is determined by assessing the broadening of the XRD peaks and utilising the Williamson-Hall method. Figure 4.2.5(b) shows the crystallite size near the specimens' treated surface. However, the variation of crystallite size across the cross-section of SA3, SA6, and SA9 (for 2000% coverage) is displayed in Figure 4.2.5(c). Crystallite size is influenced by surface coverage and colliding ball velocity (Figure 4.2.5(b)). The higher the surface coverage and ball velocity, the better the microstructural refinement. The SA9 shows the smallest crystallites of ~25 nm, indicating maximum grain

refinement. On the other hand, SA1 exhibits the largest crystallite size of ~31 nm for 2000% coverage, reflecting the lowest degree of grain refinement.

4.2.1.2 Microhardness Distribution

Figure 4.2.6(a) depicts the surface microhardness variation of the SMATed specimens. The highest microhardness value of ~118 $HV_{0.05}$ is observed at the SA9 specimen's surface, while the SA1 specimen reports the lowest surface hardness value of ~68 HV0.05. There is a ~109% (~2.1 times) increase in the microhardness of SA9 compared to the microhardness of non-SMATed specimens (~56 $HV_{0.05}$). The microhardness distribution across the cross-section of SMATed specimens (SA3, SA6 and SA9) is demonstrated in Figure 4.2.6(b). The microhardness gradient is observed in all the cases. As the distance from the SMATed surface increases, the microhardness value decreases, eventually reaching a plateaued trend. Figure 4.2.6(c) depicts a 3D plot generated using MATLAB illustrating the variation of surface microhardness concerning ball velocity and surface coverage. This plot depicts elevated microhardness values attributed to higher colliding ball velocities and surface coverages.
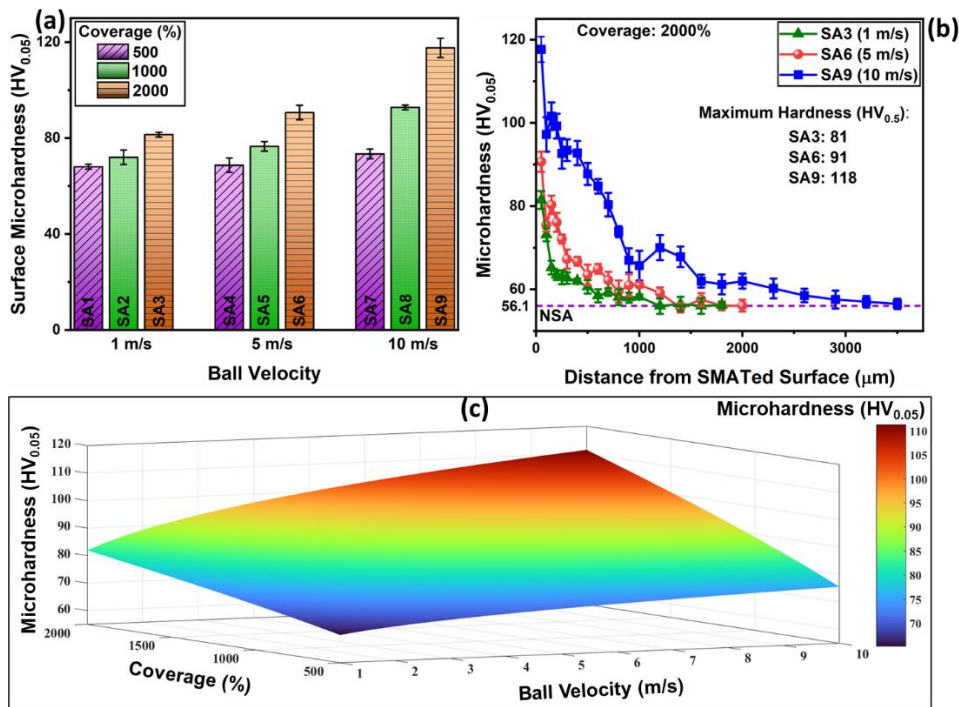
Figure 4.2.6: *(a) Surface microhardness variation for the SMATed specimens. (b) Microhardness gradient across the cross-section of SA3, SA6 and SA9. (c) A 3D plot representing the variation in surface microhardness of the specimens SMATed at different ball velocities and surface coverages*

4.2.1.3 Residual Stress Distribution

To measure the residual stress in the SMAT-affected region, an XRD peak of $(203)_{\alpha\text{-hcp}}$ ($2\theta = 90.46°$) is selected. Figure 4.2.7(a)) shows an example of such peaks corresponding to the 50 μm distance from the SMATed surface. The d-spacing versus $\sin^2(\psi)$ method is employed to estimate the distribution of residual stress within the SMATed layer (representative plots are shown in Figure 4.2.7(b)).
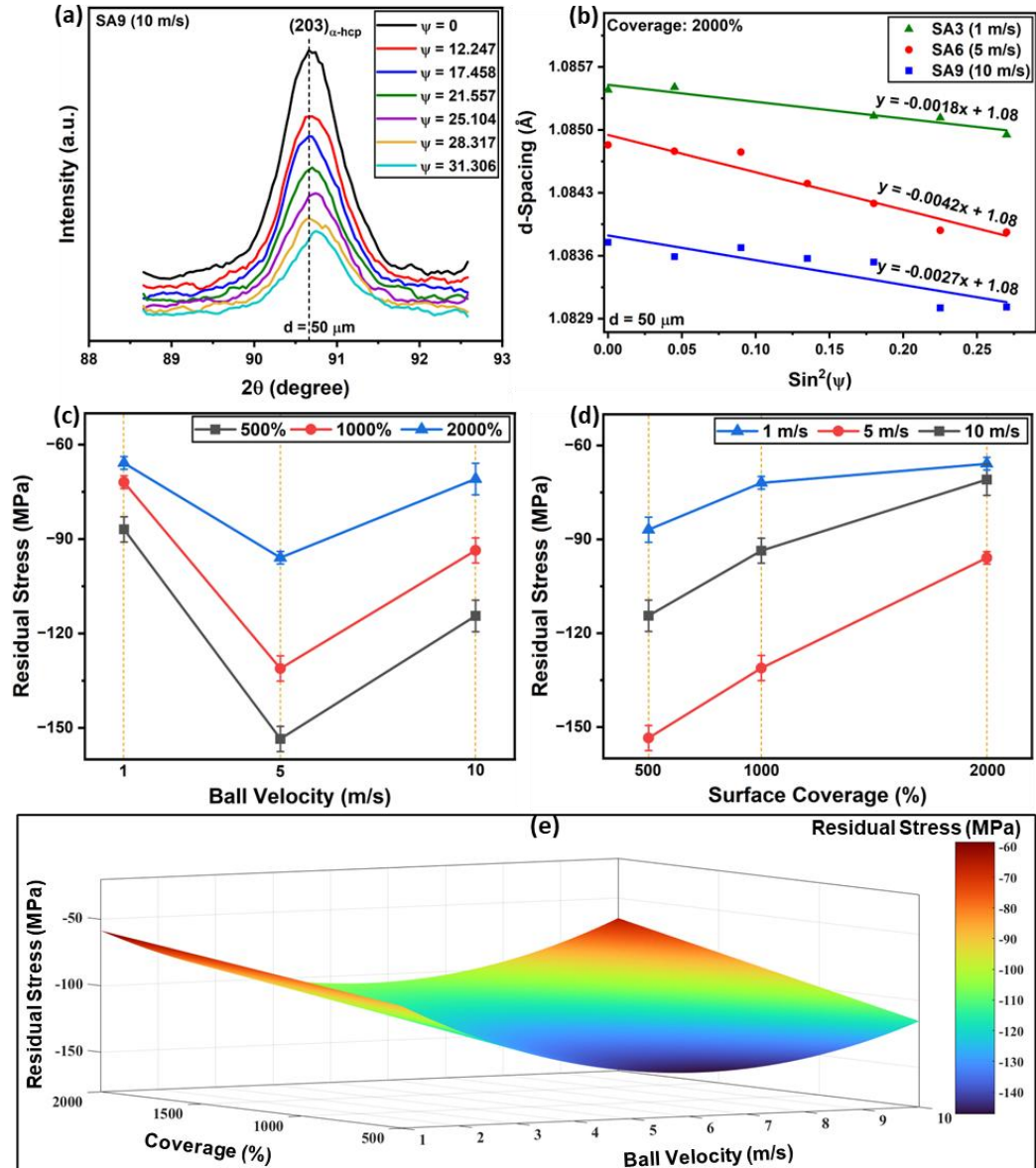
Figure 4.2.7: *(a) $(203)_{\alpha\text{-hcp}}$ XRD peaks of SA9 recorded at 50 μm depth. (b) d-spacing vs $\sin^2(\psi)$ plot at 50 μm depth for SA3, SA6 and SA9. (c)-(d) Surface residual stresses for the SMATed specimens. (e) A 3D plot representing residual surface stress distribution at different ball velocities and surface coverages*

Data points of the graphical presentation confirm the negative slope (m) through fitted lines, which are used to calculate the residual stress. Scattered data points are observed in this plot, which can be attributed to the X-ray penetration depth [121]. The peak position is also influenced by grain size, micro-texture, and the gradient structure resulting from SMAT. Surface roughness has also been identified as a contributing factor to the formation of residual stress [122] and hence these values are also measured by using 2-D profilometer. The measured surface roughness (R_a) values for 500%, 1000% and 2000% surface coverages are 0.2904 μm, 0.9616 μm, and 1.5215 μm respectively. Increase in the ball velocity from 1 m/s to 10 m/s correspondingly elevated the R_a values from 0.2904 μm to 1.5215 μm. Even though surface roughness plays an important role in influencing the local concentration of stress and subsequent relaxation behaviour within a material, however, quantifying the effect of surface roughness on the residual stresses developed within the material is intricate in nature. The presence of numerous parameters within the stress relaxation mechanism adds to this complexity. The following expression (Eq. 4.2.1) is used to calculate the residual stress [123, 124]:

$$\sigma_R = m \frac{E}{(1+\nu)} \tag{4.2.1}$$

where, σ_R is residual stress, ν is Poisson's ratio, and E is Young's modulus for magnesium alloy. In this study, the considered elastic constants are a Poisson's ratio of 0.35 and an elastic modulus of 46 GPa [44]. The SMATed specimens show compressive residual stresses generated at the surfaces (Figure 4.2.7) and within the SMAT-affected layer (Figure 4.2.8).

Figure 4.2.7(c-d) and a 3D plot (Figure 4.2.7(e)) generated using MATLAB show the surface residual stress variation at different ball velocities and surface coverages. In a 3D plot (Figure 4.2.7(e)), the R^2 value of ~0.96 ensures the closeness of fit. Hence, this profile illustrates a continuous and smooth transition without any undulations across various surface coverages and ball velocities. This plot also highlights that higher surface coverage leads to a reduction in compressive residual stress values. However, there is an initial increase in residual stress magnitude with higher ball velocity, followed by a subsequent decrease as ball velocity continues to rise.

Notably, the specimens SMATed with a ball velocity of 5 m/s exhibit the highest (among the different ball velocities) amount of surface compressive residual stress for all surface coverages. Maximum compressive residual stress values at the surface are observed at 500% coverage for all ball velocities. The highest surface compressive residual stress of -153.5 ± 4.2 MPa is observed for SA4 (5 m/s ball velocity and 500% coverage). For a given ball velocity, residual stress becomes less compressive with an increased surface coverage (Figure 4.2.7(d)), suggesting a decrease in locked-in stress at the specimen surface with an increase in the SMATed layer thickness (Figure 4.2.4) or an increase in the SMAT duration.
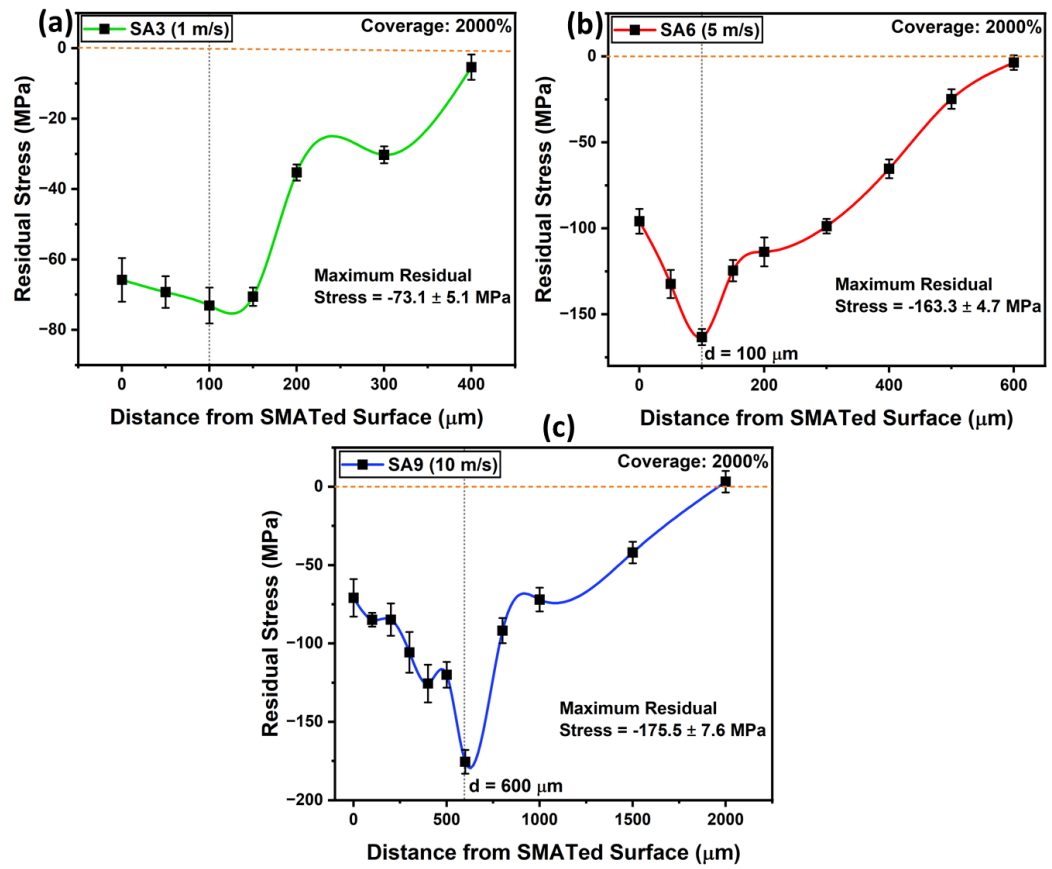
Figure 4.2.8: *(a) Distribution of residual stress across the cross-section of (a) SA1, (b) SA4, and (c) SA7*

Figure 4.2.8(a-c) demonstrates the residual stress distribution across the cross-section for SA3, SA6 and SA9 at 2000% surface coverage. At some distance from the SMATed surface, the maximum compressive residual stress is observed. As the distance increases away from such depth towards the surface and core (i.e., non-SMATed region of the cross-section), compressive residual stress decreases.

The extent to which this decrement occurs towards the surface depends on the depth corresponding to the maximum compressive stress and the magnitude of this stress. SA3 and SA6 show the highest compressive stress almost at a similar distance from the surface (i.e., ~100 μm). However, SA6 has a higher magnitude of compressive stress (-163.3 ± 4.7 MPa) than SA3 (-73.1 ± 5.1 MPa) due to the higher kinetic energy of colliding balls (which is linked to the higher velocity of the balls). In other words, about the same volume of material (due to the similar depth of ~100 μm) closer to the SMATed surface experiences more accumulation of compressive stress for the SA6 than SA3. However, as the depth corresponding to the maximum compressive stress increases considerably, a near-surface region experiences lower compressive stress (even if the maximum compressive stress is somewhat higher). The SA9 specimen shows the highest magnitude of compressive residual stress (-175.5 ± 7.6 MPa) at ~600 μm depth. This magnitude of maximum stress is close to that of SA6 (-163.3 ± 4.7 MPa); however, the residual surface stress of SA9 is lower than SA6 (due to the substantially higher relevant depth: ~600 μm vs ~100 μm).

Mg5Zn0.2Ca alloy subjected to SMAT with a ball velocity of 5 m/s (SA6, SA5, and SA4) exhibits a thinner SMATed layer (Figure 4.2.4) but notably higher surface compressive residual stress (Figure 4.2.7) and optimal surface hardness (Figure 4.2.6). However, the specimen treated at 10 m/s ball velocity exhibits the thicker SMAT-induced layer, high surface hardness, and maximum compressive residual stress in the layer. Consequently, SMAT processing of this alloy holds promise for further exploration and potential utilisation in commercial applications.

4.2.2 Discussion

4.2.2.1 Microstructure Analysis

An intermetallic compound $Ca_2Mg_6Zn_3$ is evidenced in the microstructure of non-SMATed Mg5Zn0.2Ca alloy that is the primary form of Zn in the α-Mg matrix (Figure 4.2.1(a)). The phase proportion of $Ca_2Mg_6Zn_3$ in the microstructure is ~2.2%. The precipitation of $Ca_2Mg_6Zn_3$ significantly influences the properties of the α-Mg alloy. These secondary phase particles act as obstacles to dislocation movement, especially at the grain boundaries, enhancing the alloy's overall strength [125].

On the other side, the influence of increased ball velocities during SMAT is observed for constant surface coverage (Figure 4.2.2). For example, with a surface coverage of 2000%, SA9 demonstrates a higher twin density than SA6 and SA3, suggesting a higher degree of deformation of the specimens' surface due to the increased strains and strain rates generated by the higher velocity of colliding balls. Under constant ball velocity conditions, such as 1 m/s (Figure 4.2.2(a-c)), SA3 (2000% coverage) exhibits denser twins compared to SA2 (1000% coverage) and SA1 (500% coverage). These consequences are attributed to an increased dislocation activity due to higher ball velocities and an increased percentage coverage.

Since magnesium alloy is an hcp material, dislocation slip and twinning are the predominant deformation mechanisms. This behaviour can be further attributed to its low stacking fault energy. Initially, the impact of colliding balls during SMAT significantly enhances the strain and strain rate in the region near the specimens' surface. Prolonged SMAT duration enables the colliding balls to penetrate deeper into the material, leading to an increased thickness of the SMAT-affected layer and even greater strains and strain rates in those regions. As a result of increased strain in the material, the movement of the dislocations occurs, leading to plastic deformation [40, 126–128]. When a material deforms, strain and stress are not uniformly distributed across the cross-section, and variations can occur in areas where they concentrate/localise. Consequently, non-uniformly distributed dislocations and twins can readily be observed.

The density of fine twins progressively reduces with an increased distance from the SMATed surface (Figure 4.2.3), and eventually, coarser twins form in the deeper regions. Strain variations and underlying microstructural changes across the material during deformation are the probable reasons for twin gradients [119]. However, higher thickness of SMAT affected region as in case of SA9 specimen (Figure 4.2.4) can be attributed to the higher impact energies and the increased rate of deformation.

As shown in Figure 4.2.5(a), a peak broadening is observed for the XRD peaks after SMAT and lattice defects, strain accumulation, and grain refinement are the major reasons for that. Smaller crystallite size often reflects the broader diffraction peaks; hence, peak broadening indicates the nanocrystalline nature of

materials [40, 129]. On the other side, the crystallite size gradually increases from the SMATed surface to the core (Figure 4.2.5(c)). In other words, the SMAT-affected regions of all the SMATed specimens exhibit gradient structure concerning the crystallite size. It indicates that the variations in crystallite size can be attributed to the complex interaction among dislocations and twins and their density gradients (Fig. 4.2.2 and 4.2.3).

Due to the low shear stress requirements, the basal plane (0001) is the primary slip plane in magnesium alloys. Dislocations can serve as nucleation sites for twin formation, and the stress concentrations around them can facilitate the initiation and propagation of twinning deformations [119]. As stain and strain rate increase (due to the increased ball velocity, percentage coverage, or SMAT duration), the density of dislocations increases, which interacts with twins and twin boundaries. These interactions between dislocations and twins influence the overall deformation behaviour of the alloy. Dislocations can either pile up at twin boundaries (leading to their pinning) or glide through twin boundaries (causing their motion) [103]. A higher density of dislocations and their interaction with twin boundaries further promotes twin formation, leading to dislocation-twin and twin-twin interactions. Consequently, the larger grains undergo fragmentation/division, leading to a refinement in grain size. Hence, due to comparatively higher strain and strain rates caused by a ball velocity of 10 m/s, SMATed specimens (SA7, SA8 and SA9) experience better grain refinement.

4.2.2.2 Microhardness Distribution

The gradient in microhardness (Figure 4.2.6) and fluctuations in the microhardness profiles could be linked to the variation in the density of crystal defects (like twins and dislocations) in the specimen cross-section (Figure 4.2.3). From a 3-D plot (Figure 4.2.6(c)), an empirical relationship is established for surface microhardness by fitting the profile as a function of ball velocity and surface coverage. The R^2 value of ~0.91 ensures the closeness of fit. Therefore, this profile demonstrates a smooth transition without any fluctuations across various surface coverages and ball velocities. Eq. 4.2.2 expresses the established empirical relationship:

$$H_S = H_0 + V^{1/3}C^{3/4} \qquad\qquad (4.2.2)$$

where, H_S is the surface microhardness, H_0 is the initial microhardness, V is the ball velocity (m/s), and C is the surface coverage (%). This equation indicates an increased microhardness value with an increased colliding ball velocity and surface coverage. However, from Eq. 4.2.2, it is clear that surface coverage is a more dominating parameter than the colliding ball velocity. The presence of lattice defects, strain hardening, and grain refinement are the most probable reasons for increased hardness value after deformation.

Increasing dislocation activity (due to SMAT) allows more significant strain hardening and better grain refinement [126]. The effect of grain size on hardness could be linked to the Hall-Petch relation [81]. Due to the hcp crystal structure, magnesium alloys have inadequate slip systems and a larger Taylor factor [130], influencing the material constant (k) in the Hall-Petch equation and increasing the sensitivity of hardness value on grain size.

4.2.2.3 Residual Stress Distribution

The main cause of residual stress generation (Figure 4.2.7(a) and Figure 4.2.8) is the resistance encountered by the material during plastic deformation. Further, this behaviour can be attributed to dislocation generation/accumulation, twin density, strain gradients, and grain refinement [131]. Variations in ball velocities and surface coverages during SMAT exert a notable impact on several critical aspects of the material's behavior. Specifically, they influence the degree of grain refinement, the distribution and density of twins, the formation of dislocation loops, and the non-uniform distribution of strain. This collective influence subsequently extends to the fluctuations in the magnitude of compressive residual stress that develops within the material and the intricate mechanism through which this stress relaxes over time [132–134].

The material attempts to relax and reach equilibrium after the complete deformation process. The material, however, is in a metastable state due to the non-uniform distribution of strain and defects [132, 135]. This response results in the generation of residual stress. Stress accumulation and defects near the deformed surface prevent the material from relaxing and increase residual stresses. In the

presence of dislocations, twins, and grain boundaries, the stress is locked in the material and hinders it from completely relaxing [132–134]. Hence, due to the non-uniform distribution and accumulation of strain during the deformation process, residual stress is often higher beneath the deformed surface [136].

The dependency of the residual surface stress on the ball velocity (which governs the kinetic energy of colliding balls) for a given surface coverage indicates the role of the amount of strain accumulation in the SMATed layer. Moreover, the surface stress variation depends on the residual stress distribution across SMATed specimens and the stress relaxation phenomenon [132, 133, 135]. Therefore, the residual surface stress is a complex function of the cross-sectional width of the SMAT-affected region, surface coverage (which is also linked to the SMAT duration), the amount of maximum residual stress in the SMATed layer, and the depth at which the maximum residual stress accumulates.

Compressive residual stress typically enhances the resistance to deformation and failure of materials [108]. It increases fatigue resistance and extends the material's service life by counteracting tensile stresses, which otherwise can initiate and propagate cracks [137]. Especially in high-stress environments, compressive residual stress helps prevent premature failure and prolongs component durability.

In summary, the observed gradient microstructure and refined grains contribute to enhanced surface hardness and residual compressive stress, which are vital for resisting early-stage deformation in a load-bearing implant. This supports the strategic aim of improving mechanical reliability for biomedical deployment of Mg5Zn0.2Ca.

4.3 The effect of severe surface deformation on microstructure refinement, corrosion, and biocompatibility of Mg5Zn0.2Ca alloy

This section focuses on the influence of severe surface deformation induced by SMAT on the microstructure refinement, corrosion resistance, and biocompatibility of the Mg5Zn0.2Ca alloy. The study investigates the degradation behaviour through immersion testing and electrochemical analyses, including open circuit potential (OCP), electrochemical impedance spectroscopy (EIS), and linear sweep voltammetry (LSV) in physiologically relevant media. Particular attention is given to Mg^{2+} ion release, surface film stability, and corrosion kinetics. Furthermore, the biological response is assessed through in vitro cytocompatibility tests using murine fibroblast (L929) cells and protein adsorption analysis, simulating human plasma conditions (Section 3.3). The findings demonstrate the potential of SMAT-treated surfaces to enhance both corrosion resistance and biological performance for biomedical implant applications.

4.3.1 Results

4.3.1.1 Microstructure

The microstructural features and corresponding EDS spectra of NSM specimens are presented in Figure 4.3.1. The Mg5Zn0.2Ca alloy exhibits two phases, α-Mg, and the secondary phase $Ca_2Mg_6Zn_3$, as depicted in Figure 4.3.1(a), and the same is further validated using EDS spectra (Figure 4.3.1(b) and (c)). This secondary phase is located predominantly along grain boundaries. The XRD analysis further confirms the presence of the secondary phase in the alloy (Figure 4.3.3(a)). A minor peak corresponding to the $Ca_2Mg_6Zn_3$ phase is observed for NSM (an amplified view of this region is provided as an insert in Figure 4.3.3(a)). XRD pattern also highlights the predominance of α-Mg.

Figure 4.3.1(d) and (e) depict the microstructure of SM-3v and SM-10v specimens, respectively. SM-10v features a highly refined region adjacent to the surface, followed by fine and dense twins (Figure 4.3.1(e1)) and then coarse twins, whereas SM-3v displays fine and dense twins near the treated surface before transitioning to coarser twins (Figure 4.3.1(d1)). The twin density diminishes from the SMATed surface to the core. SM-10v shows finer twins at similar depths than

SM-3v (Figure 4.3.1(d1) vs. 2(e1)). SM-10v has a deeper fine-twined region than SM-3v (Figure 4.3.1(d) and (e)).
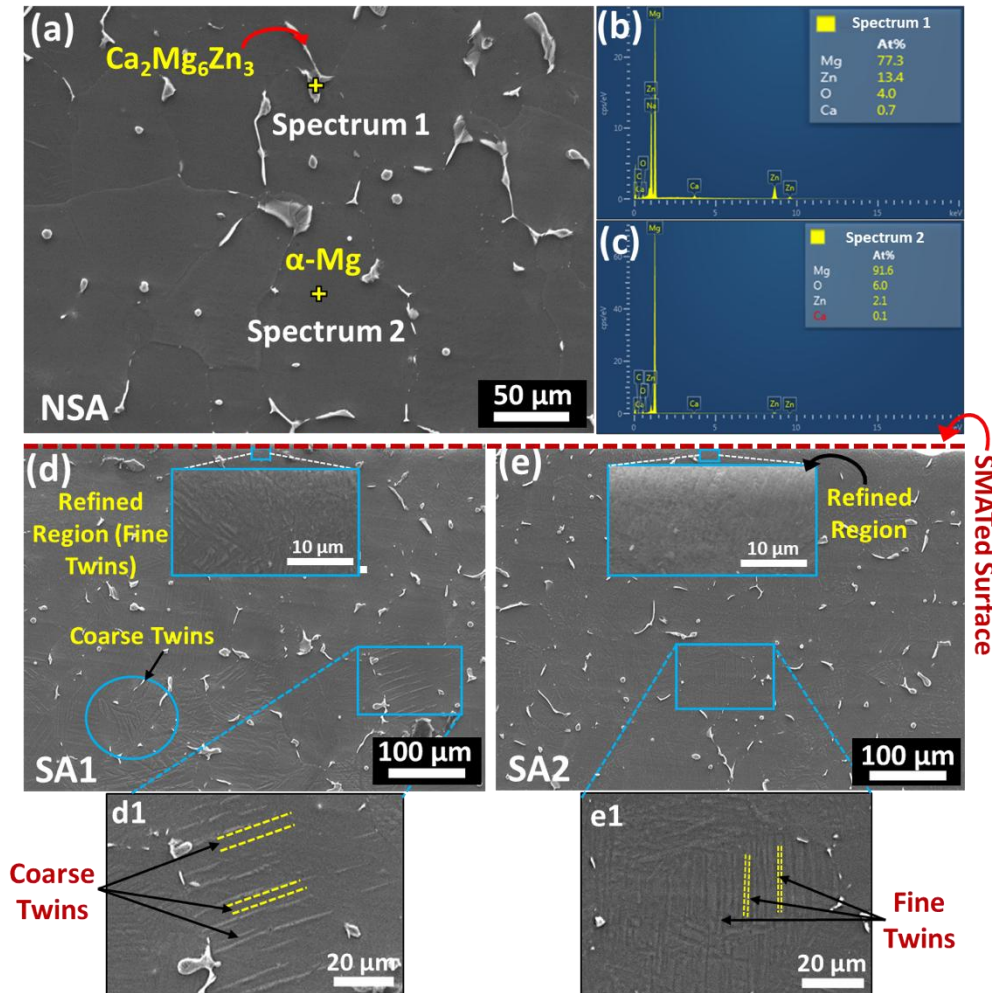
Figure 4.3.1: *SEM micrograph for NSM (a) with corresponding EDS spectra (b-c), SEM micrographs of SM-3v ((d), with magnified views of coarse twins (d1)) and SM-10v ((e), with magnified views of fine twins (e1))*

EBSD measurements are performed to comprehensively understand the microstructural changes in the Mg5Zn0.2Ca alloy induced by SMAT. Figure 4.3.2 shows the image quality (IQ) and orientation image (OIM) maps for the SMATed samples. These results display a gradient microstructure in the SMATed layer.
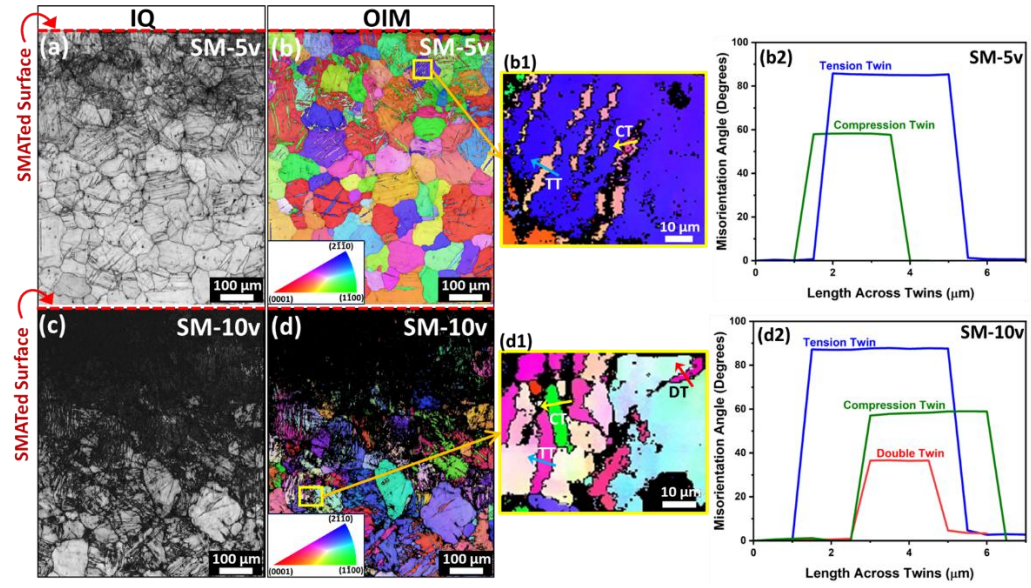
Figure 4.3.2: *EBSD results demonstrating IQ maps and OIMs for (a-b) SM-3v and (c-d) SM-10v, along with the amplified regions of OIMs (b1 and d1) and the corresponding misorientation angles for the twins (b2 and d2)*

Figure 4.3.2(c) and (d) show that the region near the surface of SM-10v is highly deformed, making a significant portion unindexed. The unindexed regions in EBSD results are ~11.6% for SM-3v and ~56.1% for SM-10v. In SM-3v, fine and dense twins are evident near the surface, with their density decreasing with increasing depth. The SM-10v shows highly dense twins even at greater depths from the SMATed surface. This behaviour indicates that the higher velocity colliding balls penetrate deeper into the material, resulting in more significant grain refinement. Figure 4.3.2(b) and (d) present the OIMs for SM-3v and SM-10v, respectively. The grains in SM-3v appear to be relatively uniform in size and orientation (within the grains), indicating that the SMAT process at 5 m/s does not lead to extreme refinement and reorientation of the grains (Figure 4.3.2(b)). However, the higher deformation energy input at 10 m/s results in more pronounced reorientation effects, with the grains showing higher misorientation. This is evidenced by the broader range of colours (across the cross-section and within the grains) and more distinct boundaries between differently oriented grains. A TEM observation was also performed to investigate the highly refined region near the SMATed surface, detailed in subsequent text.

Furthermore, Figure 4.3.2(b1) and (d1) present the different types of twins in the SMATed regions of SM-3v and SM-10v, respectively. The corresponding

misorientation angles for the twins are displayed in Figure 4.3.2(b2) and (d2). The misorientation profiles for SM-v (Figure 4.3.2(b2)) and SM-10v (Figure 4.3.2(d2)) show distinct twin patterns. Tension twins (TTs), compression twins (CTs), and double twins (DTs) are observed with characteristic misorientation angles of ~86.10°, ~57.26°, and ~36.50°, respectively. The fraction of $\{10\bar{1}2\}$ TTs is considerably high for SM-3v, and these twins are evident almost everywhere. Along with TTs, near-surface regions (at ~100 μm depth from SMATed surface) reveal $\{10\bar{1}1\}$ CTs. In contrast, Figure 4.3.2d(2) shows the presence of TTs, CTs, and $\{10\bar{1}1\} - \{10\bar{1}2\}$ DTs even at ~550 μm depth from the SMATed surface, indicating that the strain induced by SMAT in SM-10v is sufficiently high to activate TTs, CTs, and DTs even at larger depths. Moreover, higher strain and strain rate leads to a higher degree of misorientation in SM-10v specimens. The presence of double twins in SM-10v increases the misorientation, contributing to the higher unindexed areas in the EBSD maps.

XRD results in Figure 4.3.3(a) indicate a peak broadening in all SMATed specimens. The Scherrer formula is employed to analyse this broadening and determine the crystallite size near the specimen surface [40] and the resulting crystalline sizes are shown in Figure 4.3.3(b). The NSM shows ~35 nm crystallite size. Crystallite size is significantly affected by SMAT, where a higher ball velocity results in the smallest crystallite size of ~24 nm due to a higher degree of grain refinement.
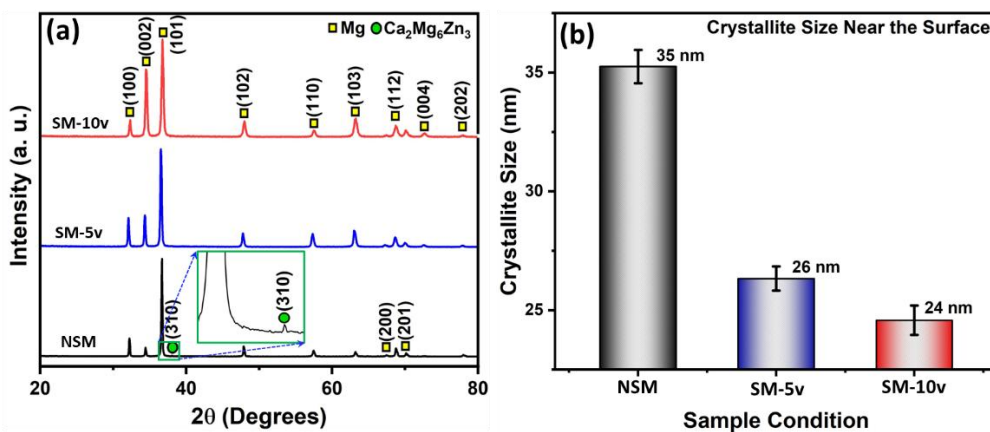
Figure 4.3.3: *XRD patterns for (a) NSM, SM-3v, and SM-10v with (b) variation of crystallite size near the surface*

Furthermore, TEM analysis is performed at depths of ~50 μm (subsurface region) for SM-3v and SM-10v. Figure 4.3.4(a) shows a bright-field (BF) TEM

image with the related selected area electron diffraction (SAED) pattern (Figure 4.3.4(b)) and the distribution of nanograins (Figure 4.3.4(c)) for SM-10v. Figure 4.3.4(d) represents the BF TEM image for SM-3v. As a result of the transformation from coarse grains to refined grains, nanograins (~21 nm) are observed in the case of SM-10v (Figure 4.3.4(a) and (c)). In contrast, TEM analysis reveals fine twins near the surface of SM-3v, which is attributed to a lower degree of grain refinement caused by the lower velocity of colliding balls during the SMAT process.
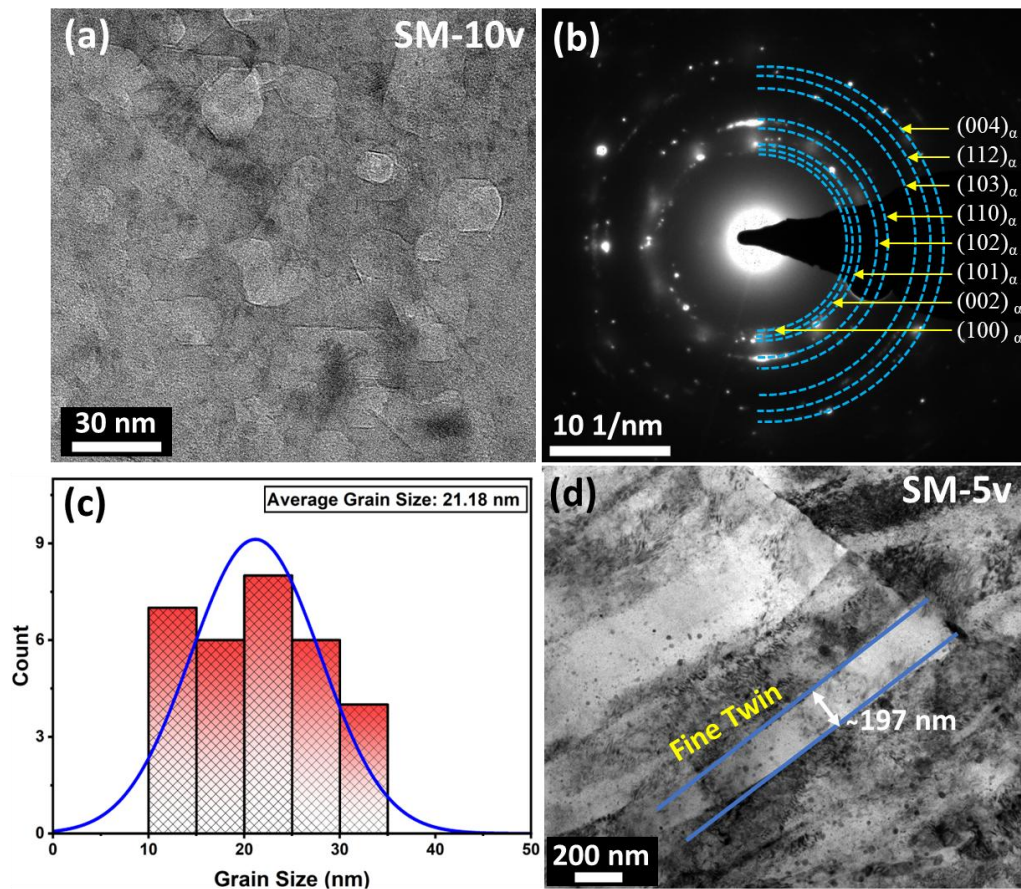
Figure 4.3.4: *Bright field TEM images of the region close to the surface of SM-3v (d) and SM-10v (a) with corresponding SAED pattern (b) and nanograins distribution (c)*

The microstructural changes induced in the Mg5Zn0.2Ca alloy by varying the intensity of colliding balls during SMAT have significantly influenced the hardness. The maximum surface microhardness value observed is ~117 $HV_{0.05}$ for SM-10v and ~91 $HV_{0.05}$ for SM-3v. These values indicate an increase of ~112% (~2.1 times) in the microhardness for SM-10v and ~65% (~1.6 times) for SM-3v when compared to the microhardness of NSM (~55 $HV_{0.05}$).

4.3.1.2 Biocorrosion

4.3.1.2.1 Electrochemical Measurements

Potentiodynamic polarisation curves and pH variation in pre- and post-corrosion tests for NSM, SM-3v, and SM-10v are presented in Figure 4.3.5. The corrosion characteristics, i_{corr}, E_{corr}, E_{pit}, and Tafel slopes (β_c and β_a), derived from the polarisation curves (through Tafel analysis), are presented in Table 4.3.1.
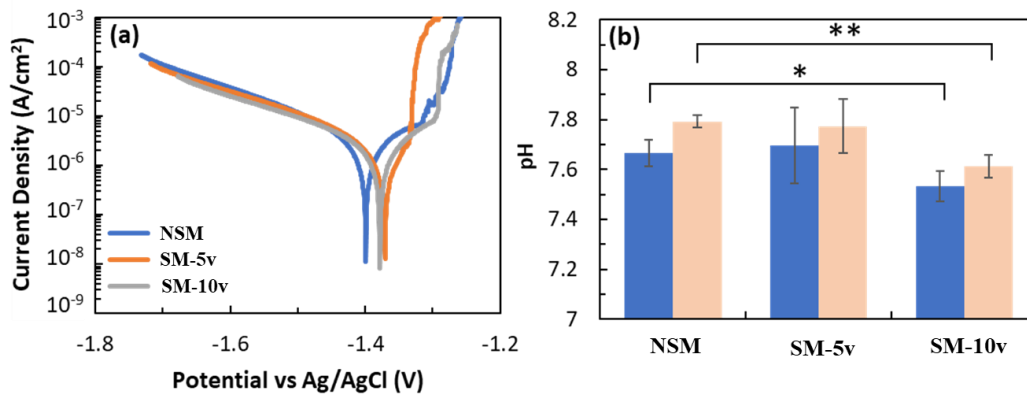
Figure 4.3.5: *Examples of the potentiodynamic measurements (a) and the pH values before and after electrochemical tests (b). Experiments are performed in EMEM-FBS in a 5% CO_2 incubator*

Table 4.3.1: Corrosion parameters derived from polarisation curves

Specimens	E_{corr} (V)	i_{corr} ($\mu A/cm^2$)	E_{pit} (V)	β_c (V)	β_a (V)
NSM	-1.393 ± 0.006	5.93 ± 0.67	-1.280 ± 0.006	-0.231 ± 0.004	0.275 ± 0.020
SM-3v	-1.383 ± 0.041	5.31 ± 2.27	-1.305 ± 0.018	-0.251 ± 0.010	0.254 ± 0.080
SM-10v	-1.417 ± 0.036	4.89 ± 1.09	-1.314 ± 0.018	-0.245 ± 0.012	0.224 ± 0.053

The Tafel slopes (β_a and β_c) provide insights into the electrochemical reactions' kinetics at the electrode surfaces. SM-3v and SM-10v show slightly higher β_c and slightly lower β_a values than those of NSM, but no significant difference is observed in the statistical analysis by Student's *t*-test. This behaviour indicates that the SMAT process may alter reaction kinetics but not drastically.

The parameter i_{corr} directly relates to the corrosion rate; lower i_{corr} values indicate higher corrosion resistance. The i_{corr} value for SM-10v (4.89 $\mu A/cm^2$) is

lower than that for SM-3v (5.31 µA/cm^2), which is subsequently lower than NSM (5.93 µA/cm^2); however, a statistically significant difference is not observed between the SMATed and non-SMATed specimens. This comportment suggests that the SMATed specimens tend to have enhanced corrosion protection, and a ball velocity of 10 m/s results in considerably better corrosion resistance compared to 5 m/s ball velocity. This corrosion behaviour can be correlated with the pH values measured before and after the electrochemical test. The pH values before the test have minor variances due to an unavoidable difference in the timing of pH measurement after taking out the EMEM-FBS from the CO$_2$ incubator and pouring it into the test chamber (when the electrolyte contacted the specimen surface).

On the other hand, the increase in pH (for which a statistically significant difference ($p < 0.01$) is noticed in Figure 4.3.5(b)) after the electrochemical measurement can be attributed to the difference in corrosion reaction during the immersion period (24 h) and PD measurement. There is a 0.13 ± 0.03 unit increase in the pH values for NSM, 0.08 ± 0.08 unit for SM-3v, and 0.08 ± 0.02 unit for SM-10v, as demonstrated in Figure 4.3.5(b). This behaviour shows that the enhanced corrosion resistance for SM-3v and SM-10v aligns with the observed pH variations. The values of E_{corr}, which indicate a material's corrosion susceptibility in a specific environment, do not show any significant difference between the specimens tested. However, the values of E_{pit} slightly shifted towards negative potential by SMAT application, indicating that the SMAT process enhances the corrosion susceptibility against pitting.

The typical Nyquist plots of NSM, SM-3v, and SM-10v specimens are displayed in Figure 4.3.6, and the parameters obtained by fitting with an equivalent circuit model (Figure 4.3.7(a)) are detailed in Table 4.3.2.
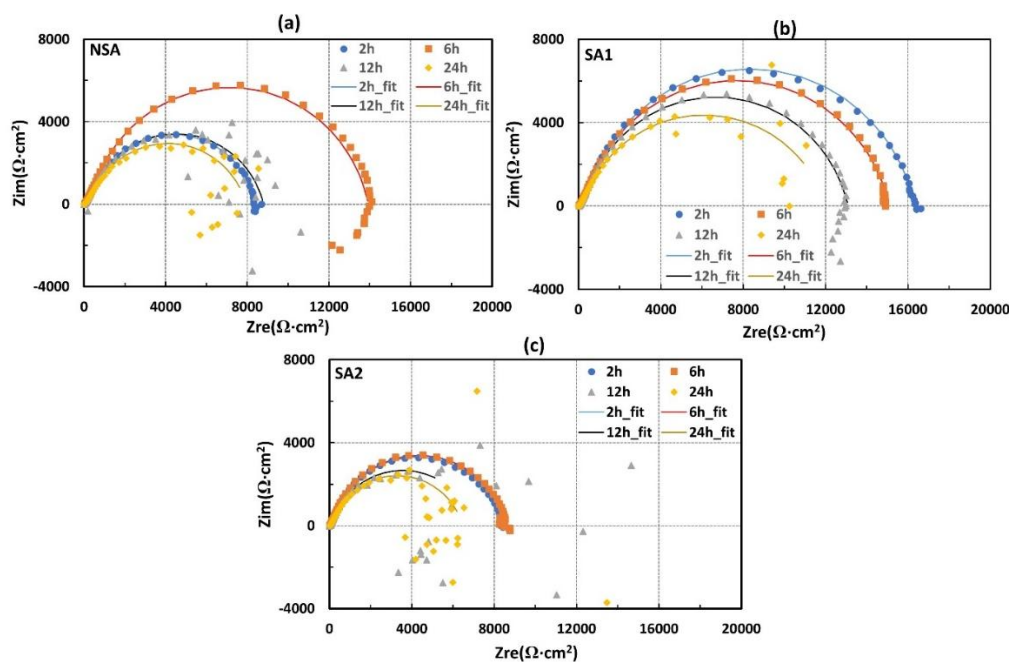
Figure 4.3.6: *Examples of the Nyquist plots for NSM (a), SM-3V (b), and SM-10V (c) specimens measured in EMEM-FBS in the 5% CO₂ incubator*

In the case of NSM, the capacitive semicircle enlarges from 2 to 6 h and diminishes after that. In the case of SM-3v, the capacitive semicircle is the largest at 2 h, then decreases. In the case of SM-10v, the size of the capacitive semicircle is stable up to 6 h of immersion and slightly decreases after that.
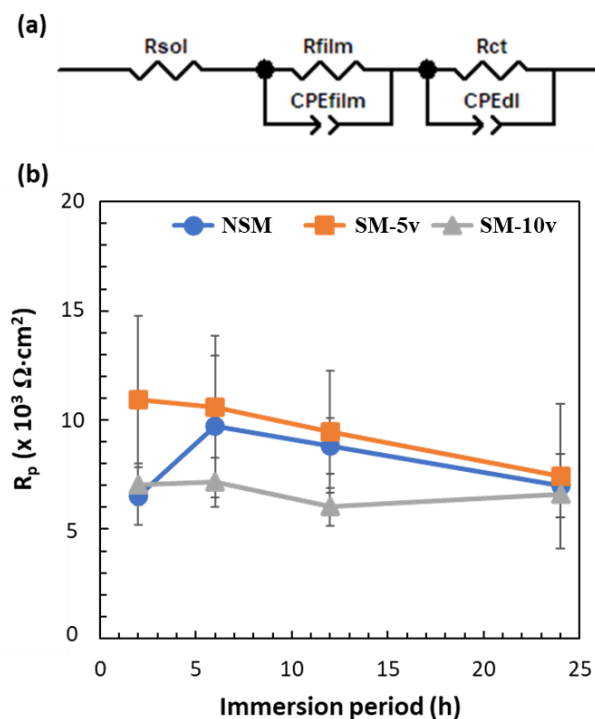
Figure 4.3.7: *Equivalent circuit model for EIS analysis (a) and obtained polarisation resistance (R_P) plotted against the immersion period in EMEM-FBS in a 5% CO₂ incubator (b, mean ±SD)*

The polarisation resistance, R_p, is defined as the sum of the resistance for the surface layer (R_{film}) and charge transfer resistance (R_{ct}), which is calculated for each specimen and time point, as shown in Table 4.3.2 and Figure 4.3.7(b). It indicates the decreasing trend in R_p of SM-3v as immersion period increases whereas that of NSM increases from 2 to 6 h and decreases thereafter. For SM-10v, however, R_p is rather stable during the 24 h of immersion. These results suggest that the SMATed process influenced the corrosion behaviour depending on its conditions. It should be noted that all the specimens have a similar level of R_p at 24 h of immersion.

Table 4.3.2: EIS parameters of SMATed and non-SMATed alloy samples after different immersion times

	Immersion period (h)	R_{sol} ($\Omega \cdot cm^2$)	R_{film} ($\Omega \cdot cm^2$)	R_{ct} ($\Omega \cdot cm^2$)	$T_{CPEfilm}$ ($\times 10^{-5}$ F$\cdot$S$^{p-1}\cdot$cm^2)	$P_{CPEfilm}$	T_{CPEdl} ($\times 10^{-4}$ F$\cdot$S$^{p-1}\cdot$cm^2)	P_{CPEdl}	R_p ($\Omega \cdot cm^2$)
NSM	2	25.8 ± 2.6	5850 ± 1280	682 ± 224	1.40 ± 0.28	0.866 ± 0.039	3.70 ± 3.31	0.441 ± 0.068	6540 ± 1320
	6	25.9 ± 2.4	8810 ± 3330	888 ± 257	1.36 ± 0.37	0.844 ± 0.049	4.40 ± 4.10	0.416 ± 0.073	9700 ± 3240
	12	26.6 ± 3.5	7940 ± 790	869 ± 654	1.44 ± 0.31	0.814 ± 0.036	1.89 ± 1.02	0.454 ± 0.069	8810 ± 1290
	24	21.5 ± 4.4	6430 ± 1500	560 ± 497	2.15 ± 0.46	0.719 ± 0.055	0.74 ± 0.73	0.533 ± 0.059	6990 ± 1460
SM-3v	2	24.6 ± 2.4	10470 ± 3680	471 ± 149	1.13 ± 0.09	0.883 ± 0.016	3.37 ± 3.15	0.476 ± 0.079	10940 ± 3820
	6	25.5 ± 3.8	10010 ± 3110	559 ± 195	1.04 ± 0.12	0.877 ± 0.020	2.61 ± 1.41	0.456 ± 0.050	10570 ± 3300
	12	22.8 ± 3.3	8880 ± 2620	573 ± 180	1.23 ± 0.18	0.850 ± 0.016	4.19 ± 3.17	0.400 ± 0.073	9450 ± 2790
	24	23.3 ± 2.3	7160 ± 3390	262 ± 147	1.62 ± 0.42	0.799 ± 0.061	1.48 ± 0.82	0.484 ± 0.073	7430 ± 3300
SM-10v	2	23.7 ± 1.6	6560 ± 990	484 ± 112	1.30 ± 0.12	0.871 ± 0.001	3.05 ± 0.81	0.455 ± 0.016	7040 ± 940
	6	25.1 ± 0.7	6650 ± 1120	494 ± 67	1.30 ± 0.16	0.854 ± 0.009	5.43 ± 2.82	0.396 ± 0.034	7150 ± 1140
	12	24.0 ± 1.3	5500 ± 860	517 ± 129	1.44 ± 0.25	0.827 ± 0.022	7.99 ± 4.01	0.347 ± 0.047	6020 ± 850
	24	20.0 ± 1.6	6070 ± 420	514 ± 102	1.51 ± 0.09	0.832 ± 0.009	5.31 ± 3.37	0.383 ± 0.055	6590 ± 370

After the potentiodynamic polarisation test, the morphology of corroded surfaces was evaluated using SEM and OM (Figure 4.3.8). The NSM specimen shows both uniform corrosion and localised corrosion at multiple points, which further leads to the formation of pits; hence, significant material degradation (Figure 4.3.8(a) and (d)). In contrast, the corrosion of SM-3v and SM-10v appears more localised at a few points over the exposed area (Figure 4.3.8(b), (c), (e), and (f)). These results are consistent with the findings of the PD measurement, suggesting higher pitting corrosion susceptibility and a lower corrosion rate of SMATed specimens than those of NSM.
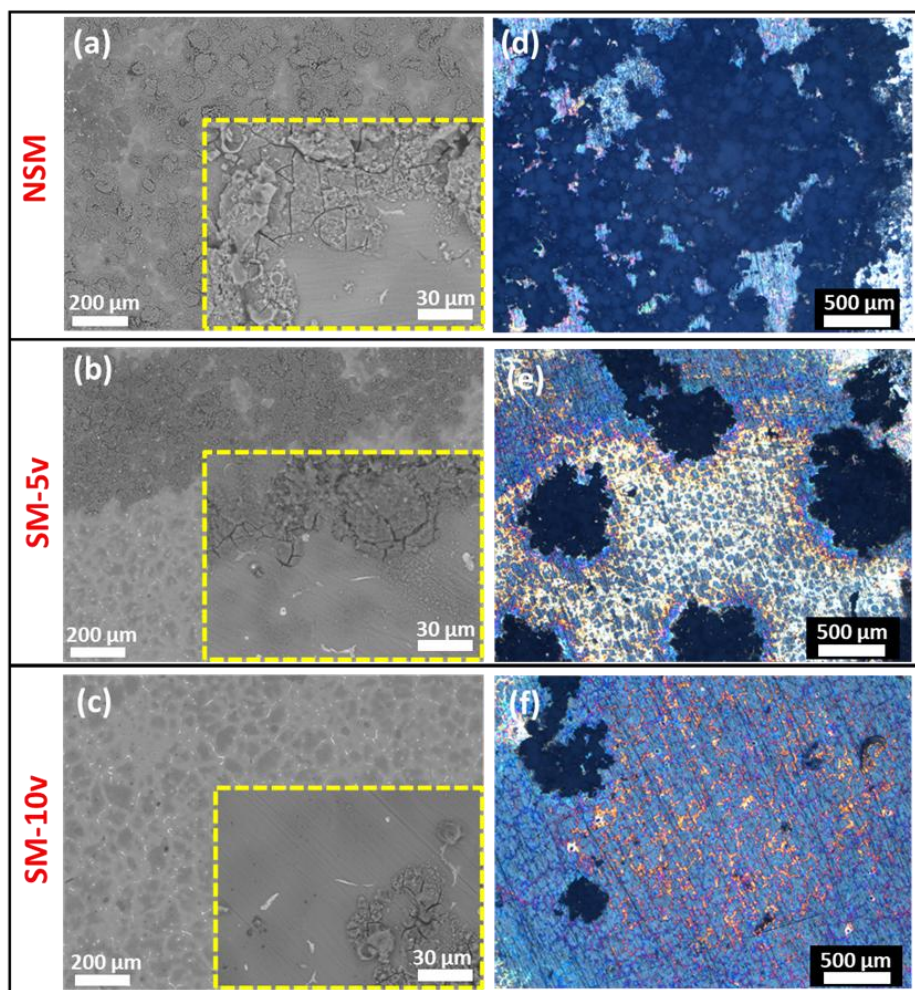
Figure 4.3.8: *Morphology of corroded surfaces: SEM micrographs for (a) NSM, (b) SM-3v, and (c) SM-10v and Optical images for (d) NSM, (e) SM-3v, and (f) SM-10v*

4.3.1.2.2 Immersion Test

The corrosion behaviour of SMATed and non-SMATed specimens was analysed up to 7 days of immersion in EMEM-FBS. Figure 4.3.9 presents the

94

calculated weight loss and corrosion rates after 1, 4, and 7 days for these specimens with Mg^{2+} ion release after 1 day of immersion.
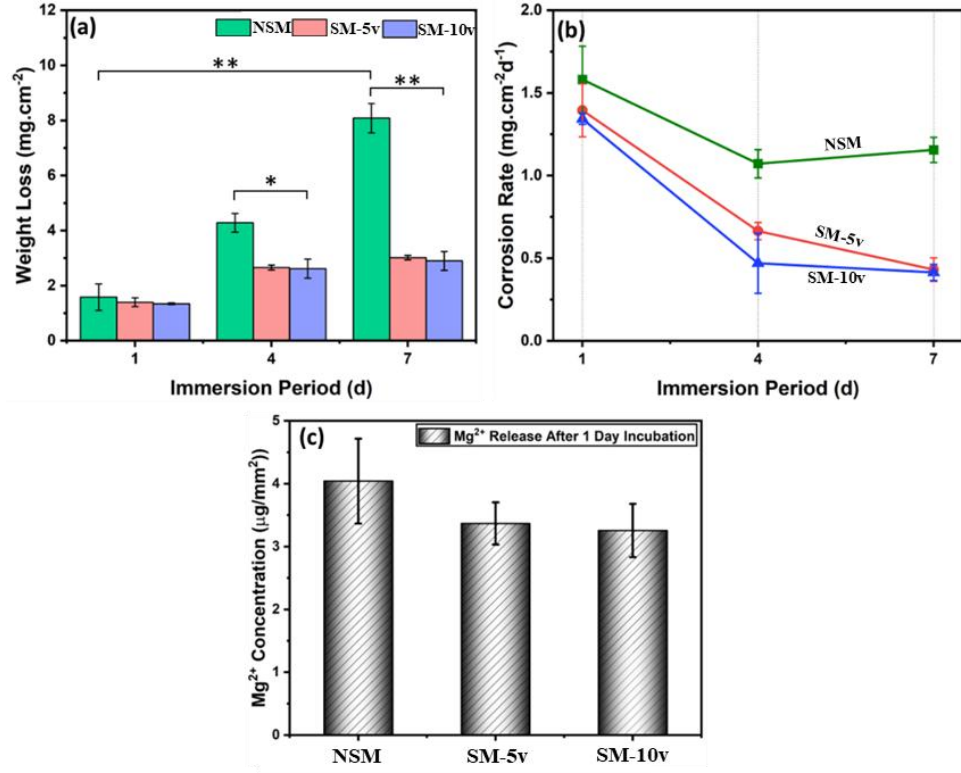
Figure 4.3.9: *Weight loss measured over different immersion durations (a), corresponding corrosion rates (b), and Mg^{2+} ion release after 1 day of immersion (c) for NSM, SM-3v, and SM-10v*

After 1 day, the weight loss is minimal for all three types of specimens. NSM reports weight loss of 1.58 ± 0.48 mg/cm^2, which is higher than that of SM-3v (1.39 ± 0.16 mg/cm^2) and SM-10v ($1.34 \pm 0.0.32$ mg/cm^2). However, Tukey's HSD post-hoc analysis discloses no statistically significant disparity between the weight loss values of NSM, SM-3v, and SM-10v after day 1 ($p > 0.05$). For day 4, the NSM exhibits considerably greater weight loss than the SMATed specimens, which is statistically significant ($p < 0.05$). Additionally, for day 7, this difference is further increased, and NSM shows the highest weight loss of 8.08 ± 0.53 mg/cm^2. This behaviour leads to a more statistically significant difference between the weight loss values of NSM and the SMATed specimens on day 7 and between day 1 and day 7 ($p < 0.01$). The average corrosion rate of NSM, SM-3v, and SM-10v is calculated using Eq. 4.3.1 [138]:

$$CR = \frac{m_0 - m_1}{A \cdot t} \qquad (4.3.1)$$

where, m_0 and m_1 are the masses (mg) of the specimen before and after immersion, respectively, t is the immersion time (d), and A is the total exposed surface area (cm^2). By considering the weight loss (Figure 4.3.9(a)), specimens' corrosion rates are determined for 1, 4, and 7 days (Figure 4.3.9(b)). The findings show that the corrosion rate of non-SMATed and SMATed specimens decreases rapidly between 1 day and 4 days of immersion, followed by a slower decline between 4 days and 7 days. This behaviour can be linked to forming a protective layer on the specimen's surface.

Initially, after 1 day of immersion, the corrosion rates for all specimens are relatively high compared to other immersion durations. However, on day 1, no statistically significant difference is noticed between the non-SMATed and SMATed specimens ($p > 0.05$). For NSM, the corrosion rate at day 1 is ~1.58 ± 0.47 mg/cm^2·d, which is slightly more than those of SM-3v (~1.39 ± 0.16 mg/cm^2·d) and SM-10v (~1.34 ± 0.03 mg/cm^2·d). This correlation can further be linked to the Mg^{2+} ion release after one day of incubation in the atmosphere maintained at 5% CO_2 and 37 °C. NSM exhibits maximum Mg^{2+} ion release, which is ~20% more than SM-3v and ~24% more than SM-10v. The corrosion rate of NSM remains higher than that of SM-3v and SM-10v on days 4 and 7. Moreover, the difference in corrosion rates increases considerably. On day 7, the corrosion rate of NSM slightly increases in comparison with day 4, whereas a decreasing trend is observed for SM-3v and SM-10v. For SM-3v, the corrosion rate has drastically reduced from day 1 to day 7 with strong statistical significance ($p < 0.01$). Additionally, a considerable difference is observed in the corrosion rates between the NSM (higher corrosion rate) and SMATed specimens after 7 days of immersion, which is statistically significant ($p < 0.05$). This performance could be attributed to the stable, thicker, and more uniform insoluble salt layer formation on SM-3v and SM-10v, in contrast to the unstable, weaker, and thinner layer on NSM. This behaviour is elaborated in the subsequent section.

Figure 4.3.10 presents microfocus X-ray CT images with an average pitting depth on non-SMATed and SMATed specimens after 7 days of immersion. Even though corrosion appears to be more uniform in the case of NSM, the average pitting depth is higher. The maximum average pitting depth of 227.4 ± 9.5 µm is observed for NSM, which is around 13.8% deeper than SM-3v and 11.4% that of

SM-10v (Figure 4.3.10(d)). These results indicate that, in addition to uniform corrosion, NSM experiences localised corrosion.
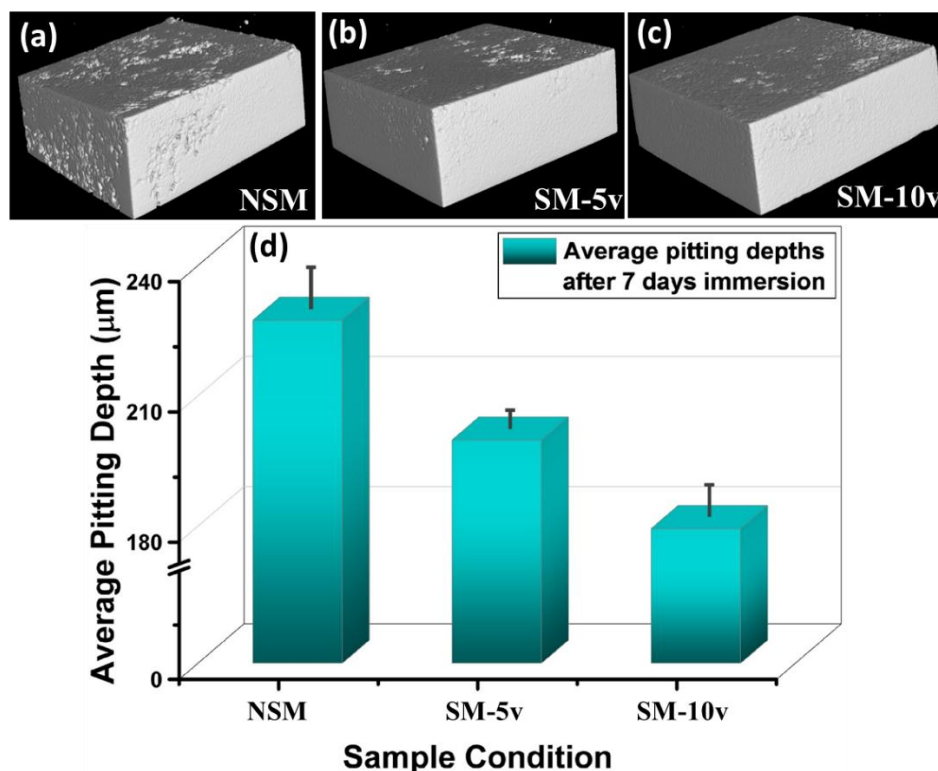
Figure 4.3.10: *Microfocus X-ray CT images (a-c) with pitting depths (d) for NSM, SM-3v, and SM-10v after 7 days of immersion*

4.3.1.2.3 Surface Analysis after Corrosion

Figure 4.3.11 shows SEM micrographs, EDS maps, and atomic percentage of different elements present on the corroded surfaces of NSM (Figure 4.3.11(a-b)), SM-3v (Figure 4.3.11(c-d)), and SM-10v (Figure 4.3.11(e-f)) after 7 days of immersion. High percentages of phosphorus (P), oxygen (O), calcium (Ca), and Mg on the SMATed specimens suggest the formation of hydroxides and phosphates of Ca and Mg (refer Table 4.3.3). Furthermore, EDS maps display high carbon content on the corroded samples (Figure 4.3.11), which could be explained as follows. EMEM-FBS contains various carbon-based compounds, such as amino acids and glucose, which can adsorb onto the Mg alloy surfaces. Witecka et al. [139] also investigated an increased precipitation of carbonates ($CaCO_3$ and $MgCO_3$) on the surfaces of casted and ECAPed ZM21 Mg alloy. This phenomenon is attributed to the carbonate buffer system in EMEM-FBS, just like an interstitial fluid, working under the equilibrium condition with a 5% CO_2 atmosphere.
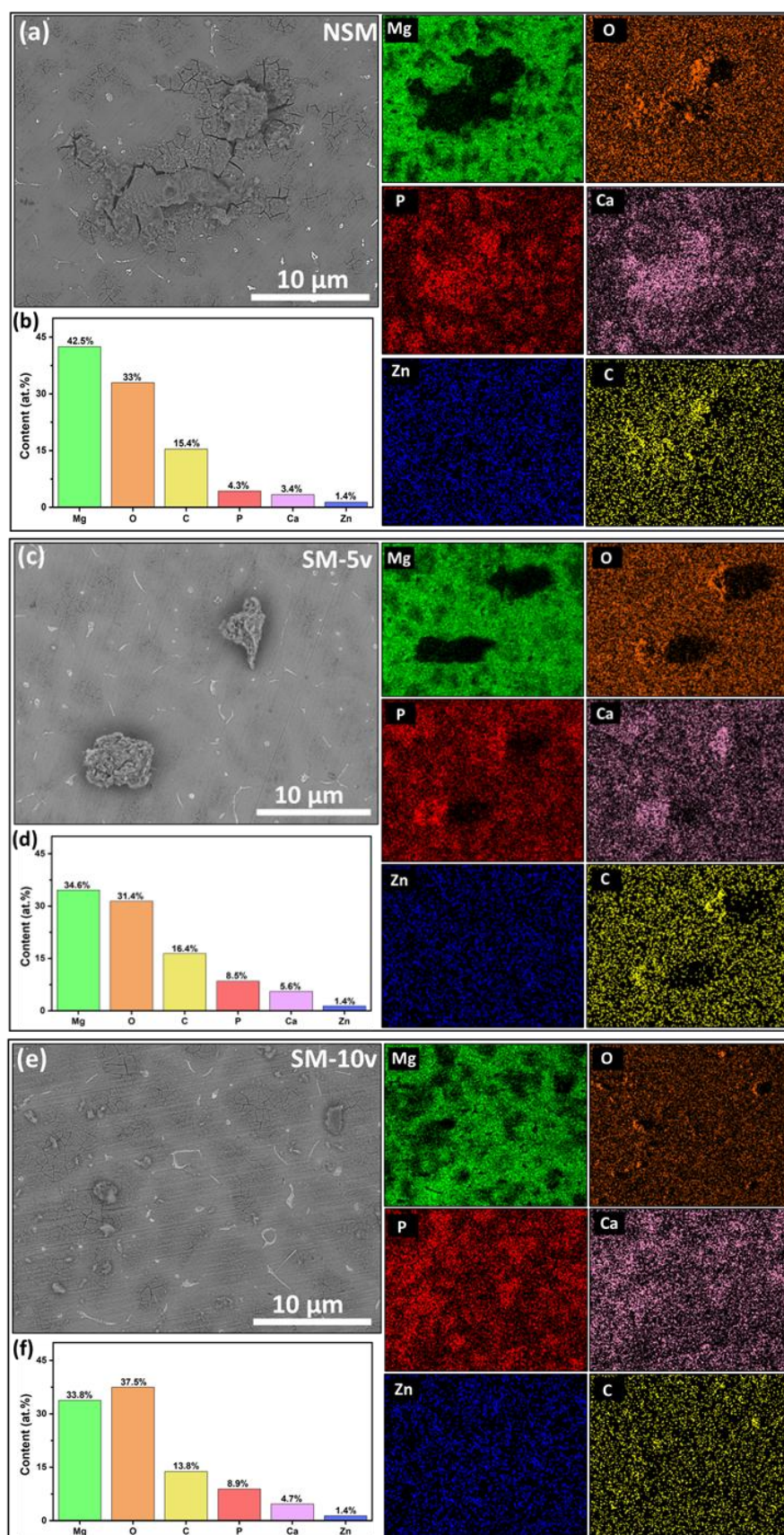
Figure 4.3.11: *SEM micrographs with corresponding EDS maps (a,c,e) and atomic percentages (b,d,f) for corroded NSM, SM-3v, and SM-10v surfaces after 7 days of immersion*

Table 4.3.3: Results of EDS analysis (at.% of elements) of specimens after 7 days of immersion

	Mg	O	C	P	Ca	Zn
NSM	43.5 ± 6.15	31.9 ± 7.98	14.5 ± 2.16	4.9 ± 1.13	3.4 ± 1.56	1.8 ± 0.83
SM-3v	33.5 ± 5.06	32.5 ± 6.01	17.6 ± 3.15	8.9 ± 2.15	6.1 ± 3.65	1.4 ± 0.45
SM-10v	30.6 ± 5.63	38.6 ± 8.15	14.2 ± 4.45	9.1 ± 3.25	5.8 ± 2.77	1.7 ± 0.55

The XRD patterns in Figure 4.3.12(a) illustrate the development of the insoluble salt layer on the NSM, SM-3v, and SM-10v specimens after 7 days of immersion. Key peaks correspond to Mg, $Mg_3(PO_4)_2$, $Ca_3(PO_4)_2$, and $Mg(OH)_2$, phases. The presence of these phases indicates the insoluble salt layer formation on the specimen surface [37, 93], which is essential for the retardation of the corrosion reaction. The SMATed specimens exhibit more pronounced $Mg(OH)_2$ and phosphates peaks, indicating a thicker and more stable insoluble salt layer.

The thickness of the insoluble salt layers on the specimens after 7 days of immersion is confirmed by SEM micrographs presented in Figure 4.3.12(b-d). SM-3v and SM-10v exhibit the thicknesses of $\sim 9.56 \pm 1.01$ μm and $\sim 11.12 \pm 1.23$ μm, respectively. A comparatively thinner layer ($\sim 6.73 \pm 0.78$ μm) is observed for NSM. Figures 4.3.11 and 4.3.12 insinuate less protectiveness and more susceptibility to corrosion of NSM than the SMATed specimens.
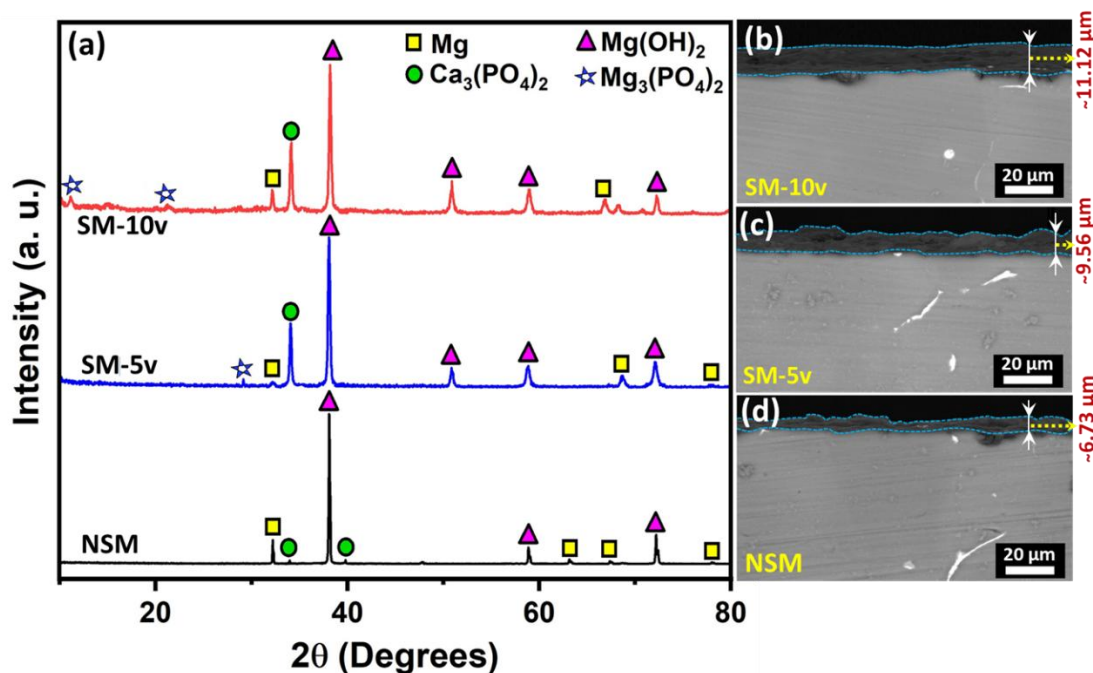
Figure 4.3.12: *(a) XRD patterns presenting salt layer formation behaviour with (b-d) SEM micrographs that indicate its thickness for NSM, SM-3v, and SM-10v after 7 days of immersion*

4.3.1.3 Cytocompatibility

Figure 4.3.13 depicts the images of the colonies exposed to 50% extract concentrations for NSM, SM-3v, and SM-10v specimens together with the control (exposed to EMEM-FBS). A gradient in the number of cell colonies is observed as the extract concentration increases (see Figure 4.3.14). At a 50% extract concentration, few cell colonies are evident for SM-3v and SM-10v. In contrast, almost no cell colonies are observed for NSM. The pH of the extracts for NSM, SM-3v, and SM-10v are 9.65 ± 0.64, 8.90 ± 0.28, and 8.80 ± 0.14, respectively. The higher pH of NSM than others agree with the electrochemical and immersion test results, suggesting its lower corrosion resistance than the others. In other words, the NSM extract contains more released ions than the SMATed specimens.
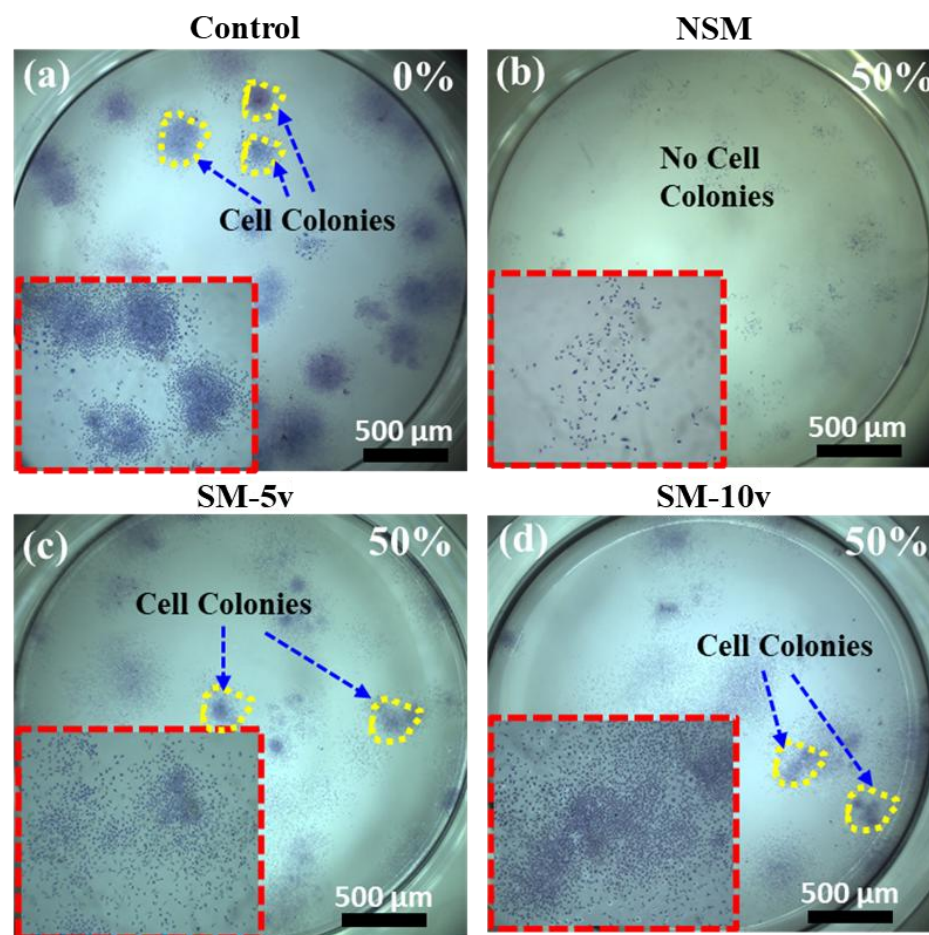
Figure 4.3.13: *Typical images of the colonies for control (a) and those exposed to 50% extract concentrations for NSM (b), SM-3v (c), and SM-10v (d) specimens*

Relative plating efficiency (RPE) reflects the ability of cells to attach, spread, and proliferate under a certain (cytotoxic) condition compared to the control condition. Figure 4.3.14 illustrates the impact of various extract concentrations of NSM, SM-3v, and SM-10v specimens on the RPE of L929. As the extract concentration increases, the RPE of NSM decreases significantly, dropping to zero at 50% extract concentration, indicating a substantial reduction in colony formation ability. In contrast, SMATed specimens exhibit considerably higher RPE than NSM across all extract concentrations. The RPE of SM-3v and SM-10v remains around 0.2 at 50% extract concentration, demonstrating better performance in terms of cell viability. Based on the RPE for each type of specimen, the inhibitive concentration of the extract giving RPE 0.5 (=50%), which is abbreviated as IC$_{50}$, was calculated using the probit method. NSM has the lowest IC$_{50}$ at 8.4%, followed by those of SM-3v and SM-10v at 18.9% and 19.2%, respectively. These results clearly

indicate the higher cytotoxicity of NSM extract than those of SMATed specimens. This behaviour may be related to the lower corrosion rate of SMATed specimens than NSM in EMEM-FBS. As mentioned above, the greater intensity of SMAT treatment results in a finer surface microstructure (Figures 4.3.3(b) and 4.3.4(a)) and better corrosion resistance, especially through immersion tests.
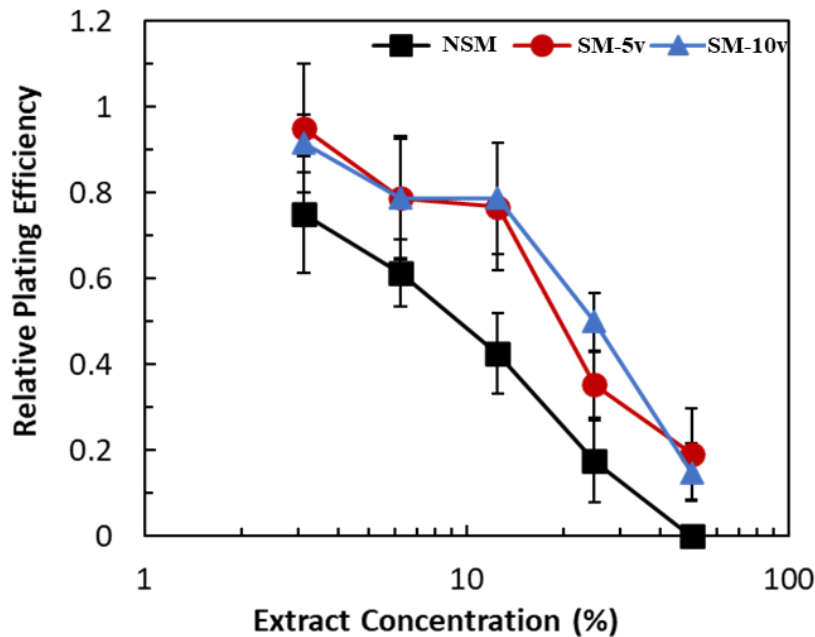
Figure 4.3.14: *Effect of different extract concentrations on the relative plating efficiencies of NSM, SM-3v, and SM-10v*

4.3.1.4 Protein adsorption

For BSA and FN, a protein adsorption assay was conducted in an artificial plasma in the CO_2 incubator, as depicted in Figure 4.3.15. The results reveal variations in the adsorption values, highlighting the influence of the SMAT process on protein adsorption behaviour. Following SMAT, there is an increase in FN adsorption but not BSA adsorption. SMATed specimens display higher FN adsorption than NSM; the SM-3v exhibits the highest FN adsorption with statistical significance against NSM (by student *t*-test, $p < 0.01$).
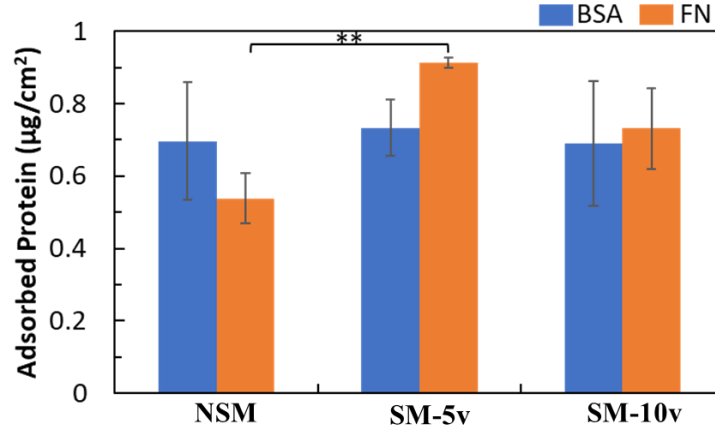
Figure 4.3.15: *Bovine serum albumin (BSA) and fibronectin (FN) adsorption for NSM, SM-3v and SM-10v*

4.3.2 Discussion

This study addresses five crucial parameters that significantly impact the biocompatibility of the Mg5Zn0.2Ca alloy (Figure 4.3.16). Although all five parameters are interconnected, it is known from recent studies that microstructural developments due to SPD methods have a significant impact on the material's biocompatibility [91, 140, 141]. In other words, any change in the microstructure will affect the remaining four parameters. As a biodegradable implant material, the corrosion rate should match the tissue healing rate, but this depends on establishing the insoluble salt layer on the material surface. This behaviour, in turn, influences the cytotoxicity of released metal ions and protein adsorption onto the material surface, which can also influence subsequent biological responses such as cellular attachment, growth, inflammation, and wound healing. Improved protein adsorption helps cellular growth, thus reducing cytotoxicity [142, 143]. This study addresses the relationships between these five important parameters influencing biocompatibility.
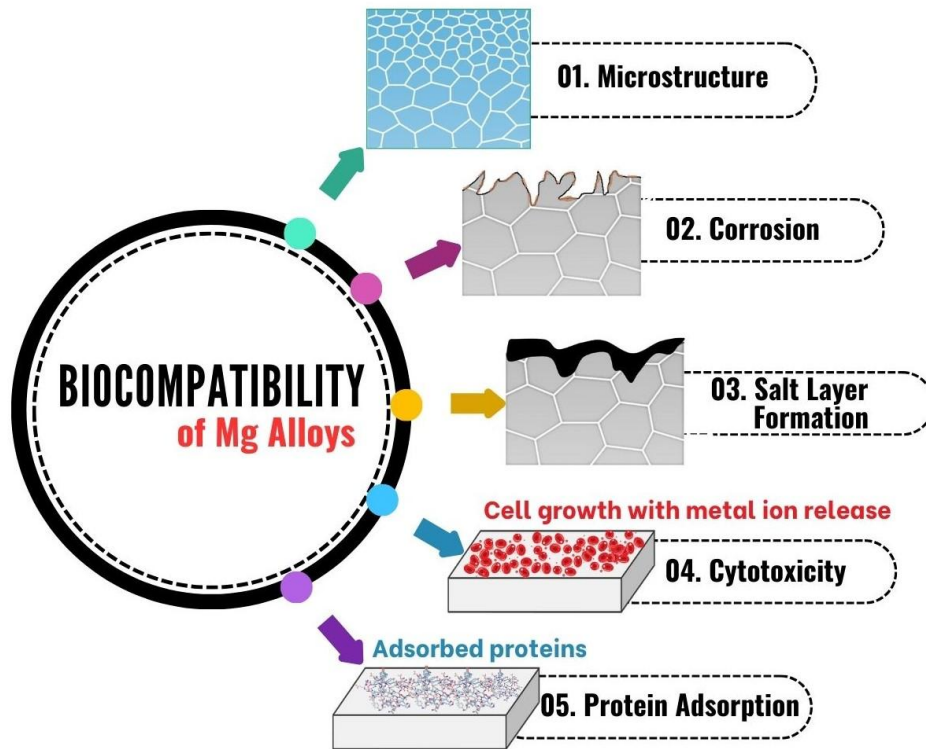
Figure 4.3.16: *Biocompatibility influencing parameters for SMATed and non-SMATed Mg5Zn0.2Ca alloy*

4.3.2.1 Microstructure

The non-SMATed alloy's microstructure reveals the presence of secondary phase $Ca_2Mg_6Zn_3$ and α-Mg, which is confirmed with SEM (Figure 4.3.1(a-c)) and XRD analysis (Figure 4.3.3(a)). This secondary phase could act as a temporary barrier against localised corrosion [12, 63]. However, although Mg5Zn0.2Ca alloy is a favourable material for biodegradable implants [21, 64, 66], the alloy's corrosion resistance and overall strength are insufficient. With this motivation, SMAT operation is performed on Mg5Zn0.2Ca alloy in the current study, where the velocity of colliding balls is crucial in introducing various microstructural features (Figures 4.3.1(d-e) and 4.3.4). The pronounced grain refinement and wider SMAT-affected region in SM-10v than in SM-3v are primarily attributed to the increased strain and strain rates imposed by the faster balls in the SMAT process [40, 102]. The higher velocity leads to more intense impacts, fostering extensive plastic deformation across the deeper region of the material. This extensive deformation facilitates the formation of nanograins near the surface (Figure 4.3.4(a-c)) and finer and denser twins (Figure 4.3.1(d-e)), which modify the material's

properties and result in a gradient microstructure [102]. The crystallite size of SM-3v and SM-10v is found to be significantly reduced near the surface (Figure 4.3.3(b)). Further, this gradient microstructure (Figure 4.3.2) induced by SMAT within the alloy's deformed layer can also be attributed to the strain gradient created during the process [102].

The specimen surface experiences intense deformation, progressively decreasing as distance from the surface increases. This results in a multi-stage surface microstructure evolution [79]. Initially, the surface undergoes lower strain (comparable to the microstructural development of deeper regions of SM-3v), then intermediate strain (like the near-surface regions of the SM-3v), and finally, higher strain (corresponding to the near-surface regions of the SM-10v). In magnesium's hexagonal close-packed (HCP) system, twinning is a significant deformation mechanism to accommodate plasticity due to the inadequate number of available slip systems. Therefore, twins play a vital role in the overall grain refinement process. In the initial stage of severe deformation (low strain), dislocations accumulate within the coarse grains [79, 144]. Conversely, prismatic and basal slips could readily activate at this lower strain level because they require a lower resolved shear stress (RSS). As strain increases, the refined grains exhibit a higher density of dislocations, and higher RSS leads to the activation of the pyramidal <c+a> slip system. Typically, the four main types of twins observed in magnesium alloys are $\{10\bar{1}1\} < 10\bar{1}2 >$ compression twins; $\{10\bar{1}2\} < 10\bar{1}1 >$ tension twins and $\{10\bar{1}1\} - \{10\bar{1}2\}$ and $\{10\bar{1}2\} - \{10\bar{1}2\}$ double twins.

As the SMAT progresses, the density of twins within the grains increases, leading to their interactions (Figure 4.3.1). Moreover, these twins obstruct dislocations during deformation. Consequently, interactions amongst twins/dislocations and between twins and dislocations contribute to grain refinement (Figure 4.3.4(a-c)). At a later stage, sub-grains with low-angle boundaries form, introducing numerous defects caused by lattice rotation. The direction of rotation varies depending on the slip system. The sub-grains experience increased misorientation and gradual rotation, accommodating higher strain m. This process eventually forms high-angle boundaries and nanograins of ~21 nm for SM-10v (Figure 4.3.4(a-c)) in the near-surface region, whereas SM-3v shows fine twins (Figure 4.3.4(d)), attributed to intermediate strain levels.

As strain decreases with depth, a gradient in grain size develops within the magnesium alloy's SMATed layer [79]. Additionally, a noticeable reduction in twin thickness and density occurs with increasing distance from the surface (Figure 4.3.1). Many researchers also documented a similar grain refinement mechanism, where coarse grains transformed into nanograins in severely deformed Mg alloys. Sun et al. [145] performed SMAT on AZ91D alloy for 20 min with 50 Hz frequency in a vacuum and reported ~40 nm of grain size. Laleh et al. [28] observed an ~8 nm grain size near the surface, which increased with the ball size when SMAT was performed on AZ91D alloy with a 20 kHz vibrating frequency in a vacuum using various ball sizes (2-5 mm diameter) for 30 min. Duan et al. [102] also evaluated the SMAT duration effect on AZ31D and reported grain sizes of ~84.3, ~51.7, and ~46.5 nm for 2, 4, and 6 min, respectively. During the SMAT processing of softer materials like the Mg5Zn0.2Ca alloy, the surface undergoes varying degrees of deformation and compression due to the squeezing action of colliding balls. This action creates different zones with varying rates of deformation/compression[146], leading to a nonuniform density of twins and dislocations, changing twin thickness and grain size distribution within the SMATed layer (Figures 4.1.1(d-e)) [40].

Microstructural changes influence mechanical properties. Mechanical properties of metallic implant materials, including hardness, are crucial factors that influence the durability of implants. SM-3v and SM-10v exhibit increased surface microhardness values. Significant lattice defect density and refinement of grains within the SMATed layer are the primary contributors to the improvement of microhardness. The movement of dislocations generated during SMAT could be impeded by twin boundaries, restricting further slip [147, 148]. Such interaction between twins and dislocations conceivably leads to strain-hardening, increasing the hardness of the SMATed specimens [149].

Bandyopadhyay et al. [22] and Gerhatova et al. [8] presented the improved biocompatibility of metallic implants with higher surface hardness. As Mg5Zn0.2Ca is a biodegradable material, the enhanced microhardness values could contribute to improved biocompatibility at each stage of degradation.

4.3.2.2 Corrosion behaviour

In the current study, the corrosion behaviour of Mg5Zn0.2Ca alloy is evaluated by electrochemical and immersion tests under similar conditions inside the human body. EMEM-FBS, which has a similar composition to that of the interstitial fluid inside the human body, is employed under 5% CO_2-95% air atmosphere. Compared to strong acids or artificial seawater, this environment is mild but more complicated, with various inorganic and organic components. As described in detail in the following section, an insoluble salt layer formation is observed to retard the corrosion reaction of Mg even with the existence of a carbonate buffer system [140, 150].

In the potentiodynamic polarisation, the SMATed specimens tend to have slightly lower i_{corr}, but the differences are relatively small and not statistically significant. However, in EIS (Figures 4.3.6-4.3.7 and Table 4.3.2), R_p behaviour differs with specimens. The increase in R_p of the NSM between 2 and 6 h indicates the insoluble salt layer growth. In contrast, the decrease in R_p can be linked to the insoluble salt layer's partial disruption, such as localised corrosion. An increased R_p is not observed for the SMATed specimens, suggesting a faster insoluble salt layer formation. Since the SMATed specimens have higher defect densities, the initial corrosion reaction can be faster than the NSM, resulting in faster growth of an insoluble salt layer which reaches its maximum retardation on substrate corrosion within the first 2 h of immersion. In the case of SM-3v, the decreasing trend of R_p suggests the effect of the disruption of the salt layer is more significant than its growth. In the case of SM-10v, however, the R_p is stable through the testing time of 24 h, indicating the salt layer leaches to the stable state between its growth and disruption. The refined grains and higher defect densities of SM-10v lead to the even faster salt layer formation in the electrolyte, which may be less dense (or more porous) than that of SM-3v, giving the lower R_p but more balanced and stable through the experimental period. These findings show that the SMAT treatment effectively controls the surface reaction of the Mg alloy specimens by ball velocity. Notably, the R_p of all three types of specimens are in the comparable range at 24 h of immersion, similar to the results of PD measurement.

In the immersion test, a higher weight loss and corrosion rate are observed for NSM than the SMATed specimens at every time point. Still, the difference is

the largest on day 7 (Figure 4.3.9). This clear and significant difference between the NSM and the SMATed specimens can be derived from the different experimental conditions between the electrochemical and immersion tests, such as the electrolyte volume-to-specimen surface area ratio, the specimen's exposed surface, and the immersion periods. The microfocus X-ray CT observation of the immersed specimens reveals the increased localised corrosion across a larger surface area of NSM (Figure 4.3.10). One key reason for such behaviour is the lack of gradient microstructure and grain refinement in NSM, as discussed earlier. Further, compressive residual stress induced by SMAT in the deformed layer of the Mg alloy [146] helps mitigate the initiation and growth of pits, making the surface more resistant to crack formation and propagation.

The EDS analysis on the corroded specimens revealed increased percentages of oxygen, phosphorus, calcium, and carbon (Figure 4.3.11) compared to those before the immersion (Figure 4.3.1(b-c)), indicating the insoluble salts (hydroxides, phosphates, and carbonates) formation. The slightly higher percentages of phosphorus and calcium (refer to Table 4.3.3) on the SMATed specimens than those on the NSM may improve the protective layer's characteristics, giving better corrosion behaviour. Additionally, the salt layer's stability and thickness (Figure 4.3.12) are crucial in the pit formation and overall corrosion behaviour (discussed in the subsequent section).

Although there is some ambiguity, as few researchers reported a decrease in corrosion resistance after severe plastic deformation (SPD) of Mg alloys, many others have documented its increase. Wu et al. [138] presented a 31.3% decrease in corrosion current density after applying high-energy shot peening to Mg-4Y-3.3RE-0.5Zr alloy. Severely deformed AZ91D Mg alloy (using hydrostatic cyclic expansion extrusion) also showed higher E_{corr} and lower i_{corr} [150]. Lopes et al. [90] processed pure Mg, AZ91, and AZ31 alloys using HPT and conducted polarisation tests in Hank's solution. This processing resulted in passivation-like behaviour, which enhanced the corrosion resistance of the HPT-treated alloys. Conversely, ZK60 alloy treated with HPT lacks a tendency toward passivation, resulting in an increased corrosion rate [90]. Therefore, the material's propensity to develop a protective layer of insoluble salts governs the corrosion behaviour of different Mg alloys to a greater extent. A stable and uniform protective film shields the alloy

from rapid corrosion in biological environments and minimises the release of potentially harmful degradation products [37, 93].

The corrosion behaviour of implant materials, including orthopaedic screws and plates, can influence the pH of the surrounding solution. It is commonly accepted that pH variations outside the physiological range (~7.4) damage tissues and cells, as they could inhibit cellular growth and other functions [12, 92, 151, 152]. Despite the buffering capacity of body fluids, which minimises pH fluctuations, considerable changes in pH are possible in the tissues surrounding the metallic implants. The corrosion reaction of magnesium alloy accelerates the pH of the solution [151]. The pH levels are increased for all specimen conditions (NSM, SM-3v, and SM-10v) after the electrochemical and immersion tests; however, the increased level in pH is notably higher for NSM than those of the SMATed specimens (Figure 4.3.5(b) and 4.3.S1 (supplementary data)).

4.3.2.3 Protective salt layer formation

The immersion medium's chemical composition and pH significantly alter the corrosion behaviour of magnesium alloys in an aqueous environment. Generally, magnesium alloys exhibit better corrosion resistance in low-chloride and highly alkaline environments [140]. However, understanding the electrochemical reactions of the alloy in EMEM-FBS is crucial to comprehend its corrosion behaviour in a biological environment.

The following equations describe the cathodic and anodic reactions of Mg in an aqueous medium.

$$Mg \rightarrow Mg^{2+} + 2e^-$$

$$2H_2O + 2e^- \rightarrow H_2 + 2OH^-$$
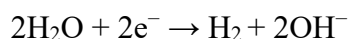
The cathodic reaction leads to an increase in local pH. The Mg^{2+} ions subsequently react with these hydroxide ions to produce Mg hydroxide, precipitating at a local pH of over 11.

$$Mg^{2+} + 2OH^- \rightarrow Mg(OH)_2$$
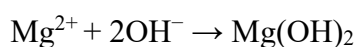
Exposure of magnesium and its alloys to humidified air at room temperature leads to the formation of an oxide layer on their surface [138]. However, MgO dissolves in water, forming $Mg(OH)_2$.

$$MgO + H_2O \rightarrow Mg(OH)_2$$
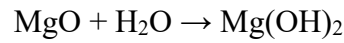
The resulting $Mg(OH)_2$ inhibits substrate dissolution and enhances corrosion resistance in alkaline conditions [92]. A properly developed $Mg(OH)_2$ layer can further impede mass diffusion between the substrate and the surrounding medium, reducing the corrosion kinetics in alkaline conditions. Even in a chloride environment (0.9 wt.% NaCl solution), Wu et al. [138] demonstrated that shot-peened WE43 alloy exhibited the protective behaviour of the $Mg(OH)_2$ layer. Consequently, the measured corrosion rate was 0.017 mg/cm²·h after 15 min of shot-peening, compared to 0.024 mg/cm²·h for the as-received alloy. This improvement was attributed to shot-peening-induced nanocrystallisation near the surface, increasing grain boundaries and modifying the surface reactivity.

Although $Mg(OH)_2$ is the primary salt layer formed in a simple aqueous environment, carbonates and phosphates could act as predominant salt layers in the body fluid, significantly influencing corrosion behaviour. Calcium and magnesium ions react with phosphate and carbonate ions in the immersion solution to form insoluble phosphate and carbonates:

$$3M^{2+} + 2PO_4^{3-} \rightarrow M_3(PO_4)_2 \ (M: Ca^{2+} \text{ or } Mg^{2+})$$

$$M^{2+} + CO_3^{2-} \rightarrow MCO_3 \ (M: Ca^{2+} \text{ or } Mg^{2+})$$
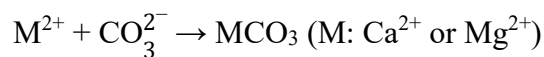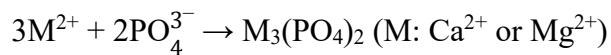
In human body fluids such as interstitial fluid and blood plasma, the presence of phosphates and carbonates leads to insoluble salt precipitation, even with a slight increase in pH, which is insufficient for the precipitation of $Mg(OH)_2$ [153]. Additionally, these fluids contain a relatively high concentration of carbonate, which works as a carbonate buffer system with 5% CO_2-95% air atmosphere to maintain their pH of 7.4. However, any fluctuations in pH and the presence of certain ions, such as chloride (Cl^-), can considerably impact the rate of substrate dissolution and uniformity of the protective layer. Even small amounts of chlorides are typically sufficient to compromise the protective film formed in a simple aqueous environment, such as 0.9% NaCl.

$$Mg(OH)_2 + 2Cl^- \rightarrow MgCl_2 + 2OH^-$$
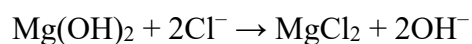
Generally, a coarse grain structure has fewer grain boundaries, resulting in limited nucleation sites for producing a dense and uniform oxide layer. In contrast, SMAT produces a refined microstructure at the surface (Figures 4.3.1-4.3.4), increasing the number of sites for nucleation [138]. Additionally, SMAT enhances surface energy and activity, which promotes a more uniform and denser protective layer formation [30]. In the present study, the NSM specimen, after 7 days of immersion, showed distinct peaks of Mg and insoluble salts on its XRD pattern (Figure 4.3.12(a)). The intensity of the Mg peak derived from the substrate suggests a thinner salt layer than the SMATed specimens (Figure 4.3.12(b-d)).

Literature also reveals the role of microstructure in governing the protective layer's characteristics and the corrosion response of pure magnesium and its alloys in low-chloride environments. Birbilis et al. [30] observed a lower i_{corr} value in 0.1M NaCl solution for pure Mg processed by ECAP, attributing to the refined microstructure with a high misorientation angle of grain boundaries. Gollapudi [154] explained the results of Birbilis et al. [30] as the contribution of a stable and protective layer of MgO and $Mg(OH)_2$ formed on fine-grained pure Mg in comparison with a more porous layer formed on a coarse-grained Mg surface. In simulated body fluid (SBF), Gao et al. [155] documented a lower i_{corr} value for HPT-treated MgZnCa alloy than the as-received alloy. This behaviour was ascribed to increased dislocations and other defects, providing extra nucleation sites necessary for the protective layer's uniform growth. These literature studies support that the protective layers with increased thicknesses formed on the SMATed specimens (SM-3v and SM-10v) are more stable and robust (Figure 4.3.12), offering better corrosion retardation compared to NSM specimens (Figures 4.3.6, 4.3.7, and 4.3.8).

In summary, the improved corrosion resistance observed in SMATed specimens is highly significant for promoting Mg5Zn0.2Ca as a biomedical implant material. By reducing the corrosion rate in a biological medium, the SMAT process helps achieve more controlled and gradual biodegradation, minimizing sudden mechanical failure and excessive Mg^{2+} ion release. This supports safer, more predictable in vivo performance, which is a critical requirement for biodegradable implants. Therefore, these corrosion findings directly advance the strategic

objective of enabling Mg5Zn0.2Ca to serve as a reliable, biocompatible implant alloy.

4.3.2.4 Cytocompatibility

Generally, cell and tissue compatibility of a material mainly depends on the material's stability in an implanted environment, which means releasing metal ions and degradation products such as wear debris is crucial for compatibility. When the toxicity of released ions and debris is relatively mild, the direct interaction between the surface of a material and surrounding tissues/cells is more influential in controlling tissue and cellular response. Cytotoxicity evaluation by the extract method in ISO10993-5 focuses on the effect of released ions and degradation products. Therefore, the extracting condition employs the low ratio of extracting medium to the specimen surface area to increase the concentrations of released ions and degradation products.

In the present study, we performed the cytotoxicity tests by extract method at the extract medium to specimen surface area of 0.33 mL/cm^2, which is much lower than those of the electrochemical and immersion tests. The obtained results show higher cytocompatibility for the SMATed specimens than the NSM (Figures 4.3.13 and 4.3.14), which can be attributed to their lower corrosion rates with a smaller increase in pH. Several factors contribute to the higher corrosion resistance of SMATed specimens, as described earlier: a more uniform and stable protective layer formation (improving corrosion resistance) and a decrease in the release of harmful metal ions. A high density of defects, grain refinement, and increased surface energy contribute to the effective protective layer formation of insoluble salts on the SMATed specimen surface. Martynenko et al. [156] also reported that the WE43 alloy's reduced grain size due to the ECAP and multiaxial deformation (MAD) processes enhances the mesenchymal stromal cell proliferation on the alloy's surface. Additionally, Anisimova et al. [94] evaluated the viability of osteogenic mesenchymal stromal cells (by extract and direct methods) on the WE43 alloy's surface treated with multiaxial deformation (MAD). The alloy exhibited a more controlled biodegradation, less damage, and better growth of the cells on the alloy specimen with MAD treatment.

Furthermore, in physiological environments, corrosion of magnesium alloys leads to the release of magnesium ions and hydrogen gas, adversely affecting cells' survival [89]. A high corrosion rate in the case of NSM can result in the release of excessive hydrogen, significantly raising pH levels and toxicity. Conversely, a lower corrosion rate of SM-3v and SM-10v reduces the release of hydrogen, promoting uniform protective layer formation (Figure 4.3.12) and minimal variations in pH and toxicity levels (Figures 4.3.5(b) and 4.3.9(c)). Therefore, the cells have better chances of survival on the SMATed surface.

Overall, the improved cytocompatibility of the SMATed specimens is an essential outcome supporting their biomedical application. The reduced corrosion rate and stabilized surface nanostructure help maintain a favorable local environment, minimizing pH shifts and harmful ion release that could damage surrounding tissues. This directly promotes better cell viability and safe biological interactions, aligning with the strategic goal of advancing Mg5Zn0.2Ca for biodegradable implant use.

4.3.2.5 Protein adsorption

Several factors influence the adsorption of proteins onto material surfaces, including protein structure, solution pH, ionic strength, and the material's surface properties [141, 143, 157]. The sequence of amino acids in a protein, which determines active sites for surface interaction, is crucial. A stable salt layer mediates the interaction between proteins and the underlying metal surface, enhancing mechanical stability and bio-corrosion resistance. Even though electrostatic interactions between the material's surface and cells play a vital role in initial cell attachment, adsorbed proteins onto the surface predominantly regulate stable cell adhesion [141]. The current study has investigated the adsorption behaviours of FN and BSA on the Mg5Zn0.2Ca specimen surface. BSA is known to have non-specific adsorption to the material surface, which can be substituted by other proteins with more stable and specific adsorption, such as FN. FN is one of the cell adhesion proteins that promote a certain type of cells, including fibroblasts, to adhere, proliferate, and express a specific cellular function.

Our study shows that BSA adsorption on the NSM and SMATed surface (with a similar surface roughness (Ra = 0.5 μm)) is comparable (Figure 4.3.15). In contrast, the amount of FN adsorption on SMATed specimens is significantly higher. SMAT treatment introduces numerous high-energy defects, such as dislocations, triple junctions (TJs), non-equilibrium grain boundaries (GBs), etc. These defects and the associated long-range stress contribute to the increased surface energy of the nanostructured alloys. The increased energy and possibly the metal surface's chemical composition/reactivity do not influence the BSA adsorption much. Still, they benefit FN probably due to its multiple binding domains onto the material surface. As mentioned earlier, the higher surface energy of the SMATed specimens endorses the fast formation of the protective salt layer containing calcium or magnesium phosphates (Figure 4.3.12), which has a high affinity for the organic compounds and controls protein adsorption behaviour. That means SMAT-induced changes in surface energy and chemical reactivity could create more favourable conditions for FN adsorption. Compared to NSM, the substantial FN adsorption on SM-3v and SM-10v aligns with higher levels of cellular adhesion and proliferation, highlighting the effective enhancement of specific surface properties by SMAT.

The increase in surface energy or changes in surface chemistry due to the SMAT process enhances protein-surface interactions for FN better than for BSA [89]. This response is crucial for proteins like FN, which require specific binding sites to maintain their functional conformation. The difference in adsorption behaviours of BSA and FN demonstrates that surface chemistry modifications bear significant importance in facilitating or preventing certain protein adsorption. Kubacka et al. [141] reported that the titanium surfaces treated with hydrostatic extrusion favour the adsorption of BSA but inhibit the adsorption of FN. Since the mechanism of protein adsorption is competitive, and although some studies have attempted to elucidate the protein adsorption mechanism for deformed Mg alloys, further investigation is necessary to gain a complete understanding of the conformation and functional consequences of adsorbed proteins on these modified surfaces.

In summary, the enhanced protein adsorption observed on SMATed surfaces, particularly bovine fibronectin, is highly relevant to biomedical performance. Improved protein attachment promotes early cell adhesion and integration of the implant with host tissue, accelerating the healing process. This highlights the critical contribution of SMAT-induced surface modifications toward realizing Mg5Zn0.2Ca as a clinically effective biodegradable implant alloy.

4.4 Effect of Surface Strengthening on Tensile and Tribological Properties of Mg5Zn0.2CaAlloy: Role of Gradient Microstructure

This section investigates the influence of SMAT-induced surface strengthening on the tensile (Section 3.2.3) and tribological (Section 3.4) behaviour of the Mg5Zn0.2Ca alloy, with emphasis on the role of the gradient microstructure. This study evaluates mechanical performance through uniaxial tensile testing, wear resistance under circular loading conditions (5, 10, and 20 N), and scratch behaviour under constant (50 N) and progressive (20-80 N) loads. Detailed analyses using SEM, surface profilometry, and acoustic emission monitoring provide insights into wear track morphology, surface damage evolution, and failure mechanisms. The combined effects of grain refinement, increased dislocation density, and the presence of a gradient-structured surface layer are critically examined, demonstrating substantial improvements in tensile strength, wear resistance, and scratch durability.

4.4.1 Microstructure Analysis

The microstructure of the NSM alloy was analysed using SEM, EDS, and EBSD. Figure 4.4.1(a) reveals a dual-phase microstructure comprising primary α-Mg grains and $Ca_2Mg_6Zn_3$ as the secondary phase [158]. This secondary phase is predominantly located along grain boundaries, with some distribution within the grains. Figure 4.4.1(a1)–(a3) provides insights into the spatial distribution of key alloying elements (Mg, Zn, and Ca), further confirming the presence of the secondary phase. The EBSD grain size distribution (Figure 4.4.1(b) and (b1)) depicts a well-defined grain structure with an average grain size of 67 ± 17 µm.
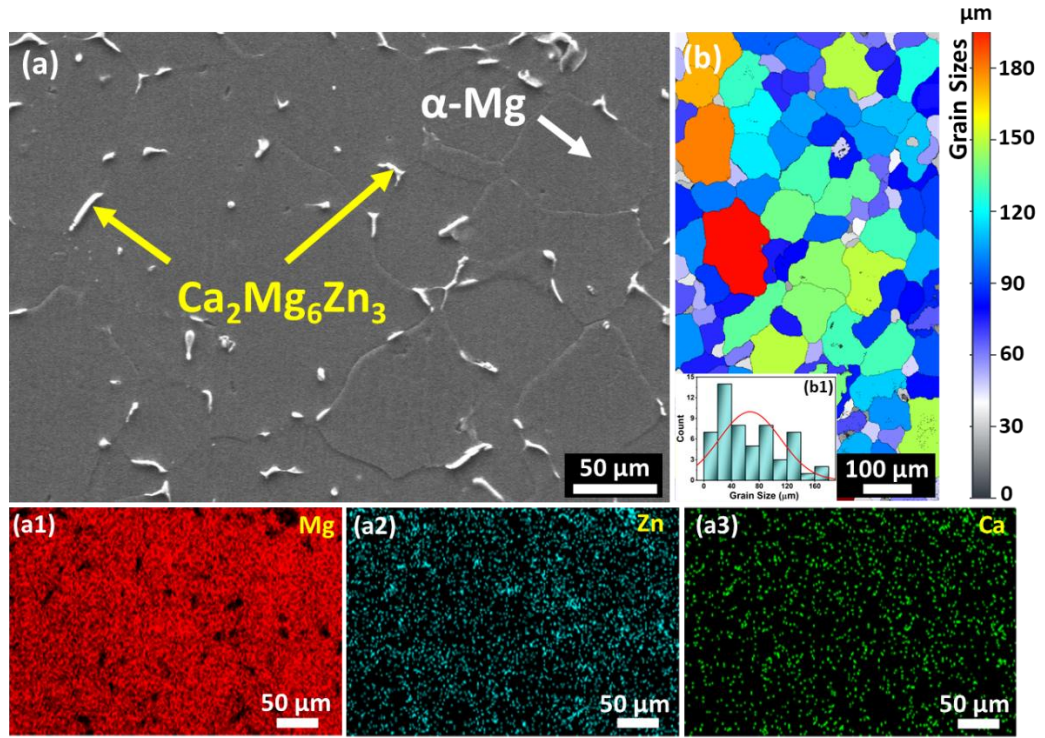
Figure 4.4.1: *(a) SEM micrograph along with elemental distribution maps (a1–a3), and (b) EBSD grain size map with grain size distribution (inset (b1)) for the NSM specimen*

EBSD analysis of the SMATed Mg5Zn0.2Ca alloy was conducted to gain deeper insight into the microstructural modifications induced by the severe surface deformation. Figure 4.4.2 presents the orientation image (OI) and image quality (IQ) maps of the SMATed specimens, illustrating the gradient nature of the microstructure. IQ maps of SM-5v and SM-10v are displayed in Figure 4.4.2(b) and (d), respectively. It is evident that the near-surface region of SM-10v has undergone substantial deformation, resulting in a significant fraction of unindexed areas. The percentage of unindexed regions is approximately ~12.4% for SM-5v, whereas it increases to ~39.4% for SM-10v, suggesting a more lattice distortion by higher velocity balls during SMAT. A high density of twins in SM-5v is localised closer to the surface, with their occurrence significantly diminishing as depth increases. In contrast, SM-10v exhibits an abundance of twins even at greater depths, indicating a more profound influence by the higher velocity balls, which triggers a more extensive microstructure refinement.
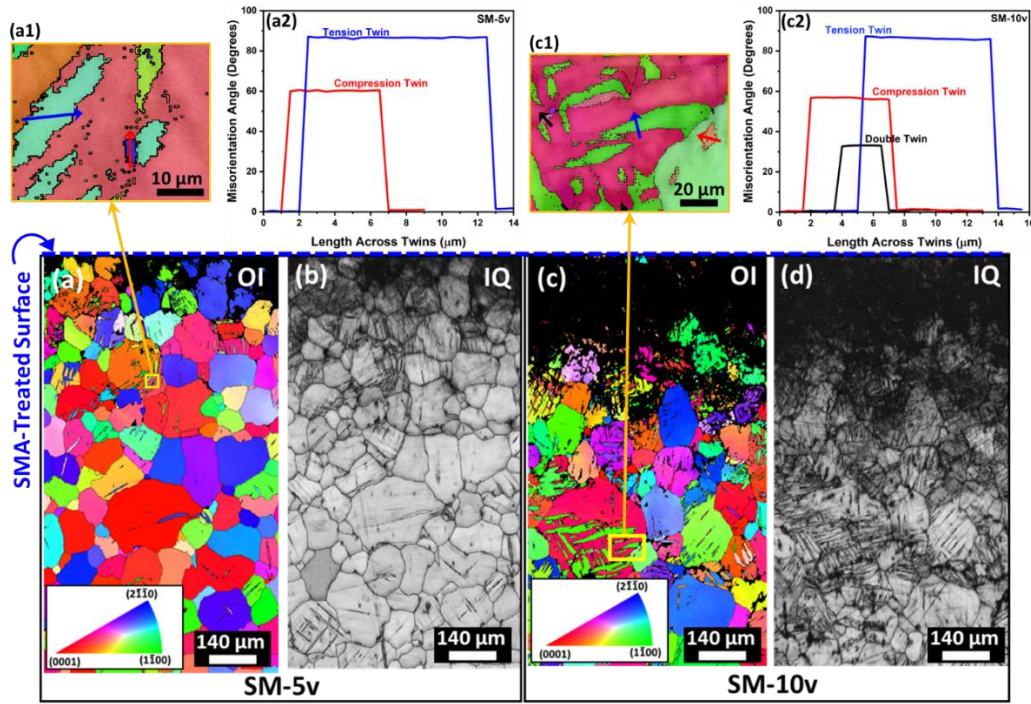
Figure 4.4.2: *EBSD analysis presenting OI and IQ maps for (a-b) SM-5v and (c-d) SM-10v specimens, accompanied by magnified OI map regions (a1 and c1) and the respective misorientation angle profiles across twins (a2 and c2)*

Furthermore, Figure 4.4.2(a) and (c) depict the OI maps for SM-5v and SM-10v, respectively. Orientation contrast within the grains is negligible in SM-5v compared to SM-10v, implying that the SMAT with the lower ball velocity does not cause extreme grain fragmentation or reorientation. However, in the case of a specimen subjected to 10 m/s ball velocity, grains exhibit pronounced misorientation and increased boundary distinction, as evidenced by the broader spectrum of colours and more fragmented regions in the OI map (Figure 4.4.2(c)).

Figure 4.4.2(a1) and (c1) highlight the various types of twins observed in SM-5v and SM-10v, while Figure 4.4.2(a2) and (c2) present the corresponding misorientation angles across the twins. The misorientation profiles for SM-5v (Figure 4.4.2(a2)) and SM-10v (Figure 4.4.2(c2)) illustrate distinct twinning characteristics. In SM-5v, tensile twins (TTs) and compression twins (CTs) are observed, with corresponding misorientation angles of around 86.1° and 57.3°, respectively. A significant fraction of $\{10\bar{1}2\}$ tensile twins is present in SM-5v, predominantly distributed across the surface region. Additionally, $\{10\bar{1}1\}$ compression twins are detected near the SMATed surface at around ~375 μm depth. In SM-10v, the twinning behaviour becomes more complex, with the additional

formation of double twins (DTs), characterised by a misorientation of ~36.5°. The SM-10v demonstrates the presence of TTs, CTs, and $\{10\bar{1}1\} - \{10\bar{1}2\}$ double twins even at a depth of ~850 μm.

These results suggest that the higher energy input by higher velocity balls in SMAT promotes more significant deformation, leading to an extensive lattice distortion, enhanced grain misorientation, and refinement. The higher strain and strain rate in the SM-10v specimen results in greater misorientation. Moreover, the higher strain energy is sufficient to activate multiple twin systems at a much greater depth than that of SM-5v, signifying the role of increased impact velocity in endorsing severe plastic deformation and twinning activity.
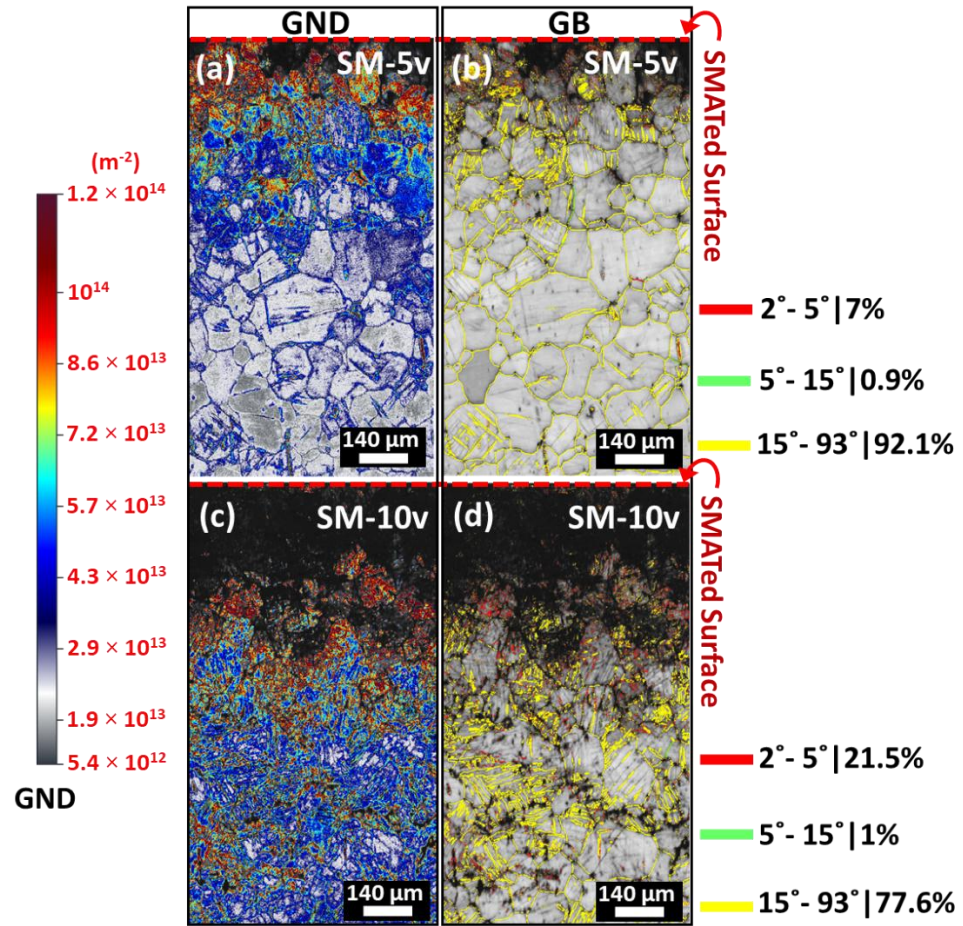
Figure 4.4.3: *GND and GB maps for (a-b) SM-5v and (c-d) SM-10v specimens*

Figure 4.4.3(a) and (c) depict the geometrically necessary dislocations (GND) maps for the SMATed specimens. They show average dislocation densities of ~4.1×10^{13} m^{-2} and ~5.3×10^{13} m^{-2} for SM-5v and SM-10v, respectively, indicating that the specimen SMATed with higher velocity balls has a higher dislocation

density and stored energy within the grains. Moreover, the grain boundary (GB) maps shown in Figure 4.4.3(b) and (d) reveal a larger density of low-angle grain boundaries (LAGBs) in the surface region of SM-10v than that of SM-5v due to more strain accumulation and higher density of twins and dislocations. A higher dislocation density and LAGBs than those mentioned in Figure 4.4.3 are possible for SM-10v due to the greater proportion of unindexed regions.

Since a considerable portion of the near-surface region remained unindexed in the EBSD analysis due to severe plastic deformation, further microstructural investigation was carried out using TEM at a subsurface depth of ~50 μm (below the SMATed surface). Figure 4.4.4(a) and (b) present the TEM micrographs for SM-5v and SM-10v, respectively, demonstrating the distinct microstructural changes induced by different impact velocities of balls. For SM-5v, the TEM micrograph (Figure 4.4.4(a)) reveals the presence of fine deformation twins dispersed throughout the microstructure, which suggests that twin-mediated plasticity significantly contributed to accommodating the deformation imparted by SMAT at 5 m/s ball velocity. The inserted SAED pattern in Figure 4.4.4(a) shows a spot pattern and not a ring pattern, which indicates that the near-surface regions have a well-defined crystallographic orientation, further validating the twinning as the primary deformation mechanism and the accumulated strain in the lower velocity SMA-treatment is insufficient to form nanograins.

In contrast, the microstructural response of the SM-10v specimen's surface region deviates from the twin formation, exhibiting a nanograined structure instead (Figure 4.4.4(b)). The higher impact energy at 10 m/s ball velocity results in more strain accumulation, which triggers the formation of nanoscale grains. The corresponding SAED pattern (Figure 4.4.4(c)) presents a diffuse ring-like structure, indicative of an ultrafine-grained or nanocrystalline microstructure. Further analysis of the grain size distribution for SM-10v (Figure 4.4.4(d)) reveals an average grain size of 28 ± 12 nm, reinforcing the significant grain refinement at higher impact velocities.

The comparison between SM-5v and SM-10v highlights a clear transition in deformation mechanisms, shifting from twin-dominated plasticity at lower velocity (5 m/s) to grain refinement via severe plastic deformation at higher velocity (10 m/s). This transformation aligns with the progressive increase in strain energy,

intensifying dislocation activity and ultimately promoting nanograin formation over twinning [76, 105]. In the deeper regions of the SM-10v specimen's deformed layer, twinning is a dominant deformation mechanism (Figure 4.4.2(c)) due to a gradual drop in the influence of high-velocity impact (concerning strain and strain rate) with an increasing depth .
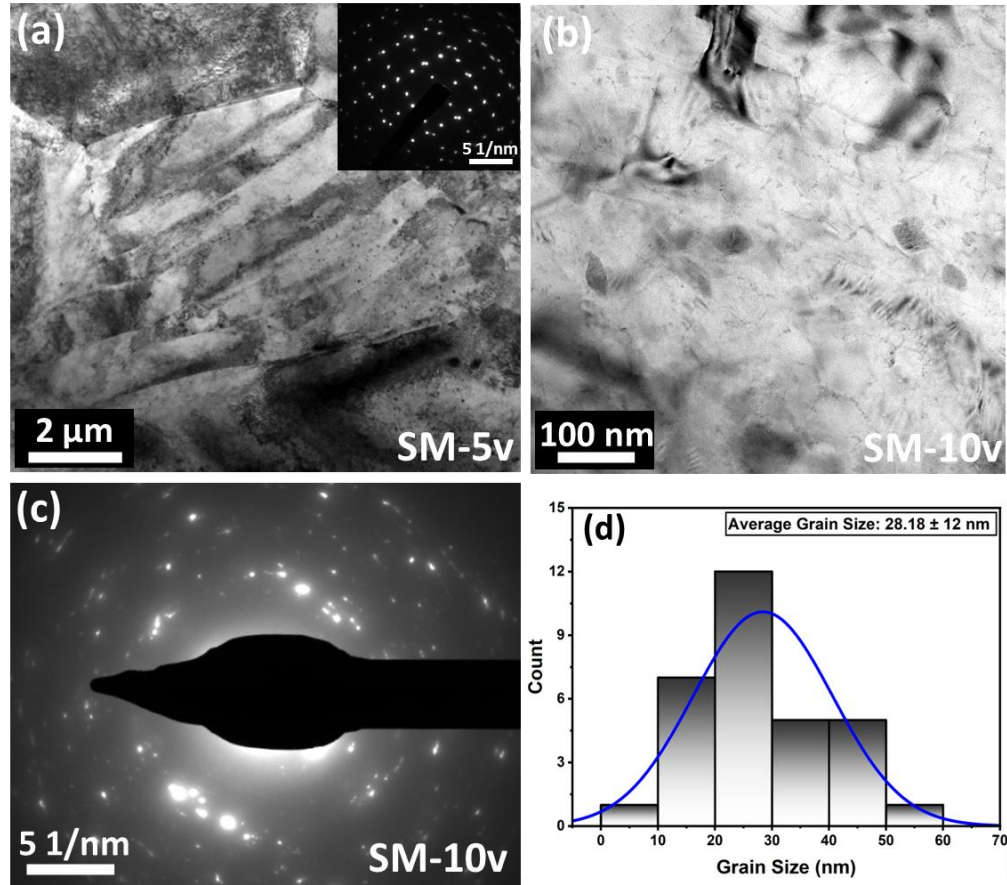
Figure 4.4.4: *(a) TEM micrograph illustrating fine twins in SM-5v specimen with the corresponding SAED pattern as an inset. (b) TEM micrograph exemplifying nanograins with (c) the associated SAED pattern, and (d) the nanograin size distribution for SM-10v specimen*

From a mechanical perspective, the presence of twins in SM-5v is expected to enhance strain hardening, contributing to improved strength and ductility [106]. Conversely, the formation of nanograins in SM-10v leads to grain boundary strengthening, potentially enhancing hardness and wear resistance, although at the expense of ductility. The observed transition from twinning to nanograin formation underscores the influence of impact velocity on deformation mechanisms, demonstrating the possibility of tailoring microstructural features for specific application requirements.

4.4.2 Microhardness and Strengthening Behaviour

4.4.2.1 Microhardness Distribution in the Deformed Layer

The microhardness distribution across the SMATed layer is consistent with the aforementioned microstructure evolution. A gradient in microhardness is observed within the deformed layer of SM-5v and SM-10v (Figure 4.4.5), which is attributed to the gradient microstructure (Figures 4.4.2-4.4.4). As shown in Figure 4.4.5(a) and (c), SM-5v exhibits a microhardness gradient up to 1300 ± 200 μm depth, while SM-10v shows a gradient up to 2400 ± 200 μm depth. The maximum microhardness value observed is ~117 ± 8.9 HV$_{0.05}$ for SM-10v, and ~91 ± 4.5 HV$_{0.05}$ for SM-5v. These values indicate a ~112% (~2.1 times) increase in the microhardness value for SM-10v and a ~65% (~1.6 times) increase for SM-5v when compared to the microhardness value of NSM (~55 HV$_{0.05}$).

Microhardness distribution (Figure 4.4.5(a) and (c)) and corresponding slopes (Figure 4.4.5(b) and (d)) highlight five distinct zones for SM-5v and SM-10v. In Zone I, a steep decrease in microhardness is observed up to a depth of ~110 μm for SM-5v and SM-10v. A significant negative slope of the microhardness versus depth profiles confirms it. In Zone II, the slope of the microhardness-depth profile is less negative, indicating a gradual decrease in microhardness values up to ~500 μm for SM-5v and ~900 μm for SM-10v. After this gradual change in microhardness, the values become almost constant, with minimal variation up to a depth of ~700 μm for SM-5v and ~1600 μm for SM-10v, which is designated as Zone III. Hardness is the material's response to the altered microstructure caused by the strain accumulation in SMAT. In the case of twinning-dominated regions, twin density is directly linked to the accrued strain [76, 105]. Therefore, the hardness stability in Zone III can be attributed to the consistent twin density observed in this region. Due to the negligible change in microhardness values with depth, this zone's slope profile remains constant, close to the zero slope. In Zone IV, a gradual decrease in microhardness values to the core's hardness is observed, extending to ~1400 μm for SM-5v and ~2500 μm for SM-10v. The slope profiles in this zone approach zero towards the end of Zone IV. Following this, SM-5v and SM-10v exhibit an almost plateaued trend in Zone V, with the corresponding slope nearing zero, indicating minimal or no change in hardness values.
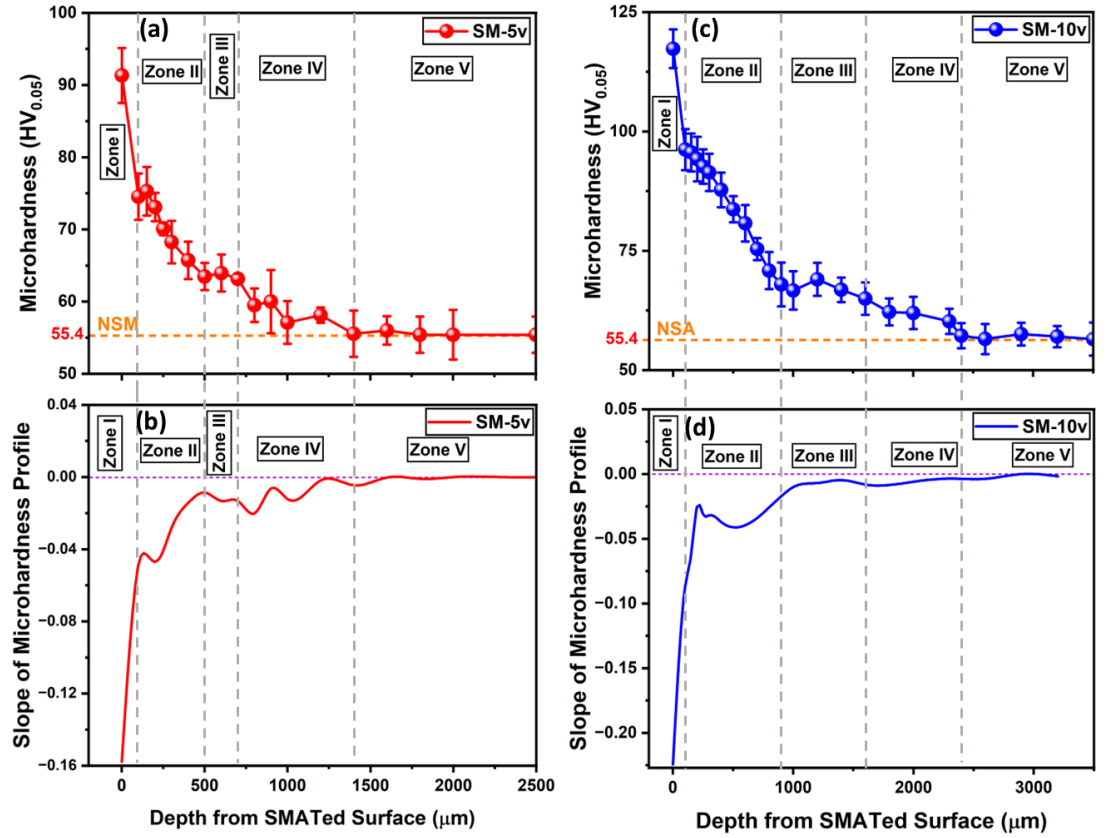
Figure 4.4.5: *(a-b) SM-5v and (c-d) SM-10v specimens' microhardness distribution (a, c) and the corresponding slope variation (b, d) with depth from SMATed surfaces*

Microstructural modifications are critical in determining the mechanical behaviour of metallic implant materials, particularly their hardness, which directly affects implant longevity and durability. During the SMAT of relatively softer materials such as Mg5Zn0.2Ca alloy, the surface experiences differential deformation and compressive stresses due to repeated high-energy impacts from colliding balls [159]. Such impacts induce distinct deformation zones (Figure 4.4.5) with varying strain and strain rates, leading to an inhomogeneous distribution of dislocations and twins (Figure 4.4.2 and 4.4.5) and alterations in twin thickness and crystallite size across the SMATed layer [146].

Both SM-5v and SM-10v exhibit an increase in surface microhardness, particularly in Zone I of the SMATed region (Figure 4.4.5). This enhancement primarily arises from microstructure refinement (Figure 4.4.4) and a high density of lattice defects (Figures 4.4.2 and 4.4.3). Given that twinning is the predominant deformation mode in Mg-alloys (Figure 4.4.2), the strain-hardening effect induced by twinning is a key contributor to the observed hardness increment in a significant

portion of the deformed layer. Twin boundaries obstruct dislocation movement, restricting further slip and promoting strain-hardening [80]. Consequently, the interaction between twins and dislocations intensifies this hardening effect, resulting in a substantial improvement in the hardness of SM-5v and SM-10v specimens.

Strain accumulation/localisation, grain refinement, and variation in density of dislocations and twins are responsible for the gradient in microhardness. Bandyopadhyay et al. [22] and Gerhátová et al. [8] reported the improved biocompatibility of metallic implants with higher surface hardness. As Mg5Zn0.2Ca is a biodegradable material, the gradient in microhardness could contribute to improved biocompatibility at each stage of degradation. The higher hardness values with gradient behaviour enhance the material's performance throughout its degradation process [22].

4.4.2.2 Surface Strengthening Properties

Microhardness measurements were performed throughout the specimens' cross-sections (5 mm thickness), which were SMATed from both sides (flat surfaces). To better understand the gradual attenuation of hardness from surface to core, an exponential decay model (Eq. 4.4.1) was employed to represent the microhardness gradient within the treated layer [160]:

$$E = H_m + (H_M - H_m)e^{-Rx} \qquad (4.4.1)$$

where H_M and H_m represent the maximum and matrix microhardness, respectively, R denotes the surface strengthening exponent (decay constant), which represents the rate at which microhardness decreases with depth, and x represents the distance from the SMATed surface. The surface strengthening energy (E, J/m²) represents the absorbed energy per unit area of the surface-strengthened specimens. The energy absorbed by the gradient layer during strengthening (i.e., the energy stored due to plastic deformation) was calculated as the area under the microhardness-depth curve using Eq. 4.4.2:

$$E = \int_0^\lambda \left((H_M - H_m)e^{-Rx} \right) dx \qquad (4.4.2)$$

In this study, the gradient layer properties, including the gradient layer thickness (λ), H_M, R, and E, are systematically analysed to characterise the behaviour of SM-5v and SM-10v. This comprehensive approach provides a unified evaluation of the microhardness gradient and the associated strengthening effects, combining mechanical properties with the microstructural features of the treated samples. The essential properties of the strengthened layer are shown in Figure 4.4.6 and summarised in Table 4.4.1. Figure 4.4.6 depicts the total surface energy stored within the deformed layers on both sides (flat surfaces) of SM-5v and SM-10v.

A lower value of R indicates a more gradual hardness transition from the SMATed surface to the core (substrate), suggesting sustained strengthening effects. The results show that for SM-10v, the value of R is 0.0016 μm^{-1}, whereas for SM-5v, it is 0.003 μm^{-1}. These results confirm that the SMAT (with a constant percentage coverage) at a higher intensity impacts results in a more profound and uniform hardening effect.

Furthermore, the surface strengthening energy is significantly higher (~3.3 times) for SM-10v (3.77 × 10^5 J/m^2) than SM-5v (1.16 × 10^5 J/m^2), indicating a greater degree of strain hardening by higher-intensity SMA-treatment. This increased energy storage can enhance the mechanical performance of the SMATed alloy by improving resistance to deformation and wear.

Overall, these findings highlight the role of an imperative process parameter, i.e., impact velocity, in influencing surface strengthening characteristics, where higher intensity SMAT contributes to improved mechanical stability. The effect of this strengthening behaviour on bulk mechanical properties is further explored in the subsequent section.
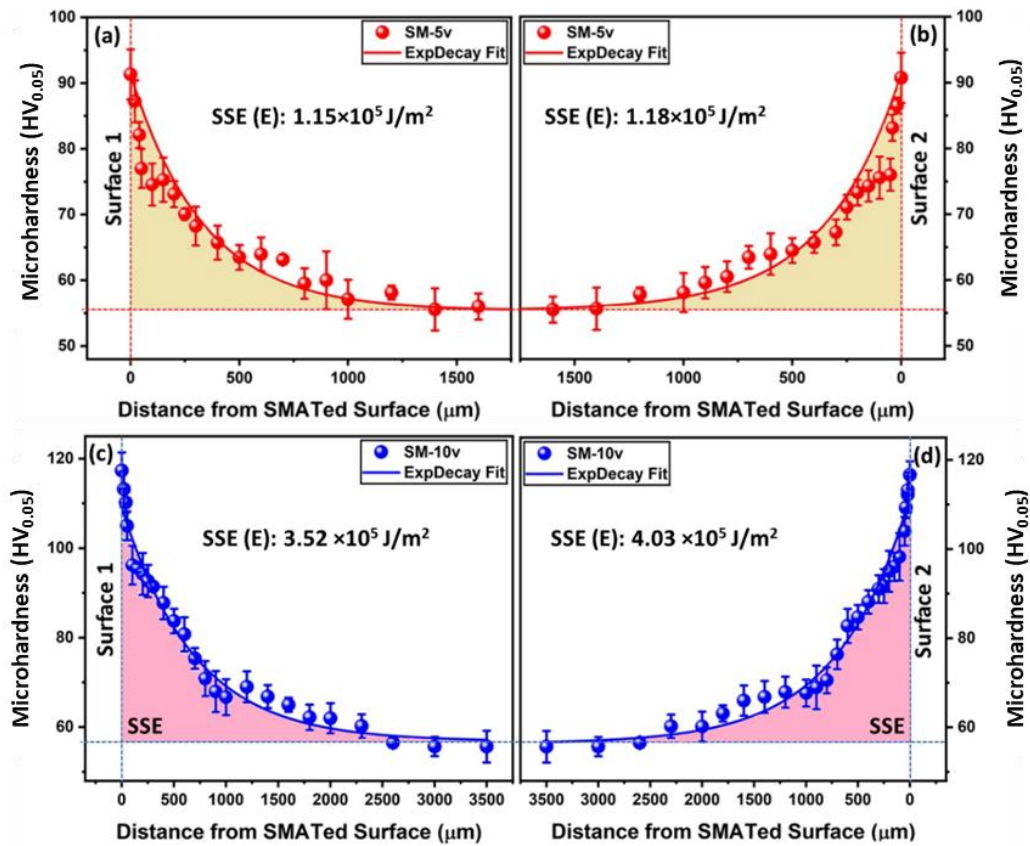
Figure 4.4.6: *Surface strengthening energy (SSE), E, for dual-surface SMATed specimens: (a-b) SM-5v and (c-d) SM-10v*

Table 4.4.1: Surface layer strengthening properties

Specimen Name	Maximum Hardness, H_M (HV$_{0.05}$)	Matrix Hardness, H_m (HV$_{0.05}$)	Gradient Layer Thickness (μm)	Surface Strengthening Exponent (or Decay Constant), R (μm)$^{-1}$	Surface Strengthening Energy, E (J/m^2)
SM-5v	91 ± 4.5	55.4 ± 2.5	1300 ± 200	0.003	1.16×10^5
SM-10v	117 ± 8.9	55.4 ± 2.5	2400 ± 200	0.0016	3.77×10^5

4.4.3 Tensile Properties

4.4.3.1 Stress-Strain Response

The effect of SMAT on the tensile properties of the Mg5Zn0.2Ca alloy is evaluated by comparing the engineering stress-strain response (Figure 4.4.7(a)) and

corresponding ultimate tensile strength (UTS) and yield strength (YS) of the NSM, SM-5v, and SM-10v specimens (Figure 4.4.7(b) and Table 4.4.2). The results reveal a significant improvement in the strength after SMAT. The NSM exhibits a lower stress level throughout deformation, with a relatively higher strain at failure, indicating a more ductile response. In contrast, SM-5v and SM-10v demonstrate higher flow stresses and reduced ductility due to the presence of hardened layers on both surfaces by SMAT (Figure 4.4.8). The SM-10v exhibits the highest strength, with a noticeable increase in YS and UTS compared to SM-5v.

The NSM exhibits a UTS of around 228 ± 22 MPa, whereas SM-5v and SM-10v significantly increase the UTS value to ~291 ± 28 MPa and ~330 ± 33 MPa, respectively. A similar trend is observed for YS, where the SMATed specimens show significantly higher values than the NSM condition (Table 4.4.2). The statistical significance of UTS and YS among NSM, SM-5v, and SM-10v is highlighted in Figure 4.4.7(b) using a single asterisk (*), indicating a statistically significant difference ($p < 0.05$) between the compared groups. Additionally, the difference between SM-5v and SM-10v is statistically significant, reinforcing that higher-intensity SMAT (using 10 m/s ball velocity) leads to superior mechanical performance.

This improvement in strength is ascribed to grain refinement strengthening, where the SMA-treatment-induced reduction in grain size due to the repeated impacts by high-velocity balls in random directions (Figure 4.4.4(b)-(d)) increases the grain boundary area, thereby restricting dislocation motion and hardness increase (Figure 4.4.5) following the Hall-Petch effect [40, 69]. Additionally, SMAT generates a high density of deformation twins (Figure 4.4.2 and Figure 4.4.4(a)) and dislocations (Figure 4.4.3), which act as barriers to plastic deformation during tensile test, further contributing to strength enhancement [161, 162].

Furthermore, the UTS/YS ratio implies the alloy's capability to sustain stress via plastic deformation (i.e., competence to absorb energy) before the occurrence of its failure. The results show a minor drop in this ratio (from ~2.15 to ~1.3) after SMAT (Table 4.4.2). Moreover, ball velocity has a negligible effect on the UTS/YS ratio for the SMATed Mg alloy (Table 4.4.2) due to a proportional enhancement in YS and UTS with an increased impact velocity (Figure 4.4.7(b)). Even though the initial surface hardness is noticeably high (Figure 4.4.8), the

UTS/YS ratio of SMATed specimens is much greater than one, possibly due to gradient microstructure.

Overall, the interplay between various strengthening mechanisms and the microstructure evolution in SMATed specimens suggests that SMAT effectively enhances mechanical properties and deformation characteristics, making the Mg alloy more suitable for biomedical and engineering applications.
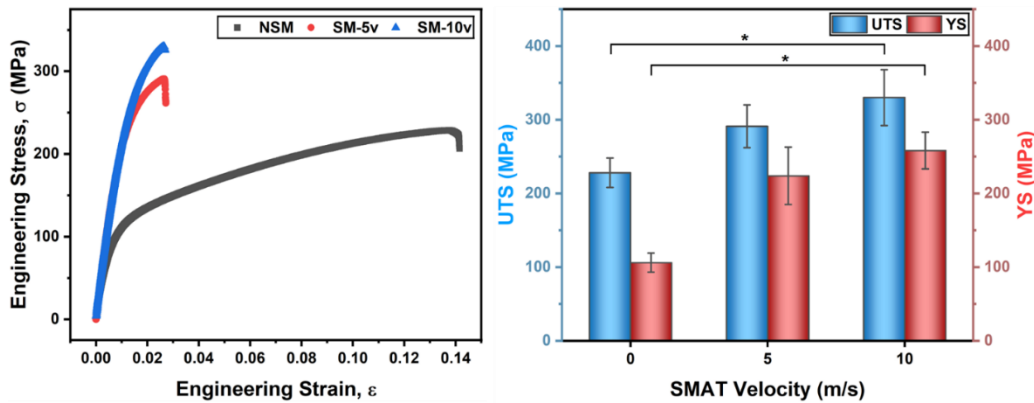
Figure 4.4.7: *(a) Stress-strain curves and (b) UTS and YS for NSM, SM-5v and SM-10v specimens*

Table 4.4.2: Tensile properties of NSM, SM-5v and SM-10v specimens

Specimen condition	Yield strength, YS (MPa)	Ultimate tensile strength, UTS (MPa)	UTS/YS Ratio	Total elongation %
NSM	106 ± 14	228 ± 22	2.15 ± 0.44	14.15 ± 2.59
SM-5v	223 ± 34	291 ± 28	1.30 ± 0.24	2.73 ± 0.41
SM-10v	258. ± 26	330 ± 33	1.28 ± 0.18	2.69 ± 0.28

4.4.3.2 Surface Layer Strengthening and Ductility

Understanding and establishing a correlation between surface-strengthening and ductility of NSM, SM-5v, and SM-10v specimens is crucial. The improvements in UTS and YS observed in the previous section (Section 4.4.3.1) for the SMATed specimens are linked to the gradient-hardened layer. The microhardness depth profiles shown in Figure 4.4.8 illustrate the influence of SMAT on the SM-5v and SM-10v specimens' strengthening behaviour, where the specimens are 1 mm thick, and both sides (flat faces) are SMA treated before tensile testing. The SM-10v exhibits the highest surface hardness (~117 $HV_{0.05}$), followed by SM-5v (~91

HV$_{0.05}$), while the NSM sample maintained a uniform hardness of ~55 HV$_{0.05}$. As discussed above, this hardness increase directly impacts the material's ability to resist plastic deformation, contributing to its improved tensile strength. The difference in the hardness profiles of SM-5v and SM-10v is also essential. The hardness profile of SM-10v uniformly shifts upward throughout the thickness due to the higher strain energy stored in the material during plastic deformation by higher velocity balls (Section 4.4.2.2). The hardness profiles of SM-5v and SM-10v indicate that the thickness of the gradient-hardness region is ~400 μm for both specimens; however, SM-10v has a higher hardness in the central region of ~200 μm width (due to the overlap of straining in this region during SMAT on both flat faces of the specimen).
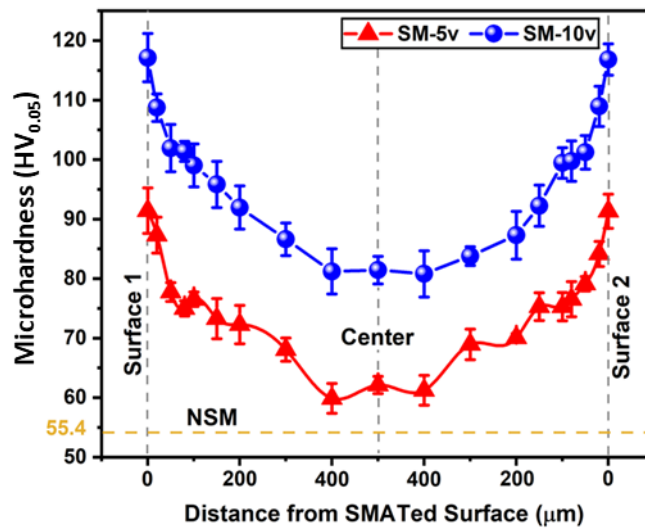
Figure 4.4.8: *Microhardness gradient profiles for SM-5v and SM-10v specimens*

Beyond hardness, percentage elongation (Table 4.4.2) offers additional insight into the SMAT's influence on plastic deformation behaviour. The NSM specimen exhibits the highest percentage of total elongation (~14%), indicating a greater capacity for strain hardening and more gradual work-hardening behaviour. In contrast, SMATed specimens show considerably lower percentage elongation (~3%), suggesting that while their surfaces are significantly hardened, their ability to undergo further strain hardening and deformation is circumscribed.

The reduced ductility of SMATed specimens aligns with the observed increase in initial (pre-existing) hardness (Figure 4.4.8) and dislocation saturation in the microstructure (Figure 4.4.3), which limits additional plasticity during tensile deformation. Moreover, the *E* values from Section 4.4.2.2 support this trend, where

impacts by balls lead to the stored energy in the treated layer, contributing to an enhanced surface hardness but less available capacity for further straining during subsequent tensile loading.

In summary, although SMAT improves tensile strength and surface hardness, it leads to a more saturated microstructure with lower strain-hardening potential. Further, even though higher-velocity SMAT considerably enhances hardness (Figure 4.4.8) and strength (Figure 4.4.7), an insignificant change in the UTS/YS ratio is noticed (Table 4.4.2), which suggests the role of microstructure refinement in making the material stronger without compromising ductility and retaining some strain-hardening capacity during subsequent loading. The strain-hardening behaviour is further discussed in detail in subsequent sections.

4.4.3.3 Strain-Hardening Behaviour During Tensile Loading

Figure 4.4.9(a)–(d) illustrates the evolution of true stress-strain curves, strain hardening rate ($d\sigma/d\varepsilon$), and instantaneous strain hardening exponent (n) for NSM, SM-5v, and SM-10v Mg5Zn0.2Ca specimens. The calculated n-values, derived from Hollomon's equation (Figure 4.4.9(d)), indicate a reduction in strain-hardening capacity with increasing SMAT intensity. This trend can be justified based on dislocation density evolution, twinning activity, and dynamic recovery; all are influenced by severe surface deformation. To better understand the deformation behaviour, the tensile response is divided into four distinct zones (I–IV).
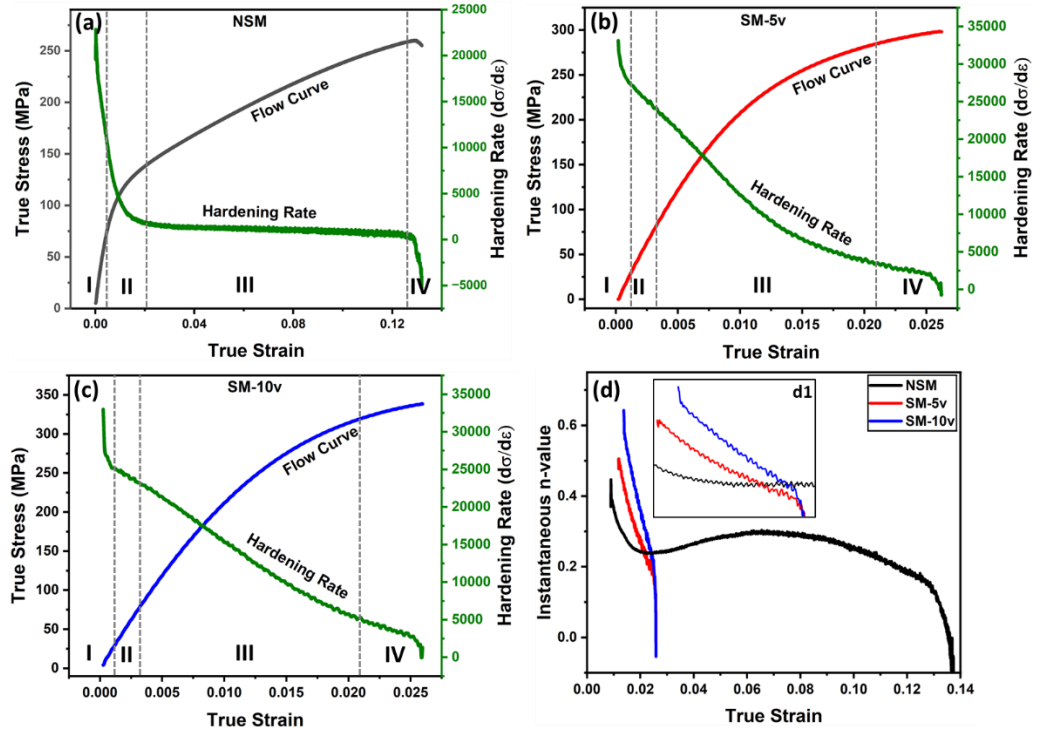
Figure 4.4.9: *True stress-strain curves and strain hardening rate under tensile loading for (a) NSM, (b) SM-5v, (c) SM-10v, and (d) The corresponding instantaneous n-value vs true strain*

Zone I has a steep rise in true stress; however, the strain hardening rate (dσ/dε) drops rapidly from a very high initial value. In the case of SMATed specimens, this response is significantly sharper due to a nanograined surface layer produced by surface mechanical attrition treatment. This surface layer's high dislocation density and grain boundary area enhance initial resistance to plastic flow. However, because the material is already dislocation-rich (due to SMAT), there is limited room for further hardening, so the hardening rate drops quickly. In contrast, the NSM specimen's coarser and uniform grain structure shows a smoother and broader yielding transition, reflecting homogeneous dislocation activation [161].

Zone II is marked by a continued but more gradual decrease in hardening rate after the initial rapid drop seen in Zone I. In the SM-10v, which has the most refined gradient structure in a treated layer (Figures 4.4.2(c)-(d) and 4.4.4(b)-(d)), the hardening rate continues to decline steadily, indicating early saturation of dislocation accumulation and the onset of dynamic recovery in the ultrafine grains [103]. The SM-5v sample, with a relatively coarser subsurface grain structure (Figure 4.4.4(a)), also shows a downward trend in hardening rate but at a slower

pace than SM-10v, suggesting a somewhat better balance between dislocation storage and recovery. In contrast, the NSM specimen maintains a relatively stable hardening rate during this zone, as dislocation multiplication and the initiation of deformation twinning are active throughout the bulk grains, sustaining a more consistent strain-hardening response.

Zone III is the dominant plastic deformation stage, where significant differences among the specimens emerge. The NSM specimen's coarse grain structure (Figure 4.4.1) effectively activates the basal slip and deformation twinning. Twinning dynamically subdivides grains and acts as a strong barrier to dislocation motion, thereby enhancing the strain-hardening rate and sustaining a high instantaneous n-value [160–162] over a broader strain range (Figure 4.4.9(d)). This behaviour results in a prolonged Zone III in NSM. In the SM-5v, this region is moderately sustained. While the grain-refined layer near the SMATed surface saturates quickly, the relatively coarser grains in the subsurface and core continue to accommodate plastic strain through dislocation glide and limited twinning, ensuring some hardening. The SM-10v specimen shows a much narrower Zone III. The extensive nanograined structure suppresses twinning almost entirely, and the high dislocation density from SMAT causes early dynamic recovery. As a result, the material's ability to accumulate further dislocations diminishes, leading to a faster reduction in hardening rate and n-value.

Finally, in Zone IV (softening and necking region), the hardening rate approaches zero (or turns negative), marking the onset of necking and eventual failure. The SMATed specimens move into Zone IV earlier than NSM. These specimens' ultrafine grains and high surface dislocation density cause rapid softening due to dominant dynamic recovery and shear localisation. Cleavage facets observed in its fracture surface (elaborated in the subsequent section) further confirm the brittle response in this zone. In contrast, the NSM specimen delays entry into Zone IV owing to continued twinning and dislocation interaction, which sustain the material's strain-hardening capacity and postpone localisation and fracture.

These zone-wise differences reflect how the gradient microstructure of SMATed specimens influences deformation and strain-hardening response during

tensile deformation. These results reinforce the idea that surface modification through SMAT plays a crucial role in optimising the strength and plasticity of Mg-Zn-Ca alloys based on application needs.

4.4.3.4 Analysis of Fractured Surfaces

To further understand the failure mechanisms and the influence of SMAT on the fracture behaviour of the Mg5Zn0.2Ca alloy under tensile loading, SEM fractography analysis is performed on NSM, SM-5v, and SM-10v specimens, as presented in Figure 4.4.10. The fracture surface characteristics provide insights into the deformation and damage evolution under tensile loading.

The fractured surface of the non-SMATed specimen (Figure 4.4.10(a)) appears strikingly different than that of the SMATed specimens (Figure 4.4.10(b) and (c)). The NSM specimen (Figure 4.4.10(a) and (a1)) exhibits a classic ductile fracture morphology, which is dominated by the presence of large and deep dimples, typically formed via microvoid coalescence [163, 164]. This dense dimpled pattern reflects substantial plastic deformation before fracture, consistent with the high ductility and sustained strain-hardening comprehended in the stress-strain response (Figures 4.4.7(a) and 4.4.9).
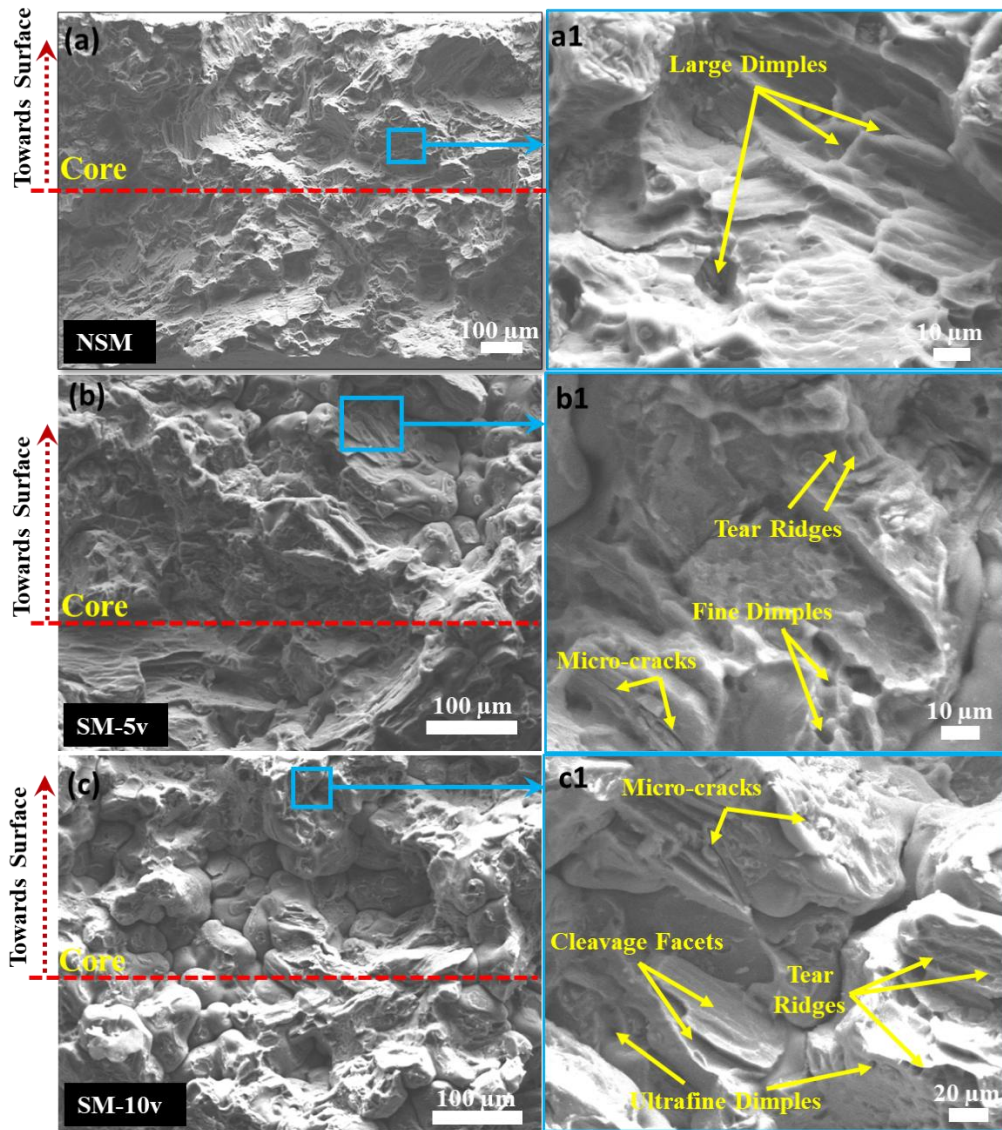
Figure 4.4.10: *SEM micrographs depicting the fracture surface morphologies of (a) NSM, (b) SM-5v, and (c) SM-10v*

In comparison, the SM-5v specimen (Figure 4.4.10(b) and (b1)) shows a refined ductile fracture surface featuring fine dimples and tear ridges, with occasional micro-cracks. The fine dimples indicate void nucleation and growth at a smaller scale due to grain refinement near the SMATed surface. The tear ridges (with raised ligaments between dimples) highlight zones of localised plastic deformation, suggesting enhanced strain accommodation in confined regions of the gradient microstructure. Although plastic deformation is still significant, micro-cracks presence suggests that some localised strain accretion occurs near the fine-grained surface due to high dislocation density and reduced twin activity.

The fracture surface of the SM-10v (Figure 4.4.10(c) and (c1)) shows a clear transition toward a mixed-mode fracture, with a combination of ultrafine dimples, cleavage facets, tear ridges, and more frequent micro-cracks. This morphology reflects the effect of the ultrafine and twin-suppressed grains in the surface layer, where dislocation activity could saturate early, and twinning is mainly absent. The limited strain-hardening and rapid strain-localisation in these regions promote early void coalescence and brittle fracture features. The observed cleavage facets suggest crack propagation along crystallographic planes or grain boundaries, while the shallow dimples indicate minimal plastic flow before fracture. These features correlate well with the mechanical response of SM-10v, specifically, its reduced uniform elongation and early saturation of the hardening rate (Figures 4.4.7 and 4.4.9).

Overall, the progression from large and uniformly distributed dimples in NSM to fine dimples in confined regions with cleavage-like features in SMATed specimens reflects the influence of microstructural refinement and gradient structure on fracture behaviour. While SMAT improves strength through grain refinement, it increases stored strain energy. It promotes early strain localisation, leading to microvoid coalescence and premature fracture once the ductility limit is exceeded during tensile loading.

4.4.4 Surface Roughness and Tribological Behaviour

Figure 4.4.11 shows the surface roughness profiles and surface appearance of NSM, SM-5v, and SM-10v specimens. Here, the average surface roughness values are obtained by considering 8.5 mm of sampling length on the specimens' surfaces (Figure 4.4.10(a)). The surface roughness (R_a) values of the SMATed surfaces (SM-5v and SM-10v) are significantly larger than that of the non-SMATed (NSM) surface (Figure 4.4.11(a)). Moreover, the highest R_a is observed for SM-10v. This trend is pragmatic during SMAT because the rapid deformation caused by the balls with higher velocity produces the craters with the highest peaks and deepest valleys on the specimen surface (Figure 4.4.11(b) and (c)). Such a surface deformation during SMAT further results in a greater number of wider surface micro-irregularities, leading to an increased R_a value. Hence, the specimen's initial surface roughness of 0.09 ± 0.005 μm increases to 0.85 ± 0.15 μm for SM-5v and

1.35 ± 0.3 μm for SM-10v. Chen et al. [80] also observed a rise in AZ31B Mg alloy's surface roughness after the SMAT.
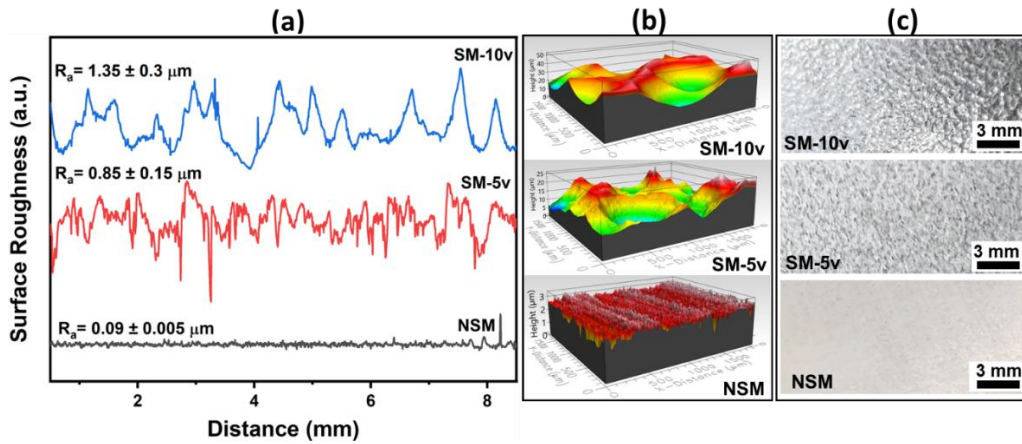
Figure 4.4.11: *(a) 2D surface roughness profiles with corresponding (b) 3D topographies and (c) actual surface appearance (under the optical microscope) of NSM, SM-5v, and SM-10v specimens*

A tribological study of NSM, SM-5v, and SM-10v under 5, 10, and 20 N loads and dry friction conditions is performed using ball-on-disc tribometers. Time and load-dependent coefficient of friction (COF) results are shown in Figure 4.4.12. All specimen conditions exhibit higher COF under higher loads. In general, the average values of COF (Figure 4.4.12(d)) for NSM and SM-5v do not differ much in all loading conditions, but the values are considerably reduced for SM-10v. In other words, higher ball velocity during SMAT is advantageous in reducing COF even if initial surface roughness is the highest (Figure 4.4.11). This behaviour suggests that higher surface hardness and thicker gradient SMATed layer (Figure 4.4.5 and Table 4.4.1) play crucial roles in controlling the tribological response of the Mg alloy. Such characteristics of the SMATed layer could have minimised the formation of wear debris and enhanced the load-bearing capacity of the SM-10v, leading to a considerable reduction in COF. Similar behaviour is also reported in the literature [69].
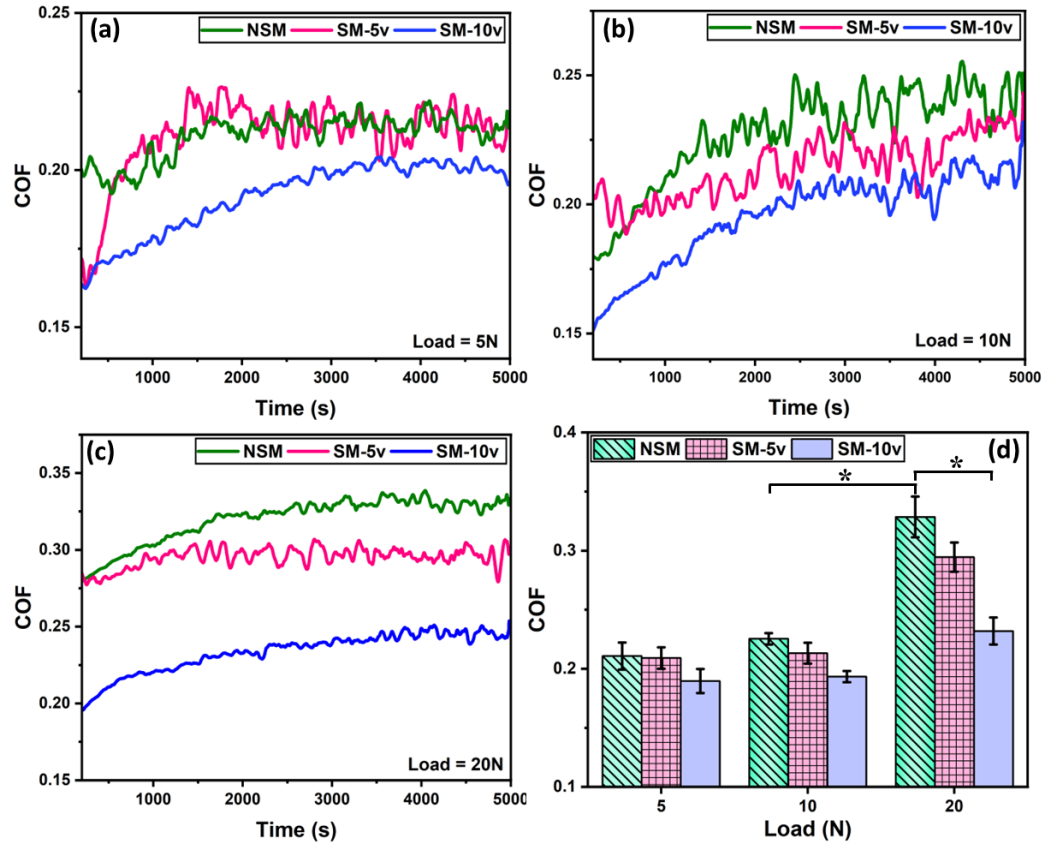
Figure 4.4.12: *Variation of COF with sliding time under (a) 5 N, (b) 10 N, and (c) 20 N for NSM, SM-5v, and SM-10v. (d) Average COF of these specimens under different loads*

Some examples of 2D profiles across the wear tracks under all loading conditions for NSM, SM-5v, and SM-10v are shown in Figure 4.4.13. These profiles indicate the material removal trend. Under the investigated loading conditions, the wear track depths of NSM are more than those of SMATed specimens (Figure 4.4.13). Further, the wear track widths are measured using SEM micrographs (Figure 4.4.14). A consistent trend is observed across all specimens. The results indicate that the wear track depth and width progressively increase as the applied load increases from 5 to 20 N. However, the extent of wear under a given load differs significantly among NSM, SM-5v, and SM-10v, highlighting the influence of SMA-treatment-induced strengthening of the gradient layer on wear performance. The wear tracks are narrower on the SMATed surface than on the NSM specimen under all load conditions (Figure 4.4.14). These results confirm the superior wear resistance of SMATed specimens, especially SM-10v, under the increased load conditions. The higher surface hardness and thicker SMATed layer (Figure 4.4.5) help enhance wear resistance.
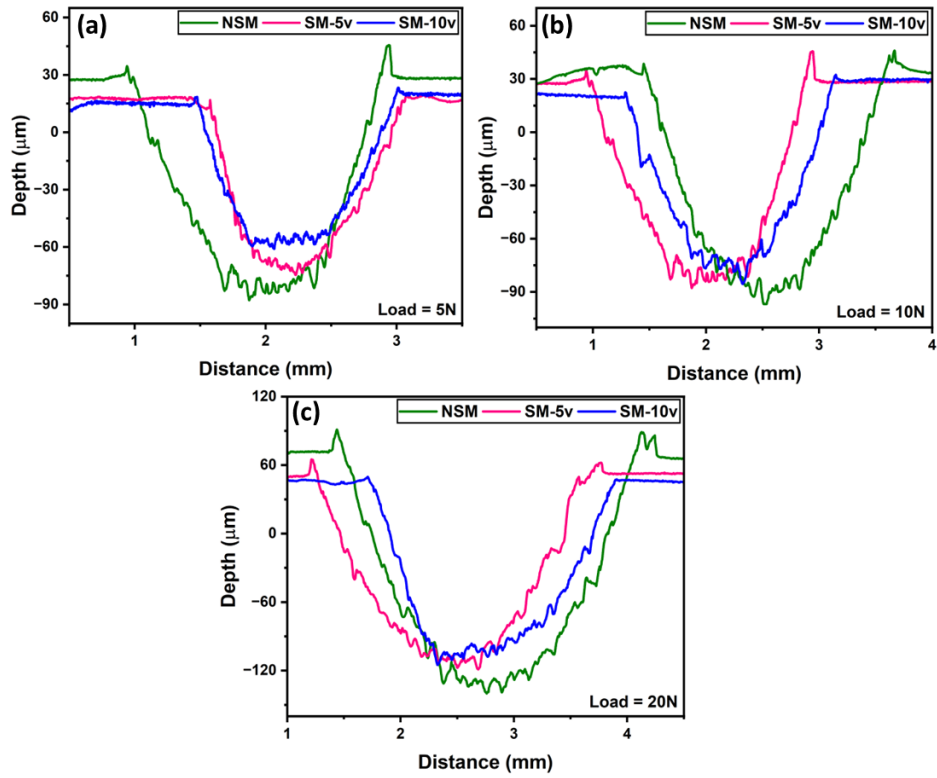
Figure 4.4.13: *2D wear track profiles under different loads for NSM, SM-5v, and SM-10v specimens*
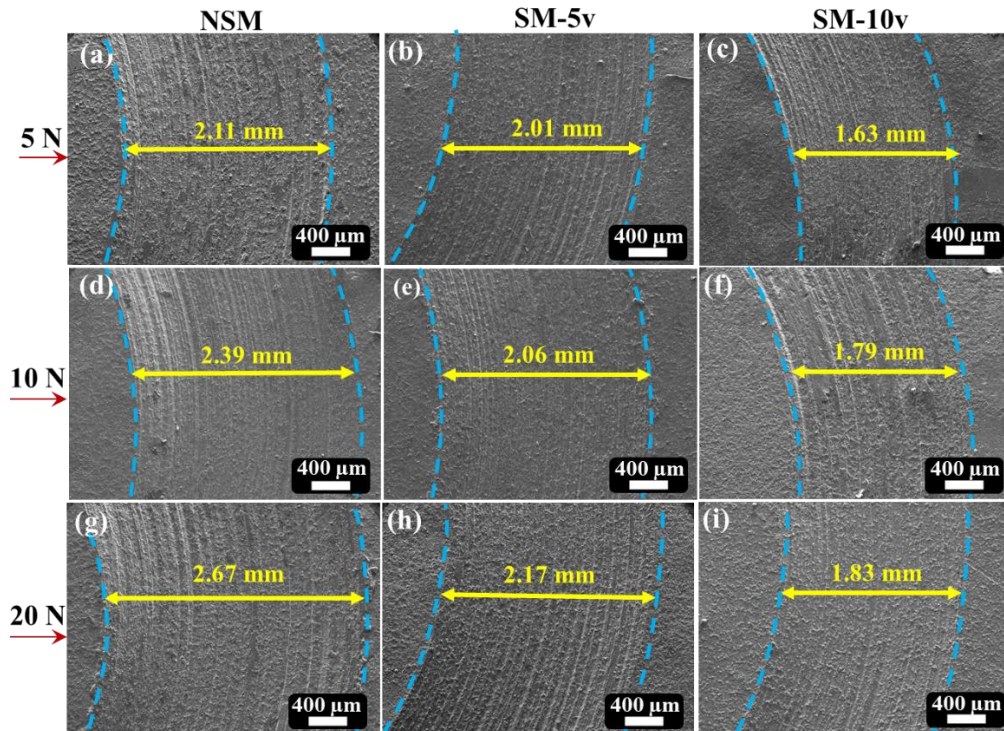
Figure 4.4.14: *SEM micrographs showing wear track widths for NSM, SM-5v and SM-10v specimens*

Furthermore, the specimens' wear volume loss and wear rate are presented in Figure 4.4.15. The statistical significance of wear volume loss across different conditions is illustrated in Figure 4.4.15(a). A notable increase in wear volume loss is observed across all specimens as the load increases from 5 to 20 N, reflecting the expected load-dependent wear behaviour. Such a trend is attributed to the increased stresses (due to increased applied load) between the contact interfaces [165]. At 10 and 20 N, a statistically significant difference ($p < 0.05$) between the volume loss of NSM and SM-10v is evident, with prominence of the improved wear resistance of SMATed specimens, particularly under higher velocity SMAT. Improved mechanical properties (Section 4.4.3) due to the refined and gradient microstructure (Section 4.4.1) enhance the SMATed specimens' load-bearing capacity, resulting in reduced wear rate [3].

The slope of the wear rate vs load plots indicates the specific wear rate (SWR) (Figures 4.4.15(b) and 4.4.16). In other words, the SWR represents the material loss normalised by the applied load and sliding distance. One of the major factors that influence SWR is surface hardness. Archard equation can be used to estimate the wear volume loss (V) theoretically [78, 165] and is given by,

$$V = K \frac{\text{PL}}{3H} \qquad (4.4.3)$$

where, K is a sample-specific dimensionless wear coefficient, H is the hardness (GPa), P is the applied load (N), and L is the total sliding distance (m). As per Eq. 4.4.3, the wear loss is inversely proportional to the surface hardness. In the current study, a linear relationship between SWR and surface hardness is evident in Figure 4.4.16. This trend aligns with Archard's wear equation (Eq. 4.4.3). The regression equation provided in Figure 4.4.16 suggests a strong dependency of SWR on microhardness, where the higher surface hardness leads to lower SWR. A maximum SWR of 0.93×10^{-3} mm³/Nm is found in the case of NSM; however, SM-10v exhibits the lowest specific wear rate of 0.6×10^{-3} mm³/Nm. These results underscore the effectiveness of SMAT, especially with higher velocity balls, in enhancing the wear resistance (Figures 4.4.13-4.4.16) of the Mg5Zn0.2Ca alloy, along with a reduction in the COF (Figure 4.4.12). It should be noted that SWR trend can be a complex function of various factors. Along with the hardness, it can be attributed to the material's modified microstructural features, localised surface

heating, initial surface roughness, phase transformation during wear (for example, the dissolution of the secondary phase through plastic deformation), etc. [112,120].

The wear volume of the counter surface (alumina balls) is shown in Figure 4.4.15(c). This volume loss is considerably lower than the specimens' wear volume loss (Figures 4.4.15(a) vs 4.4.16(c)). Nevertheless, the counter surface's volume loss increases with applied load, indicating an enhanced mechanical interaction at higher contact pressures. Interestingly, the highest counter surface wear is observed for the SMATed specimens (Figure 4.4.15(c)), particularly SM-10v, despite their lower wear volume loss (Figure 4.4.15(a)). Conversely, the NSM surface's sliding leads to a relatively lower counter surface wear. This trend suggests that the SMATed specimens impose greater abrasive effects on the alumina ball due to increased surface hardness (Figure 4.4.5) and reduced adhesion tendency. However, the softer NSM surface results in less severe mechanical interaction with the alumina ball, reducing counter surface wear. These observations highlight the trade-off between the enhanced wear resistance of SMATed specimens and increased wear on the counter surface, a common phenomenon in tribological systems involving surface-hardened materials [165, 166].
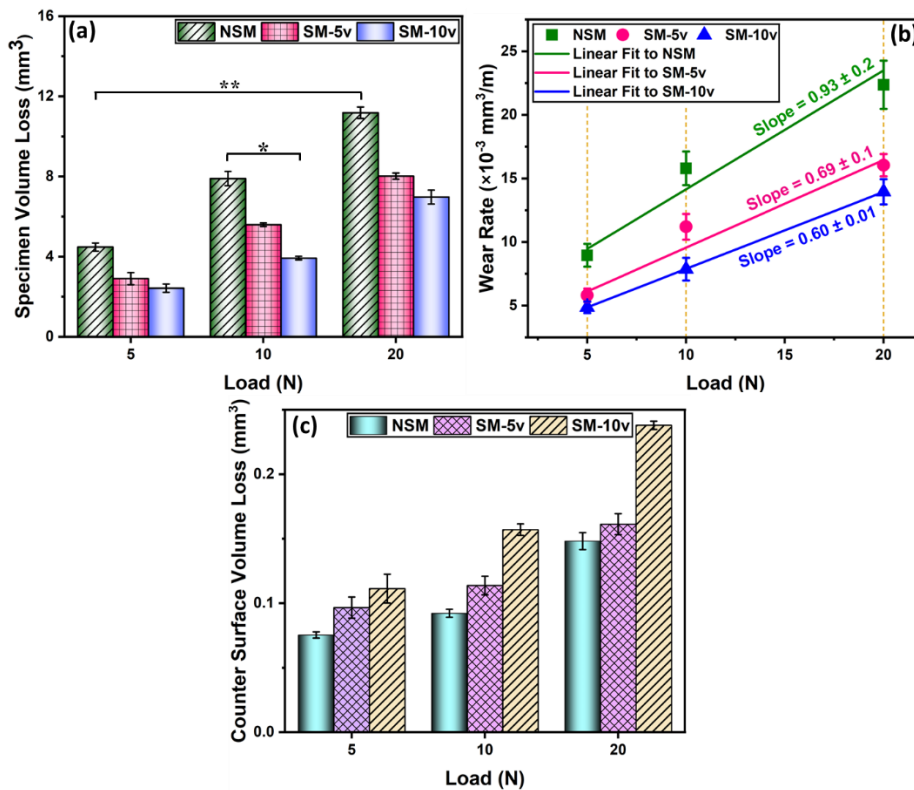
Figure 4.4.15: *(a) Specimen wear volume loss, (b) wear rate, and counter surface wear volume loss for NSM, SM-5v, and SM-10v under different loading conditions*
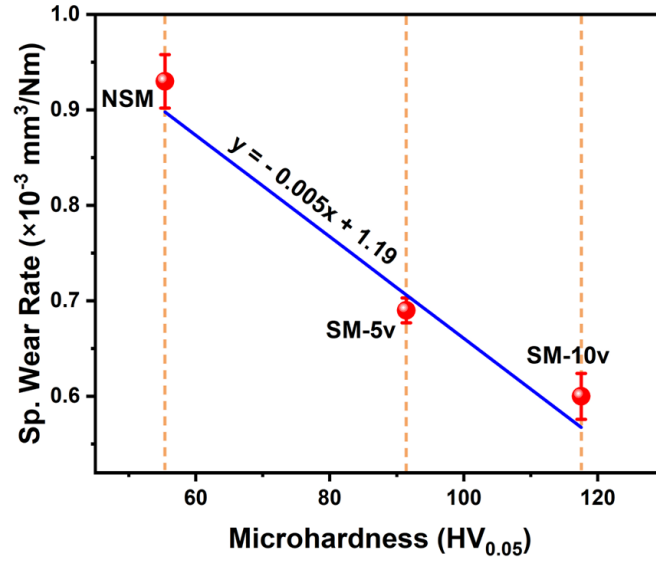
Figure 4.4.16: *Specific wear rate vs surface hardness for NSM, SM-5v and SM-10v under different loading conditions*

Further, the SEM micrographs presented in Figure 4.4.17 focus on the wear tracks formed on the specimens' surface under 20 N to examine the dominant wear mechanisms under high-load conditions. SMA-treatment-induced surface modifications could significantly influence the wear mechanisms, including grain refinement, strain hardening, and compressive residual stresses.

The NSM exhibits adhesive wear, ploughing, delamination, and wear debris formation, indicating severe material removal under sliding conditions. The presence of deep grooves and ploughed surfaces, as marked in Figure 4.4.17(a), suggests that the relatively soft surface of the non-SMATed specimen experiences substantial plastic deformation. Delamination and wear debris accumulation further indicate a dominance of adhesive wear, which is commonly observed in Mg alloys with insufficient surface strengthening [167, 168]. The lack of surface work-hardening in NSM results in rapid material transfer and debris formation, accelerating wear damage. These findings align with literature that reports the poor wear resistance of as-cast magnesium alloys due to their low hardness and high ductility [167].

The SM-5v reveals a notable reduction in adhesive wear compared to NSM, as seen in Figure 4.4.17(b). The primary wear mechanisms observed are delamination, scratching, and localised fracture. The increase in surface hardness due to SMAT contributes to decreased adhesive wear, but the wear track still

exhibited signs of fracture and material pull-out. Compared to NSM, the wear debris size is smaller and less prominent for SM-5v, supporting the influence of higher hardness and refined microstructure in the enhanced wear resistance. However, localised micro-fractures indicate that the relatively brittle surface of SM-5v might have experienced sub-surface crack initiation under high load, leading to material removal via delamination and pull-out. This behaviour is typical for surface-treated Mg alloys, where an increase in hardness can lead to a transition from adhesive wear to more brittle failure mechanisms under severe loading conditions [166].
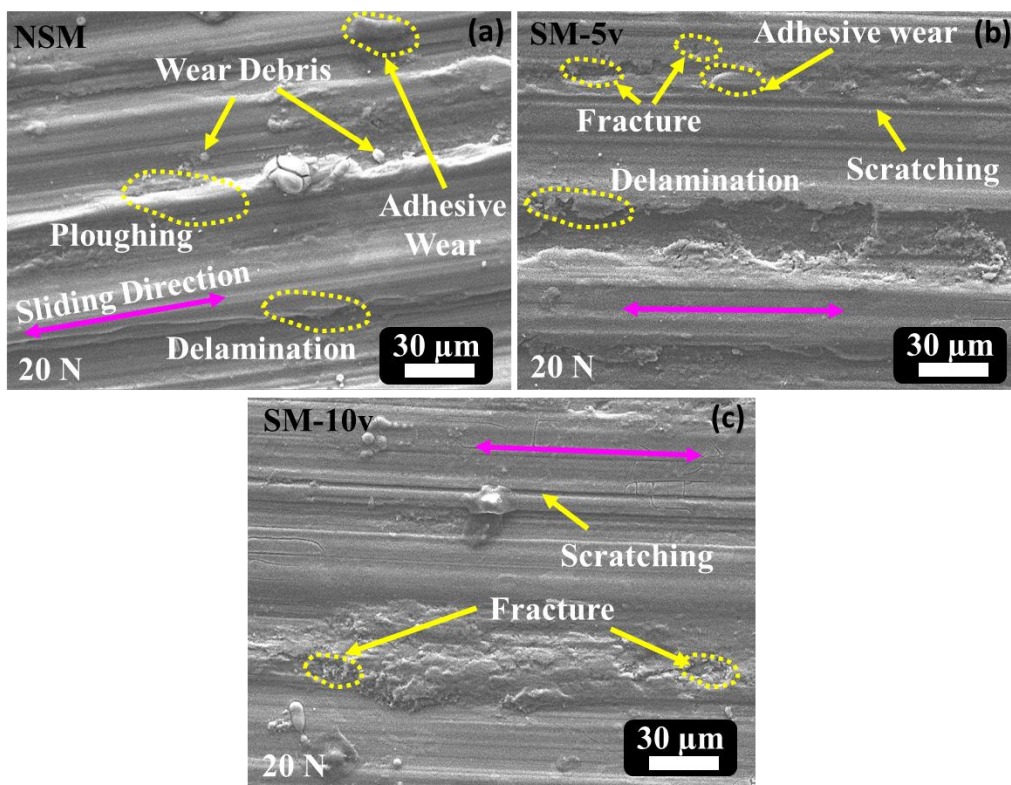
Figure 4.4.17: *Wear mechanisms for NSM, SM-5v, and SM-10v specimens under a 20 N load*

Among all tested specimens, SM-10v exhibits the most favourable wear-resistant characteristics. The wear track in Figure 4.4.17(c) shows minimal wear debris and a predominance of scratching and localised fracture, with significantly reduced delamination compared to NSM and SM-5v. The absence of significant ploughing or deep grooves suggests that the higher intensity SMAT (using higher velocity balls) leads to improved wear resistance, primarily due to the following factors:

1. *Increased surface hardness*: Higher hardness reduces the depth of penetration by the counter-body, instigating a lower material loss.

2. *Strain hardening and grain refinement*: The SMAT introduces a nanostructured surface layer (Figure 4.4.4(b)-(d)), which enhances the strength (and hence, load-bearing capacity) and mitigates severe plastic deformation during sliding, as supported by previous studies on SMATed alloys [78, 165, 166].

3. *Compressive residual stresses*: SMAT induces compressive residual stress [146] that counteracts crack propagation, reducing delamination and fracture-related wear [121].

The comparatively smooth wear track with minor fracture suggests that SMAT at 10 m/s ball velocity significantly enhances the alloy's ability to resist adhesive and abrasive wear mechanisms, making it a superior choice for applications requiring high wear resistance. The augmented wear resistance of SM-10v is consistent with the surface strengthening phenomena discussed in Section 4.4.2.2. The higher E for SM-10v (Figure 4.4.6) resulted in a more effective surface strengthening effect, which is directly linked to the enhanced wear resistance.

4.4.5 Microscratching Properties

4.4.5.1 Scratch Behaviour Under Constant Loading (50 N)

Figure 4.4.18 displays scratch morphology, pile-up characteristics, and deformation response of NSM, SM-5v, and SM-10v specimens during microscratching (5 mm scratch length) under a 50 N load. The width of the scratch is maximum for NSM and minimum for SM-10v. The NSM unveils the deepest scratch, accompanied by significant pile-up ridges on both sides of the groove (Figure 4.4.18(a1) and (a2)). The scratch depth measures ~45 μm, and the pile-up height and width are ~43 μm and ~27 μm, respectively. The NSM scratch track (Figure 4.4.18(a1)) displays severe plastic flow and ploughing, with noticeable shear lips at the groove edges, indicating extensive material displacement. This broad deformation zone suggests that NSM undergoes unrestricted plasticity due to its lower hardness (Figure 4.4.5) and yield strength (Figure 4.4.7).

In contrast, the SMATed specimens demonstrate reduced scratch depths and smaller pile-up. The SM-5v specimen (Figure 4.4.18(b1) and (b2)) shows a shallower scratch depth of ~38 μm and smaller pile-up dimensions of ~39 μm in height and ~19 μm in width. The SM-10v specimen (Figure 4.4.18(c1) and (c2)) exhibits the smallest scratch depth of ~35 μm and minimal pile-up of ~31 μm in height and ~14 μm in width. The shallower scratches and reduced pile-up formation in SMATed specimens suggest that strain-hardening and microstructure refinement contribute to confining deformation beneath the scratch. The SM-10v surface, in particular, indicates that the nanostructured surface layer effectively absorbs and distributes the applied load without excessive plastic upheaval.
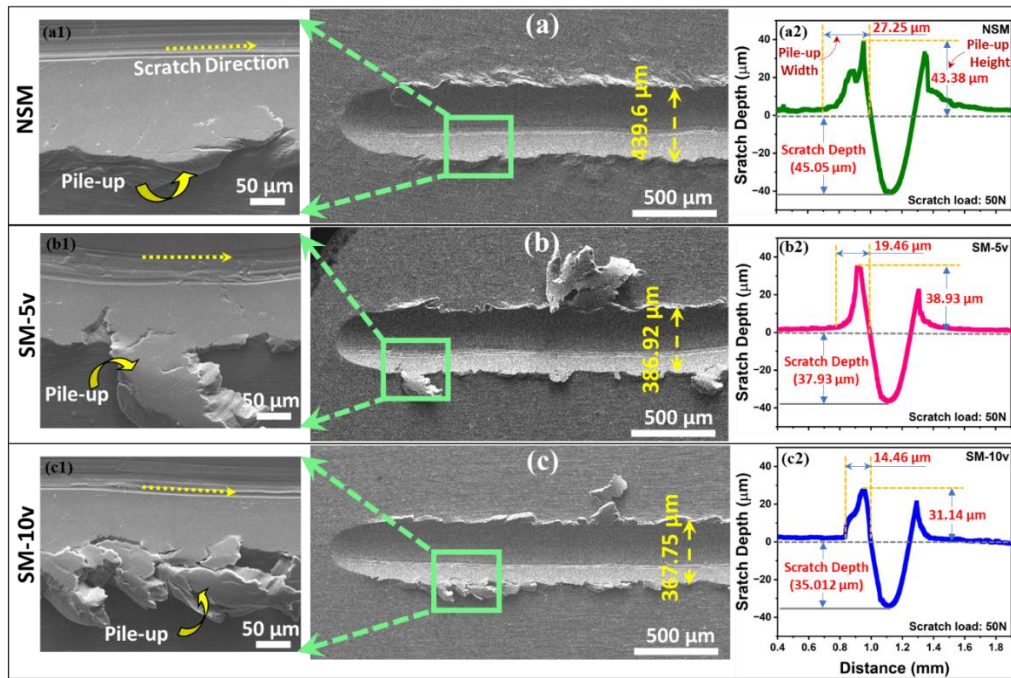
Figure 4.4.18: *SEM images and scratch depth profiles of (a) NSM, (b) SM-5v, and (c) SM-10v under a 50 N load*

The COF and scratch wear volume for the specimens under a 50 N load are shown in Figure 4.4.19. These results provide additional insight into the scratch response and material deformation behaviour, complementing the findings discussed in the previous section. The trend in the results observed in Figure 4.4.19 is similar to that observed in the tribological study using a pin-on-disc tribometer (Figures 4.4.12(d) and 4.4.15(a)).

An initial increase in COF with time in Figure 4.4.19(a), seen across all specimens, corresponds to the contact stabilisation phase, after which a steady-state

value is reached. Higher width and deeper scratch (Figure 4.4.18(a)) indicate greater contact area between the indenter and specimen surface, resulting in more resistance to scratching (i.e., more COF) on the NSM surface. The opposite behaviour is observed for the SMATed surfaces. Moreover, the lower pile-up formation in SM-5v and SM-10v (Figure 4.4.18(b) and (c)) reduces interfacial ploughing and adhesion, thereby minimising frictional resistance. The SM-10v specimen, with its highest hardness and lowest scratch width and depth, exhibits the smoothest (i.e., the most stable) interaction during scratching, resulting in the lowest COF among all conditions. The progressive reduction in wear volume from NSM to SM-5v to SM-10v (Figure 4.4.19(b)) further supports the effectiveness of SMAT in limiting material displacement during scratching, thereby improving scratch resistance and overall surface durability.
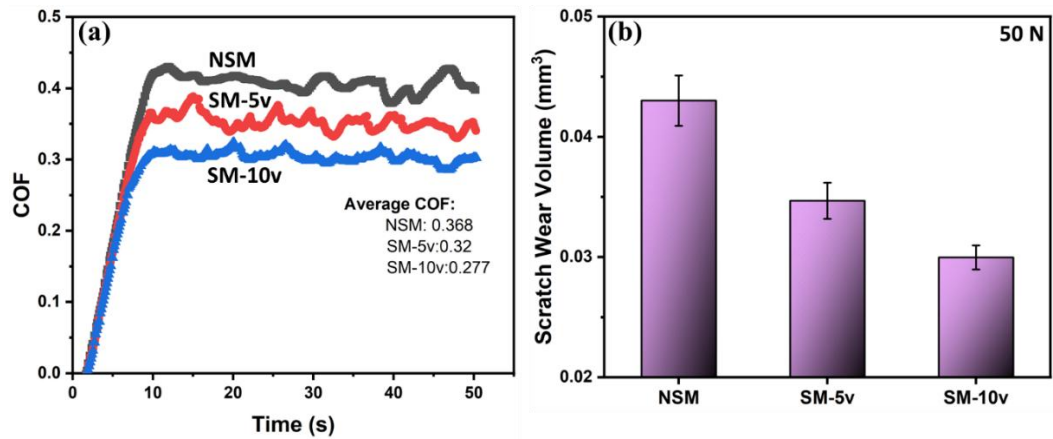
Figure 4.4.19: *(a) COF variation over time and (b) scratch wear volume for NSM, SM-5v, and SM-10v under a 50 N load*

4.4.5.2 Scratch Behaviour under Progressive Loading (20 N – 80 N)

Figure 4.4.20 presents the scratch morphology, COF evolution, and acoustic emission (AE) response of NSM, SM-5v, and SM-10v under a progressive load ramp (20 to 80 N). The progressive loading condition reveals how the specimen surface responds to increasing stress, highlighting the role of SMAT in stabilising deformation and minimising surface damage.

The SEM scratch profiles in Figure 4.4.20(a)–(c) illustrate distinct differences in deformation mechanisms between the non-SMATed and SMATed specimens. The width of the scratch increases with an increasing load for all specimens. Further, the wider scratch is noticed for NSM, followed by SM-5v and

then SM-10v. The NSM track (Figure 4.4.20(a)) exhibits extensive material pile-up, irregular surface features, and signs of severe plastic flow (close to the scratch edges), suggesting instabilities in material response as the load increases. This behaviour is consistent with the above findings, where NSM showed deeper grooves and higher material displacement (Figure 4.4.18(a)). In contrast, SMATed specimens (Figure 4.4.20(b) and (c)) display smoother scratch tracks, with significantly reduced pile-up and material upheaval, indicating a more controlled and stable deformation response under progressive loading. The progressive load condition further validates that SMAT enhances resistance to increasing mechanical stress, ensuring a smoother deformation profile compared to NSM.
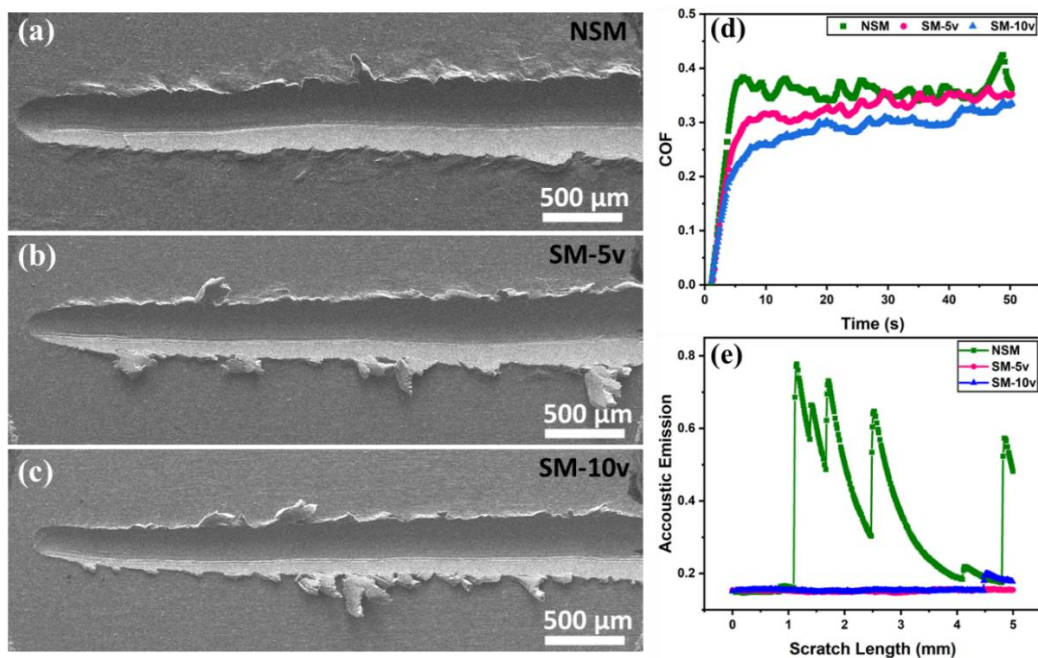
Figure 4.4.20: *(a-c) Scratch morphology, (d) COF, and (e) acoustic emission (AE) response for NSM, SM-5v, and SM-10v under a progressive load ramp (20 to 80 N)*

The COF evolution (Figure 4.4.20(d)) follows a trend similar to that observed under the constant load (Figure 4.4.19(a)), with NSM demonstrating the highest COF, followed by SM-5v and SM-10v. After the initial contact stabilisation phase, a steady-state zone with some fluctuations in COF is observed for all specimens (Figure 4.4.20(d)). Strikingly, the SMATed specimens maintain a more stable COF response than NSM, reflecting a reduced frictional resistance and a smoother contact interface. The lower COF values for SM-5v and SM-10v align with their less severe surface deformation, reinforcing the positive effect of microstructure refinement and increased hardness on reducing interfacial adhesion

146

and increasing ploughing resistance. Unlike NSM, the SMATed specimens show a slightly increasing COF trend after the initial contact stabilisation phase (Figure 4.4.20(d)). This behaviour could be linked to a gradual drop in hardness in the SMATed layer, due to which the indenter interacts with a relatively softer region with an increasing load.

The AE response (Figure 4.4.20(e)) provides further insight into the deformation mechanisms occurring during progressive loading. NSM exhibits multiple high-amplitude AE bursts, indicating instabilities in plastic deformation, localised material failure, and potential micro-fracture initiation [169, 170]. These abrupt energy releases correlate with the rougher scratch morphology observed in Figure 4.4.20(a), where severe pile-up and irregular surface features suggest that material flow is inconsistent and prone to sudden instability. Conversely, SMATed specimens show significantly reduced AE activity, with lower signal amplitudes and a more stable trend throughout the scratch length. This behaviour indicates that deformation in these specimens is more controlled, with fewer sudden failure events or material disruptions. The enhanced surface properties imparted by SMAT effectively suppress localised failure and allow a more uniform deformation under progressive loading.

Chapter 5: Conclusions and Future Scope

This research comprehensively investigates the role of SMAT in modifying the microstructure and enhancing the functional performance of Mg alloys, with a specific focus on AZ91D and Mg5Zn0.2Ca systems. The study begins by examining the evolution of gradient structures in AZ91D alloy under varying ball velocities, revealing critical insights into twin formation, grain refinement, and surface hardening mechanisms. Building upon this, the subsequent investigation explores the influence of SMAT parameters such as ball velocity and surface coverage on the microstructure, hardness gradient, and residual stress distribution of the Mg5Zn0.2Ca alloy. The third phase delves into the biodegradation behaviour and cytocompatibility of SMATed Mg5Zn0.2Ca surfaces, highlighting the improvements in corrosion resistance, ion release characteristics, and in vitro biological response. Finally, the study evaluates the tensile and tribological performance of the gradient-structured surfaces, establishing strong correlations between microstructural refinement, dislocation density, and enhanced load-bearing capability. This chapter outlines the key conclusions drawn from these findings and identifies potential directions for future research and application in structural and biomedical domains.

5.1 Major Findings

5.1.1 Evolution of Gradient Structure in Surface Mechanical Attrition Treated AZ91D Alloy: An Effect of Colliding Balls Velocity

This study dealt with the SMAT-induced severe plastic deformation of AZ91D magnesium alloy's surface. The specimens SMATed using ball velocities of ~3 m/s and ~10 m/s were investigated, maintaining the same percentage coverage (2000%). The velocity of the colliding balls during SMAT directly influenced the evolution of gradient microstructure and properties. The following are some critical concluding remarks:

1. The microstructural study confirmed the presence of dislocation cells, tangles, planer faults, and deformation twins in the SMATed layer. The SMATed specimens showed higher twin density near the surface, which was

reduced gradually with increasing depth from the surface. Twin density was higher in the specimen SMATed with higher ball velocity. The thinner twins (~180 nm thickness) were close to the SMATed surface, while coarser twins were present in deeper regions of the cross-section. High-velocity balls caused better grain refinement. The average grain size in the near-surface region of the specimen SMATed with higher ball velocity was ~32 nm. SMAT reduced the volume percentage of the β-phase in the surface region by ~28% and ~39% for the specimens SMATed with ~3 m/s and ~10 m/s ball velocities, respectively.

2. Ball velocity considerably affected the thickness and mechanical properties of the gradient layer. Attrition of AZ91D specimen surface with higher velocity balls helped form a considerably thicker layer (~3000 μm) with higher hardness (~2 GPa at the surface) within a shorter SMAT duration (~10 min). The nanohardness values in the surface of specimens SMATed with ~3 m/s and ~10 m/s ball velocities were increased by ~3.1 and ~2.6 times, respectively, compared to the non-SMATed specimen's hardness (~0.63 GPa). Different zones with varying trends in hardness and residual stress were formed in the SMATed layer.

3. The maximum residual stress of -281 ± 18 MPa was observed for the specimen SMATed with higher ball velocity at ~600 μm depth. However, the specimen SMATed with lower ball velocity reported -170 ± 8 MPa as the maximum residual stress at ~200 μm depth. These stresses were about 2.3-2.5 times the residual stresses at the SMATed surface.

4. In the nanomechanical study, the h_f/h_{max} ratio near the SMATed surface was ~0.72. However, this ratio in the non-SMATed region (i.e., core) was in the range of 0.82-0.85, indicating more elastic recovery of the material close to the SMATed surface than the core. Further, the highest creep rate was observed for the non-SMATed specimen (0.034 s^{-1}), followed by the specimen SMATed with lower ball velocity (0.029 s^{-1}) and then the specimen SMATed with higher ball velocity (0.026 s^{-1}).

5. The gradient microstructure caused by SMAT also influenced the rate-dependent behaviour of AZ91D alloy. The SRS of the non-SMATed alloy was in the range of 0.037-0.040. The SRS value in the near-surface region

(where the reduced grain size dominates) was ~0.018 for the specimen SMATed with lower ball velocity and ~0.027 for the specimen SMATed with higher ball velocity. It dropped suddenly (to ~0.01) when the distance from the SMATed surface increased to some extent (~200 μm), and subsequently, it increased with an increased distance in the SMATed layer (where twins played a dominating role).

6. By carefully controlling the SMAT parameters, it is possible to tailor the gradient in microstructure and properties to suit specific applications and requirements.

The summary of this study is shown in Figure 5.1.1.
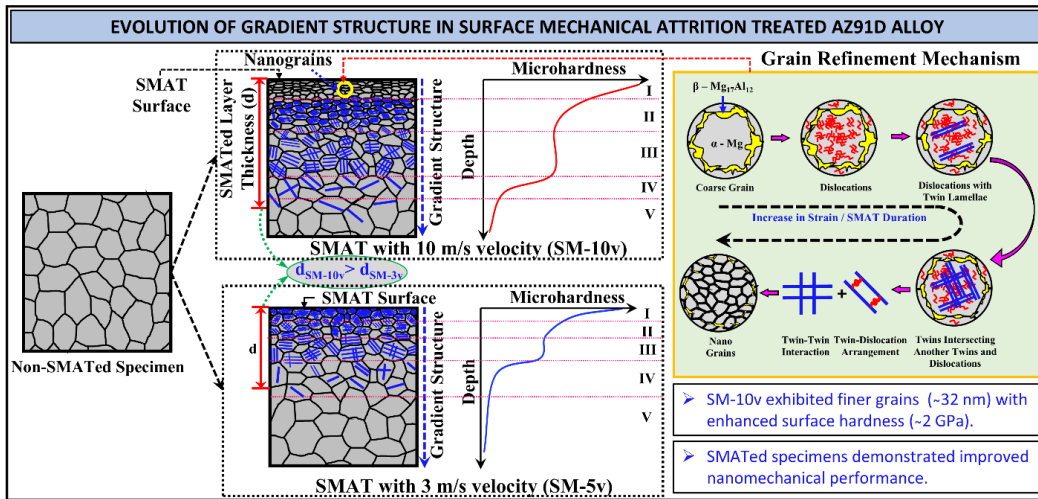
Figure 5.1.1: *Summary highlighting the influence of colliding ball velocity during the SMAT process on microstructural evolution and hardness variation in the AZ91D alloy*

5.1.2 Influence of Surface Mechanical Attrition Treatment Parameters on Microstructure and Residual Stress of Mg5Zn0.2Ca Alloy

This study investigated the impact of SMAT process parameters on the microstructure, microhardness, and residual stress of Mg5Zn0.2Ca alloy. Specimens SMATed with different ball velocities (~1, ~5, and ~10 m/s) and surface coverages (500, 100, and 2000%) were examined to comprehensively explore the relationships between the SMAT parameters and their influence on the final material properties. The following are some significant concluding remarks:

(i) SMAT formed a layer with a gradient in hardness, crystallite size, and twins. The microhardness increased with an increased colliding ball velocity and

surface coverage. Surface coverage was a more influencing parameter than the colliding ball velocity. The surface hardness value ranged between 68 $HV_{0.05}$ and 118 $HV_{0.05}$, higher than the hardness of non-SMATed specimens (~56 $HV_{0.05}$).

(ii) SMAT induced compressive residual stress in the alloy's surface layer. The highest compressive residual was observed at some distance from the SMATed surface. The compressive residual stress decreased as the distance increased from such depth towards the surface and core. High ball velocity (~10 m/s) and surface coverage (2000%) induced high compressive residual stress of about -175.5 MPa at ~600 µm depth. The residual surface stress was observed depending on the magnitude of maximum residual stress in the SMATed region and the depth at which maximum residual stress accumulated. Among the different ball velocities, the specimens SMATed with a ball velocity of ~5 m/s exhibited the highest compressive residual stress at the surface for all surface coverages. The maximum surface compressive residual stress of about -153.5 MPa was observed for the specimens SMATed at ~5 m/s ball velocity and 500% coverage.

(iii) The overall analysis revealed that the specimen treated at ~10 m/s ball velocity and 2000% surface coverage exhibited the most refined grain structure, finely and densely distributed twins, maximum SMAT-induced thickness (~3000 µm), highest surface hardness (~2.1 times the hardness of non-SMATed specimen), and highest compressive residual stress at a certain distance away from the surface.

The summary of this study is shown in Figure 5.1.2.
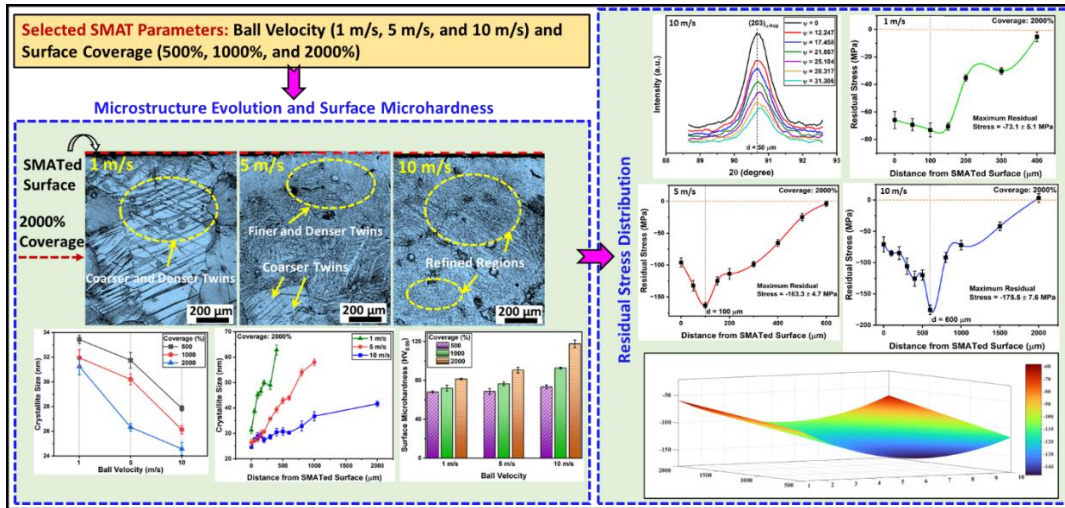
Figure 5.1.2: *Summary of influence of SMAT process parameters on microstructure and residual stress of Mg5Zn0.2Ca alloy*

5.1.3 The Effect of Severe Surface Deformation on Microstructure Refinement, Corrosion, and Biocompatibility of Mg5Zn0.2Ca Alloy

This study proposed SMAT, a novel severe surface plastic deformation technique that emphasised the role of ball velocity as a critical parameter. The Mg5Zn0.2Ca alloy's microstructure refinement (by SMAT) and its influence on the biocompatibility behaviour of the alloy were examined. The specimens were SMATed in this work with ~5 and ~10 m/s ball velocities. The investigation commanded the following significant conclusions:

1. SEM, EBSD, and TEM analysis revealed significant grain refinement in SMATed specimens, with higher ball velocity enabling the formation of the finest grain structure (grain size of ~21 nm). This behaviour was caused by the substantial strain and strain rate imposed by high-velocity colliding balls.

2. Microhardness measurement showed surface hardness values of 117 $HV_{0.5}$ for SA2, 91 $HV_{0.5}$ for SA2, and 55 $HV_{0.5}$ for NSA. The significant density of lattice defects and refined grains within the SMATed layer were the primary contributors to the improvement of microhardness.

3. Electrochemical and immersion tests performed in E-MEM + 10% FBS have indicated the highest corrosion resistance for the specimen SMATed using higher ball velocity, followed by the specimen treated using lower ball velocity, with the non-SMATed specimen exhibiting the least resistance. This

response was ascribed to the thicker and more stable protective layer formation on the SMATed specimens' surfaces, which was characterised by a higher concentration of phosphates and carbonates.

4. Cytotoxicity tests performed by the extract method using murine fibroblast L929 showed lower cytotoxicity (better relative plating efficiency) for the SMATed specimens with larger IC_{50}s (18.9% and 19.2% for the specimens treated with lower and higher ball velocities, respectively, which were higher than that of the non-SMATed one (8.4%)). The lower corrosion rate with reduced Mg^{2+} ion release and smaller pH increase were vital in enhancing cytocompatibility for SMATed specimens.

5. The solutions of bovine serum albumin (BSA, 20 μg/mL in artificial plasma) and bovine fibronectin (FN, 30 μg/mL in artificial plasma) were used for protein adsorption analysis. Enhanced FN adsorption on the specimens SMATed with lower ball velocity (0.913 μg/cm^2) and higher ball velocity (0.732 μg/cm^2) in protein adsorption tests further supported the improved biological performance of the SMATed specimens. SMAT-induced changes in surface energy and chemical reactivity could create more favourable conditions for FN adsorption.

6. These findings highlighted the SMAT process's potential to optimise the Mg alloys' properties for biodegradable implants.

The summary of this study is shown in Figure 5.1.3.
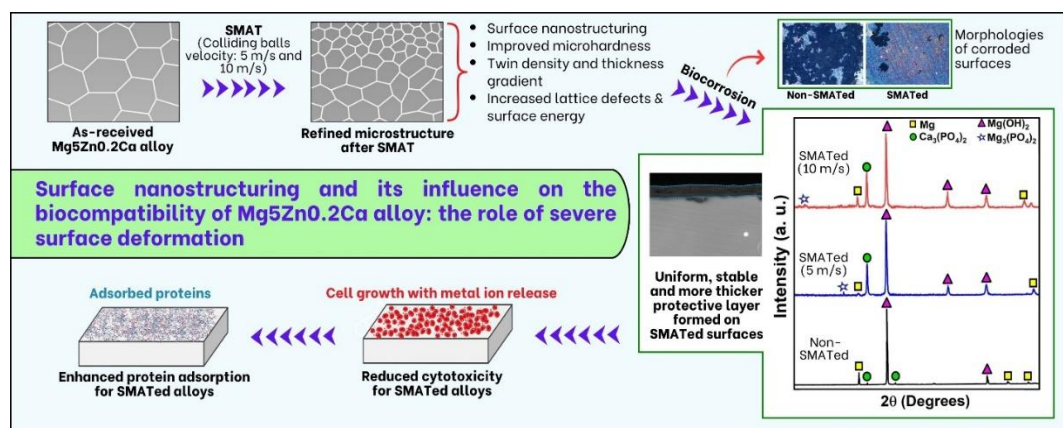
Figure 5.1.3: *Summary of the effect of microstructural modifications on the corrosion resistance and cytocompatibility of the Mg5Zn0.2Ca alloy*

5.1.4 Effect of Surface Strengthening on Tensile and Tribological Properties of Mg5Zn0.2CaAlloy: Role of Gradient Microstructure

This study comprehensively investigated the impact of SMAT on the microstructure, mechanical performance, and surface durability of the biodegradable Mg5Zn0.2Ca alloy. Two SMAT intensities were employed, using ball velocities of ~5 and ~10 m/s, to explore the correlation between treatment severity and resulting property enhancements. The following are some major concluding remarks:

(i) Microstructural analysis revealed that higher ball velocity induced finer surface grains and a substantially deeper gradient layer, along with higher surface hardness (117 ± 8.9 HV) and increased surface strengthening energy (~3.5 × 10^5 J/m^2), compared to the specimen SMATed with lower ball velocity and the non-treated specimen.

(ii) Tensile testing showed significant improvements in the mechanical strength of SMATed specimens, with higher ball velocity specimens achieving a yield strength of ~258 MPa and UTS of ~330 MPa that was significantly higher than that of non-SMATed specimens, though accompanied by a reduction in ductility.

(iii) Tribological evaluations demonstrated a marked decline in wear volume, specific wear rate (as low as 0.6 × 10^{-3} mm^3/Nm), and coefficient of friction with increasing SMAT intensity. Furthermore, scratch testing revealed that SMATed surfaces, particularly with higher velocity, displayed shallower scratch grooves, reduced material pile-up, and lower acoustic emissions (AE) under progressive loading, indicating enhanced resistance to localised deformation and improved surface stability.

(iv) These findings highlighted the potential of SMAT, especially at higher intensities, as an effective surface modification technique to enhance the functional and structural integrity of Mg5Zn0.2Ca alloys for advanced biomedical and load-bearing applications.

The summary of this study is shown in Figure 5.1.4.
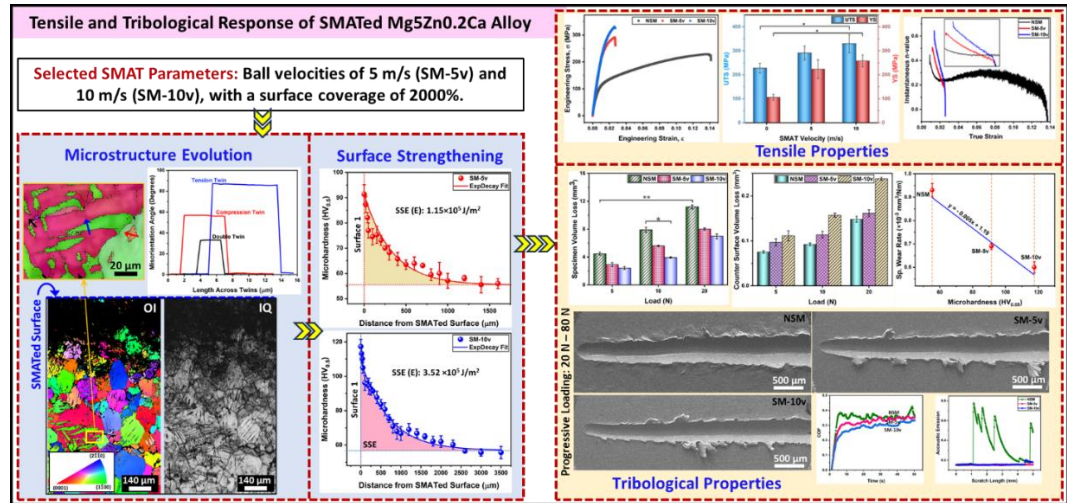
Figure 5.1.4: *Overview of the influence of microstructural refinement on the tensile and tribological performance of SMAT-treated Mg5Zn0.2Ca alloy*

5.2 Overall Summary: Key Findings of the Study

Overall, this research systematically demonstrated the effectiveness of SMAT in enhancing the structural, mechanical, and biological performance of magnesium alloys, specifically AZ91D and Mg5Zn0.2Ca systems. The following key insights were obtained:

- **Gradient Microstructure Development in AZ91D:** The study established that increasing ball velocity during SMAT leads to enhanced twin density, finer surface grains (~32 nm), and a significant reduction in β-phase volume near the surface. The highest hardness (~2 GPa) and thickest gradient layer (~3000 μm) were achieved at higher ball velocities (~10 m/s).

- **Residual Stress and Microstructure in Mg5Zn0.2Ca Alloy:** The SMAT parameters like ball velocity and surface coverage had a pronounced impact on surface integrity. The optimal condition (10 m/s, 2000% coverage) resulted in the finest grain structure, the highest compressive residual stress (−175.5 MPa), and maximum hardness enhancement.

- **Corrosion and Biocompatibility:** SMAT-treated Mg5Zn0.2Ca exhibited significant grain refinement (down to ~21 nm), directly correlated with improved corrosion resistance and lower Mg^{2+} ion release. Cytotoxicity assays revealed better cell viability for SMATed samples, and enhanced fibronectin adsorption indicated improved biological affinity for implant applications.

- **Tensile and Tribological Properties:** The gradient microstructure induced by SMAT led to a marked improvement in tensile strength (YS ~258 MPa, UTS ~330 MPa) and a notable reduction in wear volume and scratch-induced damage. High-velocity SMAT specimens displayed superior resistance to plastic deformation, improved acoustic response under loading, and increased surface strengthening energy.

- Overall, although previous studies have recognized the promise of SMAT for magnesium alloys, systematic investigations into how SMAT velocity (intensity) influences both mechanical and biomedical properties remain extremely limited. This thesis addresses that gap by establishing clear correlations between SMAT parameters, microstructural gradients, and multifunctional performance, representing an important and novel contribution to the field.

Collectively, the findings confirm that optimising SMAT parameters offers a powerful route for tailoring the surface and bulk properties of magnesium alloys, enabling their advanced use in structural and biomedical sectors.

5.3 Future Scope

Building on the insights gained through this work, several future research directions are proposed:

1. **Long-Term In Vivo Biocompatibility:** While the in vitro biocompatibility of SMATed Mg5Zn0.2Ca alloy has been demonstrated, extended in vivo studies are essential to evaluate degradation kinetics, tissue response, and systemic effects in physiological environments.

2. **SMAT Process Optimisation via Simulation:** Incorporating advanced computational techniques such as crystal plasticity finite element modelling (CPFEM) or discrete element methods (DEM) can help simulate ball-material interactions and predict microstructure evolution under varying SMAT conditions.

3. **Integration with Coatings:** The synergistic effect of SMAT, followed by biocompatible or corrosion-resistant coatings (e.g., hydroxyapatite,

polymeric, or ceramic layers), can be explored to enhance further the surface performance for clinical applications.

4. **Thermomechanical Stability:** Investigating the thermal stability and ageing behaviour of SMAT-induced nanostructures can provide insight into the material's reliability under prolonged mechanical or environmental exposure.

5. **Scaling and Industrial Adaptation:** Developing SMAT techniques adaptable to complex geometries and scaling for industrial-grade components, especially for orthopaedic implants or lightweight structural parts, remains a critical step toward real-world implementation.

6. **Extrapolation to Other Alloys:** The methodology and findings from this work can be extended to other magnesium-based or lightweight alloys (e.g., titanium, aluminium) to achieve similar surface strengthening and functional improvements. Future studies should consider alloy-specific deformation mechanisms and phase stability while tailoring SMAT parameters for broader industrial and biomedical applications.

These future directions will further elevate the understanding and application potential of SMATed Mg alloys across biomedical, aerospace, and automotive industries.

References:

1.   Easton MA, Qian M, Prasad A, StJohn DH (2016) Recent advances in grain refinement of light metals and alloys. Curr Opin Solid State Mater Sci 20:13–24

2.   Zhenquan Yang, Aibin Ma, Huan Liu, Dan Song, Yuna Wu, Yuchun Yuan, Jinghua Jiang, Jiapeng Sun (2019) Managing strength and ductility in AZ91 magnesium alloy through ECAP combined with prior and post aging treatment. Material Characterization 152:213–222

3.   Zhao X, Liu K, Xu D, Liu Y, Hu C (2020) Effects of ultrasonic surface rolling processing and subsequent recovery treatment on the wear resistance of az91d mg alloy. Materials 13:1–16

4.   Luo AA, Mishra RK, Powell BR, Sachdev AK (2012) Magnesium alloy development for automotive applications. In: Materials Science Forum. Trans Tech Publications Ltd, pp 69–82

5.   Durán KS, Hernández N, Rueda LM, Hernández-Barrios CA, Coy AE, Viejo F (2021) Design of multilayer hybrid sol-gel coatings with bifunctional barrier-bioactive response on the Elektron 21 magnesium alloy for biomedical applications. Journal of Magnesium and Alloys 9:2097–2112

6.   Rashi R, Lee SY, Singh SS, Chiu YL, Jones IP, Jain J (2025) Friction and wear maps of Mg-Er alloys with varying Er content. Tribol Int. https://doi.org/10.1016/j.triboint.2024.110337

7.   Kuah KX, Blackwood DJ, Ong WK, Salehi M, Seet HL, Nai MLS, Wijesinghe S (2021) Analysis of the corrosion performance of binder jet additive manufactured magnesium alloys for biomedical applications. Journal of Magnesium and Alloys. https://doi.org/10.1016/j.jma.2021.11.016

8.   Gerhátová Ž, Paták J, Babincová P, Hudáková M, Palcut M (2024) Analysis of Biocompatible Metallic Materials used in Medicine. J Phys Conf Ser 2712:012006

9.   Witecka A, Yamamoto A, Dybiec H, Swieszkowski W (2012) Surface characterization and cytocompatibility evaluation of silanized magnesium alloy AZ91 for biomedical applications. Sci Technol Adv Mater. https://doi.org/10.1088/1468-6996/13/6/064214

10.   Hong K, Park H, Kim Y, Knapek M, Minárik P, Máthis K, Yamamoto A, Choe H (2019) Mechanical and biocorrosive properties of magnesium-aluminum alloy scaffold for biomedical applications. J Mech Behav Biomed Mater 98:213–224

11. Peruzzi N, Galli S, Helmholz H, et al (2021) Multimodal ex vivo methods reveal that Gd-rich corrosion byproducts remain at the implant site of biodegradable Mg-Gd screws. Acta Biomater 136:582–591

12. Baigonakova G, Marchenko E, Zhukov I, Vorozhtsov A (2023) Structure, cytocompatibility and biodegradation of nanocrystalline coated Mg–Ca–Zn alloys. Vacuum. https://doi.org/10.1016/j.vacuum.2022.111630

13. Bagherifard S, Hickey DJ, Fintová S, Pastorek F, Fernandez-Pariente I, Bandini M, Webster TJ, Guagliano M (2018) Effects of nanofeatures induced by severe shot peening (SSP) on mechanical, corrosion and cytocompatibility properties of magnesium alloy AZ31. Acta Biomater 66:93–108

14. Prithivirajan S, Nyahale MB, Naik GM, Narendranath S, Prabhu A, Rekha PD (2021) Bio-corrosion impacts on mechanical integrity of ZM21 Mg for orthopaedic implant application processed by equal channel angular pressing. J Mater Sci Mater Med. https://doi.org/10.1007/s10856-021-06535-5

15. Amanov A, Penkov O V., Pyun YS, Kim DE (2012) Effects of ultrasonic nanocrystalline surface modification on the tribological properties of AZ91D magnesium alloy. Tribol Int 54:106–113

16. Zhang J, Ou XB (2010) Thermal stability of nanocrystalline in surface layer of magnesium alloy AZ91D. Transactions of Nonferrous Metals Society of China (English Edition) 20:1340–1344

17. Vaira Vignesh R, Padmanaban R, Govindaraju M (2019) Investigations on the surface topography, corrosion behavior, and biocompatibility of friction stir processed magnesium alloy AZ91D. Surf Topogr. https://doi.org/10.1088/2051-672X/ab269c

18. Ren XD, Huang JJ, Zhou WF, Xu SD, Liu FF (2015) Surface nano-crystallization of AZ91D magnesium alloy induced by laser shock processing. Mater Des 86:421–426

19. Kumbhar NK, Joshi MD, Kumar V, Hosmani SS (2023) An Impact of the Recent Developments in Coating Materials and Techniques on the Corrosion Response of AZ91D Alloy: A Review. Adv Eng Mater 2201680

20. Zhang T, Wang W, Liu J, Wang L, Tang Y, Wang K (2022) A review on magnesium alloys for biomedical applications. Front Bioeng Biotechnol. https://doi.org/10.3389/fbioe.2022.953344

21. Tsakiris V, Tardei C, Clicinschi FM (2021) Biodegradable Mg alloys for orthopedic implants – A review. Journal of Magnesium and Alloys 9:1884–1905

22. Bandyopadhyay A, Mitra I, Goodman SB, Kumar M, Bose S (2023) Improving biocompatibility for next generation of metallic implants. Prog Mater Sci 133:101053

23. Sun Y, Zhang B, Wang Y, Geng L, Jiao X (2012) Preparation and characterization of a new biomedical Mg-Zn-Ca alloy. Mater Des 34:58–64

24. Nandy S, Tsai SP, Stephenson L, Raabe D, Zaefferer S (2021) The role of Ca, Al and Zn on room temperature ductility and grain boundary cohesion of magnesium. Journal of Magnesium and Alloys 9:1521–1536

25. Makkar P, Sarkar SK, Padalhin AR, Moon BG, Lee YS, Lee BT (2018) In vitro and in vivo assessment of biomedical Mg–Ca alloys for bone implant applications. J Appl Biomater Funct Mater 16:126–136

26. Nanda IP, Hassim MH, Idris MH, Jahare MH, Abdulmalik SS, Arafat A (2019) Mechanical and degradation properties of zinc adopted magnesium alloys for biomedical application. IOP Conf Ser Mater Sci Eng. https://doi.org/10.1088/1757-899X/602/1/012094

27. Witecka A, Bogucka A, Yamamoto A, Máthis K, Krajňák T, Jaroszewicz J, Święszkowski W (2016) In vitro degradation of ZM21 magnesium alloy in simulated body fluids. Materials Science and Engineering C 65:59–69

28. Laleh M, Kargar F (2011) Effect of surface nanocrystallization on the microstructural and corrosion characteristics of AZ91D magnesium alloy. J Alloys Compd 509:9150–9156

29. Zeller-Plumhoff B, Robisch A-L, Pelliccia D, et al (2020) Nanotomographic evaluation of precipitate structure evolution in a Mg–Zn–Zr alloy during plastic deformation. Sci Rep 10:16101

30. Birbilis N, Ralston KD, Virtanen S, Fraser HL, Davies CHJ (2010) Grain character influences on corrosion of ECAPed pure magnesium. Corrosion Engineering Science and Technology 45:224–230

31. Huang R, Suo W, Wang Y, Pan Y, Ren G, Hu H, Huang L (2024) Enhancing wear resistance, anti-corrosion property and surface bioactivity of a beta-titanium alloy by adopting surface mechanical attrition treatment followed by phosphorus ion implantation. Appl Surf Sci 671:160766

32. Li L, Zhang Z, Zhang D, Qi F, Dai Y, Wei W, Ouyang X (2024) Effects of metal ion implantation (Fe, Ti, Zn and Zr) on mechanical properties, corrosion resistance and biocompatibility of WE43 Mg alloy. Journal of Magnesium and Alloys. https://doi.org/10.1016/j.jma.2024.05.005

33. Wang X, Liu X, Dai Y, She J, Zhang D, Qi F, Wei W, Ouyang X (2023) A novel Ca-Mg-P/PDA composite coating of Mg alloys to improve corrosion resistance for orthopedic implant materials. Surf Coat Technol 471:129920

34.   Gatey AM, Hosmani SS, Arya SB, Figueroa CA, Singh RP (2016) Plasma nitriding of AISI 2205 steel: Effects of surface mechanical attrition treatment and chemical etching. Surface Engineering 32:61–68

35.   Karademir I, Celik MB, Husem F, Maleki E, Amanov A, Unal O (2021) Effects of constrained groove pressing, severe shot peening and ultrasonic nanocrystal surface modification on microstructure and mechanical behavior of S500MC high strength low alloy automotive steel. Appl Surf Sci 538:147935

36.   Efe Y, Karademir I, Husem F, Maleki E, Karimbaev R, Amanov A, Unal O (2020) Enhancement in microstructural and mechanical performance of AA7075 aluminum alloy via severe shot peening and ultrasonic nanocrystal surface modification. Appl Surf Sci 528:146922

37.   Ghali E (2011) Activity and passivity of magnesium (Mg) and its alloys. In: Corrosion of Magnesium Alloys. Elsevier Inc., pp 66–114

38.   Jablonská E, Kubásek J, Vojtěch D, Ruml T, Lipov J (2021) Test conditions can significantly affect the results of in vitro cytotoxicity testing of degradable metallic biomaterials. Sci Rep. https://doi.org/10.1038/s41598-021-85019-6

39.   Peng J, Zhang Z, Guo P, Liu Z, Li Y, Zhou W, Wu Y (2019) The effect of surface mechanical attrition treatment on texture evolution and mechanical properties of AZ31 magnesium alloy. Mater Charact 148:26–34

40.   Singh D, Basha DA, Wadsö L, Orlov D, Matsushita Y, Singh A, Hosmani SS (2021) Evolution of gradient structured layer on AZ91D magnesium alloy and its corrosion behaviour. J Alloys Compd. https://doi.org/10.1016/j.jallcom.2021.160659

41.   Peral LB, Zafra A, Bagherifard S, Guagliano M, Fernández-Pariente I (2020) Effect of warm shot peening treatments on surface properties and corrosion behavior of AZ31 magnesium alloy. Surf Coat Technol. https://doi.org/10.1016/j.surfcoat.2020.126285

42.   Lyon P, Syed I, Heaney S (2007) Elektron 21 - An aerospace magnesium alloy for sand cast and investment cast applications. Adv Eng Mater 9:793–798

43.   Barati Darband G, Aliofkhazraei M, Hamghalam P, Valizade N (2017) Plasma electrolytic oxidation of magnesium and its alloys: Mechanism, properties and applications. Journal of Magnesium and Alloys 5:74–132

44.   Moosbrugger C (2017) Engineering Properties of Magnesium Alloys.

45.   Neil WC, Forsyth M, Howlett PC, Hutchinson CR, Hinton BRW (2009) Corrosion of magnesium alloy ZE41 - The role of microstructural features. Corros Sci 51:387–394

46. Aghion E, Bronfin B (2000) Magnesium Alloys Development towards the 21st Century. Materials Science Forum 350–351:19–30

47. Jayasathyakawin S, Ravichandran M, Baskar N, Chairman CA, Balasundaram R (2020) Mechanical properties and applications of Magnesium alloy – Review. In: Mater Today Proc. Elsevier Ltd, pp 909–913

48. Pekguleryuz M, Celikin M (2010) Creep resistance in magnesium alloys. International Materials Reviews 55:197–217

49. Ambat R, Aung NN, Zhou W (2000) Evaluation of microstructural effects on corrosion behaviour of AZ91D magnesium alloy. Corros Sci 42:1433–1455

50. Wang RM, Eliezer A, Gutman EM (2003) An investigation on the microstructure of an AM50 magnesium alloy. Materials Science and Engineering A 355:201–207

51. McLean AA, Powell GLF, Brown IH, Linton VM (2003) Friction stir welding of magnesium alloy AZ31B to aluminium alloy 5083. Science and Technology of Welding and Joining 8:462–464

52. Styczynski A, Hartig C, Bohlen J, Letzig D (2004) Cold rolling textures in AZ31 wrought magnesium alloy. Scr Mater 50:943–947

53. Wang CY, Wang XJ, Chang H, Wu K, Zheng MY (2007) Processing maps for hot working of ZK60 magnesium alloy. Materials Science and Engineering A 464:52–58

54. Liu W, Cao F, Chang L, Zhang Z, Zhang J (2009) Effect of rare earth element Ce and La on corrosion behavior of AM60 magnesium alloy. Corros Sci 51:1334–1343

55. Song GL (2009) Effect of tin modification on corrosion of AM70 magnesium alloy. Corros Sci 51:2063–2070

56. Lamaka S v., Knörnschild G, Snihirova D v., Taryba MG, Zheludkevich ML, Ferreira MGS (2009) Complex anticorrosion coating for ZK30 magnesium alloy. Electrochim Acta 55:131–141

57. Witte F, Fischer J, Nellesen J, Vogt C, Vogt J, Donath T, Beckmann F (2010) In vivo corrosion and corrosion protection of magnesium alloy LAE442. Acta Biomater 6:1792–1799

58. Gu XN, Zheng YF (2010) A review on magnesium alloys as biodegradable materials. Front Mater Sci China 4:111–115

59. Hamdy Makhlouf AS, Gajarla Y (2019) Advances in smart coatings for magnesium alloys and their applications in industry. In: Advances in Smart

Coatings and Thin Films for Future Industrial and Biomedical Engineering Applications. Elsevier, pp 245–261

60. Qin FX, Ji C, Dan ZH, Xie GQ, Wang H, Yamaura SI, Niinomi M, Li Y De (2016) Corrosion behavior of MgZnCa bulk amorphous alloys fabricated by spark plasma sintering. Acta Metallurgica Sinica (English Letters) 29:793–799

61. Walker J, Shadanbaz S, Kirkland NT, Stace E, Woodfield T, Staiger MP, Dias GJ (2012) Magnesium alloys: Predicting in vivo corrosion with in vitro immersion testing. J Biomed Mater Res B Appl Biomater 100 B:1134–1141

62. Ramalingam VV, Ramasamy P, Kovukkal M Das, Myilsamy G (2020) Research and Development in Magnesium Alloys for Industrial and Biomedical Applications: A Review. Metals and Materials International 26:409–430

63. Zander D, Zumdick NA (2015) Influence of Ca and Zn on the microstructure and corrosion of biodegradable Mg-Ca-Zn alloys. Corros Sci 93:222–233

64. Martynenko N, Anisimova N, Kiselevskiy M, et al (2020) Structure, mechanical characteristics, biodegradation, and in vitro cytotoxicity of magnesium alloy ZX11 processed by rotary swaging. Journal of Magnesium and Alloys 8:1038–1046

65. Gu X, Wang F, Xie X, Zheng M, Li P, Zheng Y, Qin L, Fan Y (2018) In vitro and in vivo studies on as-extruded Mg- 5.25wt.%Zn-0.6wt.%Ca alloy as biodegradable metal. Sci China Mater 61:619–628

66. Meng J, Zhang Y, Yu X, Jiao J, Tan L, Yu B (2024) In vivo biodegradation and biological properties of a Mg-Zn-Ca amorphous alloy for bone defect repair. Materials Technology. https://doi.org/10.1080/10667857.2024.2307846

67. HOU L feng, WEI Y hui, LIU B sheng, XU B she (2008) Microstructure evolution of AZ91D induced by high energy shot peening. Transactions of Nonferrous Metals Society of China (English Edition) 18:1053–1057

68. Wang H-T, Yao H-L, Zhang M-X, Bai X-B, Yi Z-H, Chen Q-Y, Ji G-C (2019) Surface nanocrystallization treatment of AZ91D magnesium alloy by cold spraying shot peening process. Surf Coat Technol 374:485–492

69. Praveen TR, Shivananda Nayaka H, Swaroop S, Gopi KR (2020) Strength enhancement of magnesium alloy through equal channel angular pressing and laser shock peening. Appl Surf Sci. https://doi.org/10.1016/j.apsusc.2020.145755

70. Tao NR, Wang ZB, Tong WP, Sui ML, Lu J, Lu K (2002) An investigation of surface nanocrystallization mechanism in Fe induced by surface mechanical attrition treatment.

71. Sun HQ, Shi YN, Zhang MX, Lu K (2008) Surface alloying of an Mg alloy subjected to surface mechanical attrition treatment. Surf Coat Technol 202:3947–3953

72. Yin K, Cao L, Wang N (2019) Mechanical properties and residual stresses of 5083 to AM60B dissimilar friction stir welding with different process parameters. J Adhes Sci Technol 33:2615–2629

73. Ke LU, Jian LU (1999) Surface Nanocrystallization (SNC) of Metallic Materials-Presentation of the Concept behind a New Approach. J Mater Sci Technol 15:193–197

74. Mansoor P, Dasharath SM (2020) A review paper on magnesium alloy fabricated by severe plastic deformation technology and its effects over microstructural and mechanical properties. In: Mater Today Proc. Elsevier Ltd, pp 356–364

75. Bočan J, Maňák J, Jäger A (2015) Nanomechanical analysis of AZ31 magnesium alloy and pure magnesium correlated with crystallographic orientation. Materials Science and Engineering A 644:121–128

76. Wang F, Agnew SR (2016) Dislocation transmutation by tension twinning in magnesium alloy AZ31. Int J Plast 81:63–86

77. Guo T, Siska F, Barnett MR (2016) Distinguishing between slip and twinning events during nanoindentation of magnesium alloy AZ31. Scr Mater 110:10–13

78. Mao B, Siddaiah A, Zhang X, Li B, Menezes PL, Liao Y (2019) The influence of surface pre-twinning on the friction and wear performance of an AZ31B Mg alloy. Appl Surf Sci 480:998–1007

79. Shi XY, Liu Y, Li DJ, Chen B, Zeng XQ, Lu J, Ding WJ (2015) Microstructure evolution and mechanical properties of an Mg-Gd alloy subjected to surface mechanical attrition treatment. Materials Science and Engineering A 630:146–154

80. Chen G, Gao J, Cui Y, Gao H, Guo X, Wu S (2018) Effects of strain rate on the low cycle fatigue behavior of AZ31B magnesium alloy processed by SMAT. J Alloys Compd 735:536–546

81. Naik SN, Walley SM (2020) The Hall–Petch and inverse Hall–Petch relations and the hardness of nanocrystalline metals. J Mater Sci 55:2661–2681

82. Wei Y hui, Liu B sheng, Hou L feng, Xu B she, Liu G (2008) Characterization and properties of nanocrystalline surface layer in Mg alloy induced by surface mechanical attrition treatment. J Alloys Compd 452:336–342

83. Jiang P, Blawert C, Hou R, Bohlen J, Konchakova N, Zheludkevich ML (2020) A comprehensive comparison of the corrosion performance, fatigue behavior and mechanical properties of micro-alloyed MgZnCa and MgZnGe alloys. Mater Des. https://doi.org/10.1016/j.matdes.2019.108285

84. Chang C, Yue S, Li W, Lu L, Yan X (2022) Study on microstructure and tribological behavior of the selective laser melted MgZnCa alloy. Mater Lett. https://doi.org/10.1016/j.matlet.2021.131439

85. Chen L, Guo C, Blawert C, Yang J, Chen D, Wang X, Yu Z, Zheludkevich ML, Li W (2021) Evaluation of the biodegradation product layer on Mg-1Zn alloy during dynamical strain. Journal of Magnesium and Alloys 9:1820–1833

86. Kai Soon F (2018) HIGH TOUGHNESS MAGNESIUM ALLOY THROUGH SEVERE PLASTIC DEFORMATION AND SHORT ANNEALING.

87. Hayashi M, Yamamoto A, Aizawa T, Yusa Y, Shimizu Y, Imai Y (2024) In vitro analysis of insoluble salt formation mechanism associated with Mg corrosion—variations depending on the diffusion environment in model tissue. Biomedical Materials (Bristol). https://doi.org/10.1088/1748-605X/ad1d7f

88. Školáková A, Lovaši T, Pinc J, Kačenka Z, Rieszová L, Žofková Z (2020) The Effect of Zinc and Calcium Addition on Magnesium Alloy. Manufacturing Technology 20:668–676

89. Fatehi Mollayousef M, Malekan M, Bahmani A, Lotfpour M (2024) Influence of sample orientation on cytocompatibility of pure magnesium. Mater Chem Phys. https://doi.org/10.1016/j.matchemphys.2024.129247

90. Lopes DR, Silva CLP, Soares RB, Pereira PHR, Oliveira AC, Figueiredo RB, Langdon TG, Lins VFC (2019) Cytotoxicity and Corrosion Behavior of Magnesium and Magnesium Alloys in Hank's Solution after Processing by High-Pressure Torsion. Adv Eng Mater. https://doi.org/10.1002/adem.201900391

91. Silva CLP, Oliveira AC, Costa CGF, Figueiredo RB, de Fátima Leite M, Pereira MM, Lins VFC, Langdon TG (2017) Effect of severe plastic deformation on the biocompatibility and corrosion rate of pure magnesium. J Mater Sci 52:5992–6003

92. Sudha P, Tun KS, Pillai J, Dutta M, Gupta M, Kumar VS (2024) Biocorrosion and Cytotoxicity Studies on Biodegradable Mg-Based Multicomponent Alloys. Bioengineering. https://doi.org/10.3390/bioengineering11060621

93. Li Y, Lu X, Mei D, Zhang T, Wang F (2022) Passivation of corrosion product layer on AM50 Mg by corrosion inhibitor. Journal of Magnesium and Alloys 10:2563–2573

94. Anisimova N, Martynenko N, Novruzov K, et al (2022) Modification of Biocorrosion and Cellular Response of Magnesium Alloy WE43 by Multiaxial Deformation. Metals (Basel). https://doi.org/10.3390/met12010105

95. Kumar V, Pruncu CI, Wang Y, Figueroa CA, Singh I, Hosmani SS (2023) The role of microstructure modifications on electrochemical and plasma-nitriding behaviour of 316L steel produced by laser powder bed fusion. Philosophical Magazine 103:1855–1896

96. Oliver WC, Pharr GM (1992) An improved technique for determining hardness and elastic modulus using load and displacement sensing indentation experiments.

97. Thornby J, Verma D, Cochrane R, Westwood A, Manakari VB, Gupta M, Haghshenas M (2019) Indentation-based characterization of creep and hardness behavior of magnesium carbon nanotube nanocomposites at room temperature. SN Appl Sci. https://doi.org/10.1007/s42452-019-0696-9

98. Rifai M, Mujamilah, Miyamoto H (2022) NanoIndentation Behaviour on Magnesium Alloy Subjected by Equal Channel Angular Pressing. AIP Conf Proc. https://doi.org/10.1063/5.0095496

99. Somekawa H, Schuh CA (2013) Nanoindentation behavior and deformed microstructures in coarse-grained magnesium alloys. Scr Mater 68:416–419

100. Muhammad M, Masoomi M, Torries B, Shamsaei N, Haghshenas M (2018) Depth-sensing time-dependent response of additively manufactured Ti-6Al-4V alloy. Addit Manuf 24:37–46

101. Ahmadian H, SallakhNiknezhad R (2021) The Effect of Shot Peening Duration on Corrosion Properties of Magnesium Alloy AZ91 in 3.5% NaCl Solution. Journal of The Institution of Engineers (India): Series D 102:195–202

102. Duan M, Luo L, Liu Y (2020) Microstructural evolution of AZ31 Mg alloy with surface mechanical attrition treatment: Grain and texture gradient. J Alloys Compd. https://doi.org/10.1016/j.jallcom.2020.153691

103. Liu C, Chen X, Hu Y, Zhang W, Zhang Y, Li J, Pan F (2022) Microstructure and mechanical properties of gradient ultrafine-grained Mg-Gd-Zr alloy. Journal of Materials Research and Technology 21:3896–3908

104. Ould Mohamed O, Azzeddine H, Huang Y, Baudin T, Bazarnik P, Brisset F, Kawasaki M, Langdon TG (2023) Investigation of Microstructure and Texture Evolution in an AZ31/Mg–Gd Alloy Hybrid Metal Fabricated by High-Pressure Torsion. Adv Eng Mater 2201794

105. Li L, Liu W, Qi F, Wu D, Zhang Z (2022) Effects of deformation twins on microstructure evolution, mechanical properties and corrosion behaviors in magnesium alloys - A review. Journal of Magnesium and Alloys 10:2334–2353

106. Xu Y, Meng D, Jing L, Cheng Y, Jia J, Li W (2023) Grain Refinement, Texture Evolution, and Tensile Performance Improvement of AZ91D Magnesium Alloy Processed by Multi-Cycle Accumulative Back Extrusion. Adv Eng Mater. https://doi.org/10.1002/adem.202201084

107. Liu H, Zhu W, Jiang C, Guagliano M, Xing S, Wang L, Ji V, Zhan K (2020) Microstructure evolution and residual stress distribution of nanostructured Mg-8Gd-3Y alloy induced by severe shot peening. Surf Coat Technol. https://doi.org/10.1016/j.surfcoat.2020.126465

108. Eivani AR, Vafaeenezhad H, Jafarian HR, Zhou J (2021) A novel approach to determine residual stress field during FSW of AZ91 Mg alloy using combined smoothed particle hydrodynamics/neuro-fuzzy computations and ultrasonic testing. Journal of Magnesium and Alloys 9:1304–1328

109. Meng X, Duan M, Luo L, Zhan D, Jin B, Jin Y, Rao X xin, Liu Y, Lu J (2017) The deformation behavior of AZ31 Mg alloy with surface mechanical attrition treatment. Materials Science and Engineering A 707:636–646

110. Hu J, Zhang W, Peng G, Zhang T, Zhang Y (2018) Nanoindentation deformation of refine-grained AZ31 magnesium alloy: Indentation size effect, pop-in effect and creep behavior. Materials Science and Engineering A 725:522–529

111. Zhou J, He Y, Shen J, Essa FA, Yu J (2022) Ni/Ni3Al interface-dominated nanoindentation deformation and pop-in events. Nanotechnology. https://doi.org/10.1088/1361-6528/ac3d62

112. Kuhr BR, Aifantis KE (2019) The Formation and Evolution of Defects in Nanocrystalline Fe During Indentation: The Role of Twins in Pop-Ins. Phys Status Solidi B Basic Res. https://doi.org/10.1002/pssb.201800370

113. Zhang J, Wang W, Zhang T, Yan Z, Shi N (2021) Mechanical Characterization of The Plastic Deformation Behavior of AZ31 Magnesium Alloy Processed Through Spinning Using Nanoindentation. Transactions of the Indian Institute of Metals 74:1349–1359

114. Wang H, Wu P, Kurukuri S, Worswick MJ, Peng Y, Tang D, Li D (2018) Strain rate sensitivities of deformation mechanisms in magnesium alloys. Int J Plast 107:207–222

115. Zhou G, Liu R, Tang W, Li D, Peng Y, Wu P (2021) Strain-Rate Sensitivities of Different Deformation Mechanisms in AZ31B Magnesium Alloy Sheet at Various Temperatures. JOM 73:1419–1427

116. Choi IC, Lee DH, Ahn B, Durst K, Kawasaki M, Langdon TG, Jang J Il (2015) Enhancement of strain-rate sensitivity and shear yield strength of a magnesium alloy processed by high-pressure torsion. Scr Mater 94:44–47

117. Somekawa H, Schuh CA (2012) High-strain-rate nanoindentation behavior of fine-grained magnesium alloys. J Mater Res 27:1295–1302

118. Sun HQ, Shi YN, Zhang MX, Lu K (2007) Plastic strain-induced grain refinement in the nanometer scale in a Mg alloy. Acta Mater 55:975–982

119. Chen X, Liu C, Wan Y, Jiang S, Han X, Chen Z (2021) Formation of nanocrystalline AZ31B Mg alloys via cryogenic rotary swaging. Journal of Magnesium and Alloys. https://doi.org/10.1016/j.jma.2021.11.021

120. Bazhenov VE, Li A V., Komissarov AA, Koltygin A V., Tavolzhanskii SA, Bautin VA, Voropaeva OO, Mukhametshina AM, Tokar AA (2021) Microstructure and mechanical and corrosion properties of hot-extruded Mg–Zn–Ca–(Mn) biodegradable alloys. Journal of Magnesium and Alloys 9:1428–1442

121. Mahmoodi M, Sedighi M, Tanner DA (2012) Investigation of through thickness residual stress distribution in equal channel angular rolled Al 5083 alloy by layer removal technique and X-ray diffraction. Mater Des 40:516–520

122. Dastgerdi JN, Sheibanian F, Remes H, Toudeshky HH, Barton J (2021) metals Influences of Residual Stress, Surface Roughness and Peak-Load on Micro-Cracking: Sensitivity Analysis. https://doi.org/10.3390/met

123. Chen Q, Mao WG, Zhou YC, Lu C (2010) Effect of Young's modulus evolution on residual stress measurement of thermal barrier coatings by X-ray diffraction. Appl Surf Sci 256:7311–7315

124. Rathinasuriyan C, Kumar VSS (2017) Experimental investigation of weld characteristics on submerged friction stir welded 6061-T6 aluminum alloy. Journal of Mechanical Science and Technology 31:3925–3933

125. Du S, Yang K, Li M, Li JR, Ren YP, Huang QY, Pan HC, Qin GW (2022) Achieving high strength above 400 MPa in conventionally extruded Mg-Ca-Zn ternary alloys. Sci China Technol Sci 65:519–528

126. Kavyani M, Ebrahimi GR, Ezatpour HR, Jahazi M (2022) Microstructure refinement, mechanical and biocorrosion properties of Mg–Zn–Ca–Mn alloy improved by a new severe plastic deformation process. Journal of Magnesium and Alloys 10:1640–1662

127. Xia S, Liu Y, Fu D, Jin B, Lu J (2016) Effect of Surface Mechanical Attrition Treatment on Tribological Behavior of the AZ31 Alloy. J Mater Sci Technol 32:1245–1252

128. Zhang L, Han Y (2009) Twins formation and their role in nanostructuring of zirconium. Materials Science and Engineering A 523:130–133

129. Liu X, Xu R (2022) Microstructure Evolution and Thermal Stability of Mg-Sm-Ca Alloy Processed by High-Pressure Torsion. J Mater Eng Perform 31:2644–2652

130. Shen JH, Li YL, Wei Q (2013) Statistic derivation of Taylor factors for polycrystalline metals with application to pure magnesium. Materials Science and Engineering: A 582:270–275

131. Liu H, Wei X, Xing S, Wang L, Zhu W, Jiang C, Ji V, Zhan K (2021) Effect of stress shot peening on the residual stress field and microstructure of nanostructured Mg-8Gd-3Y alloy. Journal of Materials Research and Technology 10:74–83

132. Trojanová Z, Drozd Z, Lukáč P, Džugan J (2022) Stress Relaxation Tests: Modeling Issues and Applications in Magnesium Alloys and Composites. J Mater Eng Perform. https://doi.org/10.1007/s11665-022-06951-w

133. Li F, Chen G, Dong T, Zhu C, Chen K (2023) Microplastic deformation activating residual stress relief for Al alloy. Int J Mech Sci. https://doi.org/10.1016/j.ijmecsci.2023.108446

134. Wang JS, Hsieh CC, Lai HH, Kuo CW, Wu PTY, Wu W (2015) The relationships between residual stress relaxation and texture development in AZ31 Mg alloys via the vibratory stress relief technique. Mater Charact 99:248–253

135. Zhuang WZ, Halford GR (2001) Investigation of residual stress relaxation under cyclic load.

136. Yang MX, Li RG, Jiang P, Yuan FP, Wang YD, Zhu YT, Wu XL (2019) Residual stress provides significant strengthening and ductility in gradient structured materials. Mater Res Lett 7:433–438

137. Song X, Liu WC, Belnoue JP, Dong J, Wu GH, Ding WJ, Kimber SAJ, Buslaps T, Lunt AJG, Korsunsky AM (2012) An eigenstrain-based finite element model and the evolution of shot peening residual stresses during fatigue of GW103 magnesium alloy. Int J Fatigue 42:284–295

138. WU S xu, WANG S ren, WANG G qi, YU X chun, LIU W tao, CHANG Z qi, WEN D sheng (2019) Microstructure, mechanical and corrosion properties of magnesium alloy bone plate treated by high-energy shot peening. Transactions of Nonferrous Metals Society of China (English Edition) 29:1641–1652

139. Witecka A, Yamamoto A, Idaszek J, Chlanda A, Świeszkowski W (2016) Influence of biodegradable polymer coatings on corrosion, cytocompatibility and cell functionality of Mg-2.0Zn-0.98Mn magnesium alloy. Colloids Surf B Biointerfaces 144:284–292

140. Bahmani A, Lotfpour M, Taghizadeh M, Kim WJ (2022) Corrosion behavior of severely plastically deformed Mg and Mg alloys. Journal of Magnesium and Alloys 10:2607–2648

141. Kubacka D, Yamamoto A, Wieciński P, Garbacz H (2019) Biological behavior of titanium processed by severe plastic deformation. Appl Surf Sci 472:54–63

142. Wang Z, Yan Y, Qiao L (2017) Protein adsorption on implant metals with various deformed surfaces. Colloids Surf B Biointerfaces 156:62–70

143. Talha M, Ma Y, Kumar P, Lin Y, Singh A (2019) Role of protein adsorption in the bio corrosion of metallic implants – A review. Colloids Surf B Biointerfaces 176:494–506

144. Ren XD, Yang XQ, Zhou WF, Huang JJ, Ren YP, Wang CC, Ye YX, Li L (2018) Thermal stability of surface nano-crystallization layer in AZ91D magnesium alloy induced by laser shock peening. Surf Coat Technol 334:182–188

145. Sun HQ, Shi YN, Zhang MX (2009) Sliding wear-induced microstructure evolution of nanocrystalline and coarse-grained AZ91D Mg alloy. Wear 266:666–670

146. Kumbhar NK, Kumar V, Hosmani SS (2024) Influence of Surface Mechanical Attrition Treatment Parameters on Microstructure and Residual Stress of Mg5Zn0.2Ca Alloy. J Mater Eng Perform 33:3746–3757

147. Chen XF, Xiao LR, Ding ZG, Liu W, Zhu YT, Wu XL (2020) Atomic segregation at twin boundaries in a Mg-Ag alloy. Scr Mater 178:193–197

148. Sun Q, Fang X, Wang Y, Tan L, Zhang X (2018) Changes in misorientations of $\{10\bar{1}1\}$ twin boundaries in deformed magnesium alloy. J Mater Sci 53:7834–7844

149. Basha DA, Rosalie JM, Somekawa H, Miyawaki T, Singh A, Tsuchiya K (2016) Microstructure study of a severely plastically deformed Mg-Zn-Y alloy by application of low angle annular dark field diffraction contrast imaging. Sci Technol Adv Mater 17:115–127

150. Siahsarani A, Samadpour F, Mortazavi MH, Faraji G (2021) Microstructural, Mechanical and Corrosion Properties of AZ91 Magnesium Alloy Processed by a Severe Plastic Deformation Method of Hydrostatic Cyclic Expansion Extrusion. Metals and Materials International 27:2933–2946

151. Liu X, Xi T, Zheng Y (2014) Influence of the extraction parameters on the cytotoxicity test results of Mg materials. Progress in Natural Science: Materials International 24:507–515

152. Ng WF, Chiu KY, Cheng FT (2010) Effect of pH on the in vitro corrosion rate of magnesium degradable implant material. Materials Science and Engineering C 30:898–903

153. Yamamoto A, Hiromoto S (2009) Effect of inorganic salts, amino acids and proteins on the degradation of pure magnesium in vitro. Materials Science and Engineering: C 29:1559–1568

154. Gollapudi S (2012) Grain size distribution effects on the corrosion behaviour of materials. Corros Sci 62:90–94

155. Gao JH, Guan SK, Ren ZW, Sun YF, Zhu SJ, Wang B (2011) Homogeneous corrosion of high pressure torsion treated Mg-Zn-Ca alloy in simulated body fluid. Mater Lett 65:691–693

156. Martynenko N, Lukyanova E, Anisimova N, et al (2020) Improving the property profile of a bioresorbable Mg-Y-Nd-Zr alloy by deformation treatments. Materialia (Oxf). https://doi.org/10.1016/j.mtla.2020.100841

157. Barberi J, Mandrile L, Napione L, Giovannozzi AM, Rossi AM, Vitale A, Yamaguchi S, Spriano S (2022) Albumin and fibronectin adsorption on treated titanium surfaces for osseointegration: An advanced investigation. Appl Surf Sci. https://doi.org/10.1016/j.apsusc.2022.154023

158. Kumbhar NK, Yamamoto A, Wadhonkar K, Baig MS, Hosmani SS (2025) The effect of severe surface deformation on microstructure refinement, corrosion, and biocompatibility of Mg5Zn0.2Ca alloy. J Alloys Compd. https://doi.org/10.1016/j.jallcom.2024.178259

159. Kumbhar NK, Kumar V, Singh D, Hosmani SS (2023) Gradient Microstructure and Properties of Surface Mechanical Attrition–Treated AZ91D Alloy: An Effect of Colliding Balls Velocity. Adv Eng Mater. https://doi.org/10.1002/adem.202300549

160. Ren CX, Wang Q, Hou JP, Zhang ZJ, Zhang ZF (2021) Effect of work-hardening capacity on the gradient layer properties of metallic materials processed by surface spinning strengthening. Mater Charact. https://doi.org/10.1016/j.matchar.2021.111179

161. Nie JF, Shin KS, Zeng ZR (2020) Microstructure, Deformation, and Property of Wrought Magnesium Alloys. Metall Mater Trans A Phys Metall Mater Sci 51:6045–6109

162. Fata A, Faraji G, Mosavi Mashadi M, Tavakkoli V (2016) Hot tensile deformation and fracture behavior of ultrafine-grained AZ31 magnesium alloy processed by severe plastic deformation. Materials Science and Engineering A 674:9–17

163. Marya M, Hector LG, Verma R, Tong W (2006) Microstructural effects of AZ31 magnesium alloy on its tensile deformation and failure behaviors. Materials Science and Engineering: A 418:341–356

164. Miura T, Fujii K, Fukuya K, Ando M, Tanigawa H (2018) Micro-tensile testing of reduced-activation ferritic steel F82H irradiated with Fe and He ions. Nuclear Materials and Energy 17:24–28

165. Liu Y, Jin B, Li D-J, Zeng X-Q, Lu J (2015) Wear behavior of nanocrystalline structured magnesium alloy induced by surface mechanical attrition treatment. Surf Coat Technol 261:219–226

166. Sun HQ, Shi YN, Zhang MX (2008) Wear behaviour of AZ91D magnesium alloy with a nanocrystalline surface layer. Surf Coat Technol 202:2859–2864

167. Li B, Wang Z, Kong M, Li J, Wang W, Zang T, Zheng H (2025) Tailoring the surface integrity and wear resistance of WE43 Mg alloy by warm laser shock peening. Journal of Materials Research and Technology 35:1504–1518

168. Yang M, Ouyang W, Li S, Long G, Zhang D, Dai Y (2024) Microstructure, wear resistance, corrosion behavior, and cytotoxicity of Mg-Zn-Ca amorphous coatings fabricated by laser surface melting. Surfaces and Interfaces 48:104278

169. Fan Z, Kang C, Li X, Li C, Huang H, Jiang Z (2025) Advances in acoustic emission monitoring for grinding of hard and brittle materials. Journal of Materials Research and Technology 36:1379–1408

170. Čtvrtlík R, Čech J, Tomáštík J, Václavek L, Haušild P (2022) Plastic instabilities explored via acoustic emission during spherical nanoindentation. Materials Science and Engineering: A. https://doi.org/10.1016/j.msea.2022.143019

Curriculum Vitae

PERSONAL DATA

Name	Nilesh Kashinath Kumbhar
Date of Birth	8th Nov. 1988
Nationality	Indian

EDUCATION

2007 - 2011   **Karmaveer Bhaurao Patil College of Engineering, Shivaji University, Kolhapur (India)**
B.E. (Production Engineering)
Thesis Title: Design and Fabrication of Dual Friction Drive

2012 - 2014   **Rajarambapu Institute of Technology, Islampur (India)**
M.Tech. (Automobile Engineering)
Thesis Title: Synthesis and Characterization of Magneto-Rheological (MR) Fluids for Automotive MR Brake Application

2021 - 2025   **Indian Institute of Technology, Indore (India)**
Ph.D. (Metallurgical Engineering and Materials Science), Pursuing
Thesis Title: Microstructure, Mechanical Properties, and Biocompatibility Studies on Severely Surface-Deformed Mg Alloys

EXPERIENCE

2014 - 2021   **Department of Mechanical Engineering, Gharda Institute of Technology, Khed (India)**
Assistant Professor

2011 - 2012   **Cooper Corporation Pvt. Ltd. Satara (India)**
Junior Engineer

AWARDS AND HONOURS

2024   SERB International Travel Support Grant (ITS): Awarded by the Science and Engineering Research Board (SERB), India, to attend and present at the 16th Biometal Symposium held in Krakow, Poland

2023   3-Month Internship Award, National Institute for Materials Science Japan